

**Electric field-induced directed assembly of diblock  
copolymers and grain boundary grooving in metal  
interconnects**

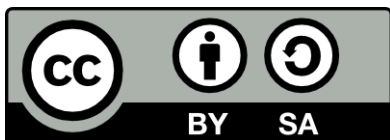
Zur Erlangung des akademischen Grades  
**Doktor der Ingenieurwissenschaften**  
von der KIT-Fakultät für Maschinenbau des  
Karlsruher Institut für Technologie (KIT)

genehmigte  
**Dissertation**

von

**M.Eng. Arnab Mukherjee**

Tag der mündlichen Prüfung :	30th April, 2019
Hauptreferent :	Prof. Dr. rer. nat. Britta Nestler
Korreferent 1 :	Prof. Dr.-Ing. habil. Marc Kamlah
Korreferent 2 :	Prof. Dr. habil. Mathis Plapp



This work is licensed under the Creative Commons Attribution-ShareAlike 4.0 International License. To view a copy of this license, visit <http://creativecommons.org/licenses/by-sa/4.0/>.

# Abstract

Application of electric field on materials lead to intriguing effects. Different class of materials are subjected to an external field either as a part of a processing treatment, or by mere virtue of its application. When employed as a processing treatment, electric field can modulate the microstructure in metals, alloys, ceramics and polymers thereby altering the material properties. Alternatively, a number of applications, for instance in electronic devices, also involve materials to be utilized as component which are subjected to intense currents on a daily basis. Permanent displacement of atoms can lead to open circuit failures, compromising the reliability of the entire device. The present dissertation explores one application each where electric field can lead to either favorable, or deleterious consequences, with the aid of phase-field modeling.

In the first part of the thesis, a diffuse-interface model is developed and employed to study the directed self-assembly of symmetric diblock copolymers under the concurrent influence of electric field, substrate affinity and confinement. Various limiting geometries are studied and a set of phase diagrams in electric-field-substrate-strength for various film thicknesses are characterized. In addition to identifying the presence of parallel, perpendicular and mixed lamellae phases similar to previous analytical calculations and experimental observations, we also find a region in the phase diagram corresponding to one-half integral lamellar spacing where hybrid morphologies such as wetting layers at the vicinity of the substrate coexisting with either holes in the middle of the film or perpendicular cylindrical domains coexist. The study is further extended to three dimensions, where, the latter morphology is characterized as a hexagonally perforated lamellar (HPL) phase. For the first time, it is shown that electric field can instigate an order-order transition from a lamellar to a HPL phase. Kinetic pathways of the transition additionally reveal the perforated lamellae to be an intermediate structure during parallel-to-perpendicular lamellar transition in thin films.

In the following part, various damage modes initiating from grain boundary (GB) grooves due to electromigration (EM) in nanoscale interconnects are elucidated. To this end, a single component polycrystalline phase-field model which takes into account the electron wind force, is employed. The model and its numerical implementation is first

benchmarked with the sharp interface theory of surface diffusion-mediated thermal grooving of Mullins. Thereafter, it is shown that GB flux due to electromigration can drastically affect the mode of progressive EM damage. Rapid atomic transport along the surface leads to a shape-preserving surface drift, while, a faster GB atomic transport localizes the damage in form of intergranular slits with a shape-preserving tip. The phase-field simulations further highlights the role of curvature- or EM-induced healing fluxes running along the surface which replenish the groove and delay damage dissemination. For the first time, a numerical model is extended to study spatio-temporal damage initiation, propagation, self-healing, grain coarsening in three-dimensional interconnects. Subsequently, a critical comparison of the solutions of grooving in finite grains obtained from sharp interface and phase-field method reveals that inconsideration of the EM-induced surface flux in the sharp interface theories can lead to significant errors both in terms of estimation of groove shapes and regime of damage modes. Finally, a new sharp interface model for finite grains, which takes into account the effect of concurrent capillarity, and EM-induced surface flux, and EM-induced GB flux is formulated to address the discrepancies. The predictions from the new model shows excellent agreement with the phase-field model.

The results of the present dissertation successfully demonstrates the feasibility and applicability of the phase-field method in capturing the essential physics of the problem and tackling the microstructure evolution in electric field-induced phenomenon efficiently and elegantly.

# Kurzfassung

Das Anlegen eines elektrischen Feldes an Materialien hat eine faszinierende Wirkung. Unterschiedliche Werkstoffklassen sind einem externen elektrischen Feld entweder als ein Teil der Verarbeitung oder aufgrund der alleinigen Applikation ausgesetzt. Wenn das elektrische Feld für die Verarbeitung verwendet wird, kann dieses die Mikrostruktur in Metallen, Legierungen, Keramiken und Polymeren verändern, wodurch die physikalischen Eigenschaften verändert werden. Alternativ können mehrere Einsatzmöglichkeiten wie beispielsweise der Einsatz in elektronischen Geräten dazu führen, dass Materialien als Komponenten verwendet werden, die täglich intensiven Stromstärken ausgesetzt sind. Eine ständige Verlagerung der Atome kann zu Fehlern im offenen Stromkreis führen, wodurch die Zuverlässigkeit des gesamten Geräts beeinträchtigt wird. Mit Hilfe der Phasefeldmethode wird in der vorliegenden Dissertation jeweils ein Anwendungsfall untersucht, in dem das elektrische Feld entweder positive oder negative Folgen haben kann.

Im ersten Teil der Arbeit wird ein diffuses Grenzflächenmodell entwickelt und für die Untersuchung der gerichteten Selbstorganisation von symmetrischen Diblock-Copolymeren verwendet, die gleichzeitig durch das elektrische Feld, die Substrataffinität und die Beschränkung beeinflusst werden. Es werden verschiedene beschränkende Geometrien untersucht und eine Reihe an Phasendiagrammen für unterschiedliche Schichtdicken charakterisiert, die das Verhältnis zwischen dem elektrischen Feld und der Substratstärke zeigen. Zusätzlich zu der Ermittlung der vorhandenen parallelen, senkrechten und gemischten Lamellenphasen findet man, ähnlich wie bei den vorausgegangenen analytischen Berechnungen und experimentellen Beobachtungen, auch einen Bereich im Phasendiagramm, der einem Lamellenabstand der Größe eines halben Integrals entspricht, in dem hybride Morphologien wie Benetzungsschichten in der Nachbarschaft des Substrats koexistieren, die entweder Löcher in der Mitte der Schicht oder senkrechte zylinderförmige Bereiche aufweisen. Des Weiteren wird die Untersuchung auf drei Dimensionen erweitert, in denen die letztgenannte Morphologie als eine hexagonal perforierte (HPL) Lamellenphase charakterisiert wird. Erstmals wird gezeigt, dass durch ein elektrisches Feld ein Ordnungs-Übergang von einer Lamellenphase zu einer HPL-Phase hervorgerufen werden kann. Außerdem zeigt der kinetische Verlauf des Übergangs, dass es sich bei den perfori-

erten Lamellen, die während des Übergangs von parallelen zu senkrechten Lamellen in Dünnschichten entstehen, um Zwischenstrukturen handelt.

Im Folgenden werden verschiedene Beschädigungsarten erläutert, die aufgrund der Elektromigration (EM) in Nanoverbindungen durch die Rille der Korngrenze verursacht werden. Dazu wird ein einkomponentiges, polykristallines Phasenfeldmodell verwendet, das die Windstärke der Elektronen berücksichtigt. Das Modell und dessen numerische Umsetzung wird erst mit der scharfen Grenzflächentheorie von Mullins verglichen, bei der die thermische Rillenbildung durch Oberflächendiffusion vermittelt wird. Anschließend wird gezeigt, dass die Art der durch die fortschreitende Elektromigration verursachten Schädigung stark durch einen Fluss durch Grenzflächen beeinträchtigt werden kann, der aufgrund der Elektromigration stattfindet. Ein schneller atomarer Transport entlang der Oberfläche führt zu einer formerhaltenden Versetzung der Oberfläche, während der Schaden durch einen schnelleren atomaren Transport durch Grenzflächen in Form von interkristallinen Schlitzen mit einer formerhaltenden Spitze lokalisiert wird. Durch die Phasenfeldsimulationen wird die Funktion von krümmungs- und EM-induzierten heilenden Strömungen entlang der Oberfläche weiter hervorgehoben, die die Rille wieder auffüllen und die Schadensausbreitung verzögern. Erstmals wird ein numerisches Modell erweitert, um die räumlich-zeitliche Schadenseinleitung, die Ausbreitung, die Selbstheilung und die Kornvergrößerung in dreidimensionalen Verbindungen zu untersuchen. Anschließend zeigt ein kritischer Vergleich der aus der scharfen Grenzflächenmethode und der Phasenfeldmethode gewonnenen Lösungen bezüglich der Rillenbildung, dass sowohl bei der Ermittlung der Rillenformen als auch beim Verlauf der Schadensart erhebliche Fehler entstehen können, wenn der durch die Elektromigration induzierte Oberflächenfluss in den Theorien der scharfen Grenzflächen nicht berücksichtigt wird. Zur Beseitigung der Diskrepanzen wird schließlich ein neues scharfes Grenzflächenmodell für finite Körner formuliert, das die zeitgleiche Kapillarwirkung und den durch die Elektromigration induzierten Oberflächen- und Grenzflächenfluss berücksichtigt. Die mit dem neuen Modell getroffenen Vorhersagen zeigen eine sehr gute Übereinstimmung mit dem Phasenfeldmodell.

Durch die Ergebnisse der vorliegenden Arbeit wird die Durchführbarkeit und Anwendbarkeit der Phasenfeldmethode in Bezug auf die Erfassung der erforderlichen Physik des Problems und in Bezug auf die Bewältigung der mikrostrukturellen Entwicklung effizient und elegant in einem Phänomen verdeutlicht, das durch ein elektrisches Feld verursacht wird.

# Preface

Electric field is known to orient ordered phases of block copolymers, thereby enabling precise control to tailor microstructures. Metal conductors on the other hand when subjected to high current density lead to atomic diffusion due to interaction between the conducting electrons and metal atoms. Permanent displacement of atoms lead to open circuit failure. The present thesis is devoted to understand the effect of the electric field on block copolymers and electromigration in metals.

To this end, numerical models based on the phase-field method are formulated in Chapters 3 and 4. The directed assembly of block copolymers under the combined influence of electric field, substrate affinity and confinement is explored in Chapters 5 and 6. Insights into the interplay of various mass transport mechanisms during grain boundary grooving due to electromigration are highlighted in Chapters 7 – 10 with a view to prolong the lifetime of device.

The numerical models and the results presented in part II and III respectively have been either published or submitted in the following peer-reviewed articles :

**Article 1** : A. Mukherjee\*, R. Mukherjee, K. Ankit, A. Bhattacharya, and B. Nestler, Phys. Rev. E, 93 (3),032514, 2016

**Article 2** : A. Mukherjee\*, K. Ankit, A. Reiter, M. Selzer, and B. Nestler, Phys. Chem. Chem. Phys., 18 (36), 25609, 2016

**Article 3** : A. Mukherjee\*, K. Ankit, R. Mukherjee, and B. Nestler, J. Electron. Mater., 45 (12), 6233, 2016

**Article 4** : A. Mukherjee\*, K. Ankit, M. Selzer, and B. Nestler, Phys. Rev. Appl., 9 (4), 044004, 2018

**Article 5** : A. Mukherjee\*, M. Selzer, and B. Nestler, To be submitted

**Article 6** : A. Mukherjee\*, J. Santoki, M. Selzer, and B. Nestler, To be submitted

The thesis is concluded in the final chapter summarizing the findings along with

---

\*Corresponding Author

possible future extensions of the presented results.

I have obtained the permission from all the co-authors and publishers to partially or entirely use the published results (including texts, equations, tables and figures) in current thesis. The corresponding contributions of the co-authors to the articles have been stated in the Declaration of Originality. Apart from these stated contributions, other scientific contributions are mine, unless otherwise declared. Figures 2.1, 2.3, 2.4, 2.6, 2.7, 2.8, 2.9 and 2.10 are taken from literature and the permission to use these figures has been granted by the corresponding publishers. The license for usage of copyrighted figures is limited to the present thesis.

# No Objection Certificate

As a coauthor, I hereby claim no objection if the first author (Mr. Arnab Mukherjee) uses the attached article(s) entirely or in-parts, for his doctoral thesis submitted to the Faculty of Mechanical Engineering, Karlsruhe Institute of Technology. Further, I do not object to the description of my contributions as laid in Arnab Mukherjee's thesis.

The specific no objection certificate is being issued on the specific request by the first author.

*- Signed by all the coauthors  
October 1, 2018*

# Declaration of Originality

## Respondents' contribution to the articles

**Article 1 :** As the first author, the respondent (Arnab Mukherjee abbreviated as AM) formulated the theoretical model with inputs from Rajdip Mukherjee (RM), Kumar Ankit (KA) and Avisor Bhattacharya (AB). AM wrote the code for the numerical implementation of the model along with the necessary post-processing tools. AM performed the numerical simulations and analyzed the data. AM wrote the manuscript with inputs from RM, KA, AB and Britta Nestler (BN).

**Article 2 :** AM wrote the preliminary code for the numerical implementation of the 3D model along with the necessary post-processing tools. AM performed the numerical simulations, analyzed the data and wrote the manuscript with inputs from KA, Andreas Reiter (AR), Michael Selzer (MS), and BN. AR and MS assisted in the parallelization of the code to facilitate computation efficiency. KA and MS assisted in the visualization of the 3D data.

**Article 3 :** AM formulated the theoretical model with inputs from KA and RM. AM wrote the code for the numerical implementation of the model along with the necessary post-processing tools. AM performed the numerical simulations and analyzed the data. AM wrote the manuscript with inputs from KA, RM, and BN.

**Article 4 :** AM performed the numerical simulations and analyzed the data. AM wrote the manuscript with inputs from KA, MS, and BN.

**Article 5 :** AM performed the analytical as well as numerical calculations and analyzed the data. AM wrote the manuscript with inputs from MS, and BN.

**Article 6 :** AM performed the analytical as well as numerical calculations and analyzed the data. AM wrote the manuscript with inputs from Jay Santoki (JS), MS, and BN. JS assisted in the calculation of the steady state solution space along with the interpretation.

# Acknowledgements

“It’s the journey, not the destination” pretty much sums up the life of a grad student. The journey in itself is an enriching one with it’s share of highs and lows, failures and successes, times spent in utter bewilderment and joys of completing the puzzle. At the end, it teaches you to be patient and like the spider from the story “Robert the Bruce and a spider”, never to give up trying, for one day, we will succeed. I take this opportunity to thank all the people who have made this journey an amazing experience.

I acknowledge my deepest gratitude to Prof. Britta Nestler for providing me the opportunity to pursue my doctoral dissertation at the Institute of Applied Materials - Computational Materials Science (IAM-CMS), Karlsruhe Institute of Technology (KIT). Her unconditional support, motivation and freedom during the last five years has not only made the journey pleasant, but has helped me evolve as an independent researcher. Thank you Ma’am for your decisive inputs and prompt attention to all matters both academic and otherwise.

I would like to thank Prof. Marc Kamlah and Prof. Mathis Plapp for agreeing to participate in the thesis committee and their invaluable time in reviewing the dissertation. Their comments and suggestions have considerably refined the thesis and motivated me to dig a bit more in my work.

I am grateful to the financial support from the ministry of the state Baden-Wuerttemberg through the initiative “Mittelbau” and from “Bundesministerium fuer Wirtschaft und Energie” within the project “KerSoLife 100” at different stages of the research.

I have been fortunate to be a part of a vibrant and an interdisciplinary research group which has allowed me to observe the multi-facets of the phase-field modeling from close corners. Special thanks to the group leaders, both former and present, Dr. Rajdip Mukherjee, Dr. Kumar Ankit, Dr. Michael Selzer and post-doc Dr. Avisor Bhattacharya for their guidance during the initial stages of my Ph.D. Acknowledgment is also due to Sumanth Nani, Dr. Fei Wang, Dr. Oleg Tschukin, Dr. Daniel Schneider, Jay Santoki, Ramanathan Perumal and Paul Hoffrogge for many a technical discussion from which I have gained immensely. Periodic feedbacks from the group members during the group

talks have enriched the quality of the work. Listening and following the research of my peers, in turn, has inspired me to strive for constant improvement. I thank all the group members for the wonderful memories.

Acknowledgement is due to the technical staff at the IAM-CMS, Christof Ratz and Halil Bayram for their support in both hardware and software related issues which helped me go about my work smoothly. Big thanks to Leon Geisen for his editorial assistance and the German translation of the abstract. I also thank the secretariat at Institute of Materials and Processes (IMP)/Institute of Digital Materials Science (IDM) at the Hochschule Karlsruhe and IAM-CMS, KIT especially Ms. Claudia Hertweck-Maurer, Ms. Stephanie Mueller and Ms. Inken Heise for all their help with the paper work during my visit to conferences and visa applications.

Life inside the lab would not have been stress-free without the quality time spent outside. The weekend group activities in form of cricket, beach volleyball and poker made up for a refreshing escape from the sometimes monotonous daily life. Nani, Jay, Walter, Nishant, Nikhil, Amol, Pavan and Ali were the constant companions in crime. Thank you guys for being my family away from home.

Finally, it would not have been possible to endure the tough periods alone without the support, love and empathy of my family : Baba, Maa, Dada, Kaka, Kaki and Ujjaini. Thank you for being there for me everytime I needed someone to talk to and my apologies for not being able to spend as much time as you would have wanted in the last couple of years. I dedicate my thesis to you.

# Contents

<b>I Introduction and Literature review</b>	<b>1</b>
<b>1 Introduction : Motivation &amp; Synopsis</b>	<b>2</b>
<b>2 Literature Review</b>	<b>9</b>
2.1 Effect of electric field on materials : Boon or Bane? . . . . .	9
2.2 Effect of surface, confinement and electric field on block copolymers . . . . .	11
2.2.1 Electrothermodynamics of BCPs . . . . .	16
2.2.1.1 Electrostatics in SSL . . . . .	17
2.2.1.2 Electrostatics in WSL . . . . .	22
2.3 Electromigration in metallic conductors . . . . .	23
2.3.1 Accelerated EM testing : Drift velocity experiments . . . . .	25
2.3.2 Pathways of EM . . . . .	28
2.3.3 Grain boundary grooving under electromigration . . . . .	28
2.4 Role of numerical modeling in addressing electric-field-induced problems . . . . .	31
<b>II Methods : Phase-field formulation</b>	<b>34</b>
<b>3 Phase-field model for directed assembly of block copolymers due to substrate affinity and electric field</b>	<b>35</b>
3.1 Ohta-Kawasaki or Non-local Cahn-Hilliard Model . . . . .	35
3.1.1 Mass conserving property . . . . .	38
3.1.2 Length scale in the system . . . . .	38
3.1.3 Linear Stability . . . . .	39

3.1.4	Two regimes of microphase separation . . . . .	41
3.1.5	Forms of $f(\psi)$ . . . . .	42
3.2	Effect of surfaces on binary mixture . . . . .	42
3.2.1	Specific choice of $\Phi(\psi_s)$ and its physical interpretation . . . . .	44
3.3	Diffuse-interface formalism to study combined effect of substrate affinity and electric field on symmetric diblock copolymers . . . . .	47
<b>4</b>	<b>Phase-field model for grain boundary grooving under electromigration</b>	<b>52</b>
4.1	Sharp-interface description . . . . .	52
4.2	Diffuse-interface model . . . . .	54
4.3	Numerical Discretization . . . . .	60
4.4	Boundary Conditions . . . . .	62
4.5	Asymptotic analysis : Motion of the free surface . . . . .	63
4.5.1	Outer expansion . . . . .	65
4.5.2	Inner expansion . . . . .	66
4.5.2.1	Leading order . . . . .	67
4.5.2.2	Next-to-leading order . . . . .	68
4.5.2.3	Higher orders . . . . .	70
4.6	Relationship to sharp-interface model . . . . .	72
4.6.1	Interfacial properties . . . . .	72
4.6.1.1	Antiphase boundary . . . . .	72
4.6.1.2	Interphase boundary . . . . .	74
4.6.1.3	Selection of gradient energy coefficients and barrier heights	76
4.6.2	Kinetic parameters . . . . .	76
4.6.3	Electrical properties . . . . .	78
4.7	Applicability, limitations and possible extensions of the model . . . . .	79
<b>III Results and Discussion :</b>		
	<b>Electric field-induced directed assembly of diblock copolymers</b>	<b>82</b>
<b>5</b>	<b>Influence of substrate interaction and confinement on electric field in-</b>	

<b>duced transition in symmetric block copolymer thin films</b>	<b>83</b>
5.1 Introduction . . . . .	83
5.2 Results . . . . .	84
5.2.1 Determination of equilibrium lamellar thickness . . . . .	85
5.2.2 Effect of electric field and surfaces . . . . .	87
5.2.2.1 Thicker films with $L_y \gg L_o$ . . . . .	87
5.2.2.2 Films with $L_y \approx L_o$ . . . . .	92
5.2.2.3 Films with $L_y < L_o$ . . . . .	94
5.2.3 Phase diagram . . . . .	97
5.2.4 Role of dielectric contrast . . . . .	102
5.3 Discussions and Conclusions . . . . .	105
<b>6 Electric-field-induced lamellar to hexagonally perforated lamellar transition in diblock copolymer thin films : Kinetic pathways</b>	<b>110</b>
6.1 Introduction . . . . .	110
6.2 Results . . . . .	111
6.2.1 Effect of substrate interaction, confinement and electric field : Phase diagram . . . . .	111
6.2.2 Lamellar to HPL transition : Kinetic Pathways . . . . .	114
6.2.2.1 Transition in monolayer films (BAB) . . . . .	114
6.2.2.2 Transition in bilayer films (BABAB) . . . . .	117
6.2.2.3 Perforated lamellae as an intermediate stage in parallel lamellar to perpendicular lamellar transition . . . . .	122
6.3 Discussion and Concluding Remarks . . . . .	124
<b>IV Results and Discussion :</b>	
<b>Grain boundary grooving due to electromigration</b>	<b>128</b>
<b>7 Theory of thermal grooving : Comparison between phase-field simulations and Mullins' theory</b>	<b>129</b>
7.1 Introduction . . . . .	129
7.2 Sharp-interface relations . . . . .	130

---

7.3	Results . . . . .	134
7.4	Discussion and Concluding remarks . . . . .	143
<b>8</b>	<b>Electromigration-induced surface drift and slit propagation in polycrystalline interconnects</b>	<b>148</b>
8.1	Introduction . . . . .	148
8.2	Results . . . . .	149
8.2.1	GB diffusion-limited regime (GBDLR) . . . . .	149
8.2.1.1	Morphological evolution . . . . .	149
8.2.1.2	Grooving-Drift characteristics . . . . .	150
8.2.1.3	Effect of electric field . . . . .	150
8.2.1.4	Effect of grain size . . . . .	152
8.2.2	Surface diffusion limited regime (SDLR) . . . . .	153
8.2.2.1	Morphological evolution . . . . .	153
8.2.2.2	Slit propagation kinetics . . . . .	154
8.2.2.3	Effect of electric field . . . . .	154
8.2.2.4	Effect of grain size . . . . .	155
8.2.3	Role of surface and GB as EM pathway . . . . .	156
8.2.4	Polycrystalline line . . . . .	158
8.3	Discussions and Concluding Remarks . . . . .	163
<b>9</b>	<b>Effect of electromigration on grain-boundary grooving at finite grain size: Comparison of sharp interface and phase-field simulations</b>	<b>166</b>
9.1	Introduction . . . . .	166
9.2	Sharp Interface Relations . . . . .	168
9.2.1	Analytical approach . . . . .	168
9.2.2	Numerical Approach . . . . .	170
9.3	Results . . . . .	171
9.3.1	No grain boundary flux . . . . .	172
9.3.1.1	Steady state groove profiles . . . . .	172

9.3.1.2	Temporal evolution of the groove depth . . . . .	173
9.3.2	Grooving under electromigration . . . . .	176
9.3.2.1	Steady state groove profiles . . . . .	176
9.3.2.2	Temporal evolution of groove depth . . . . .	177
9.3.2.3	Role of EM surface flux . . . . .	179
9.3.2.4	Drift velocity . . . . .	181
9.4	Discussion and Conclusion . . . . .	182
<b>10</b>	<b>Grain boundary grooving in finite grains due to concurrent surface and grain boundary electromigration</b>	<b>186</b>
10.1	Introduction . . . . .	186
10.2	Sharp-interface model . . . . .	187
10.3	Analytical solution of the linearized equation . . . . .	190
10.4	Results . . . . .	192
10.4.1	Effect of $M$ on the groove profile . . . . .	192
10.4.2	Effect of $\chi$ on the groove profile . . . . .	192
10.4.3	Comparison of the solution of non-linear and linearized equation .	195
10.4.4	Steady state solution space . . . . .	196
10.4.5	Comparison with Phase-field model . . . . .	200
10.5	Discussion and Conclusion . . . . .	201
<b>V</b>	<b>Conclusions and Future Directions</b>	<b>203</b>
<b>11</b>	<b>Conclusions and future directions</b>	<b>204</b>
11.1	Conclusions . . . . .	204
11.2	Future directions . . . . .	206
11.3	Other avenues .... . . . .	209
<b>VI</b>	<b>Appendices</b>	<b>211</b>
<b>Appendix A</b>	<b>Different sharp interface limits of the phase-field model of chapter 4</b>	<b>212</b>

A.1	Case I : $M \rightarrow M/\epsilon$ and $L_\eta \rightarrow L_\eta/\epsilon$ . . . . .	212
A.2	Case II : $M \rightarrow M/\epsilon$ and $L_\eta \rightarrow L_\eta/\epsilon^3$ . . . . .	213
A.3	Case III : Degenerate $L_\eta$ with different scalings . . . . .	214
<b>Appendix B Relating normal velocity <math>V_n</math> and <math>\frac{\partial y}{\partial t}</math></b>		<b>215</b>
B.1	Possibility 1 . . . . .	215
B.2	Possibility 2 . . . . .	216
B.3	What does the mass conservation equation mean ? . . . . .	216
B.4	Which possibility is consistent with the mass conservation equation ? . .	217
B.4.1	Possibility 1 . . . . .	217
B.4.2	Possibility 2 . . . . .	217
<b>Appendix C Calculation of curvature along the profile</b>		<b>219</b>
<b>Appendix D Determination of steady state</b>		<b>220</b>
D.1	Groove depth . . . . .	220
D.2	Profile perimeter . . . . .	220
D.3	Steady state velocity . . . . .	222
<b>Appendix E Additional benchmark comparisons of the sharp-interface model of chapter 10 and phase-field solutions</b>		<b>223</b>
E.1	Effect of $M$ on groove profiles . . . . .	223
E.2	Invariance of groove profile on $\chi$ for $M = \Gamma$ . . . . .	224
E.3	Effect of conductivity ratio on groove profiles . . . . .	224
<b>Appendix F Phase-field model with only grain boundary electromigration (GBEM)</b>		<b>226</b>
<b>List of Symbols</b>		<b>228</b>
<b>Bibliography</b>		<b>235</b>

# **Part I**

## **Introduction and Literature review**

# Chapter 1

## Introduction : Motivation & Synopsis

Electric field manifests as a promising method to guide and control morphological transition of block copolymers. Directed self-assembly is attained either by reorientation of domains in the direction of the field or by order-order transition to an energetically more favorable structure. The increase in field with decreasing system size lends as an effective and efficient choice in modulating morphologies especially in thin films of nano dimensions.

On the other hand, electric field in metals used in electronic devices can lead to open circuit failure by promoting void nucleation, growth and migration, hillock formation, localized thinning and grain boundary (GB) grooving by the phenomenon known as electromigration (EM). With progressive downscaling of electronic devices and a concomitant increase in the operating current densities, reliability issues pertaining to electromigration-mediated failure in interconnects is only expected to exacerbate in the years to come.

Mathematical modeling, such as the phase-field approach can help us improve the current understanding of electromigration failure mechanisms and kinetic pathways of electric field-induced pattern formation in soft matters. With the motivation to address the above mentioned phenomenon, the results of the present dissertation can be divided into two parts. In the first part, the effect of confined interacting walls on electric field-induced transition in symmetric block-copolymer thin films is elucidated in form of phase diagrams. Furthermore, hexagonally perforated lamellae, which until now is known to be only metastable in the bulk is shown to stabilize in film thicknesses close to one-half integral lamellar spacing due to concurrent influence of confinement, substrate affinity and applied field. In the second part of the thesis the role of capillary- and EM-mediated surface diffusion and EM-induced GB grooving is investigated. Two modes of damage

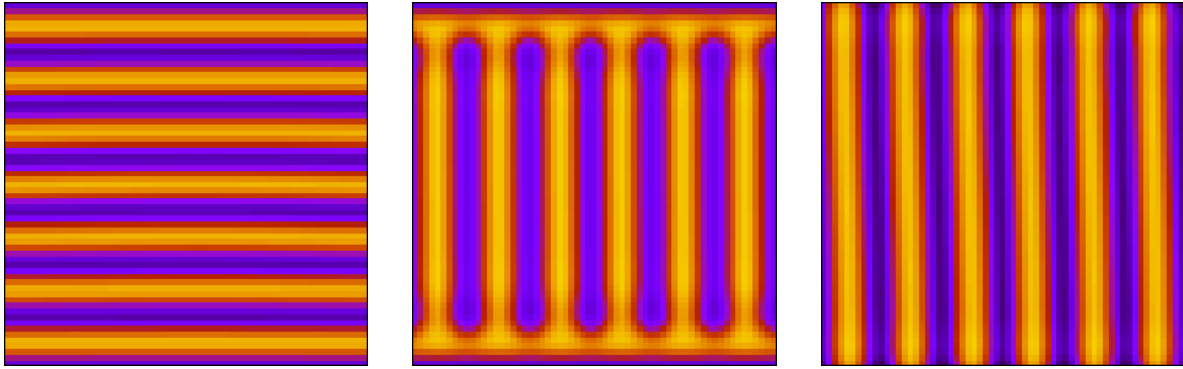


Figure 1.1: Parallel (left), mixed (center) and perpendicular (right) lamellae morphologies resulting from the competing effect of substrate interaction and applied electric field

in form of surface drift and intergranular slit are delineated depending upon the rate limiting transport mechanism. A comparison of the groove profiles obtained from phase-field method and sharp interface analytical and numerical solutions further reveal the importance of EM-induced surface flux not accounted in the latter which acts as an healing mechanism. A short graphical abstract of the results presented later in the thesis is provided below.

### 1. Influence of substrate interaction and confinement on electric-field-induced transition in symmetric block-copolymer thin films

Chapter 5 is devoted to the study of directed assembly of symmetric block copolymers (which form lamellae structure) due to competing substrate interaction, electric field, and confinement. A coarse-grained non-local Cahn-Hilliard which couples the Ohta-Kawasaki functional with Maxwell equation of electrostatics along with the contribution of substrate interaction which is proposed in chapter 3 is employed. The phase diagram consisting of parallel, mixed and perpendicular morphologies (see Fig.1.1) in electric-field-substrate strength space for different film thicknesses is calculated. In addition, the dependence of the critical fields for transition between the various phases on substrate strength, film thickness and dielectric contrast is discussed. Some preliminary three-dimensional results are also presented to corroborate the presence of other morphologies other than lamellae in symmetric system. The results presented in the chapter has been published in *Physical Review E* [1].

### 2. Electric-field-induced lamellar to hexagonally perforated lamellar transition in diblock copolymer thin films : kinetic pathways

Symmetric block-copolymers, are well known to evolve into parallel, mixed and perpendicular lamellar morphologies under the concomitant influence of an electric field and substrate affinity. In chapter 6 it is shown that an additionally imposed

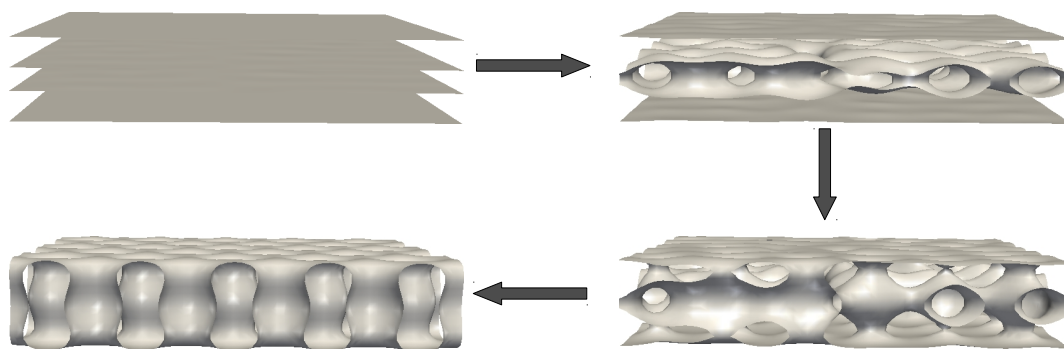


Figure 1.2: Parallel lamellar to hexagonally perforated lamellar transition in diblock copolymer bilayer films due to competing substrate interaction, electric field, and confinement

confinement can effectuate a novel parallel lamellar to hexagonally perforated lamellar (HPL) transition in monolayer and bilayer films (see Fig.1.2). HPL is shown to stabilize at large substrate affinity in a narrow region of the phase-diagram between parallel and perpendicular lamellar transitions in ultra-thin films. Additionally, perforated lamellae is also identified as an intermediate structure during parallel-to-perpendicular lamellar transition. Deeper insights into the kinetic pathways of the phase transition is systematically analyzed using the Minkowski functionals. The results presented in the chapter has been published in *Physical Chemistry Chemical Physics* [2].

### 3. Grain boundary grooving : Comparison between phase-field simulations and Mullins' theory

The phase-field model of grain boundary grooving under electromigration (EM) presented in chapter 4 (which has been published in *Journal of Electronic Materials*) is validated against the sharp-interface analytical theory of surface diffusion-mediated by Mullins' for isolated grooves in the absence of EM in chapter 7. Several benchmarking in terms of the temporal evolution of the groove depth and width (which obey a  $t^{1/4}$  law) and profile shapes (see Fig.1.3) are performed and critically compared to those obtained by Mullins'. The validity of the approximations made in deriving the sharp interface governing equation is elucidated. In addition, the self-similar behavior of the profiles and a preliminary comparison between the signatures of surface diffusion and volume diffusion-mediated profiles which can be used to discern the dominant atomic transport mechanism is also discussed.

### 4. Electromigration-induced surface drift and slit propagation in polycrystalline interconnects

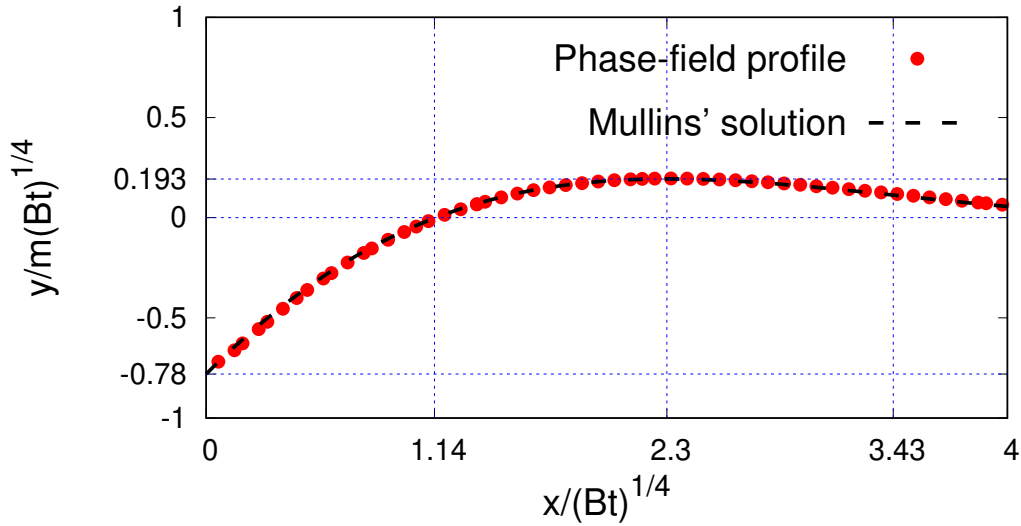


Figure 1.3: A comparison between the surface diffusion-mediated normalized groove profile obtained from sharp-interface analytical theory of Mullins and phase-field method measured along  $x$  and  $y$  directions.

In chapter 8, the electromigration damage in wide polycrystalline interconnects due to grain-boundary grooving is assessed. An interplay of surface and grain-boundary diffusion is shown to drastically influence the mode of progressive EM damage. Rapid atomic transport along the surface leads to shape preserving surface drift reminiscent of Blech drift velocity experiments as shown in Fig.1.4 (left-top). On the other hand, a comparatively faster grain-boundary transport localizes the damage resulting in the proliferation of intergranular slits with a shape preserving tip (Fig.1.4 left-bottom). In steady state, the two regimes exhibit an exponent of 1 and  $3/2$  respectively in Black's law. While surface drift obeys an inverse scaling with grain size, slits exhibit a direct relationship at small sizes with the dependence becoming weaker at larger ones. Furthermore, the influence of curvature- or EM-mediated healing fluxes running along the surface on groove replenishment is explained. Insights derived from phase-field simulations of EM in bi-crystals are extended to investigate the multiphysics of mixed-mode damage of polycrystalline interconnect line that is characterized by a drift of small grain surfaces, slit propagation and coarsening (see right column of Fig.1.4). The triple and quadruple junctions are identified as prominent sites of failure. The results presented in this chapter have been published in *Physical Review Applied* [3] and *Journal of Electronic Materials* [4].

## 5. Effect of electromigration on grain-boundary grooving at finite grain size : Comparison between sharp-interface and phase-field solution

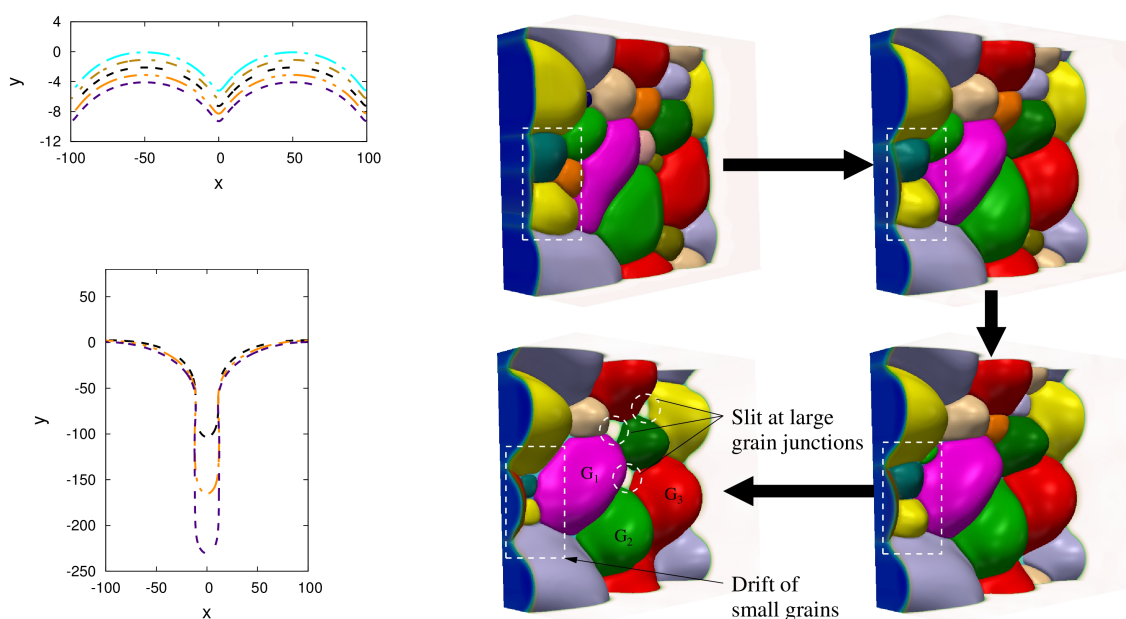


Figure 1.4: Various regimes of damage initiating from grain-boundary grooves depending upon the rate-limiting transport mechanism : surface drift (left-top), intergranular slit (left-bottom) and mixed-mode damage in polycrystalline interconnects (right).

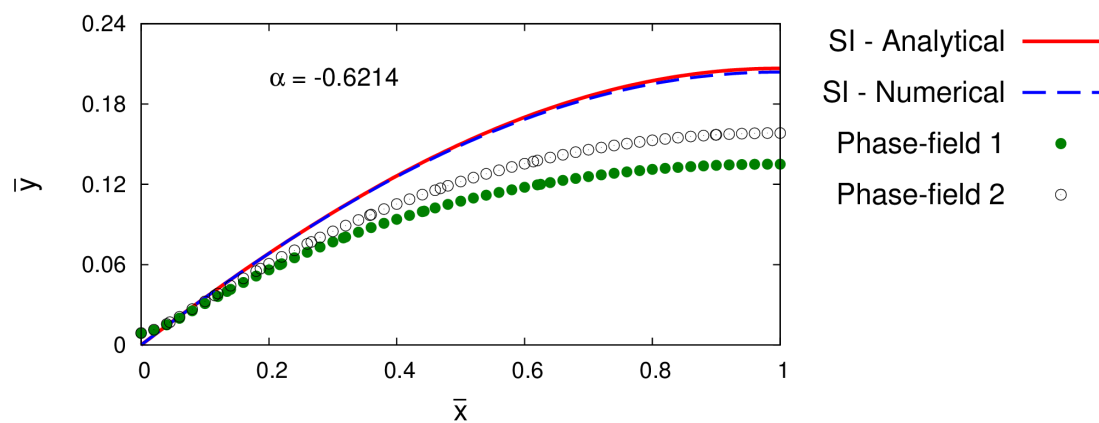


Figure 1.5: The discrepancy in the solution obtained from sharp interface analytical and numerical solution and phase-field method. While sharp interface model predicts a unique solution for a given value of  $\alpha$ , the phase-field gives rise to two solutions.

Grain boundary grooving damage due to electromigration in polycrystalline interconnect is investigated using sharp-interface and phase-field models in chapter 9. It is shown that the single parameter  $\alpha = \frac{J_{GB}\Omega L^2}{8B}$  where  $J_{GB}$  is the grain boundary flux,  $\Omega$  the atomic volume,  $L$  the grain size and  $B$  a material constant, used in the sharp-interface theory is inadequate to capture either the steady shape of the groove profile or the groove dimension when applied to the specific case of electromigration. Moreover, the sharp-interface solution is also found to be non-unique in  $\alpha$ . The discrepancies are rationalized in terms of electromigration-induced surface flux which introduces an additional degree of freedom to ascertain the morphology of the groove. The healing effect of electromigration in some cases lead to premature arrest of groove penetration in comparison to the thermal groove counterparts. Although the presence of electromigration accelerates the groove extension from a temporal  $t^{1/4}$  to a steady state  $t$  regime, the sharp interface analytical theory overestimates the displacement than the phase-field model as ascertained by performing virtual drift velocity experiments. The results presented in this chapter forms the content of a manuscript which has been submitted for publication.

## 6. Grain boundary grooving in finite grains due to concurrent surface and grain boundary electromigration

A sharp-interface model of steady state grain-boundary grooving of a periodic array of grains under isotropic conditions is formulated by considering the effect of concurrent capillarity, and electromigration-induced surface flux, and electromigration-induced grain-boundary flux in chapter 10. A second-order non-linear ordinary differential equation governing the profile shape is derived and solved numerically. It is shown that for a given inclination of the surface at the groove root  $\Gamma$  ( $\sin^{-1} \gamma_{GB}/2\gamma_s$ ), the groove profiles evolving under concurrent surface and grain-boundary electromigration is characterized by two independent parameters namely,  $\chi$  which denotes the ratio of capillary to EM force at the surface and  $M$ , depicting the competition between the rate of electromigration transport at the grain-boundary to the surface. For a given  $\chi$ , the groove depth relative to the surface maximum increases with increasing value of  $M$ . For  $M < \Gamma$ , decreasing  $\chi$  engenders a surface healing flux as a result of which the surface profiles become flatter thereby decreasing the groove depth and vice-versa for  $M > \Gamma$ . At  $M = \Gamma$ , the profiles are independent of  $\chi$  and assume a shape of constant curvature. Not all possible combinations of  $M - \chi - \Gamma$  results in a steady state and the typical steady-state solution regions are elucidated in two-dimensional  $M - \chi$ ,  $M - \Gamma$  and  $\chi - \Gamma$  space. The predictions from the theoretical model are further corroborated using the phase-field method (see Fig. 1.6) and the practical implications of the study are discussed. The results presented in this chapter form the content of a manuscript which has been

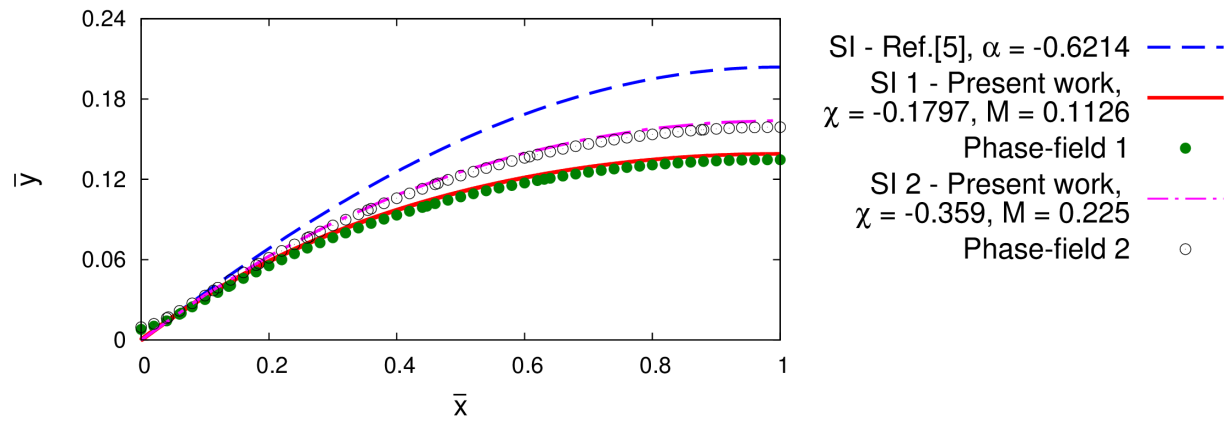


Figure 1.6: A comparison of the solution of groove profiles from sharp interface model of Ref.[5], sharp interface model presented in chapter 9 and phase-field model.

submitted for publication.

The thesis not only contributes to the advancement of our understanding of directed assembly of block copolymers and EM failure mechanisms due to GB grooving, but provides a general framework in phase-field models, exemplifying the applicability to tackle other electric field-induced physical phenomenon in materials science.

# Chapter 2

## Literature Review

### 2.1 Effect of electric field on materials : Boon or Bane?

A large number of material system in and around us are subjected to an electric field either as a part of a processing treatment or by mere virtue of its application. Different materials respond to the applied field disparately, depending upon its ability to conduct electricity. Materials can be broadly classified as conductors, insulators (or dielectrics) and semiconductors depending upon their response to the field. Conductors or metals are good carrier of electricity and contain a large number of free electrons which can move freely through the material. Most metals such as Copper, Aluminum, Gold etc. fall under this category. Poor conductors of electricity are termed as insulators. Unlike conductors which contain abundance of mobile charges, the dielectric or insulators are characterized by charges that are attached to specific atoms or molecules. However, this does not imply that they do not respond when placed in an electric field. Rather, the positively charged nucleus is displaced along the electric field and the electrons in opposite direction. As a result, a dipole moment is generated and the atom is said to be polarized. Glass, Mica, Wood, Diamond for instance are insulators. Semiconductors, such as Silicon and Germanium, are class of materials whose conductivity lies between that of conductors and insulators.

The classification of the materials can alternatively understood in terms of energy band theory. Conductors exhibit a complete overlap between the valence and the conduction bands. Hence, even at ambient temperature, a large number of electrons are available for conduction. A large forbidden gap of the order of 7 eV exists between the two bands in insulators. Only at very high temperatures or high voltage do these materials conduct. However, such conduction is rare and may lead to dielectric breakdown. The

forbidden gap in semiconductors is of the order of 1 eV. As a result, some energy in form of heat can raise the electrons from valence to conduction band leading to conductivity.

When employed as a processing treatment, electric field can be utilized to control microstructure of materials which dictates the applicability of the final product. For instance, the electric field is known to modulate morphologies in soft matter systems such as block copolymers [6, 7], polymer blends [8, 9] and fluids [10, 11]. Electrohydrodynamic processes have been exploited to replicate patterns on scales smaller than 100 nm by topographically structured electrodes [12, 13]. Application of an electric field has also been employed to control pattern formation in solidifying microstructures [14]. Rod spacing in directionally solidification of MnBi/Bi eutectics can be controlled by electric current pulsing [15]. Precise control of macro segregation or solute redistribution of impurities have been achieved in Al-Si alloys [16, 17]. Application of DC current during solidification of cast iron reduces the size of graphite flakes, alter their shapes and decrease the amount non-metallic inclusion [18]. DC and AC electric field are gaining popularity in enhancing consolidation and controlling grain growth during sintering processes of ceramics [19, 20, 21].

However, it is not always that an applied electric field act as a boon. In several applications, passage of an electric field leads to undesirable effects. Metallic conductors called interconnects invariably are subjected to intense current stressing during service conditions. Permanent displacement or loss of material known as electromigration ultimately leads to failure of devices [22, 23]. In battery technology, for instance in Lithium-ion batteries, under a certain range of current densities, highly branched dendritic structures are generated [24, 25]. Dendrites can perforate the insulating layers and lead to short circuit upon reaching the opposite electrode.

The present dissertation explores one application each where the electric field can lead to either beneficial or deleterious effect. Specifically, the intention is to study the effect of the electric field on directed self-assembly of diblock copolymers and the phenomenon of grain-boundary grooving due to electromigration in nanoscale interconnects. Each of the two topics are briefly reviewed one by one to create a necessary background and lay down the basic principles which facilitates the study and the interpretation of the results presented later in the thesis.

## 2.2 Effect of surface, confinement and electric field on block copolymers

Self-assembly of block copolymers (BCPs) has been an actively pursued field of study because of its wide technological implications [26, 27]. Diblock copolymers consist of two homopolymer units, linked by covalent bonds [26, 27]. Owing to the covalent bonding between the two blocks, these polymers undergo microphase separation below the order-disorder transition temperature (ODT), thereby, limiting the size of phase separated domains.[26] Depending upon the Flory interaction parameter( $\chi$ ) which scales inversely with temperature and the degree of polymerization  $N$ , block copolymers are categorized in two distinct regimes namely, weak segregation limit(WSL) and strong segregation limit(SSL).[27] If  $\chi N > 10$ , i.e. closer to the ODT, the block copolymers are characterized by a sinusoidal composition profile, with the microdomain period scaling as  $N^{\frac{1}{2}}$ .[28] On the other hand, if  $\chi N \gg 10$ , i.e. well below the ODT, block copolymers are characterized by a square wave composition profile with sharp interfaces between the two blocks and microdomain period scales as  $N^{\frac{2}{3}}$ .[29] The former regime is termed as weak segregation limit while the latter is termed as strong segregation limit [26, 27]. Depending upon the volume fraction of the components and segregation regime, block copolymers exhibit a range of periodic morphologies such as lamellae, gyroids, cylinders, spheres etc.[26, 27]. A typical phase diagram of a polyisoprene (PI)-polystyrene (PS) diblock copolymer system is shown in Fig.2.1.

In the absence of any external field, a symmetric diblock copolymer (equal volume fractions of both blocks) forms domains of lamellar morphology with various degrees of alignment. Practical applications, however, require complete alignment of the microphase separated domains. Effective stabilization of the desired morphologies can be instigated by means of external stimulus such as surface interaction [31], shear flow [32], electric [33] and magnetic fields [34] that is otherwise non-trivial especially in bulk samples. Microphase separation takes place on solid substrates which generally have affinity towards one of the monomer components. Typically, interfacial energy difference between the two blocks in contact with a substrate (i.e  $\gamma_{AS} \neq \gamma_{BS}$ , where  $\gamma_{AS}$  and  $\gamma_{BS}$  are the interfacial energies between a monomer A or B and substrate S) can cause surface induced ordering resulting in parallel arrangement of the domains with respect to the surface [35, 36, 37]. The extent of this parallel ordering depends upon the substrate interaction strength which ultimately determines the surface ordering length. A parallel ordered lamellae in a polystyrene- polymethyl metha acrylate thin film of thickness 300nm is shown in Fig.2.3(a). If the copolymer system is confined between two rigid substrate walls, two different interaction cases may be considered, (a) the walls are symmetric i.e. both walls

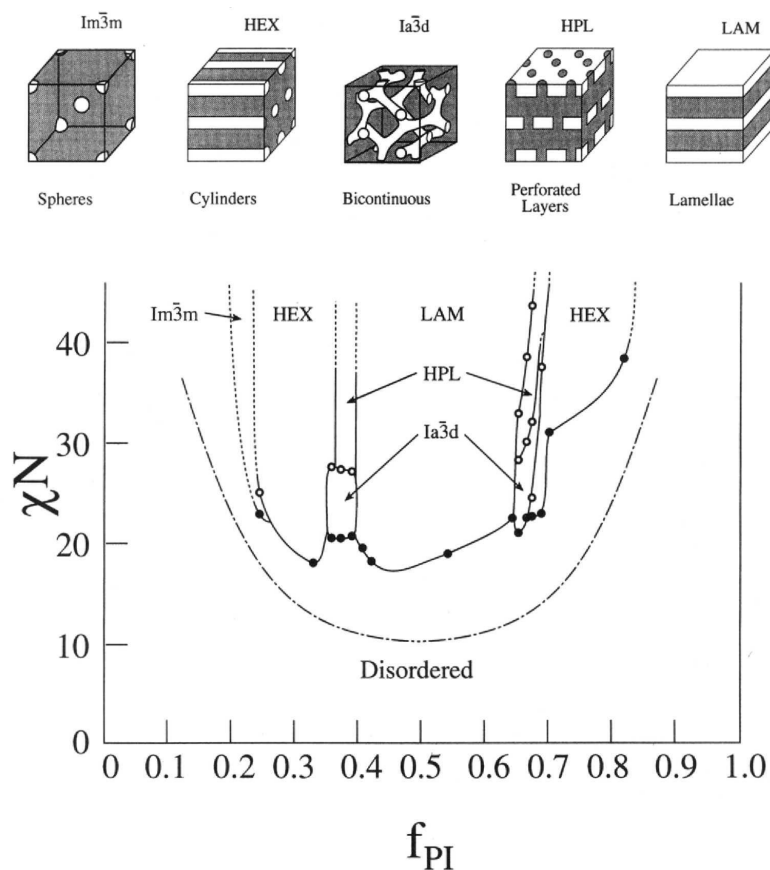


Figure 2.1: Phase diagram of a PI-PS diblock copolymer system. Five different ordered structures were reported in Ref. For a given volume fraction, increasing  $\chi N$  not only leads to disorder-order transition (filled circles) but also in certain cases to an order-order transition (open circles). Reprinted with permission from Khandpur et al. [30]. Copyright 1995 American Chemical Society.

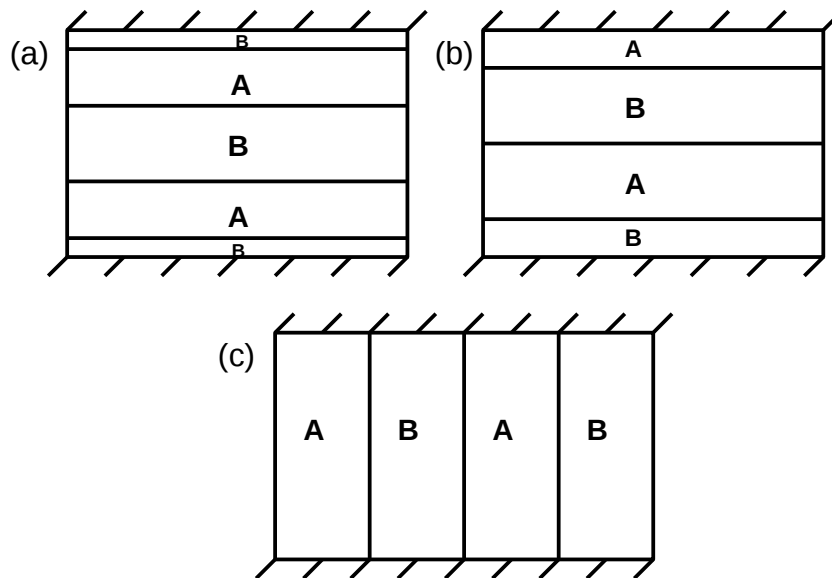


Figure 2.2: A schematic showing the various stable configurations in a symmetric diblock copolymer in presence of parallel walls/substrate (denoted by hatched lines). (a) Parallel lamellae in presence of symmetric wall interaction, (b) Parallel lamellae in presence of antisymmetric wall interaction, (c) Perpendicular lamellae arising either due to frustration or applied electric field.

attract the same monomer and (b) antisymmetric walls i.e. both walls attract different monomers [38, 39, 40, 41, 42]. As shown in Fig. 2.2 (a) and (b), the system either forms integral  $nL_o$  or half-integral  $(n + \frac{1}{2})L_o$  number of lamellae, where  $L_o$  is the equilibrium lamellar spacing, depending on whether the wall is symmetric or antisymmetric respectively [38, 39, 40, 41, 42]. Surface reconstructions are relevant in monolayer and bilayer thin films as they induce many interesting intermediate morphologies [43, 44].

Additionally, the confinement of the BCPs within parallel walls introduces a length scale constraint. If the film thickness is incommensurate with the lamellar spacing, the copolymers are said to be in a frustrated state [46]. The BCPs can either comply with this constraint by deviating from their natural length scale, which is typical in thicker films where the deviation can span over a large number of lamellae [39, 46] or alleviate frustration by adopting a perpendicular orientation with respect to the walls [38, 39, 40, 41, 42] as shown in Fig. 2.2(c). In extreme cases when the substrate interaction is large, a mere reorientation is energetically unfavorable while confinement can induce an order-order transition (OOT) to a more favorable structure [47]. For instance, in lamellae forming systems, the interference of composition waves emanating from the substrate can stabilize half-lamellae, hybrid and anti-hybrid structures [48]. Additionally, formation of holes at the center of film along with wetting layers has also been deduced in the past

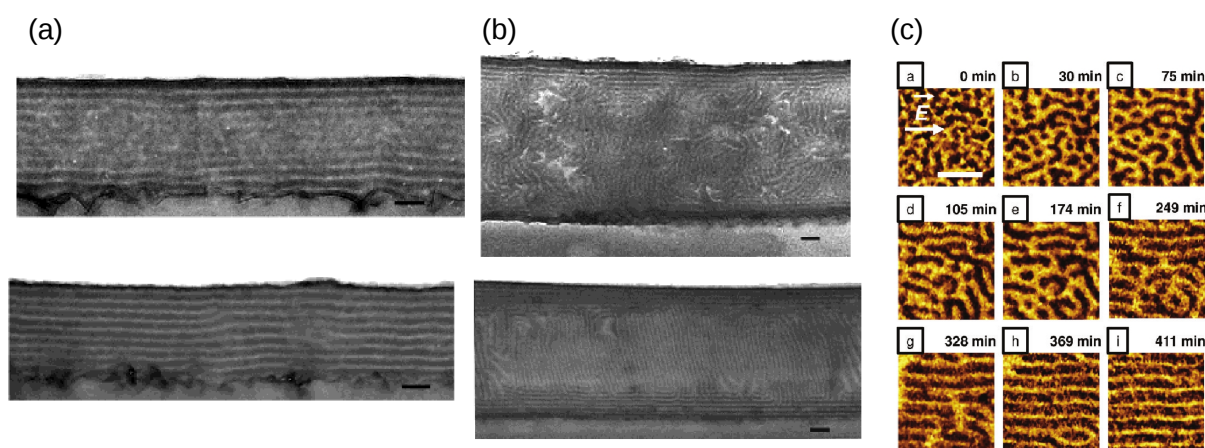


Figure 2.3: (a) Cross sectional TEM image of a 300nm PS-b-PMMA film annealed under  $40\text{V}/\mu\text{m}$  electric field of 3h (upper) and 6h (lower). The applied electric field is not high enough to overcome the effect of substrate affinity and a parallel morphology is seen to be stable. Scale bar : 100nm. (b) Cross sectional TEM image of a 700nm PS-b-PMMA film annealed under  $40\text{V}/\mu\text{m}$  electric field of 6h (upper) and 16h (lower). Few parallel layers closer to the substrate co-exist with perpendicular lamellae at the center of the film. Scale bar : 100nm. (c) Electric-field-induced complete alignment of PS-PHEMA-PMMA terblock tripolymer as observed in scanning electron microscopy starting from a disordered structure. The electric field strength corresponds to  $15\text{V}/\mu\text{m}$ . The cross section length scale corresponds to  $150\text{nm} \times 150\text{nm}$ . Fig. (a) and (b) reprinted with permission from Xu et al. [7]. Copyright 2004 American Chemical Society. Fig.(c) reprinted with permission from Olszowka et al.[45]. Copyright 2009 American Chemical Society.

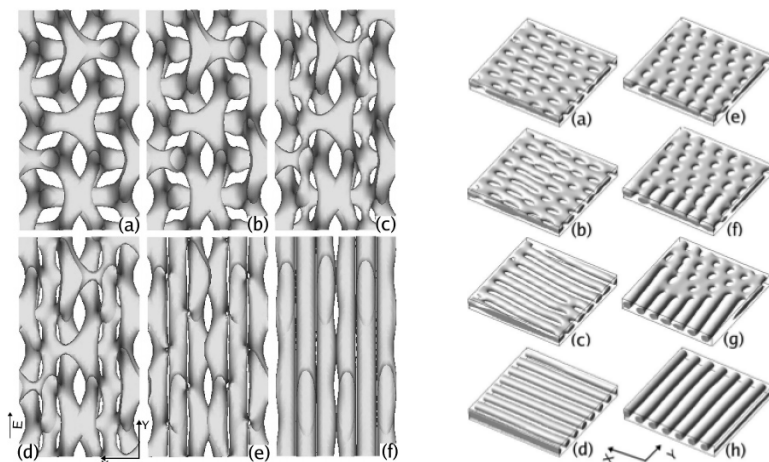


Figure 2.4: Electric-field-induced gyroid to cylinder (left) and hexagonally-perforated-lamellae to cylinder (right) transition studied using dynamical self-consistent field theory. The morphological transition takes place by elimination of electrostatically unfavorable junctions. Left fig. reprinted with permission from Ly et al [51]. Copyright 2007 American Chemical Society. Right fig. reprinted with permission from Ly et al. [52]. Copyright 2008 American Chemical Society.

[49, 50, 1]. In cylinder forming systems various combinations of parallel lamellae, parallel cylinders, perpendicular cylinders and perforated lamellae have been reported [43, 44].

From an experimental perspective, the electric field manifests as a promising external stimulus in inducing morphological transformations in BCPs because of the ease with which it can be applied, especially in thin films [53, 7]. Since the inception of the so-called “dielectric contrast” mechanism reported in the seminal work of Amundson and co-workers [6, 54], much of our understanding of electric-field-induced morphological transitions has evolved in the last decade. The suggested mechanism underpins the concept of an associated free energy penalty for perpendicular interface (with respect to the direction of electric field) between two phases possessing disparate permittivities. BCPs can elude the electrostatic penalty in two ways. One, the constituent monomers can reorient in the direction of applied electric field which is common in structures with a primary symmetry axis. Thus, parallel lamellae [55, 56, 57, 58] and cylinders [57, 59, 60] adopt a perpendicular configuration as shown in Fig.2.3(c), while spheres elongate in the direction of the applied field to form cylinders [7, 61, 62, 63]. Highly symmetric structures, on the other hand, mutate to a different motif by mutilation of electrostatically unfavorable interfaces resulting in OOT such as gyroid to cylinder [51, 64, 65] (Fig.2.4 left), hexagonally perforated lamellae (HPL) to cylinder [52, 66] (Fig.2.4 right) and HPL to lamellar transition [67] amongst others. Since electric field is readily applicable in thin films, there has been a recent upsurge in the investigations of electric-field-induced OOTs as exemplified in recent reviews [68, 69].

A lot of factors can aid or deter the evolving phase morphology in presence of electric field such as the segmental interaction or segregation  $\chi N$ , the substrate interaction strength and the confinement which can act as geometric barrier. The copolymers can be easily modulated at low segregation owing to weak segmental interaction between the two blocks [56, 59]. The substrate interaction can hinder the alignment process by electric field as then the applied field has to overcome the interfacial interaction [53] as shown in Fig.2.3(a). Confinement (film thickness) on the other hand can aid or hinder the alignment process by electric field depending upon its relation with the natural lamella period  $L_o$  [56, 70].

Concurrence of electric field, substrate affinity and confinement enhances the nature of intermediate morphologies [1]. Apparently, substrate interaction predominates closer to the walls but weakens upon translating towards the middle of the film. While, the electric field is dominant near the center of the film. As a result the morphology in the vicinity of the walls differs significantly from that in the middle. In symmetric BCPs, this trade-off leads to a mixed morphology where parallel lamellae in the proximity of the walls co-exist with perpendicular lamellae at the center of the film [55, 56, 57] as also shown in Fig.2.3(b). During electric-field-induced sphere to cylinder transition, substrate affinity instigates a surface enrichment layer possessing a hexagonal symmetry [60]. Similarly, experimental studies on gyroid forming BCPs revealed coexistence of perpendicular cylinder, perpendicular lamellar and HPL morphologies [71]. Additional complications may arise in monolayer and bilayer films where the film thickness is lower than the surface ordering length. In such cases an influence of substrate is experienced in the entire film wherein application of electric field can potentially engender novel OOTs-induced morphologies.

### 2.2.1 Electrothermodynamics of BCPs

The intention of the present section is to briefly review and understand the electrothermodynamics of BCPs and the interested readers are referred to the excellent reviews by Tsori [68] and Pester et al. [69] for details of the various effects of electric field, order-order transitions, disorder-order transitions and domain alignment mechanisms. Since the work in the dissertation focuses on symmetric BCPs which order into lamellar structure, the remaining of the section will only focus on this particular morphology. Moreover owing to the simple geometry, calculation of free energies of various configurations are analytically tractable.

As mentioned above, BCPs reorient in the direction of the applied electric field to avoid any interfaces between the two blocks. However, the basic analytical treatment

differs depending upon the weak and strong segregation regime. Both the cases are discussed separately next.

### 2.2.1.1 Electrostatics in SSL

Consider a stack of  $n$  parallel arranged lamellae (one lamellae consists of a A and a B block) with equilibrium lamellar spacing of  $L_o$  confined within a film of thickness  $L$ . Neglecting the effect of any frustration or deviation of the lamellar width from their natural value, the film thickness and lamellar spacing are related by  $L = nL_o$ . It is further assumed that the confined walls have a preferential affinity to the A block. The total interfacial energies  $F_s$  can then be written as,

$F_s =$  (Interfacial energy between the two blocks) + (Interfacial energy between A block and the surface)

For  $n$  lamellae, there are  $2n$  number of interfaces between the two blocks and two interfaces between the A block and the wall. As a result,

$$F_s = 2n\gamma_{AB}A + 2\gamma_{AS}A \quad (2.1)$$

where,  $\gamma_{AB}$  and  $\gamma_{AS}$  are the interfacial energies between the two blocks and A block and the wall respectively.  $A$  is the interfacial area. Since in SSL, the lamellae exhibit a square-wave composition profile, it is assumed that the two blocks are parallel plate capacitors with dielectric constants  $\epsilon_A$  and  $\epsilon_B$  respectively, separated by sharp interfaces connected in series. The effective capacitance of the parallel stack  $C_{\parallel}$ , can then be written as a sum of the inverse of the capacitance of  $n$  B blocks of thickness  $L_o/2$ ,  $n - 1$  inner A blocks of thickness  $L_o/2$  and the two A blocks at the surface of thickness  $L_o/4$ . In mathematical notation,

$$\frac{1}{C_{\parallel}} = \frac{nL_o}{2A\epsilon_B} + \frac{(n-1)L_o}{2A\epsilon_A} + \frac{2L_o}{4A\epsilon_A} \quad (2.2)$$

On rearranging, the effective capacitance writes as,

$$C_{\parallel} = \frac{\epsilon_A\epsilon_B}{\epsilon_A + \epsilon_B} \frac{2A}{L} \quad (2.3)$$

The electrostatic free energy  $F_{es}$  can then be written as,

$$\begin{aligned} F_{es} &= -\frac{1}{2}C_{\parallel}V^2 \\ &= -\frac{\epsilon_A\epsilon_B}{\epsilon_A + \epsilon_B} \frac{A}{L} V^2 \end{aligned} \quad (2.4)$$

where  $V$  is the applied voltage.

The net free energy per unit area of the parallel configuration  $F_{\parallel}$  can be written as the sum of interfacial and electrostatic contributions as,

$$F_{\parallel} = 2n\gamma_{AB} + 2\gamma_{AS} - \frac{\epsilon_A\epsilon_B}{\epsilon_A + \epsilon_B} \frac{V^2}{L} \quad (2.5)$$

$n$  perpendicularly arranged lamellae with the walls having an affinity towards A block is next considered. The interfacial energy  $F_s$  can be written as,

$F_s =$  (Interfacial energy between the two blocks) + (Interfacial energy between the A blocks and the surface) + (Interfacial energy between the B blocks and the surface)

$$\begin{aligned} F_s &= 2n\gamma_{AB}A + 2n\gamma_{AS}\frac{A}{2n} + 2n\gamma_{BS}\frac{A}{2n} \\ &= 2n\gamma_{AB}A + (\gamma_{AS} + \gamma_{BS})A \end{aligned} \quad (2.6)$$

It is to be noted that in the above Eq. the fact that each block has two interfaces with the walls of area  $A/2n$  has been utilized. The electrostatic part of the free energy can be deduced by considering the blocks to be connected in parallel configuration. Hence, the effective capacitance  $C_{\perp}$  writes as

$$\begin{aligned} C_{\perp} &= n\frac{A}{2n}\frac{\epsilon_A}{L} + n\frac{A}{2n}\frac{\epsilon_B}{L} \\ &= \frac{A}{2L}(\epsilon_A + \epsilon_B) \end{aligned} \quad (2.7)$$

The electrostatic energy in perpendicular configuration thus writes as,

$$\begin{aligned} F_{es} &= -\frac{1}{2}C_{\perp}V^2 \\ &= -\frac{1}{4}\frac{A}{L}(\epsilon_A + \epsilon_B)V^2 \end{aligned} \quad (2.8)$$

The net free energy per unit area of the perpendicular configuration  $F_{\perp}$  can be written as the sum of interfacial and electrostatic contributions as,

$$F_{\perp} = 2n\gamma_{AB} + \gamma_{AS} + \gamma_{BS} - \frac{1}{4L}(\epsilon_A + \epsilon_B)V^2 \quad (2.9)$$

The relative stabilities of the two configurations depend on the free energies, which in turn depends upon the parameters  $\gamma_{AB}$ ,  $\gamma_{AS}$ ,  $\gamma_{BS}$ ,  $\epsilon_A$  and  $\epsilon_B$ . The critical value of the voltage required for parallel to perpendicular transition can be found from the condition of  $\Delta F = F_{\perp} - F_{\parallel} = 0$ . This yields the critical voltage  $V_c$  as,

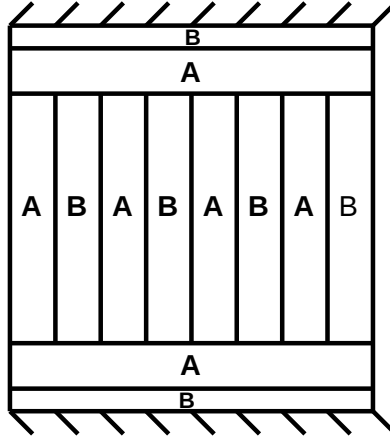


Figure 2.5: A schematic diagram of a mixed morphology with a monolayer of parallel stacking at the vicinity of the surface and perpendicular arrangement at the center of the film.

$$V_c = \frac{2(\gamma_{BS} - \gamma_{AS})^{1/2}(\epsilon_A + \epsilon_B)^{1/2} L^{1/2}}{(\epsilon_A - \epsilon_B)} \quad (2.10)$$

The critical electric field  $E_c$  reads as,

$$E_c = \frac{V_c}{L} = \frac{2(\gamma_{BS} - \gamma_{AS})^{1/2}(\epsilon_A + \epsilon_B)^{1/2}}{(\epsilon_A - \epsilon_B)} \frac{1}{L^{1/2}} \quad (2.11)$$

The above Eq. gives an important result that for an unfrustrated block copolymer within a symmetrically interacting wall, the critical field  $E_c$  scales as  $L^{-1/2}$  i.e. higher electric field is required to instigate a parallel to perpendicular lamellar transition as film thickness decreases.

As discussed above, due to short range nature of surface affinity one can also envisage a case as shown in Fig.2.5 where parallel and perpendicular lamellar structures co-exist. To derive the free energy of such a mixed morphology it is assumed that only a single alternate A-B block of thickness  $L_o/4$  and  $L_o/2$  respectively exists at the vicinity of both the walls. The interfacial energy contribution to the free energy writes as,

$$F_s = 2\gamma_{AS}A + 2\gamma_{AB}A + 2n\gamma_{AB}A + 2n\gamma_{AB}\frac{A}{2n} \quad (2.12)$$

The first term denotes the interaction between the A block and the wall on both ends. The second and the third term are the interfacial energies of A-B block in parallel and perpendicular configurations respectively. The final term represents the extra contribution at the T-junctions on either side. The effective capacitance of the configuration can

be thought of two parallel plate capacitors in series on either side at the proximity of the wall, additionally in series with  $n$  parallel plate AB capacitors. If  $C_1$  and  $C_3$  denotes the resultant capacitance of the two alternately arranged blocks then,

$$\frac{1}{C_{\parallel}} = \frac{1}{C_1} + \frac{1}{C_3} = \frac{L_o}{4A\epsilon_A} + \frac{L_o}{2A\epsilon_B} = \frac{L_o(\epsilon_B + 2\epsilon_A)}{4A\epsilon_A\epsilon_B} \quad (2.13)$$

The equivalent capacitance of the perpendicularly arranged lamellae  $C_2$  at the center is given by

$$C_2 = n \frac{A\epsilon_A}{2n(L - \frac{3}{2}L_o)} + n \frac{A\epsilon_B}{2n(L - \frac{3}{2}L_o)} \quad (2.14)$$

The effective capacitance of the mixed morphology can finally be written as,

$$\frac{1}{C_m} = \frac{1}{C_1} + \frac{1}{C_2} + \frac{1}{C_3} \quad (2.15)$$

Substituting Eqs.2.13 and 2.14 in the above Eq.,

$$C_m = \frac{4A\epsilon_A\epsilon_B(\epsilon_A + \epsilon_B)}{8\epsilon_A\epsilon_B L - 9\epsilon_A\epsilon_B L_o + 2\epsilon_A^2 L_o + \epsilon_B^2 L_o} \quad (2.16)$$

The free energy of the mixed morphology per unit area can written using Eqs.2.12 and 2.16 as

$$F_m = 2\gamma_{AS} + 3\gamma_{AB} + 2n\gamma_{AB} - \frac{\epsilon_m}{L} V^2 \quad (2.17)$$

where  $\epsilon_m = \frac{2\epsilon_A\epsilon_B(\epsilon_A + \epsilon_B)}{8\epsilon_A\epsilon_B - 9\epsilon_A\epsilon_B \frac{L_o}{L} + 2\epsilon_A^2 \frac{L_o}{L} + \epsilon_B^2 \frac{L_o}{L}}$ . Thus, depending upon the material parameters two critical electric fields  $E_{\parallel m}$  and  $E_{m\perp}$  required for parallel to mixed morphology transition and mixed to perpendicular morphology transition can be derived from Eqs. 2.5, 2.9 and 2.17 as

$$E_{\parallel m} = \sqrt{\frac{3\gamma_{AB}}{L(\epsilon_m - \epsilon_{\parallel})}} \quad (2.18)$$

$$E_{m\perp} = \sqrt{\frac{(\gamma_{BS} - \gamma_{AS}) - 3\gamma_{AB}}{L(\epsilon_{\perp} - \epsilon_m)}} \quad (2.19)$$

where  $\epsilon_{\parallel} = \frac{\epsilon_A\epsilon_B}{(\epsilon_A + \epsilon_B)}$  and  $\epsilon_{\perp} = \frac{(\epsilon_A + \epsilon_B)}{4}$ . Phase diagram based on the above free energy calculations was generated by Tsori and Andelman [56] and Pereira and Williams [55],

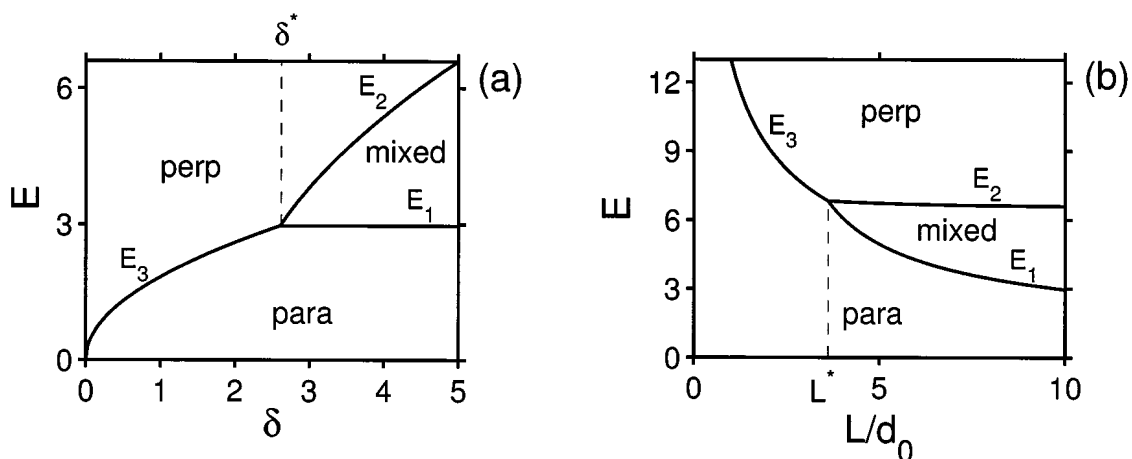


Figure 2.6: The phase-diagram of a symmetric diblock copolymer showing the stability regions of parallel, perpendicular and mixed lamellar morphology in (a)  $E - \delta$  space where  $\delta = \frac{\gamma_{BS} - \gamma_{AS}}{\gamma_T}$ ,  $\gamma_T$  denotes the interfacial energy of the T junctions and (b)  $E - L/d_0$  space where  $L$  is the film thickness and  $d_0$  is the equilibrium lamellar spacing. At lower  $\delta$  and film thickness, transition from parallel to perpendicular morphology is direct. Above a critical value of  $\delta^*$  and  $L^*$  respectively there exists two critical fields corresponding to parallel to mixed and mixed to perpendicular morphology. Reprinted with permission from Tsori and Andelman [56]. Copyright 2002 American Chemical Society.

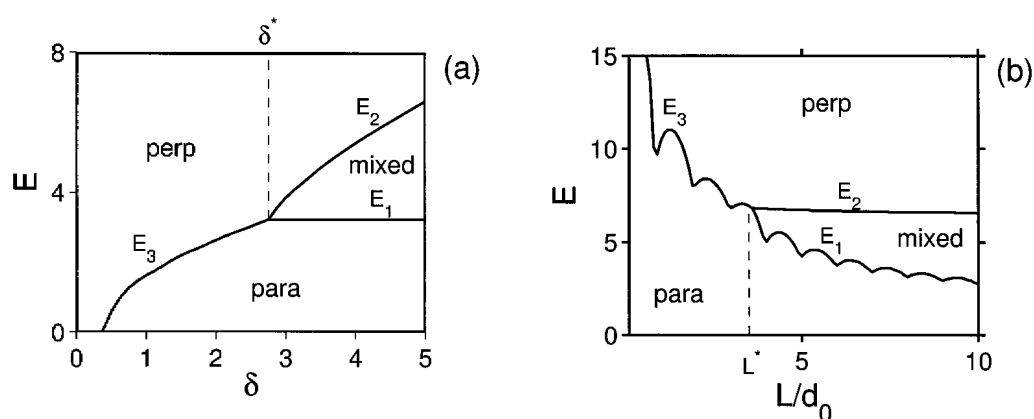


Figure 2.7: Phase diagram for strained films, where the film thickness is incommensurate with the natural lamellar spacing. (a) At lower substrate affinity a perpendicular state is favorable. (b) The critical field for parallel to mixed and parallel to perpendicular transition exhibits oscillations which can be attributed to the lower field required to achieve the morphological transition for film thickness corresponding to half-integral lamellar thickness. Reprinted with permission from Tsori and Andelman [56]. Copyright 2002 American Chemical Society.

designating the stability regions of the three morphologies. Typical slices on a  $E - \delta$  and  $E - L/d_o$  space is shown in Fig.2.6 , where,  $\delta = \frac{\gamma_{BS} - \gamma_{AS}}{\gamma_T}$  and  $d_o$  is the equilibrium lamellar width (same as  $L_o$  used here).  $\gamma_T$  denotes the interfacial energy of the T-junctions in the mixed state which can be equivalently represented in terms of  $\gamma_{AB}$ . It can be seen in Fig.2.6 that the mixed morphology is stable only above a critical value of  $\delta$  and film thickness  $L/d_o$ . In addition, the phase diagrams taking into account the effect of incommensurability was also calculated as shown in Fig.2.7 In such cases perpendicular state is favored at lower values of  $\delta$  and thin films. The critical fields for parallel to mixed and parallel to perpendicular lamellar transition exhibits oscillations. A lower value of applied electric field can instigate a morphological transition at  $L = (n + \frac{1}{2})d_o$  as compared to the  $L = nL_o$  film thicknesses.

### 2.2.1.2 Electrostatics in WSL

For the sake of simplicity, only the effect of electric field is considered in the present section with a rational of understanding the dielectric contrast mechanism. Additional effect of wall affinity can be found in Tsori and Andelman [56]. The electrostatic energy of the system is given by,

$$F_{es} = -\frac{1}{2} \int_V \epsilon(\mathbf{r}) |\mathbf{E}(\mathbf{r})|^2 d\mathbf{r} \quad (2.20)$$

$V$  is the volume of the domain. The dielectric constant  $\epsilon(\mathbf{r})$ , depends on the deviation of the local concentration from its equilibrium value  $\delta\psi(\mathbf{r}) = \psi(\mathbf{r}) - \psi^0(\mathbf{r})$ , and can be written as a Taylor series expansion until first order as,

$$\epsilon(\mathbf{r}) = \bar{\epsilon} + \Delta\epsilon\delta\psi(\mathbf{r}) \quad (2.21)$$

where,  $\bar{\epsilon} = (\epsilon_A + \epsilon_B)/2$  is the average permittivity of the mixture and  $\Delta\epsilon = (\epsilon_A - \epsilon_B)$  is the permittivity difference. The electric field can similarly be written as a sum of zeroth and first order terms as,

$$\mathbf{E}(\mathbf{r}) = \mathbf{E}_0 + \mathbf{E}_1 \quad (2.22)$$

where,  $\mathbf{E}_0$  is the applied electric field if the dielectric constant is the same everywhere in the system and  $\mathbf{E}_1$  is the deviation of the electric field from the applied value at any given point due to the variation of the dielectric constant according to Eq.(2.21).  $\mathbf{E}_1$  can further be written in terms of a scalar potential field as,

$$\mathbf{E}_1 = -\nabla\phi \quad (2.23)$$

The distribution of the electric field is given by the Maxwell Eq.,

$$\nabla \cdot [\epsilon(\mathbf{r})\mathbf{E}(\mathbf{r})] = 0. \quad (2.24)$$

Again, substituting Eqs.(2.21), (2.22) and (2.23) and taking into account terms until first-order,

$$\nabla^2 \phi = \frac{\Delta\epsilon}{\bar{\epsilon}} \nabla \delta\psi(\mathbf{r}) \cdot \mathbf{E}_0. \quad (2.25)$$

Taking Fourier transform we have,

$$\phi(\mathbf{k}) = -i \frac{1}{|\mathbf{k}|^2} \frac{\Delta\epsilon}{\bar{\epsilon}} \delta\psi(\mathbf{k})(\mathbf{k} \cdot \mathbf{E}_0) \quad (2.26)$$

Substituting the above solution in the Fourier transform of Eq.(2.23)

$$\mathbf{E}_1(\mathbf{k}) = -i\mathbf{k}\phi(\mathbf{k}) \quad (2.27)$$

we obtain

$$\mathbf{E}_1 = -\frac{\Delta\epsilon}{\bar{\epsilon}} \delta\psi(\mathbf{k}) \hat{\mathbf{k}}(\hat{\mathbf{k}} \cdot \mathbf{E}_0) \quad (2.28)$$

where  $\hat{\mathbf{k}} = \mathbf{k}/|\mathbf{k}|$  is the unit wave vectors. Therefore, substituting the above expression in Eq.(2.22), we obtain the electric field as

$$\mathbf{E}(\mathbf{k}) = \mathbf{E}_0 - \frac{\Delta\epsilon}{\bar{\epsilon}} \delta\psi(\mathbf{k}) \hat{\mathbf{k}}(\hat{\mathbf{k}} \cdot \mathbf{E}_0) \quad (2.29)$$

Using Eq.(2.29), Fourier transform of Eq.(2.21) and Parseval's theorem (which states that the total intensity of any physical amplitude is equal in real space as well as Fourier space), the anisotropic part of the free energy which is responsible for the alignment of microstructure is given by

$$F_{es} = \int \frac{1}{2} \frac{(\Delta\epsilon)^2}{\bar{\epsilon}} \delta\psi(\mathbf{k}) \delta\psi(-\mathbf{k}) (\mathbf{k} \cdot \mathbf{E}_0)^2 d^3\mathbf{k} \quad (2.30)$$

The above Eq. implies that there is a electrostatic free energy penalty for composition gradients not aligned along the field direction ( $\mathbf{k} \cdot \mathbf{E}_0 \neq 0$ ) and is proportional to the square of the dielectric contrast  $((\Delta\epsilon)^2)$ . However, it is to noted that the above Eq. is strictly valid closer to the ODT because of the assumption of small deviation of the composition from the equilibrium value which in turn allowed the use of Taylor expansion of the dielectric constant. The above Eq. is often supplemented with a Ginzburg-Landau type polynomial to study kinetic pathways of electric field-induced transition in soft matters [57, 64, 56].

## 2.3 Electromigration in metallic conductors

A metallic sample subjected to an external electric field or current exerts two distinct forces on the atoms of the conductor. Firstly, the applied field exerts a direct electrostatic force which propels the atoms in the direction of electric field. Secondly, the electrons

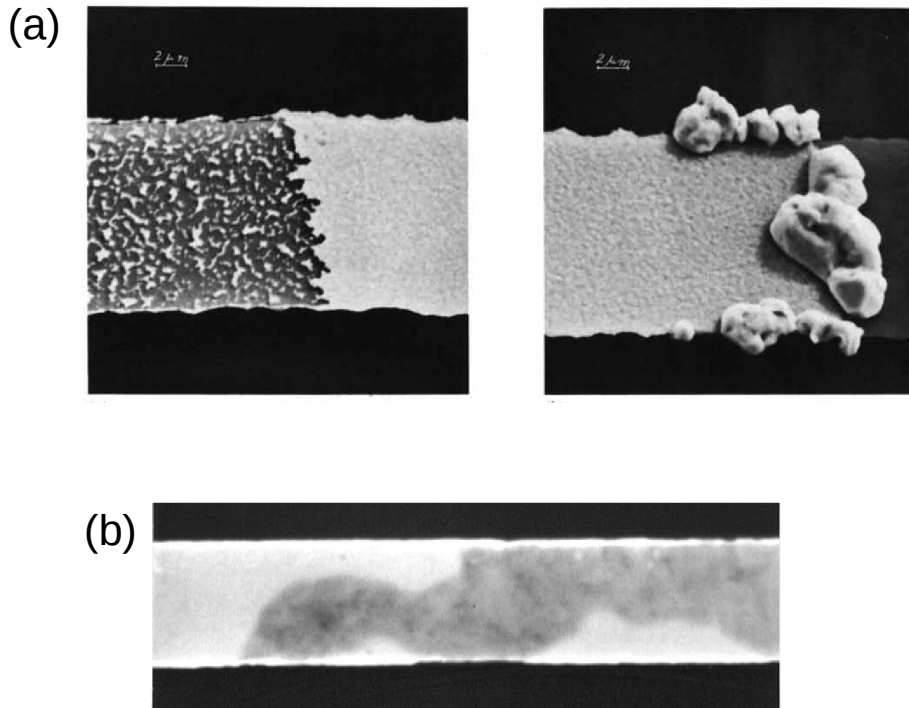


Figure 2.8: (a) Scanning-electron micrograph of a gold stripe on molybdenum substrate after passing of  $10^6 \text{ A/cm}^2$  current. The cathode side exhibits a drift with residual gold on the substrate. While mass is accumulated at the anode end. Reprinted from Blech and Klinsborn [75] with permission from Elsevier. (b) Global thinning of large areas after accelerated EM testing of thin film Copper conductors. Reprinted from Gladkikh et al. [76] with permission from IOP publishing.

which are accelerated in the direction opposite to that of the electric field collide with the diffusing atoms, thereby transferring momentum in the process which triggers atomic motion in the direction of the electron flow. Both these driving forces are proportional to the applied field and can be combined and expressed as,

$$F_{eff} = zeE \quad (2.31)$$

where  $z = z_e + z_w$  is the effective charge containing the effect due to electrostatic ( $z_e$ ) and electron wind force ( $z_w$ ),  $e$  is the electronic charge and  $E$  is the applied electric field. The phenomenon, known as electromigration (EM), raises serious reliability concern in modern integrated circuits [22, 23, 72]. EM damage in thin films has garnered much attention due to its implication in efficient designing of interconnects [73, 74].

Interconnects, often considered as the “roads” and “highways” of the modern day integrated circuits (ICs), connect various active elements comprising the microelectronics. While operational, interconnects carry intense electric current rendering them susceptible

to damage due to electromigration (EM) [72, 23, 77]. EM in interconnects, thus possess major reliability concerns, which otherwise may compromise the performance of the entire IC [73, 74, 73, 22].

The momentum transfer between conducting electrons and metal atoms can permanently displace atoms leading to material accumulation or depletion [22, 75]. Flux divergence is typically favored at microstructural heterogeneous sites such as grain boundaries (GBs) [78, 79], triple points [80, 81], dislocations [82, 83] and mixed grain size [84, 85] amongst others. EM-induced damage manifests in various forms which can broadly be classified into one of the following categories:

- The most commonly observed damage is thinning of large areas of the test piece typically observed in the SEM images of damaged lines after accelerated EM testing [76, 86]. A similar mode of damage was observed in the seminal drift velocity experiments of Blech and Kinsborn [75] and thereafter [87, 88, 89] as shown in Fig.2.8.
- The second form of damage commences through voiding, typically at sites of non-vanishing (positive) flux divergence [78]. The nucleated voids can evolve along the line preserving its shape or transform into finger-like slits [90, 91]. Slit growth may be transgranular [82, 92, 93, 94] or along the grain-boundaries (intergranular) [95, 96, 97]. Slits can also initiate from grain-boundary (GB) grooves where GBs intersect a free surface [98] or at sidewalls [99]. Some typical failed lines are shown in Fig.2.9.
- The third damage mode occurs as a result of negative flux divergence leading to mass accumulation. The material extrusions, known as hillocks as shown in Fig.2.10, lead to failure due to short circuiting between neighboring interconnect levels [100, 98, 101].

### 2.3.1 Accelerated EM testing : Drift velocity experiments

The most widely used set up for EM testing is the drift velocity set proposed by Blech and Kinsborn [75]. The test piece (such as Aluminum or Copper) is deposited on an underlayer material such as Molybdenum, Titanium nitride or Tantalum nitride. The base material is selected to have a lower conductivity than the test piece so that all the electric current should pass through it. In addition, the underlayer should not form any intermetallic compound with the test sample. High current is passed due to which the test piece drifts in the direction of electron flow. The edge displacement is measured from which an estimate of the drift velocity is inferred.

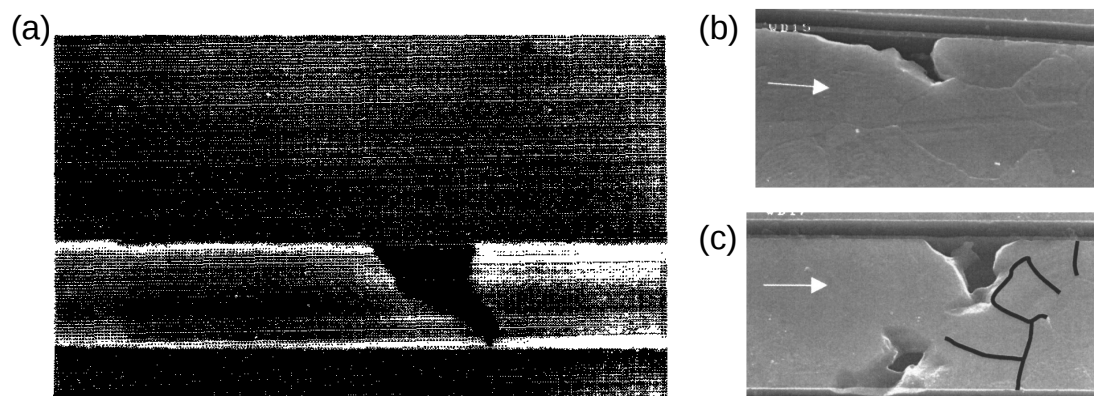


Figure 2.9: (a) Scanning-electron micrograph of transgranular slit propagation transverse to unpassivated aluminum interconnect line. Reprinted from Arzt and Kraft [91] with permission from AIP publishing. (b) Scanning electron image of EM failure in electroplated copper showing void extending along GB. (c) Scanning-electron micrograph emphasizing the role of microstructure gradient i.e. big and small grains upstream and downstream with respect to electron wind respectively. Reprinted from Arnaud et al. [85] with permission from AIP publishing.

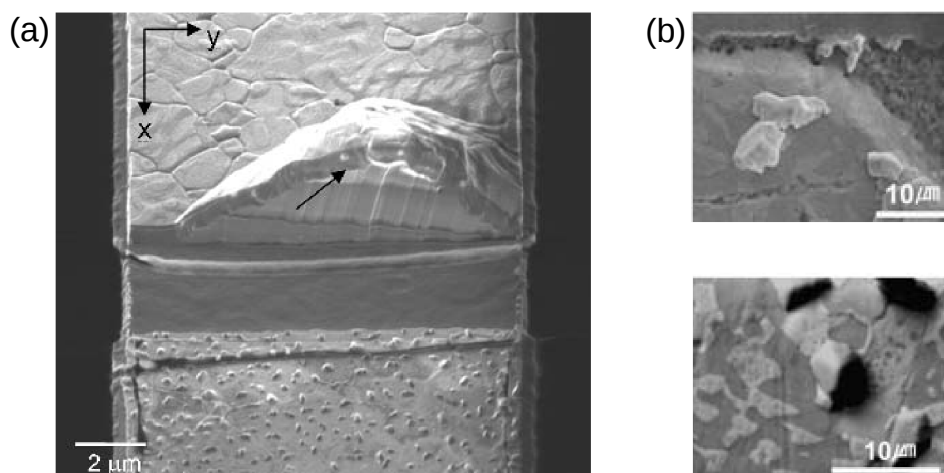


Figure 2.10: (a) Focused ion beam microscopy showing hillock at the Al/TiN interface as a result of EM testing at  $1\text{MA}/\text{cm}^2$ . Reprinted from Nucci et al. [98] with permission from Cambridge University Press. (b) Scanning electron microscopy image of hillock formation of Pb phase (top) and Sn phase (bottom) in a eutectic SnPb line conducted at  $100^\circ\text{C}$  at current density of  $6 \times 10^4 \text{A}/\text{cm}^2$ . Reprinted from Yoon et al. [101] with permission from Springer JEM.

To speed up the failure and reduce the experimental time, EM testing is carried out at higher current densities and elevated temperatures than actual service condition. The results thus obtained require careful extrapolation to gain meaningful insights. Black [102] derived a simple expression relating the mean time to failure to current density and temperature as follows. The mean time to failure  $t_f$  is inversely proportional to the rate of mass transport as,

$$t_f \propto \frac{1}{R}. \quad (2.32)$$

The rate of mass transport in turn is dependent on the number of conducting electron  $n_e$ , thermally activated ions  $N_a$  and momentum transfer  $\Delta p$  between them,

$$R \propto n_e N_a \Delta p. \quad (2.33)$$

The number of electrons transported through a unit volume and the momentum transfer with the ions are both proportional to the current density  $j$ . The number of activated ions follows an Arrhenius-type relation as,

$$N_a \propto \exp(-\Delta H/k_B T) \quad (2.34)$$

where,  $\Delta H$  is the activation energy. Combining the above relations,

$$t_f = \frac{A}{j^2} \exp(\Delta H/k_B T). \quad (2.35)$$

$A$  is a constant consisting of material properties and geometry of the test sample,  $k_B$  is the Boltzmann constant and  $T$  is the temperature. Thus, results from accelerated EM testing can be extrapolated using the above relation.

Although a number of experimental observations corroborate a  $j^{-2}$  dependence, reports on  $j^{-1}$  and even fractional values have also come up. Since then, the Black's law has been modified as,

$$t_f = \frac{A}{j^n} \exp(\Delta H/k_B T). \quad (2.36)$$

to accommodate different experimental findings. The occurrence of the fractional value can be reconciled by a void nucleation and growth process. It can be shown by invoking critical vacancy accumulation event either when vacancy concentration [73] or vacancy-accumulated stress [103] reaches a critical value, that the mean time to failure for the void nucleation process follows a  $j^{-2}$  dependence. On the other hand, considering the growth of a void at GB triple junction, it can be shown that the void growth exhibits a  $j^{-1}$  relation [73]. Thus depending upon the rate limiting failure step the exponent  $n$  lies between 1 – 2. Exponents greater than 2 requires one to consider the effect of Joule's heating [104].

### 2.3.2 Pathways of EM

Polycrystalline metallic lines are characterized by a number of potential diffusional pathways which include the lattice, GBs, surface and interphase boundaries between the film substrate or film dielectric layers, amongst others [105, 106, 107, 108]. At typical operational conditions ( $< 450^\circ\text{C}$ ), bulk diffusivity is negligible, rendering only surfaces and GBs as the potential diffusion pathways. The dominant EM pathway is typically assessed in drift velocity experiments by correlating the edge velocity with the EM activation energy via an Arrhenius-type equation,  $v_d = \frac{D_o}{k_B T} ze\rho_r j \exp\left(\frac{E_M}{k_B T}\right)$ , where,  $v_d$  is the drift velocity,  $D_o$  the diffusivity of the metal species,  $ze$  the valence,  $\rho_r$  the resistivity,  $j$  the current density and  $E_M$  the activation energy for electromigration [75, 105]. The slope of the log-normal plot between  $v_d T/j$  and  $1/T$  yields the value of activation energy, which can then be compared to the GB ( $E_{GB}$ ) and surface ( $E_S$ ) diffusion activation energies to extract the dominant path. However, on numerous occasions, the observed activation energy lies between  $E_{GB}$  and  $E_S$ , thereby reflecting the possibility of multiple pathways involved in EM [105, 109, 76, 106, 107].

Furthermore, the feasibility of diffusion occurring simultaneously via multiple pathways is also accentuated by a large scatter observed in the activation energy data plotted as a function of test piece geometry, given by  $d/w$  where  $d$  is the average grain size and  $w$  is the line width [105, 109]. This can be rationalized in terms of microstructure of the sample as follows. In bamboo type lines, if  $w \ll d$ , the average orientation of GBs is perpendicular to the electric field as shown in Fig.2.11(a), thus rendering this path, moot. As a result, the activation energy as determined from the drift velocity experiments is closer to the activation energy of the surface [108]. On the contrary, if  $w > d$ , GBs form a continuous network (Fig.2.11(b)) and EM occurs via a combination of surface and GB diffusion, thus making the line more susceptible to damage [105, 76]. Therefore, a successful assessment of damage modes in interconnect, in principle, must account for the disparate pathways in the sample.

### 2.3.3 Grain boundary grooving under electromigration

A number of models based on void nucleation have been formulated to rationalize damage by restricting EM to GBs [78, 110, 111, 103, 112]. However most of the models fail on two counts. First, the calculations performed to determine the excess vacancy concentration reveal instantaneous (of the order of seconds) attainment of equilibrium vacancy supersaturation [78, 77]. Such a short time does not concord well with the experimental observed failure times. Second, the maximum supersaturation was found to be less than 1 under all conditions. For such small supersaturation, energy barrier for void formation

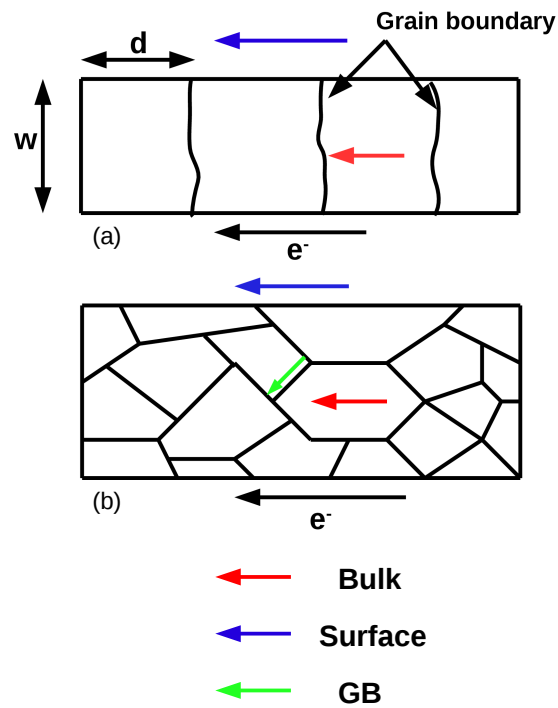


Figure 2.11: Schematic illustration depicting various EM pathways in (a) bamboo-type line and (b) wide polycrystalline line, where  $d$  represents the average grain size and  $w$  the line width. Surfaces are the predominant EM pathway in the former, while atomic transport proceeds through concurrent surface and GB diffusion in the latter.

through homogeneous nucleation is unfavorable. Thus presence of foreign particles is deemed necessary to explain void formation by vacancy-condensation mechanism [78]. Although the apparent discrepancy of void nucleation by vacancy condensation can be resolved by incorporating mechanical stress [103, 112, 77], nevertheless, it does not rule out the possibility of void growth mechanism being the lifetime limiting mechanism [73].

EM damage by GB-grooving is one such mechanism which encompasses all the aforementioned damage manifestations [113]. Grain-boundary (GB) grooving is an ubiquitous phenomenon leading to the morphological evolution of the phase interface in the vicinity of the triple junction with a GB [114, 115, 116, 117, 118]. The initial groove provides an initial seed for subsequent void growth, thereby obviating the need for invoking nucleation event. In fact most of the aforementioned observed damages can be rationalized by GB grooving. EM-induced flux along GB leads to drift of smaller grains along the line, exhibiting an impression of thinning [85, 5]. Even in bamboo-type lines where surface EM is prominent owing to the lack of continuous GB network, mass transport along the surface leads to thinning of the windward grain transverse to the line [99, 119]. The mass transport on leeward grain, on the other hand, manifest in hill-like feature [120, 121]. Furthermore accelerated grooving could also evince in cracks at GB due to rapid EM-induced atomic transport along the GB [95, 96, 3]. The phenomenon is further exacerbated in wide polycrystalline line where once a slit originates from a GB groove, subsequent propagation is rapid along the line owing to contiguous GB network [105, 81]. Slits have also been observed in bamboo type lines emerging from side walls and propagating transverse to the line along a tilted GB [99, 96].

The theory of thermal grooving was pioneered by Mullins, elucidating the morphological evolution of a free surface under various capillary-driven mass transport mechanisms [122, 123]. Although each of the transport mechanism leads to a time-dependent shape of the groove profile, the evolution is self-similar, with the groove dimensions namely, the depth and the width scaling as  $t^{1/2}$ ,  $t^{1/3}$  and  $t^{1/4}$  when the active mass transport mechanisms are evaporation-condensation [122], volume diffusion [123] and surface diffusion [122] respectively.

One of the assumptions in the original work of Mullins is that the GB does not participate in the mass transport process. However the presence of external field leads to gradients in chemical potential which drives atoms along the GB. Such cases are typical in presence of stress during sintering and creep [124, 125] and in presence of externally applied electric field for instance during electromigration [5, 126]. GB diffusion accelerates the grooving process [124, 127] which ultimately govern the stability of polycrystalline [128] and multilayer thin films [129]. The problem of GB grooving in presence of surface EM was first dealt with analytically by Ohring for bamboo-type lines in which GBs do

not participate in the mass transport process [113]. A subsequent extension to account for flux of vacancies along GB was proposed by Rosenberg and Ohring [78]. Both the above theories however are valid for isolated grooves (infinite grains) and employ the small slope approximation (SSA) i.e. the surface evolves such that the slope is small at every point along the surface.

Among the theoretical models, GB grooving model by Klinger and Glickman is of particular interest [5, 126]. The theory considers the evolution of grooves under the combined influence of capillary-mediated surface diffusion and grain boundary electromigration (GBEM). Under a single framework, the model describes the drift of grains as well propagation of channel-like intergranular slit. The transition between the two regimes takes place at a critical value of a dimensional group  $\alpha = \frac{J_{GB}\Omega L^2}{8B}$  where the GB flux  $J_{GB} = \frac{D_{GB}\delta_{GB}z_{GB}eE}{\Omega k_B T}$  and Mullins' constant  $B = \frac{D_s\delta_s\gamma_s\Omega}{k_B T}$ . Here,  $D_s$  and  $D_{GB}$  denotes the surface and GB diffusivity,  $\delta_s$  and  $\delta_{GB}$  represents the surface and GB thickness,  $\gamma_s$  is the surface energy,  $z_{GB}e$  represents the effective valence of the atomic species at the GB,  $E$  denotes the applied electric field,  $\Omega$  is the atomic volume and  $k_B T$  has the usual meaning. Below a critical value of  $\alpha$  termed as "Mode A", the surface drifts homogeneously preserving its shape. Relaxing the SSA, gives rise to the second regime, termed as "Mode B", above a critical value of  $\alpha$ , in which the root detaches from the surface to form isolated slits propagating along GB. Physically, smaller grains, lower GB flux and lower surface diffusivity promotes the former regime and vice-versa. The model to a great extent has been successful in interpreting microstructural damage [76, 86, 130, 85] as well as in partially addressing the issue of perplexing activation energy values of copper interconnects [109]. Dispersity in the activation energy values can be reconciled by considering concurrent GB and interface or surface diffusion [107, 131].

## 2.4 Role of numerical modeling in addressing electric-field-induced problems

The influence of various EM pathways on damage proliferation has been studied earlier using analytical [5, 103, 112] and numerical methods [132, 133]. Although serving as an excellent starting point, analytical methods often make simplifying assumptions to formulate a mathematically amenable problem, which can lead to over or under estimation of the lifetime of interconnects. Numerical methods, on the other hand, can circumvent this issue by effectively capturing the multiphysics of EM-induced microstructural damage, with fewer presumptions. Several computational methods encompassing different length and time scales, such as the macroscopic finite element methods [134, 135], mesoscopic phase-field [136, 137, 138, 139], level-set [140], front tracking methods [141, 142],

atomistically-informed ab-initio methods [143, 144], Monte Carlo simulations [145, 146] and more recently phase-field crystal models [147] have been successfully applied to study EM-induced void migration [134, 137, 138, 147], transgranular slit propagation [92, 136] and intermetallic growth [148, 149].

In block copolymers, self-consistent field theory (SCFT) [150, 151] and dynamic density functional theory (DDFT) [152, 153] are the current state-of-the-art numerical methodologies employed hitherto. While both the numerical methods provide a statistical framework, where chain architecture and block sequence are formulated in terms of a field-theoretic Hamiltonian, the SCFT is limited to the determination of static morphologies by comparison of free energies. DDFT, on the other hand, is supplemented with a kinetic equation similar to the Cahn-Hilliard model which facilitates additional studies pertaining to the kinetic pathways of microstructural evolution. Cell dynamical simulation (CDS) is also a popular and computationally efficient microstructure simulation technique, but lack details of the molecular interactions [154, 155]. Moreover, CDS is currently limited to linear chain architecture. The electrostatics of the problem is usually taken into account by the perturbed solution of Maxwell equation. The perturbed solution of the Maxwell equation is based on the assumption of weak fractional variation of the dielectric constant [6, 54]. Though appropriate in the proximity of the order-disorder transition(ODT) temperature, the results can be significantly marred as the segregation increases. The limitation of this approach as been highlighted in Ref. [156] where it was shown that the lowest order perturbation theory leads to a free energy which is invariant to the interchange of the two monomers. Using a complete electrostatic treatment in the SCFT framework [157, 158, 61] and a second-order perturbation theory [156] it has been further shown that the electric field couples differently to the two blocks. Same limitations also holds for the CDS [64] and DDFT [57] studies where an anisotropic term accounting for dielectric interface penalty in the evolution equation is appended (which again arises from the first-order perturbation theory).

Phase-field models or diffuse-interface models as they are popularly known can provide an efficient framework to address such time-dependent free boundary problems. A number of conserved variables which can be composition or density, or non-conserved variables such as grain order parameters representing different crystallographic orientation or phase-fields which merely act as phase indicators, are defined to describe the microstructure of the material. In this methodology, the sharp-interface between co-existing phases is replaced by an interface of finite width, across which all the field variables vary smoothly. Furthermore, no additional boundary conditions are required to be imposed at the moving boundary, obviating the need to track the same. Thus, complex pattern formation and highly non-linear phenomenon can be studied gracefully. The present work is devoted to the formulation and application of phase-field model to study di-

rected assembly of diblock copolymers and damage proliferation in polycrystalline metal interconnects.

The thesis is organized as follows. In the succeeding chapters (Chapter 3 and 4) the two phase-field models along with their numerical implementation and relationship to sharp-interface models are presented. Chapter 5 and 6 reports the application of the model to study directed self-assembly of block copolymers under substrate interaction, electric field and confinement. Chapters 7, 8, 9 and 10 are devoted towards the study of various aspects of the phenomenon of GB grooving under EM. Chapter 11 concludes the thesis with a brief summary and a discussion on the possible future directions.

## **Part II**

### **Methods : Phase-field formulation**

# Chapter 3

## Phase-field model for directed assembly of block copolymers due to substrate affinity and electric field

### 3.1 Ohta-Kawasaki or Non-local Cahn-Hilliard Model

Block copolymers are known to self assemble into variety of ordered structures following phase separation. Diblock copolymers consists of two distinct subchains, say, A and B type monomers with  $N_A$  and  $N_B$  number of each type respectively. Since the two subchains are joined together through a covalent bond, unlike polymer blends or metallic alloys, these class of materials tend to undergo microphase separation below the critical temperature. In other words, the segregated A and B domains do not continue to coarsen indefinitely following spinodal decomposition, but saturate with domains of fixed widths depending upon  $\chi N$  and  $f$ .  $\chi$  is the Flory-Huggins interaction parameter measuring the incompatibility of the two monomers and is given by

$$\chi = \epsilon_{AB} - \frac{1}{2}(\epsilon_{AA} + \epsilon_{BB}) \quad (3.1)$$

where,  $\epsilon_{AB}$ ,  $\epsilon_{AA}$  and  $\epsilon_{BB}$  are the bond energies or the monomer interaction parameters. Block copolymers exhibit a positive value of  $\chi$ , favoring phase segregation.  $N = N_A + N_B$  is the polymerization index and  $f = N_A/N$  is the relative length of A monomer chain to the entire macromolecule. It is also an indication of monomer density or volume fraction of the A block. Because of the incompressibility condition, the volume fraction of B block is given by  $1 - f$ . A number of well-ordered periodic morphologies such as lamellae, hexagonally-packed cylinders, body-centered spheres, gyroids, perforated lamellae structures have been observed and reported experimentally as a function of  $\chi N$  and  $f$  [26, 30].

In the present section, the diffuse-interface formalism to model the occurrence of such spatially periodic ordered structures found in diblock copolymers is discussed. The original derivation dates back to the mean field theory of Ohta and Kawasaki [29] which has been re-casted several times for numerical simulation either by a cell dynamical approach [159, 154, 155] or as in the present case phase-field approach [160, 161, 162]. A detailed re-derivation of the Ohta-Kawasaki density functional theory and the approximations which leads to the non-local Cahn-Hilliard-like functional has been examined by Choksi and Ren [163]. We therefore, do not delve into the derivation here, but, start from the free energy functional form providing a brief summary of the relation between the numerical and physical parameters and the derivation of the kinetic equation.

The free-energy functional can be written as a sum of short-range and long-range interaction terms to account for chain connectivity as [29, 164, 159, 160],

$$F = \int_V f(\psi) + \frac{\kappa}{2} |\nabla \psi|^2 \, d\mathbf{r} + B \int_V \int_V G(\mathbf{r}, \mathbf{r}') (\psi(\mathbf{r}) - m) (\psi(\mathbf{r}') - m) \, d\mathbf{r} \, d\mathbf{r}' \quad (3.2)$$

The terms in the first integral are the short-range part consisting of a double well potential and gradient energy term typical of modeling of any phase separation process [165].  $\psi$  is a scaled compositional order-parameter that measures the difference of the local volume fraction of  $A(\psi_A)$  and  $B(\psi_B)$  blocks as,

$$\psi = \psi_A - \psi_B. \quad (3.3)$$

Since  $\psi_A + \psi_B = 1$  we have  $\psi = 1 - 2\psi_B$ . Therefore, presence of pure monomer A i.e.  $\psi_B = 0$  is depicted by regions with  $\psi = 1$  and presence of pure monomer B i.e.  $\psi_B = 1$  is depicted by regions with  $\psi = -1$ .  $m$  denotes the difference in the global volume fraction of  $A$  and  $B$  monomers as

$$m = f - (1 - f) = 1 - 2f \quad (3.4)$$

Thus,  $m$  denotes the average of  $\psi$  over the volume as  $m = \int_V \psi \, d\mathbf{r}$ . A suitable choice of  $f(\psi)$  is a quartic potential of the form  $-\psi^2/2 + \psi^4/4$ . The parameters  $\kappa$  and  $B$  are related to the polymer architecture through the relations [29, 164, 163, 166],

$$\kappa \sim \frac{l^2}{f(1-f)\chi} \quad (3.5)$$

$$B \sim \frac{1}{2f^2(1-f)^2 l^2 \chi N^2} \quad (3.6)$$

where  $l$  is the Kuhn statistical length or the average monomer space size. The segregation  $\chi N$  is determined by  $\kappa$  and  $B$  as,

$$\chi N \sim \frac{1}{\sqrt{2B\kappa} f^{3/2} (1-f)^{3/2}}. \quad (3.7)$$

The second double integral in Eq.(3.2) contain terms that restricts the scale of phase separation.  $G$  is the Green's function having the property  $\nabla^2 G(\mathbf{r}, \mathbf{r}') = -\delta(\mathbf{r} - \mathbf{r}')$ . The double integral can be equivalently written analogous to the gradient energy term in the first integral by introducing a variable  $v$  which satisfies the Poisson problem,

$$-\nabla^2 v(\mathbf{r}) = \psi(\mathbf{r}) - m. \quad (3.8)$$

If the Green's function  $G(\mathbf{r}, \mathbf{r}')$  satisfies the above boundary value problem then,

$$v(\mathbf{r}) = \int_V G(\mathbf{r}, \mathbf{r}')(\psi(\mathbf{r}') - m) d\mathbf{r}' \quad (3.9)$$

should be the solution of the Eq.(3.8). This can be seen by applying the Laplacian operator on both sides

$$\nabla^2 v(\mathbf{r}) = \int_V \nabla^2 G(\mathbf{r}, \mathbf{r}')(\psi(\mathbf{r}') - m) d\mathbf{r}' = - \int_V \delta(\mathbf{r} - \mathbf{r}')(\psi(\mathbf{r}') - m) d\mathbf{r}' = -(\psi(\mathbf{r}) - m) \quad (3.10)$$

which is equivalent to Eq.(3.8). Now using divergence theorem,

$$\int_V |\nabla v|^2 d\mathbf{r} = - \int_V v \nabla^2 v d\mathbf{r} + \int_S v \nabla v \cdot \mathbf{n} ds. \quad (3.11)$$

Choosing the boundary condition such that the surface integral vanishes and employing Eqs.(3.9) and (3.10) we obtain,

$$\int_V |\nabla v|^2 d\mathbf{r} = \int_V \int_V G(\mathbf{r}, \mathbf{r}')(\psi(\mathbf{r}) - m)(\psi(\mathbf{r}') - m) d\mathbf{r} d\mathbf{r}'. \quad (3.12)$$

Therefore, an alternate form of free energy functional writes as,

$$F = \int_V f(\psi) + \frac{\kappa}{2} |\nabla \psi|^2 d\mathbf{r} + B \int_V |\nabla v|^2 d\mathbf{r} \quad (3.13)$$

The competition between the three energies in the free energy functional leads to the periodic structures. This can be seen as follows : (i) The first term  $f(\psi)$  which is a double well with minima located at  $\psi = \pm 1$ , is minimized when the domains are segregated to pure A and B phases. (ii) The gradient energy term penalizes sharp gradients and leads to smooth transition regions between  $\psi = -1$  and  $\psi = +1$ . However, the transition regions are fewer to minimize the interfacial energy. Therefore, the first two terms lead to larger domains of pure A and B with transition regions separating the two. The first two terms alone cannot lead to periodic structures. (iii) The third term on the other hand, penalizes regions of  $\psi$  whose local values deviate from global value  $m$ . Thus, regions with  $\psi = m$  are preferred. In order to make the free energy contribution small, the non-local term  $\psi$  has to oscillate about  $m$  which increase the interfacial or transition areas, ultimately giving rise to periodic microstructures depending on the value of  $m$ .

The kinetic equation can be derived from variational principle as,

$$\frac{\partial \psi}{\partial t} = M \nabla^2 \mu \quad (3.14)$$

where  $M$  is the phenomenological mobility assumed to be 1 and  $\mu = \frac{\delta F}{\delta \psi}$  is the chemical potential defined as,

$$\frac{\delta F}{\delta \psi} = -\psi + \psi^3 - \kappa \nabla^2 \psi + B \int_V G(\mathbf{r}, \mathbf{r}') (\psi(\mathbf{r}') - m) d\mathbf{r}' \quad (3.15)$$

Substituting into the evolution Eq.(3.14) and using Eqs.(3.8) and (3.9),

$$\frac{\partial \psi}{\partial t} = \nabla^2 [-\psi + \psi^3 - \kappa \nabla^2 \psi] - B(\psi - m). \quad (3.16)$$

A few properties of the non-local Cahn-Hilliard functional is considered next.

### 3.1.1 Mass conserving property

The non-local part does not alter the mass conserving property of the system. This can be seen as follows.

$$\frac{d}{dt} \int_V \psi(\mathbf{r}, t) d\mathbf{r} = \int_V \nabla^2 \mu_{\text{local}} d\mathbf{r} - B \int_V (\psi(\mathbf{r}, t) - m) d\mathbf{r} \quad (3.17)$$

where,  $\mu_{\text{local}} = -\psi + \psi^3 - \kappa \nabla^2 \psi$ . Using divergence theorem, the first integral can be re-written as,

$$\int_V \nabla^2 \mu_{\text{local}} d\mathbf{r} = \int_S \mathbf{n} \cdot \nabla \mu ds \quad (3.18)$$

Assuming a no-flux boundary condition, the integral vanishes at the boundaries. Hence,

$$\begin{aligned} \frac{d}{dt} \int_V \psi(\mathbf{r}, t) d\mathbf{r} &= -B \left[ \int_V \psi(\mathbf{r}, t) d\mathbf{r} - \int_V m d\mathbf{r} \right] \\ &= -B \left[ \int_V \psi(\mathbf{r}, t) d\mathbf{r} - m \right] \\ &= 0 \end{aligned} \quad (3.19)$$

where the fact that  $V$  is a scaled domain of unit volume has been assumed.

### 3.1.2 Length scale in the system

The competition between  $\kappa$  and  $B$  governs the length scale of the emerging pattern. This can be understood by suitably rescaling the governing Eq.(3.14) by,  $\tilde{\psi} = \psi - m$ ,  $\tilde{x} = \sqrt{B}x$

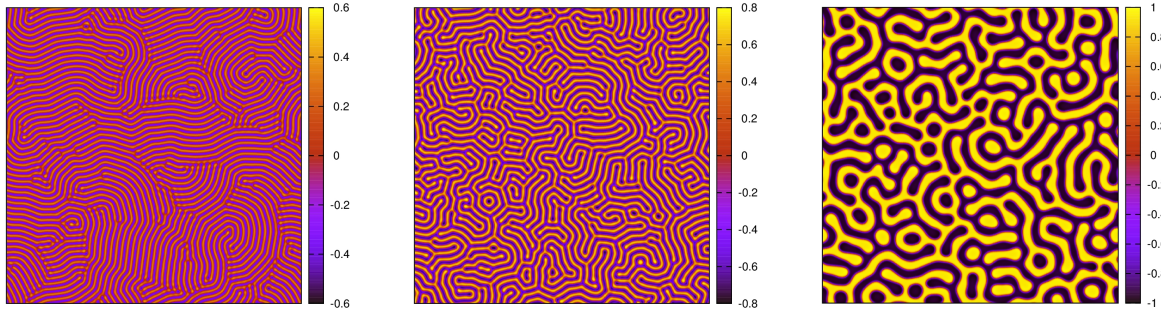


Figure 3.1: Microstructure of symmetric diblock copolymer system at  $\epsilon^2 = 0.2$ ,  $\epsilon^2 = 0.1$  and  $\epsilon^2 = 0.004$  (from left to right). With increasing  $\epsilon^2$  the equilibrium domain size characterized by the lamellar thickness increases.

and  $\tilde{t} = Bt$  [166],

$$\begin{aligned} B \frac{\partial \tilde{\psi}}{\partial \tilde{t}} &= B \tilde{\nabla}^2 \left[ -(\tilde{\psi} + m) + (\tilde{\psi} + m)^3 \right] - B^2 \kappa \tilde{\nabla}^4 \tilde{\psi} - B \tilde{\psi} \\ \frac{\partial \tilde{\psi}}{\partial \tilde{t}} &= -\tilde{\epsilon}^2 \tilde{\nabla}^4 \tilde{\psi} + \tilde{\nabla}^2 \left[ \tilde{\psi}^3 + 3m\tilde{\psi}^2 - (1 - 3m^2)\tilde{\psi} \right] - \tilde{\psi} \end{aligned} \quad (3.20)$$

where  $\tilde{\epsilon} = \sqrt{\kappa B}$ . Dropping the tildes for the sake of convenience hereafter, it is clear that the length scale depends on  $\sqrt{\kappa B}$ . This can also be verified from Eq.(3.7).

### 3.1.3 Linear Stability

The linear stability of the stationary solution in one dimension space is next considered. For this purpose, the solution is assumed to be of the form [167],

$$\psi(x, t) = m + \sum_{k=1}^{\infty} A(t) \cos(kx) \quad (3.21)$$

Substituting in the linearized version of the Eq.(3.20),

$$\frac{\partial A(t)}{\partial t} = [-\epsilon^2 k^4 + (1 - 3m^2)k^2 - 1]\beta. \quad (3.22)$$

The solution of the above Eq. takes the form  $A(t) = A(0) \exp(\eta_k t)$  where  $\eta_k = -\epsilon^2 k^4 + (1 - 3m^2)k^2 - 1$ . The maximally growing wavenumber can be found by setting  $d\eta_k/dk = 0$  as,

$$-4\epsilon^2 k^3 + 2k(1 - 3m^2) = 0 \quad (3.23)$$

which gives  $k = \sqrt{(1 - 3m^2)/2\epsilon^2}$ .

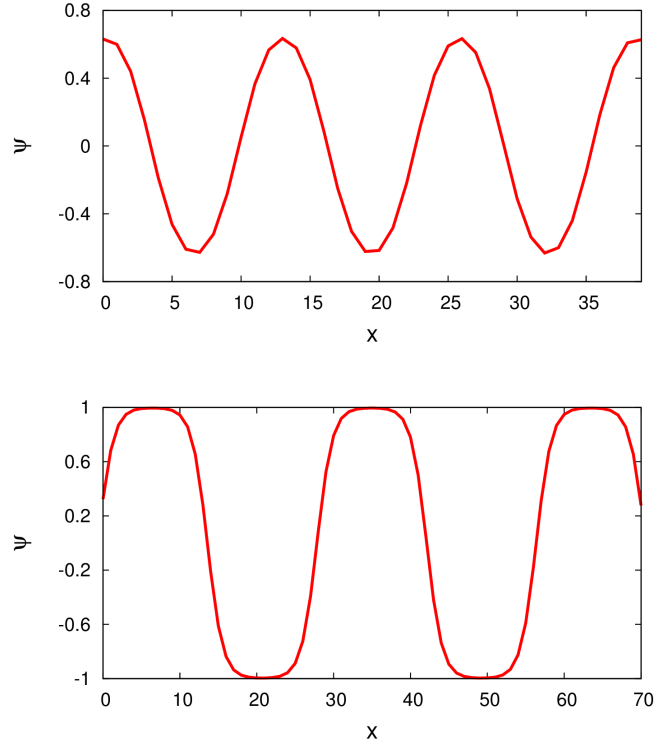


Figure 3.2: Equilibrium composition profile for a symmetric diblock copolymer system at  $\epsilon^2 = 0.05$  (top) and  $0.0001$  (bottom) corresponding to WSL and SSL respectively. The composition profile exhibit a sinusoidal behavior in WSL and a square wave characteristic in SSL.

Secondly, the  $\psi = m$  state will loose stability if  $\eta_k > 0$ . The root of  $\eta_k = 0$  gives,

$$k = \sqrt{\frac{(1 - 3m^2) \mp \sqrt{(1 - 3m^2)^2 - 4\epsilon^2}}{2\epsilon^2}} \quad (3.24)$$

A positive wavenumber is guaranteed if one of the following cases is met:

1. **Case I** : Both terms in the numerator are positive along with a positive sign in between i.e.  $-1/\sqrt{3} < m < 1/\sqrt{3}$  and  $\epsilon^2 < (1 - 3m^2)^2/4$ .
2. **Case II** : Both terms in the numerator are positive along with a negative sign in between. This gives a trivial condition of  $\epsilon > 0$ .

Thus a disordered state loses stability if the above conditions are satisfied. Thus for a symmetric diblock copolymer i.e.  $m = 0$  with a lamellar morphology the  $\psi = 0$  is unstable if  $0 < \epsilon^2 < 1/4$ .

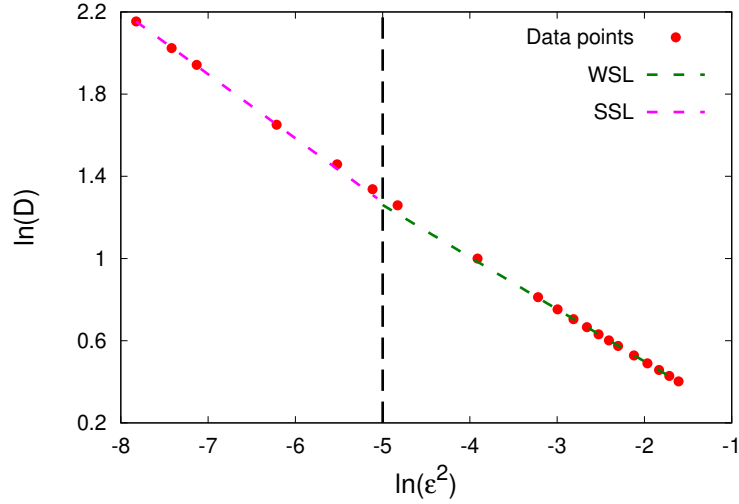


Figure 3.3: Domain width  $D$  as a function of  $\epsilon^2$  on a double logarithmic scale. For values of  $\epsilon^2 < 0.05$  the slope of the fitted line (green) exhibits a slope of  $-0.254$ , while data points with  $\epsilon^2 < 0.0025$  yields a slope of  $-0.32$  (pink).

### 3.1.4 Two regimes of microphase separation

Depending upon the value of  $\epsilon^2$  which is related to  $\chi N$ , block copolymers are categorized in two distinct regimes namely weak segregation limit (WSL) and strong segregation limit (SSL). If  $\chi N > 10$  i.e. closer to the order-disorder transition temperature, the block copolymers are characterized by a sinusoidal composition profile (as shown in Fig.3.2(a)) with domain period scaling as  $N^{1/2}$  [28]. On the other hand, if  $\chi N \gg 10$  i.e. well below the ODT, the block copolymers are characterized by a square wave composition profile with sharp interfaces between the two blocks (as shown in Fig.3.2(b)) and microdomain period scales as  $N^{2/3}$  [29]. The former regime is termed as WSL, while the latter is designated as SSL. Since  $\epsilon^2 \sim N^{-2}$ , the equilibrium domain size  $D$  follow the power law  $D \sim (\epsilon^2)^{-1/4}$  and  $D \sim (\epsilon^2)^{-1/3}$  in WSL and SSL respectively [28, 29, 168]. The double logarithmic plot of the variation of the equilibrium domain size  $D$  with  $\epsilon^2$  along with the fitted straight lines are shown in Fig.3.3. The equilibrium domain size was calculated from microstructure obtained from two-dimensional simulations starting from a disordered state with thermal noise to mimic phase separation. The simulations were run until an equilibrium, characterized by no further appreciable coarsening. The domain size was then calculated from the first moment of the structure function as mentioned in [160, 161, 169]. The two regimes with distinct slopes of  $-0.254$  and  $-0.32$  are evident.

Alternatively, the equilibrium lamellar thickness for symmetric system, that minimizes the free energy functional can also be computed analytically, at least for the SSL. The interested reader is referred to [170, 159] for the details of the derivation .

### 3.1.5 Forms of $f(\psi)$

In the present work, a usual 2 – 4 potential which has two symmetric minima located at  $\psi = \pm 1$  around a maximum at  $\psi = 0$ . Such a potential has been utilized in several works of Oono and Bahiana [170], Liu and Goldenfeld [164], Chakrabarti and co-workers [160] and Choksi and co-workers [166]. Lamellar, hexagonally-packed cylinders, gyroid, perforated lamellae, body-centered cubic spheres have been numerically found to be stable in  $\epsilon^2 - f$  space [171, 166, 172]. In CDS modeling a function  $f'(\psi) = A \tanh \psi$  has also been utilized by Oono and Puri [173, 174]. It can be seen by expanding  $\tanh$  until cubic terms as,

$$A \tanh \psi = A\psi - A\frac{\psi^3}{3} \quad (3.25)$$

that this is indeed similar to the 2 – 4 potential described above. Appropriately choosing the coefficients in both the expressions an equivalence between CDS and CH modeling can be established [175].

An alternate form of  $f(\psi)$  which contains an additional cubic term has also been employed. The specific form of  $f(\psi)$  reads as [176, 154],

$$f(\psi) = \left[ -\frac{\tau}{2} + \frac{A}{2}(1 - 2f)^2 \right] \psi^2 + \frac{\nu}{3}(1 - 2f)\psi^3 + \frac{u}{4}\psi^4 \quad (3.26)$$

where  $\tau$  depends on the quench depth and  $A, \nu$  and  $u$  are phenomenological constants. Here the scaled composition variable is given by  $\psi = \psi_A - \psi_B - m$ . It is to be noted that the effect of the  $\psi^3$  term in the free energy term is to tilt the  $\psi = -1$  state with respect to the  $\psi = +1$  state. It has been argued that such a symmetry breaking potential is desired to simulate hexagonal and cubic structures in three dimensions. However, as mentioned above it has been numerically demonstrated in the past [171, 166] that the function used in the present study can in fact enable modeling of these ordered morphologies.

## 3.2 Effect of surfaces on binary mixture

The theoretical framework to study the effect of external surface on binary mixture was pioneered by Cahn [177]. The excess free energy  $\Delta F$ , of a semi-infinite fluid (or solid) in contact with a planar surface at  $x = 0$  can be written as,

$$\frac{\Delta F}{k_B T / V_m} = \int_0^\infty \Delta f + \frac{\kappa}{2} \left( \frac{d\psi}{dx} \right)^2 dx + \Phi(\psi_s) \quad (3.27)$$

where  $V_m$  is the average molecular volume,  $\Phi(\psi_s)$  is the contribution of the free-energy per unit area of the surface and  $\psi_s$  is the scaled composition at the surface.  $\Delta f =$

$f(\psi) - f(\psi_o) - (\psi - \psi_o) \frac{\partial f}{\partial \psi} \Big|_{\psi=\psi_o}$  and  $\psi_o$  is the scaled composition of the fluid.  $\frac{\kappa}{2} \left( \frac{d\psi}{dx} \right)^2$  is the interfacial contribution of the free energy due to the presence of composition gradients.

The equilibrium composition profile near the surface can be deduced by the method of variational calculus by setting the variational derivative to be zero i.e.  $\frac{\delta(\Delta F)_e}{\delta \psi} = 0$ . The appropriate boundary condition can be derived as follows. Consider the free energy functional 3.27 to be minimized. Then the variation  $\delta(\Delta F)$  or the change in  $\Delta F$  corresponds to the change when  $\psi(x)$  changes by an infinitesimal amount  $\delta\psi(x)$  i.e.,

$$\tilde{\psi}(x) = \psi(x) + \delta\psi(x) \quad (3.28)$$

and,

$$\delta(\Delta F) = \Delta F[\tilde{\psi}(x)] - \Delta F[\psi(x)] \quad (3.29)$$

Defining,  $\delta\psi(x) = \epsilon\eta(x)$  where,  $\eta(x)$  is an arbitrary continuous function whose value is of the order of 1 and  $\epsilon$  is an infinitesimal number. Therefore,

$$\Delta F[\tilde{\psi}(x)] = \int_0^\infty F(x, \psi(x) + \epsilon\eta(x), \psi'(x) + \epsilon\eta'(x)) dx + \Phi[\psi_s(0) + \epsilon\eta(0)] \quad (3.30)$$

where  $F = \Delta f + \frac{\kappa}{2} \left( \frac{d\psi}{dx} \right)^2$ . Performing a Taylor series expansion in terms of  $\epsilon$ ,

$$\begin{aligned} \Delta F[\tilde{\psi}(x)] = \int_0^\infty F(x, \psi(x), \psi'(x)) dx + \frac{\partial F}{\partial \psi(x)} \epsilon\eta(x) + \frac{\partial F}{\partial \psi'(x)} \epsilon\eta'(x) dx \\ + \Phi[\psi_s(0)] + \frac{d\Phi}{d\psi_s} \epsilon\eta(0). \end{aligned} \quad (3.31)$$

The above Eq. can be rearranged as,

$$\begin{aligned} \Delta F[\tilde{\psi}(x)] = \int_0^\infty F(x, \psi(x), \psi'(x)) dx + \Phi[\psi_s(0)] + \int_0^\infty \left[ \frac{\partial F}{\partial \psi(x)} \epsilon\eta(x) \right. \\ \left. + \frac{\partial F}{\partial \psi'(x)} \epsilon\eta'(x) \right] dx + \frac{d\Phi}{d\psi_s} \epsilon\eta(0) \end{aligned} \quad (3.32)$$

$$\Delta F[\tilde{\psi}(x)] = \Delta F[\psi(x)] + \int_0^\infty \left[ \frac{\partial F}{\partial \psi(x)} \epsilon\eta(x) + \frac{\partial F}{\partial \psi'(x)} \epsilon\eta'(x) \right] dx + \frac{d\Phi}{d\psi_s} \epsilon\eta(0) \quad (3.33)$$

Utilizing Eq.(3.29) the above Eq. can be rewritten as,

$$\delta(\Delta F) = \left[ \int_0^\infty \left[ \frac{\partial F}{\partial \psi(x)} \epsilon\eta(x) + \frac{\partial F}{\partial \psi'(x)} \epsilon\eta'(x) \right] dx + \frac{d\Phi}{d\psi_s} \epsilon\eta(0) \right] \quad (3.34)$$

Using integration by parts on the second term in the integral,

$$\delta(\Delta F) = \epsilon \left[ \int_0^\infty \frac{\partial F}{\partial \psi} \eta(x) dx + \frac{\partial F}{\partial \psi'(x)} \eta(x) \Big|_0^\infty - \int_0^\infty \frac{\partial}{\partial x} \frac{\partial F}{\partial \psi'(x)} \eta(x) dx + \frac{d\Phi}{d\psi_s} \eta(0) \right] \quad (3.35)$$

Simple algebraic manipulation simplifies the Eq. to,

$$\delta(\Delta F) = \frac{\partial F}{\partial \psi'(x)} \epsilon \eta'(x) \Big|_0^\infty + \frac{d\Phi}{d\psi_s} \epsilon \eta(0) + \int_0^\infty \left( \frac{\partial F}{\partial \psi} - \frac{\partial}{\partial x} \frac{\partial F}{\partial \psi'(x)} \right) \epsilon \eta(x) dx \quad (3.36)$$

$$\delta(\Delta F) = \frac{\partial F}{\partial \psi'(x)} [\delta\psi(\infty) - \delta\psi(0)] + \frac{d\Phi}{d\psi_s} \delta\psi(0) + \int_0^\infty \left( \frac{\partial F}{\partial \psi} - \frac{\partial}{\partial x} \frac{\partial F}{\partial \psi'(x)} \right) \delta\psi(x) dx \quad (3.37)$$

Selecting the boundary condition at  $x = \infty$  such that  $\delta\psi(\infty) = 0$ ,

$$\delta(\Delta F) = \left[ -\frac{\partial F}{\partial \psi'(x)} + \frac{d\Phi}{d\psi_s} \right] \delta\psi(0) + \int_0^\infty \left( \frac{\partial F}{\partial \psi} - \frac{\partial}{\partial x} \frac{\partial F}{\partial \psi'(x)} \right) \delta\psi(x) dx \quad (3.38)$$

To obtain the usual Euler-Lagrange equation  $\frac{\delta(\Delta F)_e}{\delta\psi(x)} = 0$ , the first term is chosen such that it vanishes at  $x = 0$ . This generates the boundary condition as,

$$\begin{aligned} \frac{\partial F}{\partial \psi'(x)} &= \frac{d\Phi}{d\psi_s} \\ \frac{\partial \psi}{\partial x} \Big|_{x=0} &= -\frac{1}{\kappa} \frac{d\Phi}{d\psi_s} \end{aligned} \quad (3.39)$$

### 3.2.1 Specific choice of $\Phi(\psi_s)$ and its physical interpretation

Although a mathematical model to predict surface enrichment was developed by Cahn [177], a specific form of  $\Phi(\psi_s)$  was not discussed. The most commonly used form is obtained from the linear and quadratic terms in  $\psi_s$  as [178],

$$\Phi(\psi_s) = -\mu_1 \psi_s - \frac{g}{2} \psi_s^2 \quad (3.40)$$

where, the unimportant constant term has been omitted as it does not alter the free energy minimization.  $\mu_1$  represents the surface chemical potential which favors one of the species at the surface over the other and  $g/2$  is the measure of the deviation of interaction near the surface from the bulk.

The physical interpretation of these terms can be further understood from a simple lattice model consisting of A and B atoms as seen in Fig.3.4(a). It is assumed that the left layer is cut and an impenetrable wall is placed in its position. The derivation was first put forward by Jerry and Nauman [179] and their approach is followed in a slightly detailed manner.

Let the total number of lattice sites be  $N_o$ , among which  $N_A$  are occupied by A atoms and  $N_B$  by B. The probability of finding A atom at any lattice site =  $\frac{N_A}{N_o}$ . Since, the

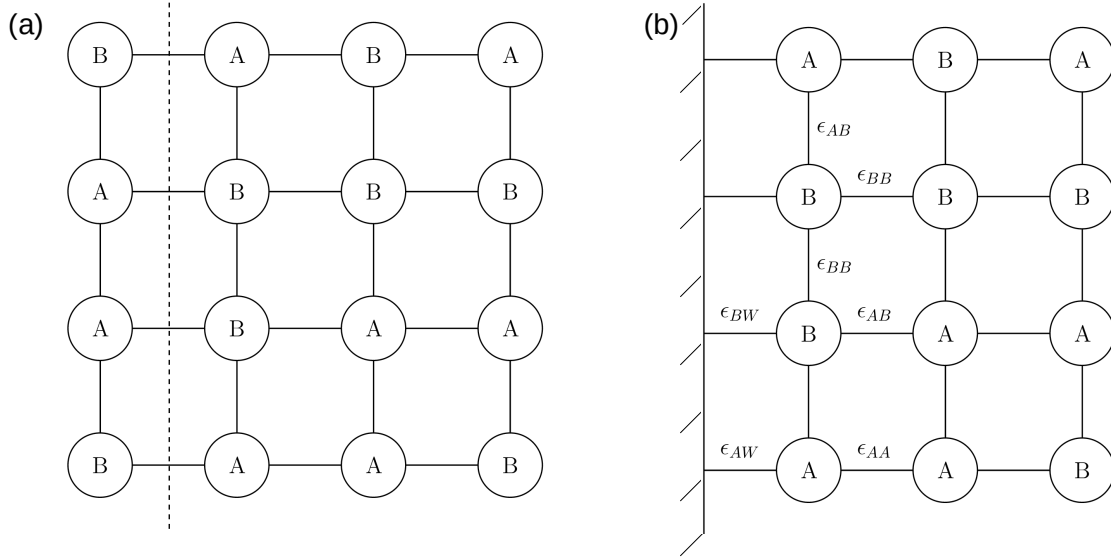


Figure 3.4: (a) A lattice consisting of equal number of A and B atoms. (b) The leftmost bonds (shown by dashed line) are cut and replaced by an impenetrable wall.

probability of finding an A atom at the layer closer to the surface is the same, the above ratio is denoted by  $\psi_s$  which can be interpreted as mole fraction of A atom. Similarly,

$$\text{Probability of finding B atom at any lattice site} = \frac{N_B}{N_o} = 1 - \psi_s.$$

Energy required to form bonds between A and B atoms of the mixture and wall is given by,

$$\xi_1 = \epsilon_{AW}\psi_s + \epsilon_{BW}(1 - \psi_s) \quad (3.41)$$

where,  $\epsilon_{AW}$  and  $\epsilon_{BW}$  are the bond energies between A atom and wall and B atom and wall respectively. The bond energies arising due to the missing nearest neighbor also needs to be considered. Energy due to missing nearest neighbor can be written as,

$$\begin{aligned} \xi_2 = & (\text{Probability of finding an A atom at a lattice site} \times \text{Probability of finding an A} \\ & \text{atom as its nearest neighbor}) \times (\text{Bond energy between A-A atoms}) \\ & + (\text{Probability of finding an B atom at a lattice site} \times \text{Probability of finding an B} \\ & \text{atom as its nearest neighbor}) \times (\text{Bond energy between B-B atoms}) \\ & + (\text{Probability of finding an A atom at a lattice site} \times \text{Probability of finding an B} \\ & \text{atom as its nearest neighbor}) \times (\text{Bond energy between A-B atoms}) \\ & + (\text{Probability of finding an B atom at a lattice site} \times \text{Probability of finding an A} \\ & \text{atom as its nearest neighbor}) \times (\text{Bond energy between A-B atoms}) \end{aligned}$$

In mathematical notation the above relation writes as,

$$\xi_2 = \psi_s^2 \epsilon_{AA} + (1 - \psi_s)^2 \epsilon_{BB} + 2\psi_s(1 - \psi_s)\epsilon_{AB} \quad (3.42)$$

The total surface energy  $\Phi(\psi_s)$  can thus be written as,

$$\Phi(\psi_s) = \frac{V_m C}{k_B T} \left[ \xi_1 - \frac{1}{2} \xi_2 \right] \quad (3.43)$$

where  $V_m$  is the average molecular volume,  $C$  denotes the number of contacts between the wall and the mixture molecules per unit area of the wall and  $k_B T$  has the usual meaning. The factor  $1/2$  eliminates the double counting. Substituting Eqs.(3.41) and (3.42) in Eq.(3.43) along with simple algebraic manipulation leads to,

$$\Phi(\psi_s) = \frac{VC}{k_B T} \left[ \left( \epsilon_{BW} - \frac{\epsilon_{BB}}{2} \right) - \psi_s (\epsilon_{BW} - \epsilon_{AW} + \epsilon_{AB} - \epsilon_{BB}) - \frac{\psi_s^2}{2} (\epsilon_{AA} + \epsilon_{BB} - 2\epsilon_{AB}) \right] \quad (3.44)$$

For simplicity the constant terms in the first parentheses are not considered henceforth for the reason mentioned above. The above expression can be arranged in a convenient form as,

$$\begin{aligned} \Phi(\psi_s) = \frac{V_m C}{k_B T} \left[ -\psi_s \left\{ \left( \epsilon_{BW} - \frac{1}{2} \epsilon_{BB} - \frac{1}{2} \epsilon_{WW} \right) - \left( \epsilon_{AW} - \frac{1}{2} \epsilon_{AA} - \frac{1}{2} \epsilon_{WW} \right) \right. \right. \\ \left. \left. + \left( \epsilon_{AB} - \frac{1}{2} \epsilon_{AA} - \frac{1}{2} \epsilon_{BB} \right) \right\} - \frac{\psi_s^2}{2} (\epsilon_{AA} + \epsilon_{BB} - 2\epsilon_{AB}) \right] \quad (3.45) \end{aligned}$$

The above expression can be written in terms of interaction parameters defined as,

$$\chi = \frac{z}{k_B T} \left( \epsilon_{AB} - \frac{1}{2} \epsilon_{AA} - \frac{1}{2} \epsilon_{BB} \right) \quad (3.46)$$

$$\chi_{BW} = \frac{z}{k_B T} \left( \epsilon_{BW} - \frac{1}{2} \epsilon_{BB} - \frac{1}{2} \epsilon_{WW} \right) \quad (3.47)$$

$$\chi_{AW} = \frac{z}{k_B T} \left( \epsilon_{AW} - \frac{1}{2} \epsilon_{AA} - \frac{1}{2} \epsilon_{WW} \right) \quad (3.48)$$

where  $z$  denotes the coordination number of the lattice. Substituting the above relations in Eq.(3.45) and rearranging,

$$\Phi(\psi_s) = -\frac{V_m C}{z} \chi \left[ 1 + \frac{\chi_{BW} - \chi_{AW}}{\chi} \right] \psi_s + \frac{V_m C}{z} \chi \psi_s^2 \quad (3.49)$$

Comparing Eqs.(3.40) and (3.49),

$$\mu_1 = \frac{V_m C}{z} \chi \left[ 1 + \frac{\chi_{BW} - \chi_{AW}}{\chi} \right] \quad (3.50)$$

$$g = -\frac{V_m C}{z} \chi \quad (3.51)$$

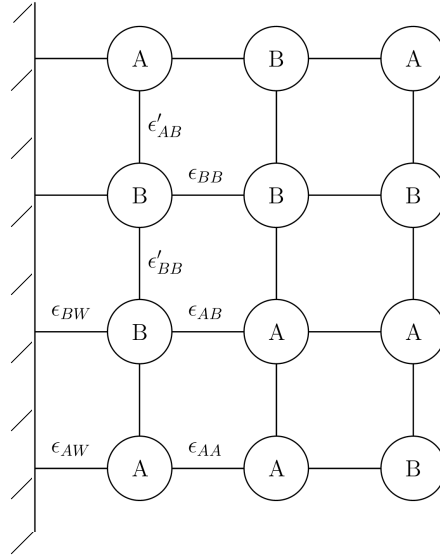


Figure 3.5: Schematic of a binary  $AB$  mixture in contact with an external surface. The presence of external surface modifies the bond energies at the adjacent layer.

In the above derivation it was assumed that the presence of wall does not alter the bond energy. However, in principle the bond energy between atoms is dependent on the relative distance from the wall. If we assume that the effect of the wall is short-ranged, the bond energies  $\epsilon_{AA}$ ,  $\epsilon_{BB}$  and  $\epsilon_{AB}$  only in the adjacent layer to the wall (first layer in Fig.3.5) are modified to  $\epsilon'_{AA}$ ,  $\epsilon'_{BB}$  and  $\epsilon'_{AB}$  respectively. Therefore, the extra energy  $\frac{V_m C}{k_B T} \frac{1}{2} (\psi_s^2 \epsilon'_{AA} + (1 - \psi_s)^2 \epsilon'_{BB} + 2\psi_s(1 - \psi_s) \epsilon'_{AB})$  should be accounted in Eq.(3.43). The above derivation can be repeated for such a case to calculate the appropriate expressions for  $g$  and  $\mu_1$  which writes as,

$$g = -\frac{V_m C}{z} (\chi - \chi_W) \quad (3.52)$$

$$\mu_1 = \frac{V_m C}{z} (\chi_{AW} - \chi_{BW} + \chi_W - \chi) + \frac{V_m C}{k_B T} \left( \frac{\epsilon'_{AA} - \epsilon'_{BB}}{2} \right) \quad (3.53)$$

where  $\chi_W = \frac{z}{k_B T} (\epsilon'_{AB} - \frac{1}{2} \epsilon'_{AA} - \frac{1}{2} \epsilon'_{BB})$ .

### 3.3 Diffuse-interface formalism to study combined effect of substrate affinity and electric field on symmetric diblock copolymers

Having gained a basic understanding to model morphologies of diblock copolymers, external surfaces and electric field, a theoretical model to study the concurrent effect of

external fields is formulated below. The total free energy functional in units of  $k_B T$  can be written as,

$$F = F_{bulk} + F_{surface} + F_{electrostatic}. \quad (3.54)$$

The bulk part is given by Eq.(3.2). The free energy of the domain surface in presence of attracting walls is written as, [178, 180]

$$\frac{F_{surface}}{k_B T} = \int_S \left[ h(\mathbf{r})\psi(\mathbf{r}) + \frac{1}{2}g_s\psi^2(\mathbf{r}) \right] d\mathbf{r}. \quad (3.55)$$

The above expression results from a Taylor series expansion of bare surface energy [178]. The terms  $h(\mathbf{r})$  and  $g_s$  have same physical interpretations as  $\mu_1$  and  $g$ . A positive value expresses preferential attraction of B component and vice-versa [178, 180].

To account for two confining walls at two ends in the current study, the above expression is rewritten in terms of a  $\delta$ -function as,

$$\frac{F_{surface}}{k_B T} = \int_S [h_o\delta(y) + h_L\delta(y - L)] \psi(\mathbf{r}) d\mathbf{r}, \quad (3.56)$$

where,  $h_o$  and  $h_L$  are the interaction strengths of the wall at  $x = 0$  and  $L$  respectively. In the present study the term  $g_s$  is set to zero, i.e. any deviation of interaction from the bulk is neglected. This specific choice of surface potential results in short range interaction. The electrostatic contribution to the free energy functional can be obtained as [181, 6],

$$\frac{F_{electrostatic}}{k_B T} = -\frac{\epsilon_o v_o}{k_B T} \int_V \frac{\epsilon(\psi)}{2} |\nabla\phi|^2 d\mathbf{r} \quad (3.57)$$

where,  $\epsilon_o$  is the permittivity of free space,  $v_o$  is the volume occupied by one polymer chain and  $\epsilon(\psi)$  is the dielectric permittivity which is taken to be phase dependent.  $\phi$  is the space dependent potential due to the applied voltage. A linear interpolation of the permittivity between the two phases assuming the polymer to behave as a linear dielectric material yields,

$$\epsilon(\psi) = \epsilon_A \left( \frac{1 + \psi}{2} \right) + \epsilon_B \left( \frac{1 - \psi}{2} \right) \quad (3.58)$$

The assumption of linear dielectric behavior has been previously employed in SCFT calculations [157, 59].

Substituting the derived expressions,

$$\begin{aligned} \frac{F}{k_B T} = & \int_V \left[ -\frac{\psi^2}{2} + \frac{\psi^4}{4} \right] + \frac{\kappa}{2} |\nabla\psi|^2 - \frac{\epsilon_o v_o}{k_B T} \frac{\epsilon(\psi)}{2} |\nabla\phi|^2 d\mathbf{r} \\ & + B \int_V \int_V G(\mathbf{r}, \mathbf{r}') \psi(\mathbf{r}) \psi(\mathbf{r}') d\mathbf{r} d\mathbf{r}' + \int_S [h_o\delta(y) + h_L\delta(y - L)] \psi(\mathbf{r}) d\mathbf{r}. \end{aligned} \quad (3.59)$$

In the absence of the electrostatic free energy contribution, the model reduces to the one from Brown et al. [41], that was used to study surface induced ordering of block copolymers. The kinetic evolution of the conserved order parameter  $\psi$  follows the dynamics underpinned by Model B [182],

$$\begin{aligned} \frac{\partial \psi}{\partial t} &= M \nabla^2 \frac{\delta F}{\delta \psi} \\ &= M \nabla^2 \left[ (-\psi + \psi^3) - \kappa \nabla^2 \psi - \frac{\epsilon_o v_o}{k_B T} \frac{\epsilon'(\psi)}{2} |\nabla \phi|^2 \right] - B \psi. \end{aligned} \quad (3.60)$$

Additionally, the Maxwell equation is employed to numerically simulate the spatial distribution of  $\phi$  as,

$$\nabla \cdot [\epsilon_o \epsilon(\psi) \nabla \phi] = 0. \quad (3.61)$$

The effect of thermal fluctuations can be accounted by adding a noise term  $\sqrt{s}\eta$  in Eq.(3.60), where,  $s$  is the strength of the noise, the reciprocal of which is roughly equal to the quench depth and  $\eta$  is noise distribution following the fluctuation-dissipation theorem  $\langle \eta(\mathbf{r}, t) \eta(\mathbf{r}', t') \rangle = -\nabla^2 \delta(\mathbf{r} - \mathbf{r}') \delta(t - t')$ . It is worth mentioning that thermal fluctuations are important as far as the order-disorder transitions in weak segregation regime are concerned. However, the equilibrium morphology which is the focus of the present work is not influenced upon incorporation of stochastic noise. The present claim is corroborated by Ref. [41], where the effect of confining surfaces was studied and the final morphology was found to be independent of noise, both in WSL as well as SSL. Therefore, it is asserted that the neglect of stochastic noise in the present work is reasonably well justified.

Next, the simulation parameters are non-dimensionalized as per characteristic energy  $F'$ , length  $L'$  and time  $t'$  scales. The free energies are non-dimensionalized using  $F' = k_B T$ ,  $L'$  is the lattice cell size and  $t' = \frac{L'^2}{M' F'}$ . The terms  $\kappa$  and  $B$  are non-dimensionalized as,  $\kappa = \frac{\kappa'}{L'^2}$  and  $B = B' L'^2$ . The dielectric constants are rendered non-dimensional using  $\epsilon_A = \frac{\epsilon'_A}{\epsilon_o}$  and the electric field by  $E = \frac{E'}{\sqrt{\frac{k_B T}{v_o \epsilon_o}}}$ . Using representative values of  $T = 430K$  and  $v_o = 100nm^3$ , the value of  $E = \frac{E'}{82V/\mu m}$  is obtained.

The simulation geometry chosen for the present study is shown in Fig. 3.6. The set-up consists of two rigid surfaces at  $y = 0$  and  $y = L_y$  confining the copolymer film across which a constant voltage is applied. Dirichlet boundary conditions are applied for voltage at  $y = 0$  and  $y = L_y$  with  $\phi|_{y=0} = +\frac{V}{2}$  and  $\phi|_{y=L_y} = -\frac{V}{2}$  while Neumann boundary condition is applied at  $x = 0$  and  $x = L_x$ . Therefore, electric field is aligned along y-direction. The confining substrates, also attract one of the copolymers which is controlled by the numerical parameter  $h$  as mentioned before. The appropriate boundary

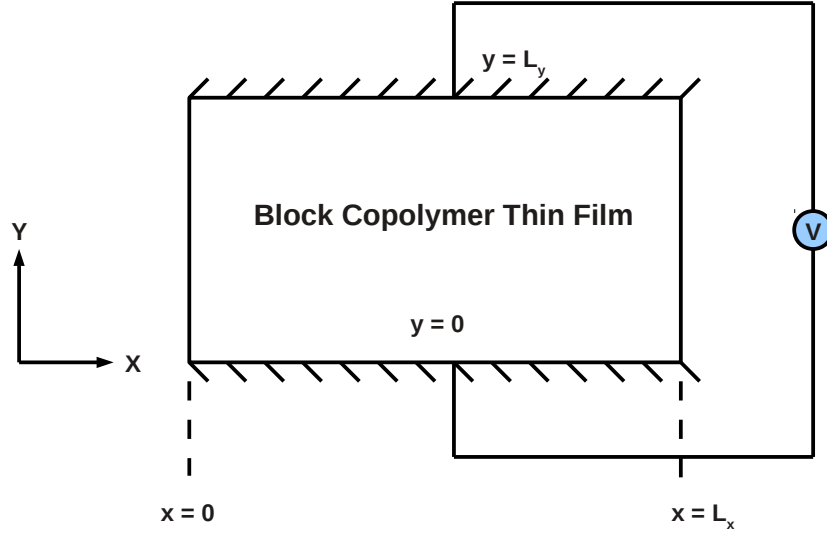


Figure 3.6: A schematic showing the simulation set up used in the present study. A diblock copolymer thin film is confined within two rigid substrates (top and bottom) which has a preferential attraction towards one of the components. Electrostatic field is generated by applying a constant voltage across the film thickness.

condition to account for attracting substrates translate into, [177, 183]

$$\begin{aligned} \left. \frac{\partial \psi}{\partial y} \right|_{y=0} &= +\frac{h_o}{\kappa} \\ \left. \frac{\partial \psi}{\partial y} \right|_{y=L_y} &= -\frac{h_L}{\kappa}. \end{aligned} \quad (3.62)$$

Additionally, no mass transport is allowed through the rigid surface by applying a no-flux boundary condition at the surfaces, [183, 37]

$$\left. \frac{\partial \mu}{\partial y} \right|_{y=0} = \left. \frac{\partial \mu}{\partial y} \right|_{y=L_y} = 0. \quad (3.63)$$

Periodic boundary condition is applied for  $\psi$  in x-direction. Eq.(3.60) is solved using an explicit finite difference method where the spatial derivatives are discretized using central difference which is second order accurate in space and temporal discretization using first order Euler technique. The equation is solved in two steps. First, the terms constituting  $\mu$  is discretized as follows,

$$\begin{aligned} \mu_{i,j} = & -\psi_{i,j} + \psi_{i,j}^3 - \kappa \left[ \left( \frac{\psi_{i+1,j} - 2\psi_{i,j} + \psi_{i-1,j}}{\Delta x^2} \right) + \left( \frac{\psi_{i,j+1} - 2\psi_{i,j} + \psi_{i,j-1}}{\Delta y^2} \right) \right] \\ & - \frac{\epsilon_o v_o^3}{k_B T} \frac{(\epsilon_A - \epsilon_B)}{4} \left\{ \left( \frac{\phi_{i+1,j} - \phi_{i-1,j}}{2\Delta x^2} \right)^2 + \left( \frac{\phi_{i,j+1} - \phi_{i,j-1}}{2\Delta y^2} \right)^2 \right\} - B\psi_{i,j} \end{aligned} \quad (3.64)$$

where  $i, j$  denote the discrete grid position in  $x$  and  $y$  directions respectively.  $\Delta x$  and  $\Delta y$  are the spatial discretization width in  $x$  and  $y$  directions respectively.

The discretized temporal evolution writes as,

$$\frac{\psi_{i,j}^{t+\Delta t} - \psi_{i,j}^t}{\Delta t} = M \left[ \left( \frac{\mu_{i+1,j} - 2\mu_{i,j} + \mu_{i-1,j}}{\Delta x^2} \right) + \left( \frac{\mu_{i,j+1} - 2\mu_{i,j} + \mu_{i,j-1}}{\Delta y^2} \right) \right] \quad (3.65)$$

where  $t$  denotes time and  $\Delta t$  is the temporal discretization width. The Laplace equation in Eq. (3.61) is solved iteratively using Successive-Over-Relaxation (SOR) method. The details of the discretization is discussed in the next chapter. The initial guess for  $\phi$  is tailored by providing a linear initial profile in  $y$ -direction (corresponding to constant electric field, since,  $E = -\nabla\phi$ ) to facilitate faster convergence.

# Chapter 4

## Phase-field model for grain boundary grooving under electromigration

### 4.1 Sharp-interface description

Before proceeding to the diffuse-interface formalism, we briefly recount the phenomenological description of the electromigration within the framework of irreversible thermodynamics. As mentioned earlier, metal ions of the conductor when subjected to an applied electric field are exposed to two forces. First, the direct electrostatic force which propels the positive ions towards the negative terminal (cathode). Second, the negatively charged electrons accelerated in the direction of the positive terminal (anode), collide with the positive ions, thus transferring momentum resulting in the movement of the ions in the direction of electron flow. This contribution is termed as “electron wind”.

Consider a pure metal conductor with species A and vacancies V occupying the normal (substitutional) lattice sites subjected to an applied field. The flux of the atom A  $J_A$  can be written as a linear combination of the driving forces as [23, 184]

$$J_A = -L_{AA}\nabla(\mu_A - \mu_V + q_A\phi) - L_{Ae}e\nabla\phi. \quad (4.1)$$

$\mu_A$  and  $\mu_V$  are the chemical potentials of the species A and V respectively.  $q_A$  and  $e$  denote the valence of A and electron charge respectively.  $\phi$  represents the electric potential.  $L_{AA}$  is the phenomenological coefficient related to the diffusion coefficient of A and  $L_{Ae}$  relates to the interaction between the ion and the electron. The flux of the atoms A will instigate the flow of vacancies  $J_V$  in the opposite direction such that

$$J_V = -J_A. \quad (4.2)$$

The term  $(\mu_A + q_A\phi)$  combined is termed as the electrochemical potential. To understand the driving forces arising out of the imposed electric field, Eq.(4.1) can be rearranged to give

$$J_A = -L_{AA}\nabla(\mu_A - \mu_V) - L_{AA}q_A\nabla\phi - L_{Ae}e\nabla\phi \quad (4.3)$$

The second term in the above equation is the consequence of the direct electrostatic force while the third term arising due to the cross effect between the diffusing species and electron is the electron wind force. In the conductor, the metal ions are shielded by the negative electrons so that the direct electrostatic force is often much less than the wind force [23, 72]. The dominance of the wind force is further corroborated by experimental observation which suggest the movement of the conductor in the direction of the electron flow [75, 87]. Hence the second term can safely be neglected so that we have

$$J_A = -L_{AA}\nabla(\mu_A - \mu_V) - L_{Ae}e\nabla\phi \quad (4.4)$$

$$= J_{chem} + J_{em} \quad (4.5)$$

Thus due to the continuity equation we have

$$\frac{\partial C_A}{\partial t} = \nabla \cdot L_{AA}\nabla(\mu_A - \mu_V) + \nabla \cdot L_{Ae}e\nabla\phi \quad (4.6)$$

The flux of the charge carriers i.e. electrons on the other hand, is given by

$$J_e = -L_{eA}\nabla(\mu_A - \mu_V + q_A\phi) - L_{ee}e\nabla\phi \quad (4.7)$$

The current in the conductor is entirely due to the imposed electron wind and the cross effect due to mass flux is negligible and hence the cross terms can be safely neglected. In addition, the timescales for the electrodynamics i.e. charge relaxation is much faster compared to the ion diffusion process. Hence, the current continuity equation translates into Laplace equation as

$$\nabla \cdot J_e = \nabla \cdot [L_{ee}e\nabla\phi] = 0 \quad (4.8)$$

Comparing the above equation to Ohm's law yields the relation between the electron conductivity  $\sigma$  and mobility as

$$\sigma = L_{ee}e \quad (4.9)$$

We next relate the constants  $L_{AA}$  and  $L_{Ae}$  to the diffusivity. The free energy of the system consisting of  $N_A$  number of atoms and  $N_{Va}$  number of vacancies is written as [184]

$$G = N_A\mu_A^0 + N_{Va}G_V^f + k_B T \left[ N_A \ln \left( \frac{N_A}{N_A + N_{Va}} \right) + N_{Va} \ln \left( \frac{N_{Va}}{N_A + N_{Va}} \right) \right] \quad (4.10)$$

where  $\mu_A^0$  is chemical potential of  $A$  atoms in a pure crystal consisting of only  $A$  atoms and  $G_V^f$  is the free energy to form a vacancy. The chemical potentials are defined as

$$\mu_A = \frac{\partial G}{\partial N_A} = \mu_A^0 + k_B T \ln \left( \frac{N_A}{N_A + N_{Va}} \right). \quad (4.11)$$

For a dilute solid solution  $N_A \ll N_{Va}$  and  $\mu_A = \mu_A^0$ . Similarly

$$\mu_V = \frac{\partial G}{\partial N_{Va}} = G_V^f + k_B T \ln \left( \frac{N_{Va}}{N_A + N_{Va}} \right) = G_V^f + k_B T \ln X_V \quad (4.12)$$

where  $X_V$  is mole fraction of vacancies. Therefore, the chemical driving force of A atoms can be written as

$$J_{chem} = -L_{AA} \nabla(\mu_A - \mu_V) = -L_{AA} \nabla(\mu_A^0 - G_V^f - k_B T \ln X_V) = \frac{L_{AA} k_B T}{X_V} \nabla X_V \quad (4.13)$$

Using the relation  $X_V = \Omega_V C_V$  where  $\Omega_V$  is the atomic volume and  $C_V$  is the concentration of the vacancy we have

$$J_{chem} = \frac{L_{AA} k_B T \Omega_V}{X_V} \nabla C_V \quad (4.14)$$

Comparing the above equation with Fick's law yields the relation between vacancy diffusivity and  $L_{AA}$  as  $L_{AA} = D_V X_V / \Omega_V k_B T$ . The process of EM is driven by the collision of the electron with the diffusing species around the sites of lattice imperfections or defects, which creates a force due to the self-consistent electronic charge distribution around the defect. The defect scatters the electrons, creating a dipole and exerts an electrostatic force [185]. This force is described phenomenologically by ascribing an effective charge  $ze$ , with the driving force reading as  $F_{em} = zeE$ . Thus it is assumed that the driving force for electromigration can be approximated by an electrostatic force. This in turn induces a drift of the atoms by a vacancy mechanism given by

$$J_{em} = - \langle v_d \rangle C_V = -M_V F_{em} C_V = -\frac{D_V C_V}{k_B T} zeE \quad (4.15)$$

where  $\langle v_d \rangle$  is the average drift velocity and  $M_V$  is the vacancy mobility. Comparing the above equation with Eq.(4.4)  $L_{Ae} = D_V C_V z / k_B T$ . Since migration of atoms takes place by a vacancy mechanism the material transport is usually written in terms of vacancy flux. Using Eqs.(4.2), (4.3), (4.14) and (4.15) the vacancy flux writes as

$$J_V = -D_V \left( \nabla C_V - \frac{ze}{k_B T} C_V E \right). \quad (4.16)$$

In thin film conductors the surface and GBs are the predominant diffusion pathways and in such cases  $L_{AA}$  and  $L_{Ae}$  can be related to surface  $D_S$  and GB diffusivities  $D_{GB}$ . The corresponding sharp-interface description is discussed later in relevant chapters.

## 4.2 Diffuse-interface model

The aim of the present chapter is to construct a simplified model that can correctly capture the concurrent diffusion and EM phenomenon in pure metal polycrystalline interconnect. In the drift velocity set up, as shown in Fig.4.1(a), the metal conductor (such

as Aluminum, Copper, Gold) is deposited on a relatively inert material (such as Molybdenum, Tantalum, Titanium nitride) which is insoluble and does not form any intermetallic compound with the test sample [75]. The electric current passes through the underlayer domain and shunts into the metal stripe whenever it gets the opportunity to do so, resulting in EM displacement. The equivalent circuit diagram of the experimental set up is shown in Fig.4.1(b). Additionally, the resistivity (conductivity) of the underlayer material is higher (lower) than the test piece, so that majority of the current is assumed to flow through the metal conductor. In the simulations, we recreate a two-dimensional version of the actual three-dimensional set up as shown in Fig.4.1(c) which is the top-view of the experimental configuration. The underlayer beneath the conductor is not explicitly considered which essentially implies that the net current flows through the conductor. The vapor or the outer environment is not considered explicitly, and the region ahead of the test piece is assigned the conductivity of the underlayer (since the vacuum cannot conduct electricity), while still modeling the leading edge as a free surface. The equivalent circuit diagram of the simulation set up is shown in Fig.4.1(d). Moreover, since our prime interest is GB grooving and initial stage drift, only the cathode end of the sample is considered. The mass deposition and the formation of hillocks which takes place at the anode end are not taken into account. Thus the simulation set up comprises of an array of periodic grains of the metal interconnect separated from the dielectric underlayer as shown in Fig. 4.1(c).

Following [186, 187, 4], a set of conserved and non-conserved order parameters to distinguish between the underlayer and the polycrystalline interconnect domain is employed. A conserved order parameter, which, in the present case is the scaled density variable  $\rho$ , distinguishes the underlayer ( $\rho = 0$ ) and the interconnect ( $\rho = 1$ ) domain. While, a set of  $N$  non-conserved order parameters ( $\eta_1, \eta_2, \dots, \eta_N$ ) are chosen to describe the multiple grains in the interconnect microstructure. The non-conserved order parameters are chosen such that the  $i^{th}$  grain of the interconnect is described by  $\eta_i = 1$  and  $\eta_j = 0 \forall j \neq i$ , where as the underlayer domain is defined by  $\eta_i = 0 \forall i$ .

With the above description, GB is defined as the region between  $i^{th}$  and  $j^{th}$  grain where  $\eta_i$  and  $\eta_j$  varies smoothly between  $0 < \eta_i, \eta_j < 1$ . Surface, on the other hand is the region between the underlayer and the  $i^{th}$  grain of the interconnect exhibiting smooth variation of  $\rho$  and  $\eta_i$  as  $0 < \rho, \eta_i < 1$ . Using the definition of conserved and non-conserved order parameters the free energy functional is defined as,

$$F = N_V \int_V f(\rho, \eta_i) + \kappa_\rho |\nabla \rho|^2 + \kappa_\eta \sum_{i=1}^N |\nabla \eta_i|^2 dV \quad (4.17)$$

where,  $\kappa_\rho$  and  $\kappa_\eta$  are the gradient energy coefficients which penalizes gradients in  $\rho$  and  $\eta$  respectively.  $V$  denotes the volume and  $N_V$  is the number of atoms per volume.  $f(\rho, \eta_i)$

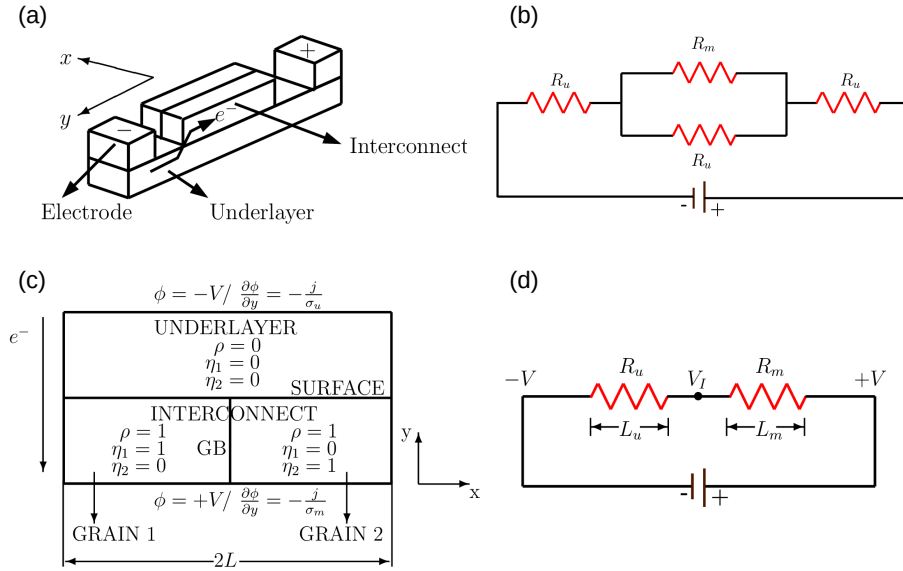


Figure 4.1: (a) Schematic illustration of a typical drift velocity experiment configuration. A conducting metal called the interconnect is deposited over a relatively high resistivity substrate known as the underlayer. The electric field is generated by an applied voltage at the electrodes. (b) An equivalent circuit diagram of the experimental set-up. (c) Schematic diagram of the two dimensional set-up used in the phase-field study. The set-up is a top view of the experimental configuration. The interconnect consists of array of periodic grains with GB aligned along the direction of electric field, a case typical of polycrystalline interconnects. The electric field is applied by either prescribing constant potential at top and bottom edges (constant voltage) or by imposing a constant potential gradient (constant current). The electron wind is directed towards the bottom electrode. (d) An equivalent circuit diagram of the simulation set-up corresponding to the constant voltage case.  $R_u$ ,  $L_u$  and  $R_m$ ,  $L_m$  are the initial resistances and lengths of the underlayer and the metal interconnect respectively.

is a Landau-type potential which creates  $N + 1$  distinct minima at  $(\rho, \eta_1, \eta_2, \dots, \eta_N) = (1, 1, 0, \dots, 0), (1, 0, 1, \dots, 0), \dots, (0, 0, 0, \dots, 0)$  in the free energy landscape. The explicit expression of  $f(\rho, \eta_i)$  can be derived considering the following symmetry arguments,

- (a)  $f(\rho, \eta_i)$  must account for two degenerate states in  $\rho$ , corresponding to the interconnect and the underlayer domain. The simplest polynomial satisfying the criteria is a double well of the form

$$f_I = A\rho^2(1 - \rho)^2 \quad (4.18)$$

where,  $A$  is the energy barrier with units of energy per atom.

- (b) Second, the interconnect defined by  $\rho = 1$  should exhibit  $N$  minima in  $\eta_i$ ,  $(\eta_1, \eta_2, \dots, \eta_N) = (1, 0, \dots, 0), (0, 1, \dots, 0), (0, 0, \dots, 1)$  corresponding to various grain orientations. Following [188, 189],

$$f_{II} = B\rho^2\xi(\eta_i) \quad (4.19)$$

where,

$$\xi(\eta_i) = \sum_{i=1}^N \left[ \frac{\eta_i^4}{4} - \frac{\eta_i^2}{2} + \epsilon \sum_{j>i}^N \eta_i^2 \eta_j^2 \right] + \frac{1}{4}. \quad (4.20)$$

The function  $\xi(\eta_i)$  is a multiwell in  $\eta_i$ . The first two terms of  $\xi(\eta_i)$  is a double-well potential with  $2^N$  minima at  $(\eta_i, \eta_j) = (\pm 1, \pm 1)$  which is unsuitable to define a multigrain structure. The cross term with a proper choice of  $\epsilon > 1/2$  is able to restrict the number of minima to  $2N$  with  $(\eta_i, \eta_j) = (\pm 1, 0)$  [190]. Restricting to only the positive values of  $\eta_i$  and without any loss of generality select  $\epsilon = 2$ . The constant  $1/4$  is added to shift the well depth to 0. An elaborate discussion on the effect of  $\epsilon$  on free energy landscape and equilibrium profiles can be found in Ref. [189].

- (c) Third, the underlayer i.e.  $\rho = 0$  is characterized by a single minima in  $\eta_i$ ,  $(\eta_1, \eta_2, \dots, \eta_N) = (0, 0, \dots, 0)$ . Thus, the final contribution writes as [188],

$$f_{III} = C(1 - \rho)^2 \sum_{i=1}^N \eta_i^2 \quad (4.21)$$

Combining Eqs. (4.18), (4.19) and (4.21),

$$f(\rho, \eta_i) = A\rho^2(1 - \rho)^2 + B\rho^2\xi(\eta_i) + C(1 - \rho)^2 \sum_{i=1}^N \eta_i^2 \quad (4.22)$$

It is to be noted that the prefactor  $\rho^2$  and  $(1 - \rho)^2$  in the second and third term will alter the free energy landscape in the interconnect and the underlayer domain respectively. The

kinetic equations of the conserved and the non-conserved order parameters are obtained from the free energy functional by variational derivatives. Thus, the non-conserved order parameters follow the dynamics of Allen-Cahn Eq. [191] as,

$$\begin{aligned}\frac{\partial \eta_i}{\partial t} &= -L_\eta \frac{\delta}{\delta \eta_i} (F/N_V) \\ &= -L_\eta \left[ \frac{\partial f(\rho, \eta_i)}{\partial \eta_i} - 2\kappa_\eta \nabla^2 \eta_i \right]\end{aligned}\quad (4.23)$$

where,  $L_\eta$  is the relaxation coefficient for the non-conserved order parameters. The conserved order parameter, on the other hand, is governed by the modified Cahn-Hilliard Eq. [165] as,

$$\frac{\partial \rho}{\partial t} = \nabla \cdot \left[ M(\rho, \eta_i) \left\{ \nabla \frac{\delta}{\delta \rho} (F/N_V) + ze \nabla \phi \right\} \right] \quad (4.24)$$

The chemical potential  $\mu$  is defined from the variational derivative as,

$$\mu = \frac{\delta}{\delta \rho} (F/N_V). \quad (4.25)$$

Strictly speaking, effective charge can assume different values in different regions of the interconnect such as effective surface charge  $z_S$ , effective grain boundary charge  $z_{GB}$  and effective charge in the bulk  $z_B$ . However, for the sake of simplicity a uniform effective charge is assumed in the present work. Thus Eq.(4.24) translates into,

$$\frac{\partial \rho}{\partial t} = \nabla \cdot M(\rho, \eta_i) [\nabla \mu + ze \nabla \phi] \quad (4.26)$$

Thus, the above Eq. implies the motion of diffusing species under the combined influence of gradient of chemical potential as well as electric potential. To account for enhanced diffusivities at the surface and GB, the mobility is expressed as a scalar function of  $\rho$  and  $\eta_i$  as [188],

$$M(\rho, \eta_i) = M_B + 4M_{GB} \sum_{j>i} \sqrt{\eta_i^2 \eta_j^2} + 16M_S \rho^2 (1 - \rho)^2 \quad (4.27)$$

where  $M_B$ ,  $M_{GB}$  and  $M_S$  stands for the atomic mobility in the bulk, at the GBs and at the surface respectively.

Few comments are in order regarding the specific choice of mobility function. The third term in Eq.(4.27) represents the surface diffusion at the interconnect-underlayer interface (interphase interface in other words). The square term in  $\rho$  and  $(1 - \rho)$  makes our mobility function biquadratic as opposed to the quadratic form used in several previous studies [192, 193, 194, 195] and serves two purposes. First,  $\rho$  by virtue of its conserved nature exhibits the Gibbs-Thomson effect, as a result of which,  $\rho$  may overshoot the prescribed limit of  $0 < \rho < 1$  depending upon the local curvature. The biquadratic mobility specifically suppresses the additional bulk diffusion contribution arising from the

local variation of  $\rho$  [196]. In fact, it has recently been shown through asymptotic analysis, that a polynomial well-type free energy in conjunction with a quadratic mobility leads to an additional contribution from bulk diffusion at the same order as surface diffusion [197, 198]. A biquadratic mobility, such as the one used in the present study, however, is able to recover pure surface diffusion limited motion i.e. motion by surface laplacian of the mean curvature [198]. It is remarked that obstacle-type free energies which restricts the value  $0 < \rho < 1$ , however, do not suffer from the above mentioned deficiencies [196, 197].

Secondly, biquadratic mobility also has the attractive feature that it always returns a non-negative value, thus obviating any numerical instabilities.

While the asymptotic analysis are carried out as the interface width tends to zero, the numerical implementation of the diffuse interface with finite width could give rise to normal diffusion currents [199]. To restrict diffusion only along the tangential direction along the surface in such cases, a tensorial form of mobility function has also been proposed given by [200, 201, 202],

$$M = M_B + 4M_{GB} \sum_{j>i} \sqrt{\eta_i^2 \eta_j^2} \mathbf{T}_{GB} + 16M_S \rho^2 (1 - \rho)^2 \mathbf{T}_S \quad (4.28)$$

where,  $\mathbf{T}_{GB}$  and  $\mathbf{T}_S$  are the surface projection tensor of the form  $\mathbf{T}_{S,GB} = \mathbf{I} - \mathbf{n} \otimes \mathbf{n}$ .  $\mathbf{I}$  represents the identity tensor and  $\mathbf{n}$  the normal to the surface and GB given as  $\mathbf{n} = \nabla \rho / |\nabla \rho|$  and  $\mathbf{n} = (\nabla \eta_i - \nabla \eta_j) / |\nabla \eta_i - \nabla \eta_j|$ .

However, considering the fact that in the present problem interface thickness is of the order of nanometers, the simplistic scalar mobility function is able to restrict the diffusion mainly along the surface and GB and is employed in the present work. Tensorial mobility, on the other hand is expected to work properly for even moderately diffuse interface widths as it inherently restricts the diffusion current along the tangential direction.

In addition to Eq.(4.23) and (4.26), the Laplace equation is solved assuming the relaxation time for electrostatic equilibrium to be much faster than the diffusive timescale to evaluate the electric potential distribution as ,

$$\nabla \cdot \left[ \sigma(\rho) \nabla \phi \right] = 0 \quad (4.29)$$

where  $\sigma$  is the conductivity taken to be  $\rho$  dependent to distinguish the electrical property of the metal interconnect  $\sigma_m$  and dielectric underlayer  $\sigma_u$ . A linear interpolation is employed between the interconnect and underlayer as,

$$\sigma(\rho) = \sigma_m \rho + \sigma_u (1 - \rho) \quad (4.30)$$

Thus Eq. (4.23), (4.26) and (4.29) combines a degenerate Cahn-Hilliard, Allen-Cahn and Laplace Eq. which constitutes coupled PDEs for the electromigration problem.

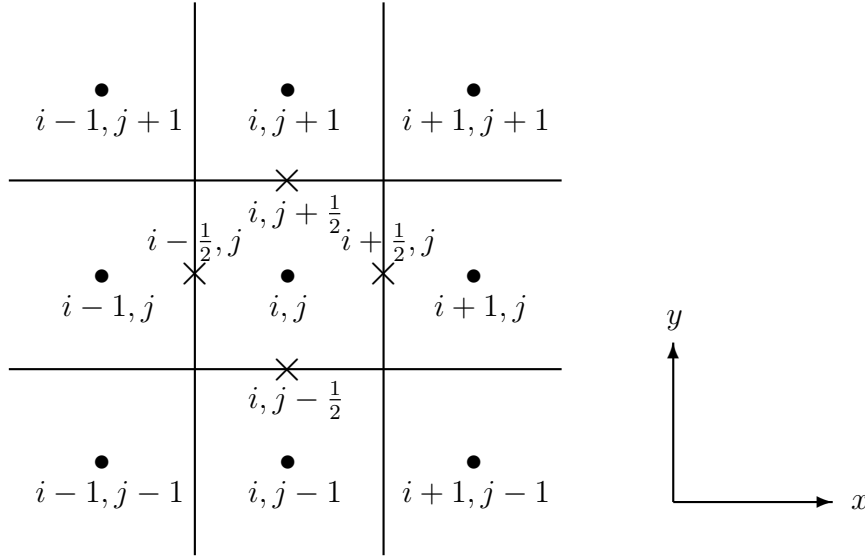


Figure 4.2: A 2-D schematic of the finite difference grid with the black dots representing the regular lattice points and the crosses depicting the staggered positions.

### 4.3 Numerical Discretization

The governing equations are discretized using explicit finite difference method on a square staggered mesh. Because of the presence of the gradient energy term in  $\rho$  in the free energy functional, the Cahn-Hilliard equation is a fourth order partial differential equation. The Cahn-Hilliard equation is solved in two steps. First the chemical potential  $\mu$  is calculated at each grid point. The laplacian is calculated using a 5 point stencil in 2 -  $D$  (7 point stencil in 3 -  $D$ ). The discretized equation writes as,

$$\mu_{i,j} = \left( \frac{\partial f}{\partial \rho} \right)_{i,j} - 2\kappa_{\rho} \left[ \frac{\rho_{i+1,j} - 2\rho_{i,j} + \rho_{i-1,j}}{(\Delta x)^2} + \frac{\rho_{i,j+1} - 2\rho_{i,j} + \rho_{i,j-1}}{(\Delta y)^2} \right] \quad (4.31)$$

Thereafter, the gradient and the divergence operator is discretized using a combination of first order forward and backward difference formulas resulting in an overall accuracy of second order. The mobility function  $M(\rho, \eta_i)$  is calculated at the center of two grid points i.e. at staggered positions denoted as  $i - 1/2, j$ ,  $i + 1/2, j$ ,  $i, j - 1/2$  and  $i, j + 1/2$  as shown in Fig.4.2. Thus,

$$\begin{aligned} M_{i+\frac{1}{2},j} &= \frac{M_{i,j} + M_{i+1,j}}{2} \\ M_{i-\frac{1}{2},j} &= \frac{M_{i,j} + M_{i-1,j}}{2} \\ M_{i,j+\frac{1}{2}} &= \frac{M_{i,j} + M_{i,j+1}}{2} \\ M_{i,j-\frac{1}{2}} &= \frac{M_{i,j} + M_{i,j-1}}{2} \end{aligned} \quad (4.32)$$

The temporal derivative is discretized using Euler method. The final difference equation writes as,

$$\begin{aligned} \frac{\rho_{i,j}^{t+\Delta t} - \rho_{i,j}^t}{\Delta t} = & \frac{1}{\Delta x} \left[ M_{i+\frac{1}{2},j} \left\{ \frac{\mu_{i+1,j} - \mu_{i,j}}{\Delta x} + ze^{\frac{\phi_{i+1,j} - \phi_{i,j}}{\Delta x}} \right\} \right. \\ & \left. - M_{i-\frac{1}{2},j} \left\{ \frac{\mu_{i,j} - \mu_{i-1,j}}{\Delta x} + ze^{\frac{\phi_{i,j} - \phi_{i-1,j}}{\Delta x}} \right\} \right] \\ & + \frac{1}{\Delta y} \left[ M_{i,j+\frac{1}{2}} \left\{ \frac{\mu_{i,j+1} - \mu_{i,j}}{\Delta y} + ze^{\frac{\phi_{i,j+1} - \phi_{i,j}}{\Delta y}} \right\} \right. \\ & \left. - M_{i,j-\frac{1}{2}} \left\{ \frac{\mu_{i,j} - \mu_{i,j-1}}{\Delta y} + ze^{\frac{\phi_{i,j} - \phi_{i,j-1}}{\Delta y}} \right\} \right] \end{aligned} \quad (4.33)$$

The Allen-Cahn equation in contrast is a second order partial differential equation and the discretized version can be written as,

$$\frac{\eta_{i,j}^{t+\Delta t} - \eta_{i,j}^t}{\Delta t} = -L_\eta \left[ \left( \frac{\partial f}{\partial \eta} \right)_{i,j} - 2\kappa_\eta \left\{ \frac{\eta_{i+1,j} - 2\eta_{i,j} + \eta_{i-1,j}}{(\Delta x)^2} + \frac{\eta_{i,j+1} - 2\eta_{i,j} + \eta_{i,j-1}}{(\Delta y)^2} \right\} \right] \quad (4.34)$$

While, the Cahn-Hilliard and Allen-Cahn equations are parabolic partial differential equations, the Laplace equation is elliptical and requires an iterative approach to the solution. The gradient and the divergence operator are discretized similar to the Cahn-Hilliard equation,

$$\begin{aligned} & \frac{1}{\Delta x} \left[ \sigma_{i+\frac{1}{2},j} \left\{ \frac{\phi_{i+1,j} - \phi_{i,j}}{\Delta x} \right\} - \sigma_{i-\frac{1}{2},j} \left\{ \frac{\phi_{i,j} - \phi_{i-1,j}}{\Delta x} \right\} \right] + \\ & \frac{1}{\Delta y} \left[ \sigma_{i,j+\frac{1}{2}} \left\{ \frac{\phi_{i,j+1} - \phi_{i,j}}{\Delta y} \right\} - \sigma_{i,j-\frac{1}{2}} \left\{ \frac{\phi_{i,j} - \phi_{i,j-1}}{\Delta y} \right\} \right] = 0 \end{aligned} \quad (4.35)$$

For  $\Delta x = \Delta y$  the above equation can be rearranged as,

$$\phi_{i,j} = \frac{\left[ \sigma_{i+\frac{1}{2},j} \phi_{i+1,j} + \sigma_{i,j+\frac{1}{2}} \phi_{i,j+1} + \sigma_{i-\frac{1}{2},j} \phi_{i-1,j} + \sigma_{i,j-\frac{1}{2}} \phi_{i,j-1} \right]}{\left[ \frac{\sigma_{i+1,j} + \sigma_{i,j+1} + \sigma_{i-1,j} + \sigma_{i,j-1} + 4\sigma_{i,j}}{2} \right]} \quad (4.36)$$

The above equation is solved iteratively at each grid point. The convergence can be further sped up by adopting the Successive-Over-Relaxation technique in which the solution at each iteration is taken to be the weighted average of the current and previous iteration as,

$$\phi_{i,j}^{n+1} = (1 - \omega) \phi_{i,j}^n + \omega \phi_{i,j}^{n+1} \quad (4.37)$$

where  $n$  denotes the iteration step and  $\omega$  is the relaxation parameter. The choice of  $\omega$  depends upon the exact form of the equation and the coefficients under consideration, but is generally taken to be in the range  $0 < \omega < 2$ . The stopping criterion is selected such that the maximum difference of the  $\phi$  value between the present and the previous iteration at any grid point is less than  $10^{-6}$  i.e.,

$$\max \left| \phi_{i,j}^{n+1} - \phi_{i,j}^n \right| \leq 10^{-6} \quad . \quad (4.38)$$

## 4.4 Boundary Conditions

The equations are discretized at nodal points referred to as  $0, 1, \dots, Nx - 1, Nx$  in  $x$  direction and  $0, 1, \dots, Ny - 1, Ny$  in  $y$  direction. The end points in each direction i.e. 0 and  $Nx$  in  $x$  direction and 0 and  $Ny$  in  $y$  direction are assumed to be the boundary points, the values at which are calculated using the prescribed boundary condition. The Cahn-Hilliard equation being a fourth order partial differential equation requires 4 boundary conditions. Because of the discretization scheme, one boundary condition in  $\mu$  and the other in  $\rho$  is employed. Periodic boundary condition is utilized in  $x$  direction as

$$\begin{aligned} \mu_{0,j} &= \mu_{Nx-1,j} & ; & & \rho_{0,j} &= \rho_{Nx-1,j} \\ \mu_{Nx,j} &= \mu_{1,j} & ; & & \rho_{Nx,j} &= \rho_{1,j} \end{aligned} \quad (4.39)$$

with  $j = 0, 1, 2, \dots, Ny$  and isolate in  $y$  direction as,

$$\begin{aligned} \mu_{i,0} &= \mu_{i,1} & ; & & \rho_{i,0} &= \rho_{i,1} \\ \mu_{i,Ny} &= \mu_{i,Ny-1} & ; & & \rho_{i,Ny} &= \rho_{i,Ny-1} \end{aligned} \quad (4.40)$$

with  $i = 0, 1, 2, \dots, Nx$ . Same boundary conditions are employed for  $\eta$  as,

$$\begin{aligned} \eta_{0,j} &= \eta_{Nx-1,j} & ; & & \eta_{i,0} &= \eta_{i,1} \\ \eta_{Nx,j} &= \eta_{1,j} & ; & & \eta_{i,Ny} &= \eta_{i,Ny-1} \end{aligned} \quad (4.41)$$

with  $j = 0, 1, 2, \dots, Ny$  and  $i = 0, 1, 2, \dots, Nx$ .

For the electric potential  $\phi$ , two types of boundary conditions corresponding to constant voltage and constant current are employed as shown in Fig.4.1(c). A constant voltage  $V$  is applied at the domain edges at  $x = 0$  and  $x = Nx$  as,

$$\begin{aligned} \phi_{x=0} &= +V \\ \phi_{x=Nx} &= -V \end{aligned} \quad (4.42)$$

Constant current along  $y$  direction can be prescribed by maintaining gradients along  $y$  direction as,

$$\begin{aligned} \left. \frac{\partial \phi}{\partial y} \right|_{x=0} &= -\frac{j}{\sigma_m} \\ \left. \frac{\partial \phi}{\partial y} \right|_{x=Nx} &= -\frac{j}{\sigma_u} \end{aligned} \quad (4.43)$$

In both the constant voltage and constant current cases as isolate boundary condition is employed at the domain edges in  $y$  direction as,

$$\begin{aligned} \phi_{0,j} &= \phi_{1,j} \\ \phi_{Nx,j} &= \phi_{Nx-1,j} \end{aligned} \quad (4.44)$$

with  $j = 0, 1, 2, \dots, Ny$ .

The explicit finite difference scheme is numerically stable and convergent only below a certain temporal width  $\Delta t$  depending upon the selected grid width  $\Delta x$  and the individual equation. The stability limit of the Cahn-Hilliard equation is given by,

$$\Delta t \leq \frac{(\Delta x)^4}{2^{2d+1}\kappa_\rho M_{max}} \quad (4.45)$$

where  $d$  is the dimensionality of the system and  $M_{max}$  is maximum value of the atomic mobility. For the Allen-Cahn equation, the stability criterion reads as,

$$\Delta t \leq \frac{(\Delta x)^2}{2d\kappa_\eta L_\eta} \quad (4.46)$$

For coupled equations, the stability criterion is selected from the minimum value of the timestep width  $\Delta t$  as,

$$\Delta t \leq \min \left\{ \frac{(\Delta x)^4}{2^{2d+1}\kappa_\rho M_{max}}, \frac{(\Delta x)^2}{2d\kappa_\eta L_\eta} \right\} \quad (4.47)$$

## 4.5 Asymptotic analysis : Motion of the free surface

The presence of interfaces of finite thickness in the phase-field formalism introduces an additional length scale in the problem. Therefore, to verify that the phase-field model reduces to the sharp-interface problem as the interface width tends to zero, we perform a formal asymptotic analysis. The asymptotic analysis of a coupled system of degenerate Cahn-Hilliard (variable atomic mobility  $M$ ) and degenerate Allen-Cahn (variable GB relaxation parameter  $L_\eta$ ) equation has been performed by Novick-Cohen [203]. More recently Ahmed et al.[199] have performed the analysis for the system of degenerate Cahn-Hilliard and Allen-Cahn equation. Both cases couple the motion of free surface by surface laplacian of the mean curvature and that of GB by mean curvature. Mahadevan et al.[204] and Bhate et al.[137] have studied the system of degenerate Cahn-Hilliard equation with a wind force term and Laplace equation for a smooth double well and obstacle type free energies respectively. The motion of the interface in such cases are governed by surface laplacian of the mean curvature and surface laplacian of the applied electric potential. Barrett et al.[138] analyzed the system of degenerate Cahn-Hilliard and Allen-Cahn equation under different scaling of  $L_\eta$ . In one limit the authors recover motion by surface laplacian of the mean curvature of the free surface, while the GB is stationary. In a different limit the free surface moves due to a combination of surface laplacian of mean curvature and surface attachment limited kinetics and the GB by mean curvature. The effect of electromigration was also studied. However, so far models with

only one-sided conductivity (non-zero conductivity in only one of the phases) have been analyzed [204, 137, 138]. In this section we extend the previous mentioned studies to a system of degenerate Cahn-Hilliard, Allen-Cahn and Laplace equation with both sided conductivity.

The governing equations are non-dimensionalized by introducing a length scale  $\tilde{x} = x/L$ , energy scale  $\tilde{G} = G/A$ , time scale  $\tilde{t} = M_S G t / (\rho_m - \rho_u)^2 L^2$ , potential  $\tilde{\phi} = \phi / E_o L$  and conductivity  $\tilde{\sigma} = \sigma / \sigma_m$ . Here,  $A$  is the free energy barrier height defined in Eq.(4.18) and  $L$  is the grain size. In addition, we define a parameter  $\epsilon = \sqrt{\kappa_\rho / A} / L$  related to the interface width and  $q = \kappa_\eta / \kappa_\rho$  which denotes the ratio of the gradient energy coefficients of the conserved and the non-conserved order parameter such that  $\kappa_\eta = q\epsilon^2$ . It is to be noted that the surface energy in phase-field models scales as  $\gamma_s \sim \sqrt{\kappa_\rho A}$ . Using the definition of  $\epsilon$ , we have  $\gamma_s \sim L\epsilon A$ . Therefore, in order to have finite surface energy as  $\epsilon \rightarrow 0$ , we choose  $A = \omega / \epsilon$ , where,  $\omega$  is a constant. Furthermore we work with the scaling  $M \rightarrow M / \epsilon$  and  $L_\eta \rightarrow L_\eta / \epsilon^3$ . Dropping tildes henceforth we obtain the governing equations as,

$$\epsilon^2 \frac{\partial \rho}{\partial t} = \nabla \cdot M(\rho) \nabla (\mu_\rho + \epsilon \Lambda \nabla \phi), \quad (4.48)$$

$$\epsilon^4 \frac{\partial \eta_i}{\partial t} = -L_\eta \mu_\eta, \quad (4.49)$$

$$\nabla \cdot [\sigma(\rho) \nabla \phi] = 0. \quad (4.50)$$

where  $\mu_\rho = \frac{\partial f}{\partial \rho} - 2\epsilon^2 \nabla^2 \rho$ ,  $\mu_\eta = \frac{\partial f}{\partial \eta} - 2q\epsilon^2 \nabla^2 \eta$  and  $\Lambda = zeE_o L / \omega$  which denotes the ratio of scale of electrostatic energy to chemical energy. Since along the surface only one of the  $\eta_i$  vary smoothly (Fig.4.1(c)), the mobility function Eq.(4.27) is only a function of  $\rho$  which has been utilized in Eq.(4.48). Furthermore, only one of the  $\eta_i$  exhibits gradient along the surface. Therefore, consideration of only one of them will suffice for further analysis.

We divide the domain into outer and inner regions where the values of field variables change slowly and rapidly respectively. Between the two, there exists an overlapping region where the solution obtained in the two regions are valid and must match with each other. The PDEs (4.48), (4.49) and (4.50) are solved subjected to the initial condition

$$\rho = 1, \eta_1 = 1, \eta_2 = 0, \sigma = \sigma_m \forall x \in \Omega_- \quad (4.51)$$

and

$$\rho = 0, \eta_1 = 0, \eta_2 = 0, \sigma = \sigma_u \forall x \in \Omega_+ \quad (4.52)$$

and the boundary conditions  $\mathbf{n} \cdot \nabla \rho = \mathbf{n} \cdot \nabla \eta_1 = \mathbf{n} \cdot \nabla \eta_2 = \mathbf{n} \cdot \nabla \mu_\rho = 0$ .  $\Omega_\pm$  denotes the bulk regions on the either side of the interface. The solution of the above PDEs are written in terms of powers of small parameter  $\epsilon$ .

### 4.5.1 Outer expansion

The outer solution for the three field variables write as,

$$\rho(x, \epsilon, t) = \rho^0(x, t) + \epsilon\rho^1(x, t) + \epsilon^2\rho^2(x, t), \quad (4.53)$$

$$\eta(x, \epsilon, t) = \eta^0(x, t) + \epsilon\eta^1(x, t) + \epsilon^2\eta^2(x, t), \quad (4.54)$$

$$\phi(x, \epsilon, t) = \phi^0(x, t) + \epsilon\phi^1(x, t) + \epsilon^2\phi^2(x, t), \quad (4.55)$$

$$\mu_\rho(x, \epsilon, t) = \mu_\rho^0(x, t) + \epsilon\mu_\rho^1(x, t) + \epsilon^2\mu_\rho^2(x, t), \quad (4.56)$$

$$\mu_\eta(x, \epsilon, t) = \mu_\eta^0(x, t) + \epsilon\mu_\eta^1(x, t) + \epsilon^2\mu_\eta^2(x, t), \quad (4.57)$$

where, superscript on the variables denotes the order while that on  $\epsilon$  denotes the power. Substituting the above expansions in Eqs.(4.48), (4.49) and (4.50) and equating terms of same order of  $\epsilon$  from the left and right hand side of the equations we obtain at the leading order  $\mathcal{O}(\epsilon^0)$

$$\nabla \cdot M(\rho^0)\nabla\mu_\rho^0 = 0, \quad (4.58)$$

$$-L_\eta\mu_\eta^0 = 0, \quad (4.59)$$

$$\nabla \cdot [\sigma(\rho^0)\nabla\phi^0] = 0 \quad (4.60)$$

where  $\mu_\rho^0 = \frac{\partial f(\rho^0, \eta^0)}{\partial \rho^0}$  and  $\mu_\eta^0 = \frac{\partial f(\rho^0, \eta^0)}{\partial \eta^0}$ . Eqs.(4.58) and (4.59) under the boundary conditions has the solution

$$\rho^0 = \eta^0 = 1 \quad \forall x \in \Omega_-, \quad (4.61)$$

$$\rho^0 = \eta^0 = 0 \quad \forall x \in \Omega_+ \quad (4.62)$$

Using the values of  $\rho^0$ , Eq.(4.60) reduces to Laplace equation in the bulk domains as

$$\nabla^2\phi^0 = 0 \quad \forall x \in \Omega_\pm \quad (4.63)$$

Next to the leading order  $\mathcal{O}(\epsilon)$  we have terms that are not trivially zero as,

$$\nabla \cdot M(\rho^0)\nabla\mu_\rho^1 + \Lambda\nabla \cdot M(\rho^0)\nabla\phi^0 = 0, \quad (4.64)$$

$$-L_\eta\mu_\eta^1 = 0, \quad (4.65)$$

$$\nabla \cdot [\sigma(\rho^0)\nabla\phi^1] + \nabla \cdot [\sigma'(\rho^0)\rho^1\nabla\phi^0] = 0 \quad (4.66)$$

Using the values of  $\rho^0 = 0, 1$  from leading order solution we have  $M(\rho^0) = 0$  and Eq.(4.64) reduces to  $0 = 0$  trivially. From Eq.(4.65) we have

$$\mu_\eta^1 = 0 \quad (4.67)$$

$$\implies \frac{\partial^2 f(\rho^0, \eta^0)}{\partial \eta^2}\eta^1 + \frac{\partial^2 f(\rho^0, \eta^0)}{\partial \eta \partial \rho}\rho^1 = 0 \quad (4.68)$$

Furthermore, from Eq.(4.22)

$$\frac{\partial^2 f(\rho^0, \eta^0)}{\partial \eta \partial \rho} = 2B\rho^0[\eta^{03} - \eta^0] - 4C(1 - \rho^0)\eta^0 \quad (4.69)$$

$$= 0 \quad \forall x \in \Omega_{\pm} \quad (4.70)$$

and

$$\frac{\partial^2 f(\rho^0, \eta^0)}{\partial \eta^2} = B\rho^{02}[3\eta^{02} - 1] + 2C(1 - \rho^0)^2 \quad (4.71)$$

$$\neq 0 \quad \forall x \in \Omega_{\pm} \quad (4.72)$$

Therefore from Eq.(4.68) we have

$$\eta^1 = 0. \quad (4.73)$$

Since,  $\rho^1$  remains undetermined, from Eq.(4.66)  $\phi^1$  also remains undetermined from the outer expansion.

## 4.5.2 Inner expansion

We next define a local orthogonal coordinate system  $(r, s)$ , where  $|r|$  measures the normal signed distance from any point on the interface given by the level set  $\rho = 0.5$  and  $s$  is tangential to the interface. We further define a rescaled coordinate  $z = r/\epsilon$  to stretch the inner region. In the moving coordinate system  $(z, s)$  the spatial and temporal derivatives transform as follows,

$$\nabla^2 = \frac{1}{\epsilon^2} \frac{\partial^2}{\partial z^2} + \frac{\kappa}{\epsilon} \frac{\partial}{\partial z} + \frac{\partial^2}{\partial s^2} + \mathcal{O}(\epsilon), \quad (4.74)$$

$$\nabla \cdot M \nabla = \frac{1}{\epsilon^2} \frac{\partial}{\partial z} \left( M \frac{\partial}{\partial z} \right) + \frac{\kappa}{\epsilon} M \frac{\partial}{\partial z} - \kappa^2 M z \frac{\partial}{\partial z} + \frac{\partial}{\partial s} \left( M \frac{\partial}{\partial s} \right) + \mathcal{O}(\epsilon), \quad (4.75)$$

$$\frac{\partial}{\partial t} = \frac{\partial}{\partial t} - \frac{V_n}{\epsilon} \frac{\partial}{\partial z} - V_t \frac{\partial}{\partial s} + \mathcal{O}(\epsilon), \quad (4.76)$$

where  $\kappa$  is the curvature of the interface,  $V_n$  and  $V_t$  are the normal and the tangential velocities respectively. The inner expansions write as

$$\hat{\rho}(z, s, \epsilon, t) = \hat{\rho}^0(z, s, t) + \epsilon \hat{\rho}^1(z, s, t) + \epsilon^2 \hat{\rho}^2(z, s, t), \quad (4.77)$$

$$\hat{\eta}(z, s, \epsilon, t) = \hat{\eta}^0(z, s, t) + \epsilon \hat{\eta}^1(z, s, t) + \epsilon^2 \hat{\eta}^2(z, s, t), \quad (4.78)$$

$$\hat{\phi}(z, s, \epsilon, t) = \hat{\phi}^0(z, s, t) + \epsilon \hat{\phi}^1(z, s, t) + \epsilon^2 \hat{\phi}^2(z, s, t), \quad (4.79)$$

$$\hat{\mu}_\rho(z, s, \epsilon, t) = \hat{\mu}_\rho^0(z, s, t) + \epsilon \hat{\mu}_\rho^1(z, s, t) + \epsilon^2 \hat{\mu}_\rho^2(z, s, t), \quad (4.80)$$

$$\hat{\mu}_\eta(z, s, \epsilon, t) = \hat{\mu}_\eta^0(z, s, t) + \epsilon \hat{\mu}_\eta^1(z, s, t) + \epsilon^2 \hat{\mu}_\eta^2(z, s, t), \quad (4.81)$$

In addition, the matching conditions provide the boundary conditions for the inner variables as,

$$\lim_{z \rightarrow \pm\infty} \hat{\rho}^0(z, s) = \rho^{0\pm}(s), \quad (4.82)$$

$$\lim_{z \rightarrow \pm\infty} \hat{\rho}^1(z, s) = \rho^{1\pm}(s) + z \frac{\partial \rho^{0\pm}}{\partial x}(s), \quad (4.83)$$

$$\lim_{z \rightarrow \pm\infty} \hat{\rho}^2(z, s) = \rho^{2\pm}(s) + z \frac{\partial \rho^{1\pm}}{\partial x}(s) + \frac{z^2}{2} \frac{\partial^2 \rho^{0\pm}}{\partial x^2}(s). \quad (4.84)$$

The derivative matching conditions read as

$$\lim_{z \rightarrow \pm\infty} \frac{\partial \hat{\rho}^0}{\partial z}(z, s) = 0, \quad (4.85)$$

$$\lim_{z \rightarrow \pm\infty} \frac{\partial \hat{\rho}^1}{\partial z}(z, s) = \frac{\partial \rho^{0\pm}}{\partial x}(s), \quad (4.86)$$

$$\lim_{z \rightarrow \pm\infty} \frac{\partial^2 \hat{\rho}^1}{\partial z^2}(z, s) = 0, \quad (4.87)$$

$$\lim_{z \rightarrow \pm\infty} \frac{\partial \hat{\rho}^2}{\partial z}(z, s) = \frac{\partial \rho^{1\pm}}{\partial x}(s) + z \frac{\partial^2 \rho^{0\pm}}{\partial x^2}(s). \quad (4.88)$$

The above matching conditions are also applicable to other variables  $\hat{\eta}$ ,  $\hat{\phi}$ ,  $\hat{\mu}_\rho$  and  $\hat{\mu}_\eta$ .

#### 4.5.2.1 Leading order

At the leading order  $\mathcal{O}(\epsilon^0)$  for  $\eta$  equation we have,

$$-L_\eta \hat{\mu}_\eta^0 = 0 \quad (4.89)$$

$$\implies \frac{\partial f(\hat{\rho}^0, \hat{\eta}^0)}{\partial \eta} - 2q \frac{\partial^2 \hat{\eta}^0}{\partial z^2} = 0. \quad (4.90)$$

Multiplying all the terms by  $\partial \hat{\eta}^0 / \partial z$ , integrating and using the boundary conditions for  $\hat{\rho}^0$  and  $\hat{\eta}^0$  from matching conditions to evaluate the constant of integration to be zero we have

$$f(\hat{\rho}^0, \hat{\eta}^0) = q \left( \frac{\partial \hat{\eta}^0}{\partial z} \right)^2 \quad (4.91)$$

which can be further integrated to give the equilibrium profile for  $\hat{\eta}^0$ .

From the leading order  $\mathcal{O}(1/\epsilon^2)$  in  $\rho$  equation we have

$$\frac{\partial}{\partial z} \left[ M(\hat{\rho}^0) \frac{\partial \hat{\mu}_\rho^0}{\partial z} \right] = 0. \quad (4.92)$$

Integrating once

$$M(\hat{\rho}^0) \frac{\partial \hat{\mu}_\rho^0}{\partial z} = A_1(s, t) \quad (4.93)$$

From matching condition  $\lim_{z \rightarrow \pm\infty} \frac{\partial \hat{\mu}_\rho^0}{\partial z}(z, s) = 0$  and  $M(\hat{\rho}^0) = M(\rho^{0\pm}) = 0$  we evaluate  $A_1(s, t) = 0$ . However, since the Eq.(4.93) is valid for the entire inner region and  $M(\hat{\rho}^0) \neq 0$  for  $\hat{\rho}^0 \neq 0, 1$  we have

$$\frac{\partial \hat{\mu}_\rho^0}{\partial z} = 0, \quad (4.94)$$

$$\implies \frac{\partial f(\hat{\rho}^0, \hat{\eta}^0)}{\partial \hat{\rho}^0} - 2 \frac{\partial^2 \hat{\rho}^0}{\partial z^2} = 0. \quad (4.95)$$

Multiplying all the terms by  $\partial \hat{\rho}^0 / \partial z$  and integrating once

$$f(\hat{\rho}^0, \hat{\eta}^0) = \left( \frac{\partial \hat{\rho}^0}{\partial z} \right)^2 \quad (4.96)$$

which can be integrated again to yield the equilibrium profile of  $\hat{\rho}^0$ . The leading order  $\mathcal{O}(1/\epsilon^2)$  in  $\phi$  equation yields

$$\frac{\partial}{\partial z} \left[ \sigma(\hat{\rho}^0) \frac{\partial \hat{\phi}^0}{\partial z} \right] = 0. \quad (4.97)$$

Integrating once

$$\sigma(\hat{\rho}^0) \frac{\partial \hat{\phi}^0}{\partial z} = A_2(s, t). \quad (4.98)$$

From matching  $\lim_{z \rightarrow \pm\infty} \frac{\partial \hat{\phi}^0}{\partial z}(z, s) = 0$  and  $\sigma(\hat{\rho}^0) = \sigma(\rho^{0\pm}) = \sigma_u, \sigma_m$ , we have  $A_2(s, t) = 0$ . Therefore in the inner region

$$\frac{\partial \hat{\phi}^0}{\partial z} = 0, \quad (4.99)$$

$$\implies \hat{\phi}^0 = A_3(s, t). \quad (4.100)$$

From matching conditions  $\lim_{z \rightarrow \pm\infty} \hat{\phi}^0 = \phi^{0\pm} = A_3(s, t)$ , which implies continuity of electric potential across the interface.

#### 4.5.2.2 Next-to-leading order

The next-to-leading order  $\mathcal{O}(\epsilon)$  in  $\eta$  equation leads to

$$-L_\eta \hat{\mu}_\eta^1 = 0, \quad (4.101)$$

$$\implies \frac{\partial^2 f(\hat{\rho}^0, \hat{\eta}^0)}{\partial \hat{\eta}^2} \hat{\eta}^1 + \frac{\partial^2 f(\hat{\rho}^0, \hat{\eta}^0)}{\partial \hat{\eta} \partial \hat{\rho}} \hat{\rho}^1 - 2q\kappa \frac{\partial \hat{\eta}^0}{\partial z} - 2q \frac{\partial^2 \hat{\eta}^1}{\partial z^2} = 0. \quad (4.102)$$

Multiplying the above Eq. by  $\partial \hat{\eta}^0 / \partial z$  and integrating within the limits  $\pm\infty$

$$\begin{aligned} & \int_{-\infty}^{+\infty} \frac{\partial^2 f(\hat{\rho}^0, \hat{\eta}^0)}{\partial \hat{\eta}^2} \hat{\eta}^1 \frac{\partial \hat{\eta}^0}{\partial z} dz + \int_{-\infty}^{+\infty} \frac{\partial^2 f(\hat{\rho}^0, \hat{\eta}^0)}{\partial \hat{\eta} \partial \hat{\rho}} \hat{\rho}^1 \frac{\partial \hat{\eta}^0}{\partial z} dz \\ & - \int_{-\infty}^{+\infty} 2q\kappa \left( \frac{\partial \hat{\eta}^0}{\partial z} \right)^2 dz - \int_{-\infty}^{+\infty} 2q \frac{\partial^2 \hat{\eta}^1}{\partial z^2} \frac{\partial \hat{\eta}^0}{\partial z} dz = 0. \end{aligned} \quad (4.103)$$

The above equation can be rewritten as

$$\begin{aligned} & \int_{-\infty}^{+\infty} \frac{\partial}{\partial z} \left[ \frac{\partial f(\hat{\rho}^0, \hat{\eta}^0)}{\partial \hat{\eta}} \right] \hat{\eta}^1 dz - \int_{-\infty}^{+\infty} \frac{\partial^2 f(\hat{\rho}^0, \hat{\eta}^0)}{\partial \hat{\eta} \partial \hat{\rho}} \hat{\eta}^1 \frac{\partial \hat{\rho}^0}{\partial z} dz \\ & + \int_{-\infty}^{+\infty} \frac{\partial^2 f(\hat{\rho}^0, \hat{\eta}^0)}{\partial \hat{\eta} \partial \hat{\rho}} \hat{\rho}^1 \frac{\partial \hat{\eta}^0}{\partial z} dz - \int_{-\infty}^{+\infty} 2q\kappa \left( \frac{\partial \hat{\eta}^0}{\partial z} \right)^2 dz \\ & - \int_{-\infty}^{+\infty} 2q \frac{\partial^3 \hat{\eta}^0}{\partial z^3} \hat{\eta}^1 dz = 0 \end{aligned} \quad (4.104)$$

where the first and the last terms in the integral in Eq.(4.103) have been simplified using chain rule of derivative and integration by parts respectively. The first and the last term in the integrals in Eq.(4.104) can be combined to give  $\frac{\partial}{\partial z} \left[ \frac{\partial f(\hat{\rho}^0, \hat{\eta}^0)}{\partial \hat{\eta}} - 2q \frac{\partial^2 \hat{\eta}^0}{\partial z^2} \right] \hat{\eta}^1 dz$ , which, from the leading order solution Eq.(4.90) is zero. Furthermore, introducing the notation  $B_1(s, t) = \int_{-\infty}^{+\infty} \frac{\partial^2 f(\hat{\rho}^0, \hat{\eta}^0)}{\partial \hat{\eta} \partial \hat{\rho}} \left[ \hat{\rho}^1 \frac{\partial \hat{\eta}^0}{\partial z} - \hat{\eta}^1 \frac{\partial \hat{\rho}^0}{\partial z} \right] dz$  Eq.(4.104) can be simplified to

$$B_1(s, t) - \int_{-\infty}^{+\infty} 2q\kappa \left( \frac{\partial \hat{\eta}^0}{\partial z} \right)^2 dz = 0. \quad (4.105)$$

The comparison of next-to-leading order  $\mathcal{O}(1/\epsilon)$  in  $\rho$  Eq. and utilizing the relations  $\frac{\partial \hat{\mu}^0}{\partial z} = 0$  and  $\frac{\partial \hat{\phi}^0}{\partial z} = 0$  we obtain

$$\frac{\partial}{\partial z} \left[ M(\hat{\rho}^0) \frac{\partial \hat{\mu}_\rho^1}{\partial z} \right] = 0. \quad (4.106)$$

Integrating once

$$M(\hat{\rho}^0) \frac{\partial \hat{\mu}_\rho^1}{\partial z} = B_2(s, t). \quad (4.107)$$

Taking the limits  $z \rightarrow \pm\infty$  we have  $M(\rho^{0\pm}) = 0$  which implies  $B_2(s, t) = 0$ . Therefore we obtain

$$\frac{\partial \hat{\mu}_\rho^1}{\partial z} = 0. \quad (4.108)$$

Integrating again

$$\hat{\mu}_\rho^1 = B_3(s, t) \quad (4.109)$$

$$\implies \frac{\partial^2 f(\hat{\rho}^0, \hat{\eta}^0)}{\partial \hat{\rho}^2} \hat{\rho}^1 + \frac{\partial^2 f(\hat{\rho}^0, \hat{\eta}^0)}{\partial \hat{\eta} \partial \hat{\rho}} \hat{\eta}^1 - 2\kappa \frac{\partial \hat{\rho}^0}{\partial z} - 2 \frac{\partial^2 \hat{\rho}^1}{\partial z^2} = B_3(s, t). \quad (4.110)$$

Multiplying both sides by  $\partial \hat{\rho}^0 / \partial z$  and integrating within the limits  $\pm\infty$  we obtain after simplification as in Eqs.(4.103) and (4.104)

$$B_1(s, t) + \int_{-\infty}^{+\infty} 2\kappa \left( \frac{\partial \hat{\rho}^0}{\partial z} \right)^2 dz = - \int_{-\infty}^{+\infty} B_3(s, t) \frac{\partial \hat{\rho}^0}{\partial z} dz \quad (4.111)$$

$$\implies B_1(s, t) + \int_{-\infty}^{+\infty} 2\kappa \left( \frac{\partial \hat{\rho}^0}{\partial z} \right)^2 dz = -B_3(s, t)[\rho^{0+} - \rho^{0-}] = \hat{\mu}_\rho^1 \quad (4.112)$$

Eliminating  $B_1(s, t)$  from Eqs.(4.105) and (4.112)

$$\hat{\mu}_\rho^1 = -\kappa\gamma_s \quad (4.113)$$

where  $\gamma_s = \int_{-\infty}^{+\infty} 2q \left( \frac{\partial \hat{\eta}^0}{\partial z} \right)^2 dz + \int_{-\infty}^{+\infty} 2 \left( \frac{\partial \hat{\rho}^0}{\partial z} \right)^2 dz$  is the surface energy. The above equation is the Gibbs-Thomson condition which occurs as a first order correction in the present phase-field model.

Next-to-leading order  $\mathcal{O}(1/\epsilon)$  for  $\phi$  equation we have

$$\frac{\partial}{\partial z} \left[ \sigma(\hat{\rho}^0) \frac{\partial \hat{\phi}^1}{\partial z} \right] = 0. \quad (4.114)$$

Integrating within the limits  $\pm\infty$  and using matching conditions we obtain

$$\sigma(\rho^{0+}) \frac{\partial \phi^{0+}}{\partial x} - \sigma(\rho^{0-}) \frac{\partial \phi^{0-}}{\partial x} = 0. \quad (4.115)$$

The above equation implies continuity of current across the interface. In the case of unequal conductivities i.e.  $\sigma(\rho^{0+}) \neq \sigma(\rho^{0-})$  we have a discontinuity of electric potential gradient or electric field across the interface.

### 4.5.2.3 Higher orders

At next order  $\mathcal{O}(\epsilon^0)$  in  $\rho$  equation we obtain terms that are not trivially zero as

$$\frac{\partial}{\partial z} \left[ M(\hat{\rho}^0) \left( \frac{\partial \hat{\mu}_\rho^2}{\partial z} + \Lambda \frac{\partial \hat{\phi}^1}{\partial z} \right) \right] = 0. \quad (4.116)$$

Integrating once we get

$$M(\hat{\rho}^0) \left( \frac{\partial \hat{\mu}_\rho^2}{\partial z} + \Lambda \frac{\partial \hat{\phi}^1}{\partial z} \right) = C_1(s, t) \quad (4.117)$$

Again as before taking the limits  $z \rightarrow \pm\infty$  we have  $M(\rho^{0\pm}) = 0$  and  $C_1(s, t) = 0$ . Therefore

$$\frac{\partial \hat{\mu}_\rho^2}{\partial z} + \Lambda \frac{\partial \hat{\phi}^1}{\partial z} = 0. \quad (4.118)$$

At order  $\mathcal{O}(\epsilon^2)$  in  $\eta$  equation we obtain

$$\hat{\mu}_\eta^2 = 0. \quad (4.119)$$

At order  $\mathcal{O}(\epsilon^0)$  in  $\phi$  equation we have

$$\frac{\partial}{\partial z} \left[ \sigma(\hat{\rho}^0) \frac{\partial \hat{\phi}^2}{\partial z} \right] + \frac{\partial}{\partial z} \left[ \sigma'(\hat{\rho}^0) \hat{\rho}^1 \frac{\partial \hat{\phi}^1}{\partial z} \right] + \kappa \sigma(\hat{\rho}^0) \frac{\partial \hat{\phi}^1}{\partial z} + \frac{\partial}{\partial s} \left[ \sigma(\hat{\rho}^0) \frac{\partial \hat{\phi}^0}{\partial s} \right] = 0 \quad (4.120)$$

At next order  $\mathcal{O}(\epsilon)$  in  $\rho$  equation we have

$$\begin{aligned} -V_n \frac{\partial \hat{\rho}^0}{\partial z} &= \frac{\partial}{\partial z} \left[ M(\hat{\rho}^0) \frac{\partial \hat{\mu}_\rho^3}{\partial z} \right] + \frac{\partial}{\partial z} \left[ M'(\hat{\rho}^0) \hat{\rho}^1 \frac{\partial \hat{\mu}_\rho^2}{\partial z} \right] + \kappa M(\hat{\rho}^0) \frac{\partial \hat{\mu}_\rho^2}{\partial z} \\ &+ \frac{\partial}{\partial s} \left[ M(\hat{\rho}^0) \frac{\partial \hat{\mu}_\rho^1}{\partial s} \right] + \frac{\partial}{\partial z} \left[ M(\hat{\rho}^0) \Lambda \frac{\partial \hat{\phi}^2}{\partial z} \right] + \frac{\partial}{\partial z} \left[ M'(\hat{\rho}^0) \hat{\rho}^1 \Lambda \frac{\partial \hat{\phi}^1}{\partial z} \right] \\ &+ \kappa M(\hat{\rho}^0) \Lambda \frac{\partial \hat{\phi}^1}{\partial z} + \frac{\partial}{\partial s} \left[ M(\hat{\rho}^0) \Lambda \frac{\partial \hat{\phi}^0}{\partial s} \right] \end{aligned} \quad (4.121)$$

From Eq.(4.118) the second and the sixth and the third and the seventh term on the right hand side can be combined to obtain zero. Integrating within the limits  $\pm\infty$

$$-V_n \int_{-\infty}^{+\infty} \frac{\partial \hat{\rho}^0}{\partial z} dz = \left[ \frac{\partial^2 \hat{\mu}_\rho^1}{\partial s^2} + \Lambda \frac{\partial^2 \hat{\phi}^0}{\partial s^2} \right] \int_{-\infty}^{+\infty} M(\hat{\rho}^0) dz \quad (4.122)$$

where from matching  $M(\rho^{0\pm}) = 0$  has been employed to eliminate other terms. Using Eq.(4.113) we obtain the velocity of the interface as

$$V_n = -\gamma_s \overline{M}_s \frac{\partial^2 \kappa}{\partial s^2} + \Lambda \overline{M}_s \frac{\partial^2 \hat{\phi}^0}{\partial s^2}. \quad (4.123)$$

where  $\overline{M}_s = \int_{-\infty}^{+\infty} M(\hat{\rho}^0) dz$ . The above equation states that at the sharp-interface limit i.e. as  $\epsilon \rightarrow 0$ , the interface moves by surface laplacian of the mean curvature and surface laplacian of the electric potential.

A few subtle points need to be mentioned. Firstly, from Eq.(4.110) and (4.113) taking the limit  $z \rightarrow \pm\infty$  and taking into account the matching conditions Eq.(4.82), (4.83), (4.85) and (4.87), we have,

$$\frac{\partial^2 f(\rho^{0\pm}, \eta^{0\pm})}{\partial \rho^2} \rho^{1\pm} + \frac{\partial^2 f(\rho^{0\pm}, \eta^{0\pm})}{\partial \rho \partial \eta} \eta^{1\pm} = -\kappa \gamma_s. \quad (4.124)$$

Using Eq.(4.70)

$$\rho^{1\pm} = -\frac{\kappa \gamma_s}{\frac{\partial^2 f(\rho^{0\pm}, \eta^{0\pm})}{\partial \rho^2}} \quad (4.125)$$

gives the first order correction to the variable  $\rho$ . Depending upon the value of the right hand side of the above equation, there will be regions in the domain which deviate from

the values of 0 and 1. This will result in contribution due to bulk diffusion in addition to surface diffusion. The higher order terms in  $\rho$  in the mobility function suppresses the contribution from bulk diffusion. From Eq.(4.102), it can be shown that

$$\frac{\partial^2 f(\rho^{0\pm}, \eta^{0\pm})}{\partial \eta^2} \eta^{1\pm} + \frac{\partial^2 f(\rho^{0\pm}, \eta^{0\pm})}{\partial \rho \partial \eta} \rho^{1\pm} = 0. \quad (4.126)$$

Using Eqs.(4.70) and (4.72)

$$\eta^{1\pm} = 0 \quad (4.127)$$

that is the non-conserved order parameter does not exhibit any higher order corrections.

## 4.6 Relationship to sharp-interface model

To facilitate a comparison between the sharp-interface and the phase-field method, the relation between the various model parameters from the two methods needs to be established.

### 4.6.1 Interfacial properties

In the phase-field model, the interfacial properties such as interfacial energy and width are related to the gradient-energy coefficients and the potential well height. Since the present phase-field model deals with antiphase (GB) as well as interphase (surface) boundaries, the interfacial characteristics of both interfaces is determined separately. Following the approach of Cahn-Hilliard [165], the interfacial energy is calculated starting from an initial planar interface across phases in local equilibrium. Although, the treatment is along similar lines to Moelans et al. [189] and Ahmed et al. [202], the derivation differs slightly from Ref. [202] because of our choice of  $f(\rho, \eta_i)$  which results in different dependence of the material and model parameters.

#### 4.6.1.1 Antiphase boundary

For the GB in the present case, the two grain structure corresponding to  $(\rho, \eta_1, \eta_2) = (1, 1, 0)$  and  $(1, 0, 1)$  as shown in Fig.4.1(c) is considered. Since the variation of  $\rho$  across the GB is negligible, it can safely be assumed that  $\rho \approx 1$  and  $(\frac{d\rho}{dx})^2 \approx 0$ . The GB energy of the system is then given by the integral,

$$\frac{\gamma_{GB}}{N_V} = \int_{-\infty}^{+\infty} \left\{ f(\rho = 1, \eta_1, \eta_2) + \kappa_\eta \left[ \left( \frac{d\eta_1}{dx} \right)^2 + \left( \frac{d\eta_2}{dx} \right)^2 \right] \right\} dx. \quad (4.128)$$

From the bulk free energy density selected in the present work,  $f(\rho = 1, \eta_1, \eta_2)$  across a grain boundary translates into,

$$f(\rho = 1, \eta_1, \eta_2) = B\xi(\eta_1, \eta_2). \quad (4.129)$$

The functions  $\eta_1(x)$  and  $\eta_2(x)$  that extremize functional (4.128) satisfy Euler-Lagrange equations,

$$\frac{\partial f}{\partial \eta_1} - 2\kappa_\eta \frac{d^2 \eta_1}{dx^2} = 0 \quad (4.130.1)$$

$$\frac{\partial f}{\partial \eta_2} - 2\kappa_\eta \frac{d^2 \eta_2}{dx^2} = 0 \quad (4.130.2)$$

and satisfy the boundary conditions,

$$\eta_1 = 1 \quad \text{and} \quad \eta_2 = 0 \quad \text{for} \quad x \rightarrow -\infty, \quad (4.131.1)$$

$$\eta_1 = 0 \quad \text{and} \quad \eta_2 = 1 \quad \text{for} \quad x \rightarrow +\infty, \quad (4.131.2)$$

$$\frac{d\eta_1}{dx} = \frac{d\eta_2}{dx} = 0 \quad \text{for} \quad x \rightarrow \pm\infty. \quad (4.131.3)$$

Multiplying Eq.(4.130.1) by  $\frac{d\eta_1}{dx}$  and (4.130.2) by  $\frac{d\eta_2}{dx}$  and adding,

$$\begin{aligned} \frac{\partial f}{\partial \eta_1} \frac{d\eta_1}{dx} + \frac{\partial f}{\partial \eta_2} \frac{d\eta_2}{dx} - 2\kappa_\eta \left[ \left( \frac{d^2 \eta_1}{dx^2} \right) \frac{d\eta_1}{dx} + \left( \frac{d^2 \eta_2}{dx^2} \right) \frac{d\eta_2}{dx} \right] \\ = 0, \end{aligned} \quad (4.132)$$

which can be rearranged to give,

$$\frac{df}{dx} - \kappa_\eta \left[ \frac{d}{dx} \left( \frac{d\eta_1}{dx} \right)^2 + \frac{d}{dx} \left( \frac{d\eta_2}{dx} \right)^2 \right] = 0. \quad (4.133)$$

Integrating the above equation and evaluating the constant of integration using the boundary conditions (4.131.1), (4.131.2) and (4.131.3) (which turns out to be zero),

$$f(\rho = 1, \eta_1, \eta_2) = \kappa_\eta \left[ \left( \frac{d\eta_1}{dx} \right)^2 + \left( \frac{d\eta_2}{dx} \right)^2 \right]. \quad (4.134)$$

The above relation, known as the equipartition of energy implies that at equilibrium, the bulk term and the gradient term contributes equally to the interfacial free energy. Simple algebraic rearrangement of the above Eq. yields the equilibrium profiles as,

$$\frac{d\eta_1}{dx} = - \sqrt{\frac{f(\rho = 1, \eta_1, \eta_2)}{\kappa_\eta \left[ 1 + \left( \frac{d\eta_2}{d\eta_1} \right)^2 \right]}}, \quad (4.135.1)$$

$$\frac{d\eta_2}{dx} = + \sqrt{\frac{f(\rho = 1, \eta_1, \eta_2)}{\kappa_\eta \left[ 1 + \left( \frac{d\eta_1}{d\eta_2} \right)^2 \right]}}. \quad (4.135.2)$$

Combining Eq.(4.128) and (4.134) gives,

$$\frac{\gamma_{GB}}{N_V} = 2 \int_{-\infty}^{+\infty} f(\rho = 1, \eta_1, \eta_2) dx. \quad (4.136)$$

Using Eq.(4.129) and changing the independent variable from  $x$  to  $\eta_1$ ,

$$\frac{\gamma_{GB}}{N_V} = 2\sqrt{\kappa_\eta B} \int_0^1 \sqrt{\xi(\eta_1, \eta_2)} \sqrt{1 + \left(\frac{d\eta_2}{d\eta_1}\right)^2} d\eta_1 \quad (4.137)$$

The above integral can only be solved analytically for  $\epsilon = 1.5$ , for which the profiles  $\eta_1(x)$  and  $\eta_2(x)$  are symmetric across  $x = 0$ , such that  $\eta_2(x) = 1 - \eta_1(x)$  and  $\frac{d\eta_2}{d\eta_1} = -1$  [189]. For all other values of  $\epsilon \neq 1.5$ , the integral needs to be evaluated numerically yielding,

$$\frac{\gamma_{GB}}{N_V} = 2\sqrt{\kappa_\eta B} I_1(\xi(\eta_1, \eta_2)) \quad (4.138)$$

where,  $I_1$  is a constant depending upon the function  $\xi(\eta_1, \eta_2)$ .

The GB width is defined heuristically as the region where  $\eta_1$  (or  $\eta_2$ ) varies from a value of 0.1 to 0.9 [205]. Thus, rearranging Eq. (4.135.1) can be written as,

$$\int_{-\delta_{GB}/2}^{+\delta_{GB}/2} dx = \sqrt{\frac{\kappa_\eta}{B}} \int_{0.1}^{0.9} \sqrt{\frac{1 + \left(\frac{d\eta_2}{d\eta_1}\right)^2}{\xi(\eta_1, \eta_2)}} d\eta_1 \quad (4.139)$$

A numerical integration of the above Eq. results in,

$$\delta_{GB} = \sqrt{\frac{\kappa_\eta}{B}} I_2(\xi(\eta_1, \eta_2)) \quad (4.140)$$

where,  $I_2$  is a constant depending upon the function  $\xi(\eta_1, \eta_2)$ . It is to be noted that one is free to choose any form of multiwell in  $\eta_i$  which would only modify the constant  $I_1$  and  $I_2$ , but not the  $\sqrt{\kappa_\eta B}$  and  $\sqrt{\frac{\kappa_\eta}{B}}$  dependency of  $\gamma_{GB}$  and  $\delta_{GB}$ . Thus, by choosing an appropriate  $\xi(\eta_i)$ ,  $\kappa_\eta$  and  $B$  one can tailor material specific  $\gamma_{GB}$  and  $\delta_{GB}$ .

#### 4.6.1.2 Interphase boundary

To calculate the surface energy, similar to the above approach, a planar interface between an interconnect grain and the underlayer corresponding to  $(\rho, \eta_1, \eta_2) = (1, 1, 0)$  and  $(0, 0, 0)$  respectively is assumed. Accordingly, the surface energy  $\gamma_S$  is given by the integral,

$$\frac{\gamma_S}{N_V} = \int_{-\infty}^{+\infty} \left\{ f(\rho, \eta) + \kappa_\rho \left(\frac{d\rho}{dx}\right)^2 + \kappa_\eta \left(\frac{d\eta}{dx}\right)^2 \right\} dx. \quad (4.141)$$

Again following the procedure outlined for the GB, the equipartition of energy at equilibrium dictates,

$$f(\rho, \eta) = \kappa_\rho \left( \frac{d\rho}{dx} \right)^2 + \kappa_\eta \left( \frac{d\eta}{dx} \right)^2. \quad (4.142)$$

To make the relationship between numerical parameters and  $\gamma_S$  apparent, Ref. [202] is followed by assuming a linear profile of both the order parameters across the interface as,

$$\frac{d\rho}{dx} \propto \frac{d\eta}{dx} \quad (4.143)$$

which according to the boundary conditions  $\rho(-\infty) = \eta(-\infty) = 1$  and  $\rho(+\infty) = \eta(+\infty) = 0$  translates into,

$$\rho(x) = \eta(x). \quad (4.144)$$

The above equality implies,

$$\frac{d\rho}{dx} = \frac{d\eta}{dx}. \quad (4.145)$$

Substituting Eq.(4.146) in (4.143),

$$\frac{d\rho}{dx} = -\sqrt{\frac{f(\rho, \eta)}{(\kappa_\rho + \kappa_\eta)}}. \quad (4.146)$$

Based on the equality (4.144), the bulk free energy translates into  $f(\rho, \eta = \rho) = (A + C)\rho^2(1 - \rho)^2 + \frac{B}{4}\rho^2(\rho^2 - 1)^2$ . Similar to the procedure used in deriving Eq. (4.136) and (4.137),  $\gamma_S$  can be approximated by the integral,

$$\frac{\gamma_S}{N_V} = 2 \int_0^1 \sqrt{(\kappa_\rho + \kappa_\eta)} \sqrt{f(\rho, \eta = \rho)} d\rho \quad (4.147)$$

Thus, it can be inferred,

$$\frac{\gamma_S}{N_V} = 2\sqrt{(\kappa_\rho + \kappa_\eta)} I_3(A, B, C). \quad (4.148)$$

It can also be shown that the surface width  $\delta_S$  is given by,

$$\delta_S = \sqrt{(\kappa_\rho + \kappa_\eta)} \int_{0.1}^{0.9} \frac{1}{\sqrt{f(\rho, \eta = \rho)}} d\rho \quad (4.149)$$

which can be simplified as,

$$\delta_S = \sqrt{(\kappa_\rho + \kappa_\eta)} I_4(A, B, C). \quad (4.150)$$

where  $I_3$  and  $I_4$  is a constant depending on the exact nature of  $f(\rho, \eta)$  and the coefficients  $A, B, C$ .

As evident from Eqs. (4.138), (4.140), (4.148) and (4.150), in the present phase-field model the model parameters  $A, B, C, \kappa_\rho, \kappa_\eta$  can be tuned to produce a range of interfacial energies. However, it should be emphasized that the above relations hold only approximately and only serve as a guideline. In the present thesis, the interfacial energies are evaluated numerically (which does not involve any approximations) as,

$$\frac{\gamma_{S,GB}}{N_V} = \int_{-\infty}^{+\infty} \left\{ f(\rho, \eta_1, \eta_2) + \kappa_\rho \left( \frac{d\rho}{dx} \right)^2 + \kappa_\eta \left[ \left( \frac{d\eta_1}{dx} \right)^2 + \left( \frac{d\eta_2}{dx} \right)^2 \right] \right\} dx \quad (4.151)$$

starting from an initial sharp planar interface between two interconnect grains for  $\gamma_{GB}$  and between an interconnect grain and the underlayer for  $\gamma_S$  with their respective equilibrium  $(\rho, \eta_1, \eta_2)$ . The kinetic Eqs.(4.23) and (4.24) are then solved (so that the interfaces become diffuse) until there is no appreciable change between two successive timesteps. The interfacial energies are then calculated by numerically integrating Eq.(4.151). A comparative study of the influence of above parameters and the equilibrium profiles can be found in Ref. [188]

#### 4.6.1.3 Selection of gradient energy coefficients and barrier heights

Although, the present work is not confined to any specific material, the parameters need to be chosen such that  $\gamma_{GB}$  and  $\gamma_S$  are related as,

$$2\gamma_S \sin \theta = \gamma_{GB} \quad (4.152)$$

where  $\theta$  is the angle between the surface tangent at the root and the horizontal axis. As a result, the permissible values follow,

$$0 \leq \frac{\gamma_{GB}}{\gamma_S} \leq 2. \quad (4.153)$$

Moreover, in metals  $\gamma_S$  is higher than  $\gamma_{GB}$ . As such the scaled values of the potential barriers  $A, B, C$  is chosen to be equal ( $= 1$ ) and the gradient energy coefficients,  $\kappa_\rho = 1$  and  $\kappa_\eta = 0.33$ , such that  $\frac{\gamma_{GB}}{\gamma_S} = 0.7$  and dihedral angle is  $139^\circ$ . The  $\delta_{GB}$  and  $\delta_S$  are calculated to be 2.4 and 3.5 respectively.

#### 4.6.2 Kinetic parameters

The selection of kinetic parameters namely the atomic mobilities and the relaxation coefficient is discussed next. The atomic mobilities in phase-field model is related to the

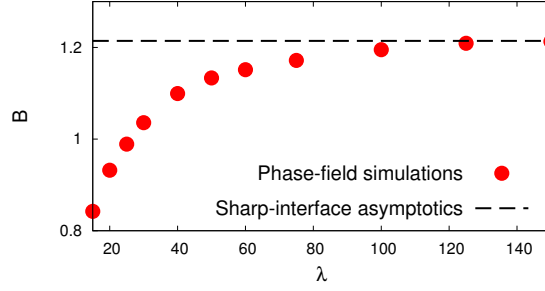


Figure 4.3: Comparison of the Mullins' constant  $B$  obtained from asymptotic analysis (dashed line) and that form the slope of the temporal decay of a sinusoidal perturbation performed using phase-field simulations. The agreement is good at higher wavelengths  $\lambda$  where the small slope approximation is fulfilled as assumed in Mullins' theory.

diffusivity. In case of bulk diffusion, the Cahn-Hilliard Eq. can be compared to the Fick's law to relate bulk atomic mobility to bulk diffusivity as [165],

$$D_B = M_B \frac{\partial^2 f}{\partial \rho^2} \quad (4.154)$$

In case of surface diffusion, the surface atomic mobility can be related to surface diffusivity by relating the normal velocity of the interface obtained from the asymptotic analysis of the phase-field model to that from the sharp-interface theory of Mullins [122] which states that,

$$V_n = B \nabla_s^2 \kappa_s \quad (4.155)$$

where,

$$B = \frac{D_s \delta_s \gamma_s \Omega}{k_B T} \quad (4.156)$$

is a constant comprising of material parameters and  $\kappa_s$  is the mean curvature. The parameter  $B$  is extracted from the simulation parameters by comparing the expression of the normal velocity of the interface from sharp-interface relation (only the capillarity part) and that obtained from the asymptotic analysis of the phase-field model Eq.(4.123) yielding an expression,

$$B = \gamma_s \overline{M}_s, \quad (4.157)$$

The values of  $\gamma_s$  and  $\overline{M}_s$  can be obtained numerically by starting from a  $1-D$  domain with an initial sharp interface between a grain of the interconnect (characterized by  $\rho = 1$ ,  $\eta_1 = 1$  and  $\eta_2 = 0$ ) and the underlayer domain (characterized by  $\rho = 0$ ,  $\eta_1 = 0$  and  $\eta_2 = 0$ ). The profile is equilibrated such that there is no appreciable change between two successive timesteps and the above expressions are evaluated. The above procedure yields a value of  $B = 1.21$  for the assigned numerical parameters. The expression can be counterchecked by comparing the value of  $B$  obtained from the Mullins' theory of

dampening of sinusoidal perturbations [206] as done in Ref. [207]. To this end, simulation by imposing a perturbation of the form  $A_o \sin(kx)$  on a planar interface between an interconnect and underlayer domain with their respective equilibrium  $\rho$  and  $\eta$  values is performed and the progressive decay of the amplitude is tracked. According to [206], the decay obeys an exponential law of the form,

$$A_t = A_o \exp[-Bk^4 t]. \quad (4.158)$$

Thus the slope of the  $\ln\left(\frac{A_t}{A_o}\right)$  vs.  $t$  curve is given by  $-Bk^4$ , from which the value of  $B$  can be evaluated. However, it is to be noted that Mullins' theory is valid for the case of  $A_o k \ll 1$  such that the temporal decay of the perturbation obeys the small slope approximation. It can be seen in Fig.4.3 that as  $\lambda$  increases (or in other words as  $k$  decreases), the value of  $B$  converges to that obtained from expression (4.158). Once the value of  $B$  is known, the value of  $\frac{D_s}{k_B T}$  can then be evaluated from Eq. 4.156 if the other parameters are known.

The GB atomic mobility  $M_{GB}$  can be related to the GB diffusivity by comparing the expression of the GB flux from sharp interface and phase-field model as,

$$\frac{D_{GB} \delta_{GB}}{\Omega k_B T} z_{GB} e E = \overline{M}_{GB} z_{GB} e E \quad (4.159)$$

which implies,

$$\frac{D_{GB}}{\Omega k_B T} = \frac{\overline{M}_{GB}}{\delta_{GB}} \quad (4.160)$$

where  $\overline{M}_{GB} = \int_{-\infty}^{+\infty} 4M_{GB} \sqrt{\eta_1^2 \eta_2^2} dz$  is evaluated similar to  $\overline{M}_s$  considering a planar interface between the two grains of the interconnect.

The surface evolution is governed simultaneously by Cahn-Hilliard and Allen-Cahn equations because of the variation of both the conserved and the non-conserved variables. Owing to the choice of our mobility values, the Cahn-Hilliard equation exhibits motion by surface laplacian of the mean curvature, in addition to the motion by mean curvature due to Allen-Cahn dynamics. As a result, for a given  $M_S$ , one needs to choose  $L_\eta$  such that the surface evolution is diffusion controlled and invariant of its choice.

### 4.6.3 Electrical properties

Moving on to the electrical parameters, the effective valence which is a sum of electrostatic and wind force can be directly used from the experimental observed values of metals. In the present work, a representative value of  $-5$  is selected which has been reported for copper interconnects. The conductivity of the metal interconnect  $\sigma_m$  is set to be 10 times higher than the dielectric underlayer  $\sigma_u$ .

To calculate  $J_{GB}$  the electric field or potential difference across the conductor due to the applied potential at the domain edges for the CV setup should be determined. This can be obtained by creating a circuit analogy of the simulation set up as shown in Fig. 4.1(d). Since the underlayer domain and the metal are connected in series, the same current flows through them. Hence from the Ohm's law, potential at an intermediate point between underlayer and interconnect can be calculated to be,

$$V_I = V \frac{\left(\frac{R_u}{R_m} - 1\right)}{\left(\frac{R_u}{R_m} + 1\right)}, \quad (4.161)$$

where  $V$  is the applied potential,  $R_u$  and  $R_m$  are resistances of the underlayer and the interconnect respectively. Thus the electric field across the conductor  $E_m$  can be written as,

$$E_m = \frac{V - V_I}{L_m} = \frac{2V}{\left(1 + \frac{\sigma_m L_u}{\sigma_u L_m}\right) L_m}, \quad (4.162)$$

where  $\sigma_m$  and  $\sigma_u$  are the conductivities of the metal interconnect and the underlayer material, while  $L_m$  and  $L_u$  are the length of the interconnect and the underlayer domain. Thus, the grain-boundary flux can be expressed as,

$$J_{GB} = \overline{M}_{GB} z e E_m. \quad (4.163)$$

It is important to note that in the CV set-up, as the surface drifts under the action of EM, the conductor length  $L_m$  decreases, as a result of which  $E_m$  (and concomitantly  $J_{GB}$ ) drops overtime. The reported  $E_m$  corresponds to the initial value. On the other hand, the CC set-up ensures a constant  $E_m = j/\sigma_m$  throughout the course of drift. Thus, the two BCs are motivated to test whether the assumption of constant GB flux  $J_{GB}$  is necessary to attain a steady state drift.

## 4.7 Applicability, limitations and possible extensions of the model

A few comments on the general applicability of the model and the results obtained from the model is in order.

1. EM in metals can either occur through the electron-current-induced diffusion of interstitial atoms or via the migration of substitutional atoms by a vacancy mechanism [184]. The present model is only applicable to the latter case.

2. The stress generation due to vacancy accumulation is neglected in the present model. The presence of gradient of stresses can further accentuate the driving force for atomic transport [111]. In addition, the generation and annihilation of vacancy is also not accounted.
3. A current carrying wire produces a magnetic field around the conductor. As a result of which the net force on the ions should be an addition of the contributions from electric and magnetic force. Since the direction of the magnetic force is perpendicular to the plane of the current (from the conventional right hand rule), its effect on diffusion is disregarded [208].
4. The effect of back stress along the line is neglected. In Blech-type test geometries as the conductor drifts in the direction of electron wind, a back stress is generated across the line which impedes the further movement [87]. This essentially implies that the slit evolves and propagates along an infinite GB. Consequently, the EM fluxes are not blocked at the domain edges. In the present framework, physics of both back-stress accumulation and stress-assisted atomic transport can be incorporated by solving a complete elastic boundary-value problem [137, 209].
5. Passage of electric current through the line causes Joule's heating that activates an additional mode of mass transport via thermomigration [210, 121]. The multiphysics of heat and mass transport can again be easily incorporated by coupling an additional heat diffusion equation.
6. Finally, all the properties of the interconnect namely interfacial energy, atomic mobility and the conductivity have been assumed to be isotropic. The assumptions, considerably simplify the analysis, however it is remarked that anisotropy in either of the properties can easily be incorporated and is not a limitation of the phase-field modeling in general. For e.g., most commercial interconnects are face-centered cubic (FCC) metals which are characterized by a strong diffusional anisotropy. This effect can be included by introducing the crystallographic direction dependence in surface atomic mobility ( $M_S$ ) [136] as  $M(\rho, \eta_i) = M_S(\rho)[1 + \delta \cos k(\theta + \psi)]$  where  $\delta$  denotes the anisotropy strength,  $\theta = \tan^{-1}(\rho_y/\rho_x)$  is the angle between normal to the surface ( $\nabla\rho$ ) and  $x$ -axis and  $\psi$  represents the misorientation angle between the fastest diffusion direction and  $x$ -axis.  $k$  depicts the number of diffusion paths on a crystalline plane. For FCC metals  $k = 2, 4, 6$  corresponds to  $\{110\}$ ,  $\{100\}$  and  $\{111\}$  planes respectively. The presence of diffusional anisotropy can lead to richness in the dynamics of GB grooving and slit formation in polycrystalline lines as has been previously demonstrated for bamboo-type lines [142] and single crystal islands [211, 212, 213]. GB diffusional anisotropy can also be modeled along similar lines.

We end the chapter highlighting a few key differences to the related electrochemical phenomenon. In electrochemical problems such as electrodeposition, the applied current densities are of the order of  $10 - 100 A/m^2$ , in contrast to EM-induced damage in metals where the imposed currents are in the range of  $10^8 - 10^{10} A/m^2$ . As a result the electron wind does not play a role in such problems. Therefore the driving force for diffusion is the electrochemical potential ( $\mu_A + q_A\phi$ ) and the cross-term is neglected. Secondly, in electrolytic solution all the ionic species contribute towards the current. The electrostatic field distribution in such systems is evaluated by solving Poisson's equation. Even if a condition of charge neutrality is assumed, the statement of current conservation does not imply the validity of Laplace equation. Instead, electrostatic potential at any spatial position is such that the flux due to concentration gradients (or chemical potentials) is balanced by that due to electric potential gradients. In electrodes, however, the primary charge carriers are electrons and the Ohm's law is typically recovered.

## **Part III**

**Results and Discussion :**

**Electric field-induced directed  
assembly of diblock copolymers**

# Chapter 5

## Influence of substrate interaction and confinement on electric field induced transition in symmetric block copolymer thin films

### 5.1 Introduction

In the present chapter, the morphologies arising due to competing substrate interaction, electric field and confinement effects on a symmetric diblock copolymer are studied. The phase diagram in electric field-substrate strength space for different film thicknesses is calculated. In addition to identifying the presence of parallel, perpendicular and mixed lamellae phases similar to analytical calculations, a region in the phase diagram where hybrid morphologies (combination of two phases) coexist is delineated. These hybrid morphologies arise either solely due to substrate affinity and confinement or are induced due to the applied electric field. The dependence of the critical fields for transition between the various phases on substrate strength, film thickness and dielectric contrast is discussed. Some preliminary 3D results are also presented to corroborate the presence of hybrid morphologies.

The organization of the chapter is as following. The results are presented in the following section 5.2. The chapter is concluded by comparing the results to that from experiments and SCFT calculations in section 5.3.

## 5.2 Results

The various non-dimensional model parameters are selected as  $\Delta x = \Delta y = 1.0$ ,  $\Delta t = 0.02$ ,  $\kappa = 1.0$ ,  $B = 0.1$ ,  $M = 1.0$ ,  $\epsilon_A = 3.0$ ,  $\epsilon_B = 2.0$ . It is remarked, that the present results are not influenced by the choice of grid resolution ( $\Delta x$  and  $\Delta y$ ). To this end, the numerical results (at  $\Delta x = \Delta y = 1.0$ ) can be replicated with finer grid spacing ( $\Delta x = \Delta y = 0.5$ ). In order to scale up the time-step width  $\Delta t$  which scales as  $(\Delta x)^4$  for Cahn-Hilliard equation, a larger grid spacing is conveniently chosen. The values of the permittivity closely resembles a PS-PMMA copolymer system [54, 70], though other values have also been used in the literature [57]. The values of  $\kappa$  and  $B$  correspond to a segregation of  $\chi N \approx 18$ . The surface interaction strength  $h$  is varied as 0.1, 0.5, 1.0 and 1.5. Since the intention is to study symmetric walls i.e. both the surfaces attract the same monomer,  $h_o = h_L$ . Moreover, the effect of confinement is also of additional interest. Simulations are carried out for different box sizes in y-direction,  $L_y = 64, 32, 16, 8, 4$ . The natural lamellar spacing  $L_o$  is around 10 grid points (as determined in Sec.5.2.1), so that the selected film thicknesses allows us to study systems with  $L_y > L_o$ ,  $L_y \sim L_o$  and  $L_y < L_o$ . Another implication of the above mentioned values of substrate interaction and film thickness is that the surface induced ordering length is greater than the film thickness. In other words, this implies that in the absence of electric field, lamellae, parallel to the substrate, span across the entire film. The surface induced ordering length for the smallest substrate affinity of  $h = 0.1$  is around  $8L_o$ . The magnitude of electric field is tuned by changing the value of applied voltage, and by normalizing it with the box size  $L_y$ , i.e.,  $E = \frac{V}{L_y}$  to maintain the same electric field for different box sizes. The box size in x-direction is kept fixed as  $L_x = 64$  in all the simulations. The initial microstructure is generated by assigning a computational noise between  $\pm 0.005$  about the average composition ( $\psi = 0$ ) corresponding to a disordered state. The system is then allowed to evolve in presence of electrostatic field and attracting substrates.

To gain insights during the microstructure evolution process two parameters are defined, average density profile along y direction  $\rho(y, t)$  [37, 214] and degree of alignment  $\beta(t)$  [215, 216] as,

$$\rho(y, t) = \frac{1}{L_x} \sum_{x=1}^{L_x} \psi(x, y, t) \quad (5.1)$$

$$\beta(t) = \frac{\sum_{k_x, k_y} \frac{k_x^2 - k_y^2}{\mathbf{k}^2} S(k_x, k_y, t)}{\sum_{k_x, k_y} S(k_x, k_y, t)} \quad (5.2)$$

where  $k_x$  and  $k_y$  are the Fourier space wave vectors in x and y direction and  $\mathbf{k}^2 = k_x^2 + k_y^2$ .  $S(k_x, k_y)$  is the magnitude of intensity of the Fourier power spectrum defined as  $\frac{1}{L} \langle \psi(\mathbf{k}, t) \psi(-\mathbf{k}, t) \rangle$ .  $L$  denotes the system size  $L_x \times L_y$  and the terms in the angular bracket

*Table 5.1: Number of lamellae at different film thickness  $L_y$  for weak surface interaction strength,  $h = 0.1$ . The box size in  $x$ -direction is kept constant at  $L_x = 64$ . There exists an interval of film thickness where a certain number of lamellae is observed. The configuration is at the maximum frustration at lower film thickness for a given interval, while it is at minimum frustration at higher value. The observed configuration is parallel at larger film thickness. However, at smaller film thickness frustration is alleviated by averting to a perpendicular configuration.*

$L_y$ (Film thickness)	No. of lamellae
78	7
70-77	8
69	6
60-68	7
51-59	6
42-50	5
34-41	4
25-33	3
16-24	2
15	6(Perpendicular)
7-14	1
<6	7(Perpendicular)

imply the product of  $\psi$  and its complex conjugate in Fourier space. In cases, where the alignment is parallel to the substrates i.e parallel lamellae along the  $y$  direction form,  $k_x \approx 0$ , as there is no relevant periodicity along this direction. As a result, the value of degree of alignment parameter is  $\beta = -1$ . In the opposite case, the alignment is perpendicular to the surface,  $k_y \approx 0$  and the value of degree of alignment parameter is  $\beta = 1$ . Thus, a value of  $\beta = -1$  implies 100% parallel lamellae, while, a value of  $\beta = 1$  implies a 100% perpendicular lamellae. A parallel lamellae arrangement in  $y$  direction is characterized by an oscillatory average density profile, whereas a flat profile about  $\rho(y) = 0$  corresponds to a perpendicular lamellar arrangement.

### 5.2.1 Determination of equilibrium lamellar thickness

The effect of confinement on the lamellae period and resulting stable arrangement is first discussed. For the case of weak substrate interaction  $h = 0.1$ , the number of lamellae along with stable configuration (configuration is parallel unless mentioned) at different

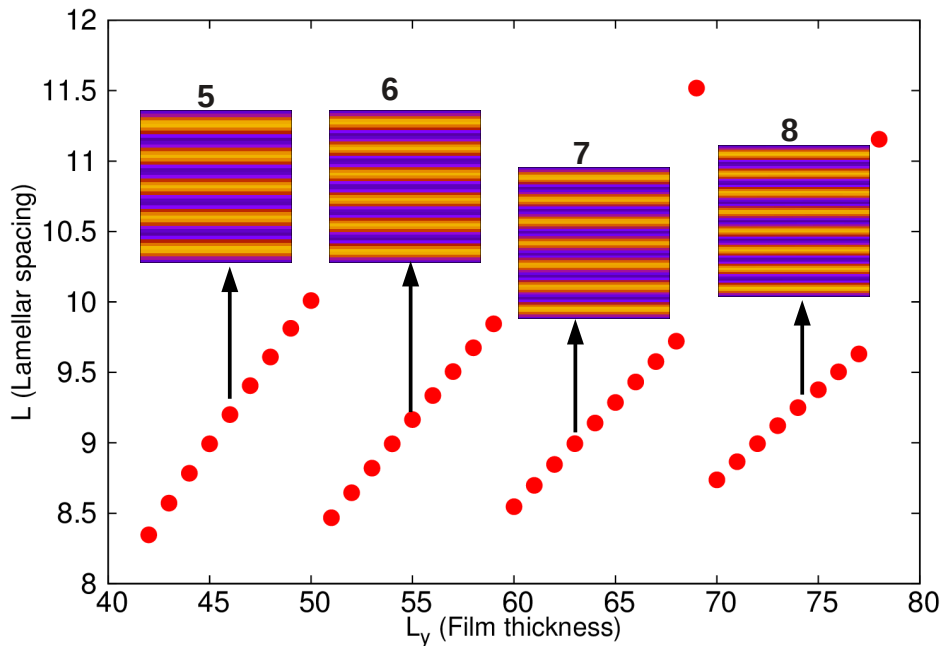


Figure 5.1: Variation of average lamellar spacing  $L$  with film thickness  $L_y$ : There exists a film thickness interval in which an integral number of lamellae exists. Within an interval, the lamellar spacing varies linearly with film thickness. The upper limit of a film thickness interval corresponds to a state of least frustration while the lower limit corresponds to maximum frustrated state.

film thickness is presented in Table 5.1. For larger film thickness, the evolving configuration is parallel and the lamellar period changes only in integral values. At lower film thickness, a change in orientation to perpendicular state takes place. By doing so, the lamellae are able to mitigate the effect of frustration. A certain number of lamellae is stable within a fixed film thickness interval. At larger film thickness there is also a distinct reversal to a lower integral value of lamellae before going to the next higher integer. For e.g. a change in the lamellar period from 7 to 8 takes place through an intermediate value of 6.

The variation of the lamellar spacing with film thickness is presented in Fig. 5.1. The average lamellar spacing,  $L$ , for different film thickness is calculated as follows. The zeros of the density profile taken to be the interface composition are linearly interpolated and a thickness of a layer (half lamellae), is calculated by the difference between the adjacent zeros.  $L$ , is then found by averaging out the differences and multiplying it by two. The following trends can be inferred from Fig.5.1. In a given film thickness interval corresponding to a fixed number of lamellae,  $L$  varies linearly. The parallel configuration is in the least frustrated state at the higher value of the interval, while

the frustration is maximum at the lower end. The plot also shows abrupt change in the lamellar spacing during transition from one lamellar period to another. Theoretically, this change is expected to occur when the frustration is maximum, i.e when the film thickness is  $L_y = (n + \frac{1}{2})L_o$ . [46] The plot bears a striking resemblance to the experimental plot of Lambooy et al [46] (Fig.3 in their paper).

Apparently,  $L$  is strongly dependent on  $L_y$  and it is difficult to pin point at a definite equilibrium value. However, a rough estimate can certainly be made. Since in a given film thickness interval corresponding to a fixed number of lamellae, the least frustrated state occurs at the upper limit, this value is presumably close to the equilibrium value. A close inspection of Fig. 5.2 reveals that the upper limit for each interval is close to 10, which can then be taken to be the equilibrium spacing. A second possibility is to ascertain the equilibrium spacing from the film thickness where a perpendicular configuration is stable. Similar methodology has been earlier used in Ref.[41] to calculate the equilibrium lamellar spacing. This state also corresponds to a state of least frustration as film thickness in  $x$  direction is not finite. The lamellar spacing for the two film thicknesses  $L_y = 15$  and 6 are calculated to be 10.55057 and 10.668968, respectively. Incidentally, this value is closer to the ones obtained for film thicknesses  $L_y = 78$  and 69 which is around 11. This observation implies that the equilibrium value is possibly between 10 and 11. The change in the lamellar period is expected to take place at half-integral values of equilibrium spacing i.e at  $(n + \frac{1}{2})L_o$ . Assuming  $L_o = 10$ , it can be seen in Table 5.1 that the change in lamellae period takes place at these values, at least for thin films. A deviation occurs for the case of larger film thicknesses, but this is natural as the change from the equilibrium spacing can be distributed across several layers. Thus, the equilibrium spacing is closer to 10 than 11. A value of  $L_o = 10$  is hence chosen as the equilibrium lamellar spacing hereafter.

## 5.2.2 Effect of electric field and surfaces

Some typical morphologies arising due to the interplay of substrate interaction, confinement and electric field is first discussed followed by an evaluation of the resulting phase diagram. The result is categorized into three different regimes depending on the film thickness  $L_y$ .

### 5.2.2.1 Thicker films with $L_y \gg L_o$

The combined effect of the substrate and electric field for model parameters  $h = 0.1$ ,  $E = 0.937$  and  $L_y = 64(6L_o)$  is presented in Fig. 5.2. The phase separation initiates from the surface leading to the formation of parallel lamellae. However, at  $t = 80$ , the

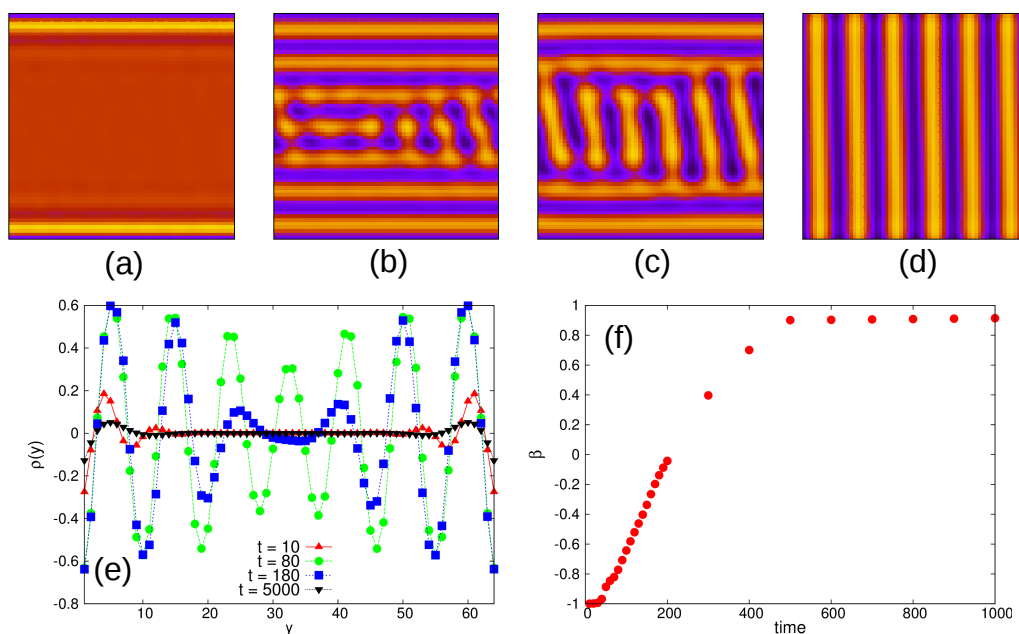


Figure 5.2: Microstructure evolution with model parameters  $h = 0.1$ ,  $E = 0.937$  and  $L_y = 64(6L_o)$  at timesteps (a)  $t = 10$ , (b)  $t = 80$ , (c)  $t = 180$  and (d)  $t = 5000$ . After the initial stages of surface induced ordering as in (a) and (b), the effect of electric field sets in resulting in a breakup of the parallel layers starting from the inner film (b) and subsequently joining in the perpendicular direction. The final stable configuration is perpendicular as shown in (d). The density profile in (e) and alignment kinetics in (f) also corroborate the fact that local break up and coalescence in the direction of applied field is the mechanism of alignment.

effect of electric field sets in, leading to undulations which ultimately break up the inner layers into smaller domains. Subsequently, the smaller domains coalesce and get aligned in the direction of the electric field. This phenomenon proceeds outwards layer by layer resulting in a perpendicular lamellar arrangement due to energetic consideration.

The average density profile in Fig. 5.2(e) during early stages (corresponding to  $t = 10$ ) is oscillatory near the surface, due to the formation of enriched and depleted layers. With time the oscillatory profile develops throughout the film thickness. At  $t = 180$ , the innermost oscillation dies out and is replaced by a flatter profile which highlights the destruction of parallel structure at the center of the film. Much later, (corresponding to  $t = 5000$ ) the density profile becomes flat in the bulk of the film. However the average value shows small enrichment layers at the immediate vicinity of the surfaces even though the microstructure at the final timestep appears to be completely perpendicular. The kinetics of alignment is presented in Fig. 5.2(f). The value of  $\beta$  is -1 during early stages corresponding to parallel ordering along the surface. There is a smooth temporal transition from -1 to a value closer to +0.9 which depicts the formation of perpendicular lamellae.

The influence of increasing the magnitude of substrate interaction strength and electric field for the same film thickness is presented in Fig. 5.3. The mechanism that leads to the formation of perpendicular lamellae is essentially the same as earlier, i.e local lamellae disruption and coalescence. However, as a result of greater substrate interaction, the parallel lamellae near the surfaces i.e. the wetting layer never break resulting in alternate enriched and depleted layers at the boundaries. In literature such a morphology is termed as mixed [55, 56, 53]. Though the surface induced ordering length is greater than the film thickness of our study, the effect of surface is predominant closer to the walls and fades away from the walls. In other words this implies that the effect of surface is non uniform over the whole ordering length. As a result, when the electric field drives the domain alignment perpendicular to the surface, above a threshold interaction strength  $h$ , and below a threshold electric field  $E$ , the substrate interaction dominates near the walls resulting in a few parallel layers. Meanwhile the effect of electric field is predominant at the center (away from the wall) and is able to induce a change in configuration in this region.

The degree of alignment achieved in the direction of electric field is around 75% in Fig. 5.3(e). Due to higher magnitude of electric field, faster kinetics is observed as can be seen by either comparing the microstructures in Fig. 5.2 and Fig. 5.3 or by comparing the slope of  $\beta$  in Fig. 5.2(e) and Fig. 5.3(e) during the transition period. The latter has a steep transition region as compared to the smoother transition region in the former case. Finally the consequences of further increasing the electric field to  $E = 2.187$  is

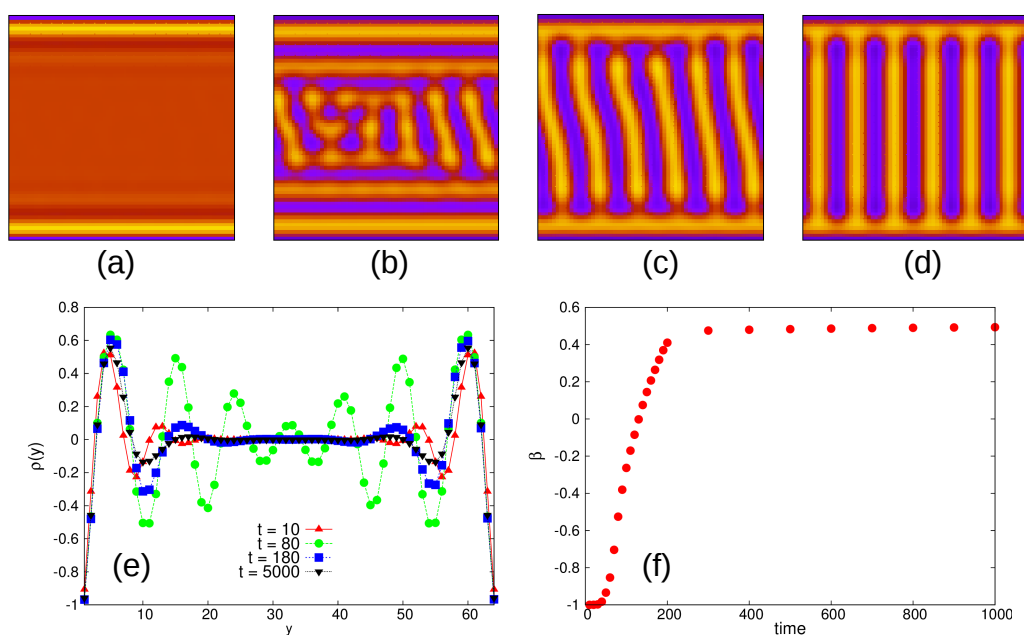


Figure 5.3: Microstructure evolution with model parameters  $h = 1.0$  and  $E = 1.25$  for film thickness  $L_y = 64(6L_o)$  at timesteps (a)  $t = 10$ , (b)  $t = 80$ , (c)  $t = 180$  and (d)  $t = 5000$ . Due to the presence of higher magnitude of surface interaction strength, the lamellae near the vicinity of the surface never break, resulting in a mixed morphology mode. (e) The average density plot  $\rho(y)$  consists of an oscillatory profile near the walls signifying a parallel arrangement where as the profile is flat at the middle, implying a perpendicular state. (f) The degree of alignment parameter  $\beta$  captures the transition from initial parallel structure ( $\beta = -1$ ) to the mixed state ( $\beta = 0.5$ ).

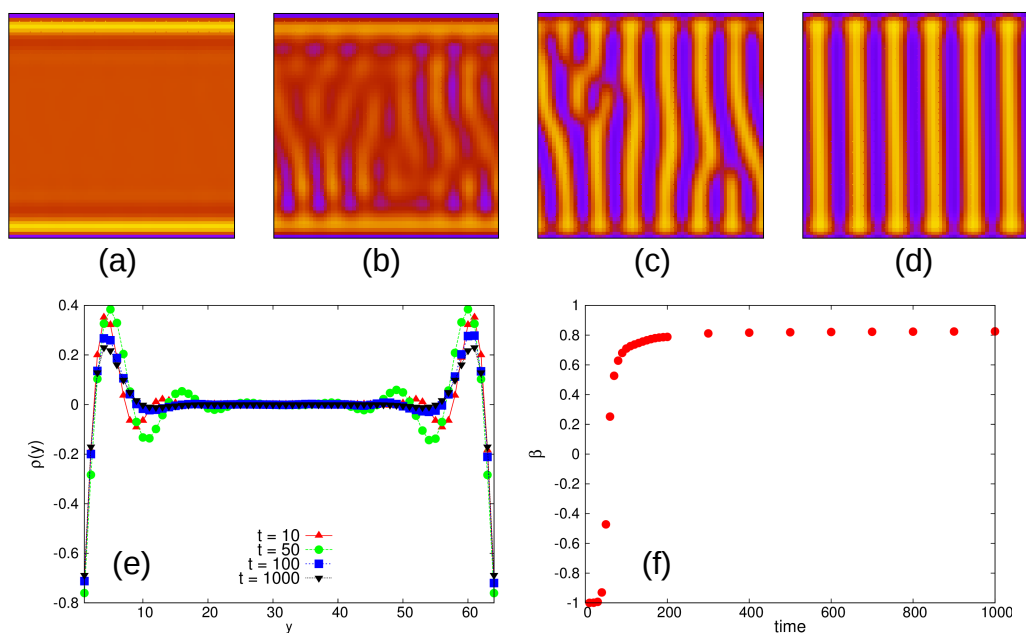


Figure 5.4: Microstructure evolution with model parameters  $h = 1.0$  and  $E = 2.187$  for film thickness  $L_y = 64(6L_o)$  at timesteps (a)  $t = 10$ , (b)  $t = 50$ , (c)  $t = 100$  and (d)  $t = 1000$ . The presence of higher magnitude of electric field leads to nucleation of perpendicular layers of alternate phases at the center of the film in contrast to the mechanism of local lamellae disruption and joining at low fields. This fact is substantiated by density profile  $\rho(y)$  in (e) and alignment parameter  $\beta$  (f). In the former graph, oscillatory profile characteristics of parallel configuration never develops in the middle of the film and in the latter graph the transition of  $\beta$  from negative to positive values is abrupt.

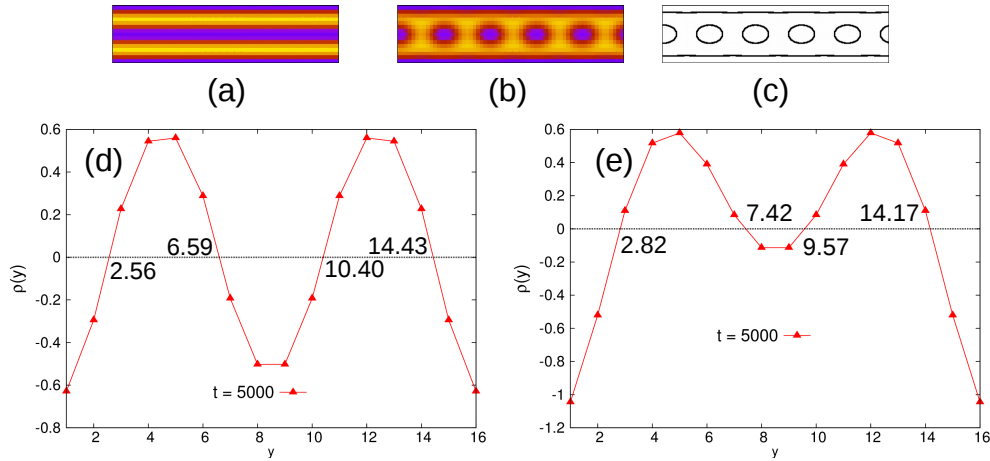


Figure 5.5: (a) microstructure corresponding to  $t = 5000$  for model parameters  $h = 0.1$ ,  $E = 0.156$  for film thickness  $L_y = 16(1.6L_o)$ , (b) microstructure corresponding to  $t = 5000$  for model parameters  $h = 1.0$ ,  $E = 0.156$  and for the same film thickness (c) contour plot corresponding to (b), (d) average density profile corresponding to (a) and (e) average density profile corresponding to (b).

studied whilst keeping the other two parameters  $h = 1.0$  and  $L_y = 64$  unaltered. The results are shown in Fig. 5.4. An interesting phenomenon to observe is the mechanism of alignment by the electric field. In contrast to the previous cases, the parallel ordering never goes beyond two layers. Instead, the electric field is sufficiently high to orient the composition fluctuations in the non-phase separated region, leading to the appearance of perpendicular lamellae at the middle of the film. Subsequently, the parallel layers near the walls also collapse and the rearrangement of perpendicular lamellae proceeds by defect annihilation mechanism [54]. The average density profile in Fig. 5.4(e) shows enrichment layers at the walls at all times but the oscillatory profile, characteristic of the parallel lamellae configuration never develops at the film center. The transition regime of alignment kinetics is abrupt as compared to the earlier cases. The value of  $\beta$  saturates to a value of  $+0.8$  which constitutes to 90% alignment in the direction of the applied field.

### 5.2.2.2 Films with $L_y \approx L_o$

The next study focuses on configurations when the film thickness is comparable to the bulk lamellar spacing. The case of film thickness of  $L_y = 16$  which is approximately equal to  $1.5L_o$  is of particular interest. For  $L_y = 16$  two cases with  $h = 0.1$  (Fig. 5.5(a)) and  $h = 1.0$  (Fig. 5.5(b)) are presented. The electric field is kept constant at  $E = 0.156$ . For low substrate interaction strengths, a parallel arrangement is found to be stable as in Fig. 5.5(a). However, with increasing substrate interaction strength, circular domains

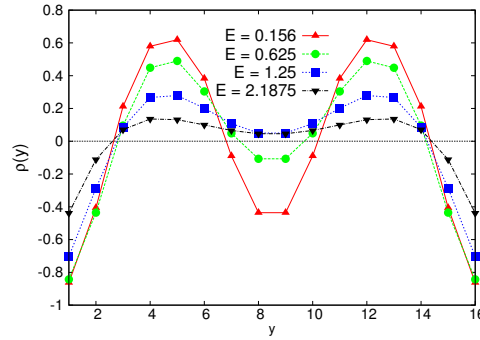


Figure 5.6: Average density profiles at different electric field strengths for  $h = 0.5$ . All the plots correspond to  $t = 5000$ .

emerge at the center of the film as in Fig.5.5(b). To differentiate the effect of electric field and substrate interaction responsible for this phenomenon, the microstructural pattern in the absence of electric field is considered. The resulting evolution (not shown) is similar, comprising of an inner layer of circular domains. Therefore, it can be inferred that the effect is solely driven by the substrate confinement independently of the applied electric field. The results can also be interpreted in terms of interference of composition waves. For higher  $h$ , the film thickness,  $L_y = 16$ , is close to half integral of equilibrium lamellar spacing. A destructive interference takes place at the center due to the composition waves emanating from the walls and an inner lamellae cannot be maintained. As a result circular domains start appearing in the middle. The breakup of the inner lamellae into circular domains is similar to the formation of holes as described by the mean-field theory of Shull [36]. The same phenomenon is absent at low  $h$ , presumably because the destructive interference at the film center is not sufficiently strong. An average density plot including the transition at  $\rho(y) = 0$  for the case of lower  $h$  is presented in Fig.5.5(d). It can be verified that the innermost layer is thinner ( $10.40 - 6.59 = 3.81$ ) than the next two adjacent layer on both sides ( $6.59 - 2.56 = 14.43 - 10.40 = 4.03$ ) and a parallel arrangement can still be maintained with the innermost layer being in a compressed state.

The average density profile presented in Fig. 5.5e) shows the asymmetry in the roots of  $\rho(y) = 0$ . The average  $\rho(y)$  value at the center is slightly B rich, clearly signifying the absence of any parallel lamellae structure. The slight asymmetry in the average density points indicates, either the evolution of a perpendicular phase or an in plane asymmetric phase. The microstructure in Fig. 5.5b) indicates the second possibility where circular domains coexist at the center simultaneously with the wetting layers. The presence of such hybrid structures (combination of two different phases) have previously been reported in cylinder forming systems at similar film thickness [43]. However their

transition in electric field has not been reported previously. Although a 3D simulation is desirable to adequately address the issue, some predictions from the current 2D study can certainly be made. The average density profile for  $h = 0.5$  at different field strengths is presented in Fig. 5.6. All the plots correspond to  $t = 5000$ . At low electric field strengths,  $E = 0.156$ , the plot is similar to Fig. 5.5d), comprising of parallel lamellae. With a slight increase in the electric field strength, the value of  $\rho(y)$  at the center of the film shifts towards zero (slightly B rich). The density profile is similar to Fig. 5.5e), and denotes the appearance of a structure other than lamellae. In this case it is not the effect of substrate and confinement alone that causes this transition, but the presence of electric field does play its part. With further increase of electric field  $E = 1.25$  and  $2.1875$ , the surface enrichment decreases. At the same time, the average value at the center of the film shifts to positive values and the profile tends to get flatter. Though it is clear that perpendicular phases now span, at least in the middle of the film, the exact nature is very difficult to determine precisely in 2D simulation. It is speculated that the perpendicular phases are either cylindrical structures (for  $E = 1.25$ ) or perpendicular lamellae (for  $E = 2.1875$ ).

### 5.2.2.3 Films with $L_y < L_o$

Next, the film thickness is further decreased below the equilibrium lamellar spacing, to  $L_y = 4(0.4L_o)$ . The results corresponding to model parameters  $h = 0.1$  and  $E = 0.156$  are shown in Fig. 5.7. The early stage microstructure corresponding to  $t = 10$  is a superposition of parallel and perpendicular lamellae. With time ( $t = 30$  and  $70$ ), the system evolves through a metastable antisymmetric configuration and transforms into a perpendicular state. This observation is also corroborated by the average density profile. The result is consistent with the findings of Walton et al. [39] who argue in favor of a transient antisymmetric arrangement in symmetric thin films during the formation of vertical configuration.

Even with the smallest electric field strength (used in the course of this study), a perpendicular arrangement is seen to be stable. Even in the absence of the electric field, a stable perpendicular arrangement establishes implying that the geometrical confinement predominates over the electric field. Interestingly,  $\beta$  reaches the value of  $+1$  in this case. This observation points towards the following important fact : When the arrangement is guided by substrate confinement, deviation from perfect perpendicular morphology is negligible. However, significant deviation in perpendicularity is observed when the ordering is achieved due to the application of electric field.

For  $h_o \geq 1.0$ , parallel arrangement is found to be stable in the absence and at low strength of electric fields. At higher electric field strengths, the microstructure is a su-

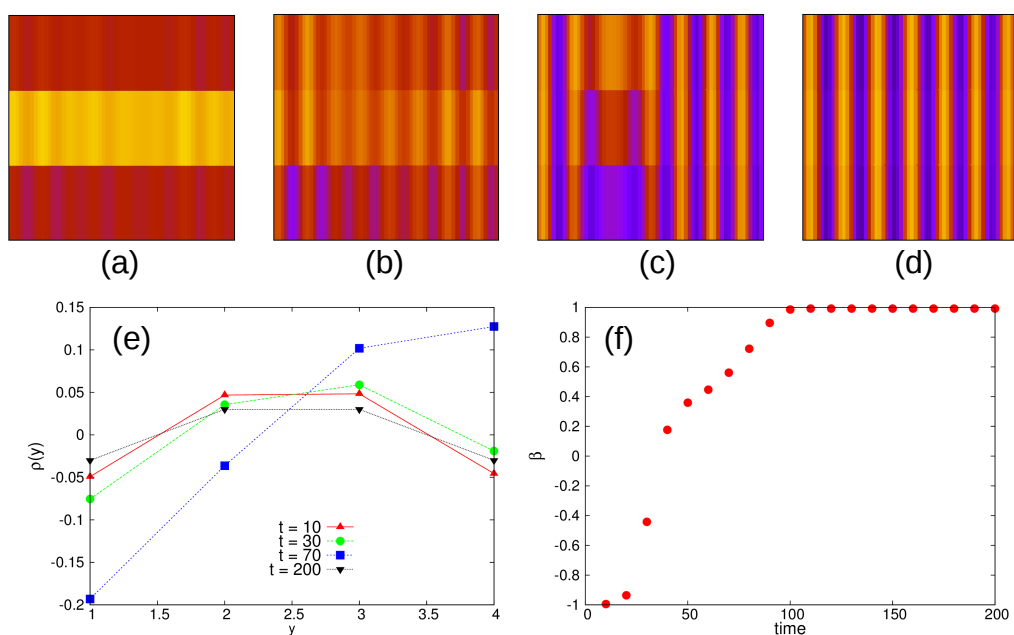


Figure 5.7: Microstructure evolution with model parameters  $h = 0.1$  and  $E = 0.156$  for film thickness  $L_y = 4(0.4L_o)$  at timesteps (a)  $t = 10$ , (b)  $t = 30$ , (c)  $t = 70$  and (d)  $t = 200$ . The microstructure has been drawn in 1 : 1 scale for clarity. To relieve the frustration due to confinement, the copolymer arranges in a stable perpendicular configuration even in the absence of electric field. The early time microstructure in (a) is a superposition of parallel and perpendicular lamellae. The final perpendicular state is achieved through a transition state of asymmetric configuration as also seen in the density profile in (e) ( $t = 70$ ). (f) The degree of alignment parameter corresponds to a perpendicular state.

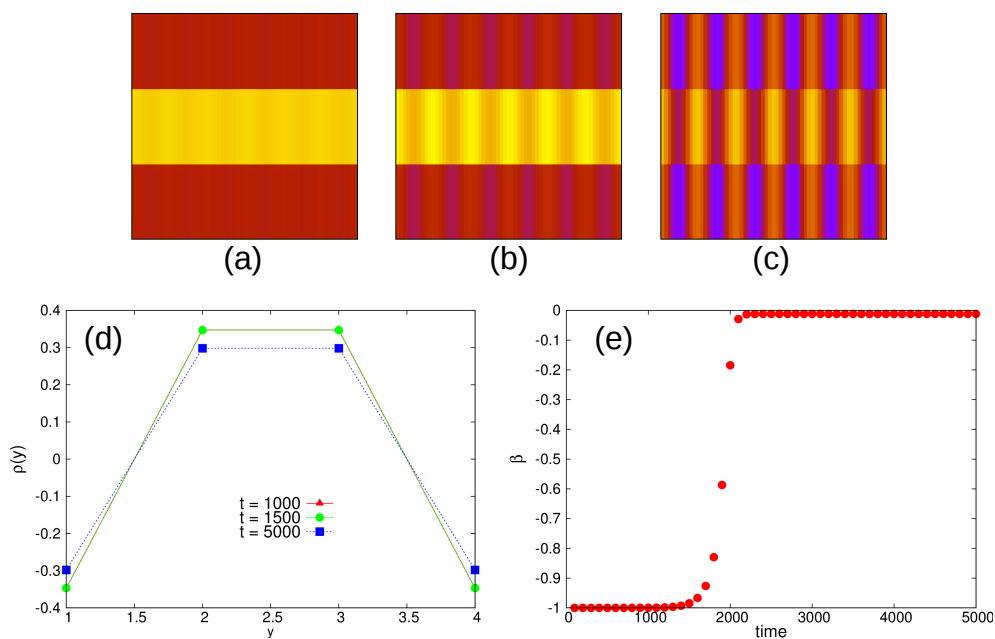


Figure 5.8: Microstructure evolution with model parameters  $h = 1.0$  and  $E = 2.188$  for film thickness  $L_y = 4(0.4L_o)$  at timesteps (a)  $t = 1000$ , (b)  $t = 1500$  and (c)  $t = 5000$ . The microstructure has been drawn in 1 : 1 scale for clarity. The microstructure at final step is a superposition of parallel and perpendicular lamellae. The perpendicular lamellae are thinner at the center. (d) The average density profile is also not flat in the region of  $\rho(y) = 0$ , implying a significant deviation from perpendicular arrangement. (e) The value of degree of alignment indicates a 50% aligned structure in the direction of field.

perposition of parallel and perpendicular lamellae as can be seen in Fig. 5.8. Because of the small film thickness, the substrate interaction is predominant and electric field is not able to completely eradicate the previous surface ordering phenomenon. Correspondingly  $\beta$  saturates to a value of 0 which is midway between parallel and perpendicular configuration.

### 5.2.3 Phase diagram

A phase diagram to summarize the influence of electric field  $E$ , surface interaction strength  $h$  and film thickness  $L_y$  on the evolving morphologies by classifying them into parallel, perpendicular and mixed category is next constructed. The morphology mixed is designated only when there exists at least one completely parallel layer ( $L = L_o/4$  since the layers closer to the substrate are one-half of the inner layers). Classification based on such criteria will allow us to compare the resulting phase diagram with the analytical calculations [56, 55]. Any other combination of phases is denoted as hybrid structure. The resulting configuration stability diagram is shown in Fig. 5.9. The following points can be appreciated,

1. For a given film thickness, the magnitude of applied electric field to induce a perpendicular arrangement increases with increasing magnitude of substrate interaction strength. Any deviation from this generality occurs only for very thin films e.g.  $L_y = 4$  (Fig. 5.9(e)) and closer to half-integral lamellar thickness i.e.  $(n + \frac{1}{2})L_o$  (in our case  $L_y = 16$ , Fig. 5.9(c)).
2. At low strength of substrate interaction ( $h = 0.1, 0.5$ ) and electric fields, parallel arrangement is found to be stable. However beyond a certain critical value of the electric field e.g.  $E = 0.937$  corresponding to  $h = 0.1$ , the configuration oscillates between perpendicular and parallel configuration (Fig. 5.9 (a)-(e)). The present findings accentuate the previous analytical results [56]. In general : As  $L_y$  decreases, the effect of substrate interaction becomes more prominent. Therefore a higher magnitude of electric field is required to induce a transition from parallel to perpendicular configuration. However, for  $L_y$  incommensurable with the bulk lamellar spacing (say  $(n + \frac{1}{2})L_o$ ) i.e. halfway between integral lamellar spacings, the free energy of the parallel configuration is maximum and hence a lower electric field can induce a perpendicular transition.
3. For unstrained films e.g.  $L_y = 64, 32$ , the critical electric field  $E_c$  required for a parallel to perpendicular transition scales as  $L_y^{-1/2}$  [56]. Though the numerical calculations are carried out at discrete values of electric field, this behavior can still

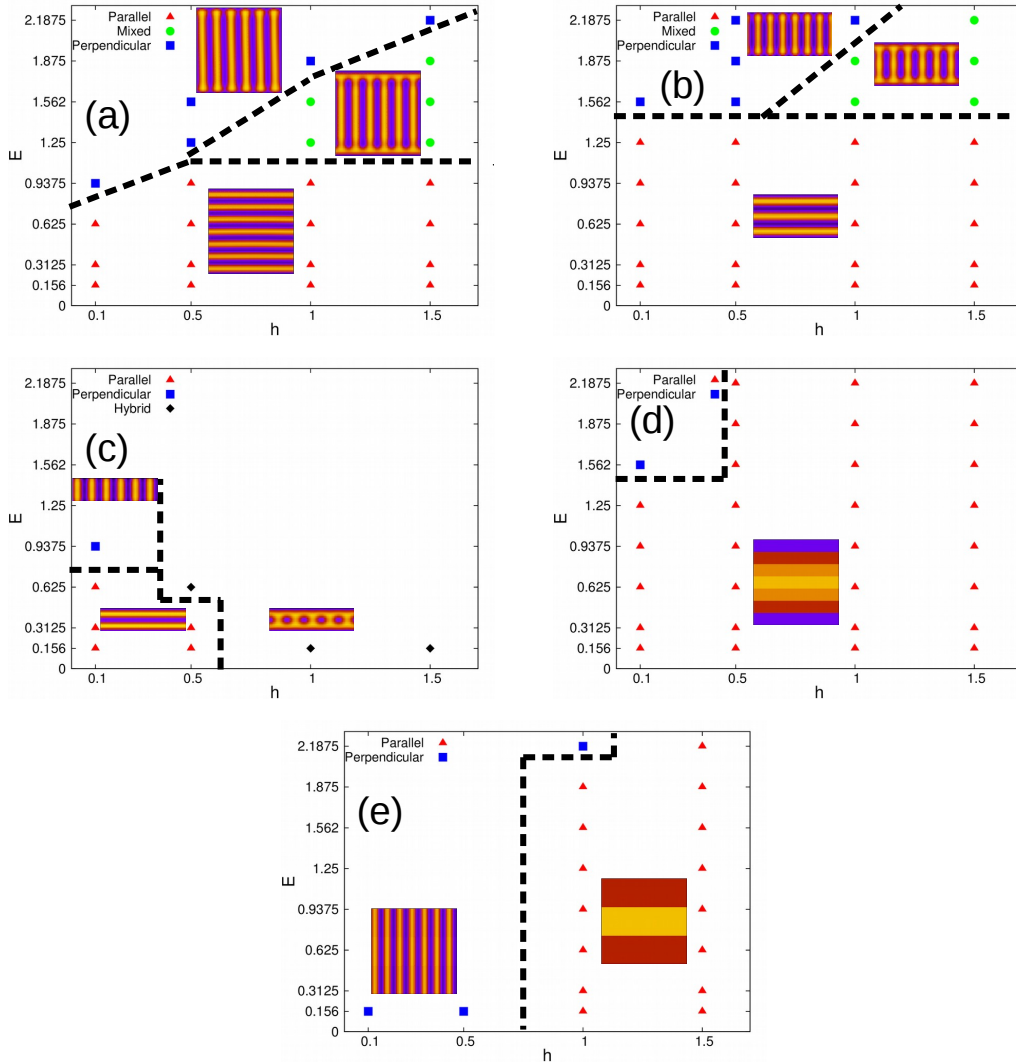


Figure 5.9: Phase diagram showing the stable arrangement at different magnitudes of electric field  $E$  and substrate interaction strength  $h$  for different film thicknesses (a)  $L_y = 64(6L_o)$ , (b)  $L_y = 32(3L_o)$ , (c)  $L_y = 16(1.6L_o)$ , (d)  $L_y = 8(0.8L_o)$  and (e)  $L_y = 4(0.4L_o)$ . The microstructures for  $L_y = 8$  and 4 have been drawn in 1 : 1 scale. All the above plots are for permittivity values of  $\epsilon_A = 3.0$  and  $\epsilon_B = 2.0$ .

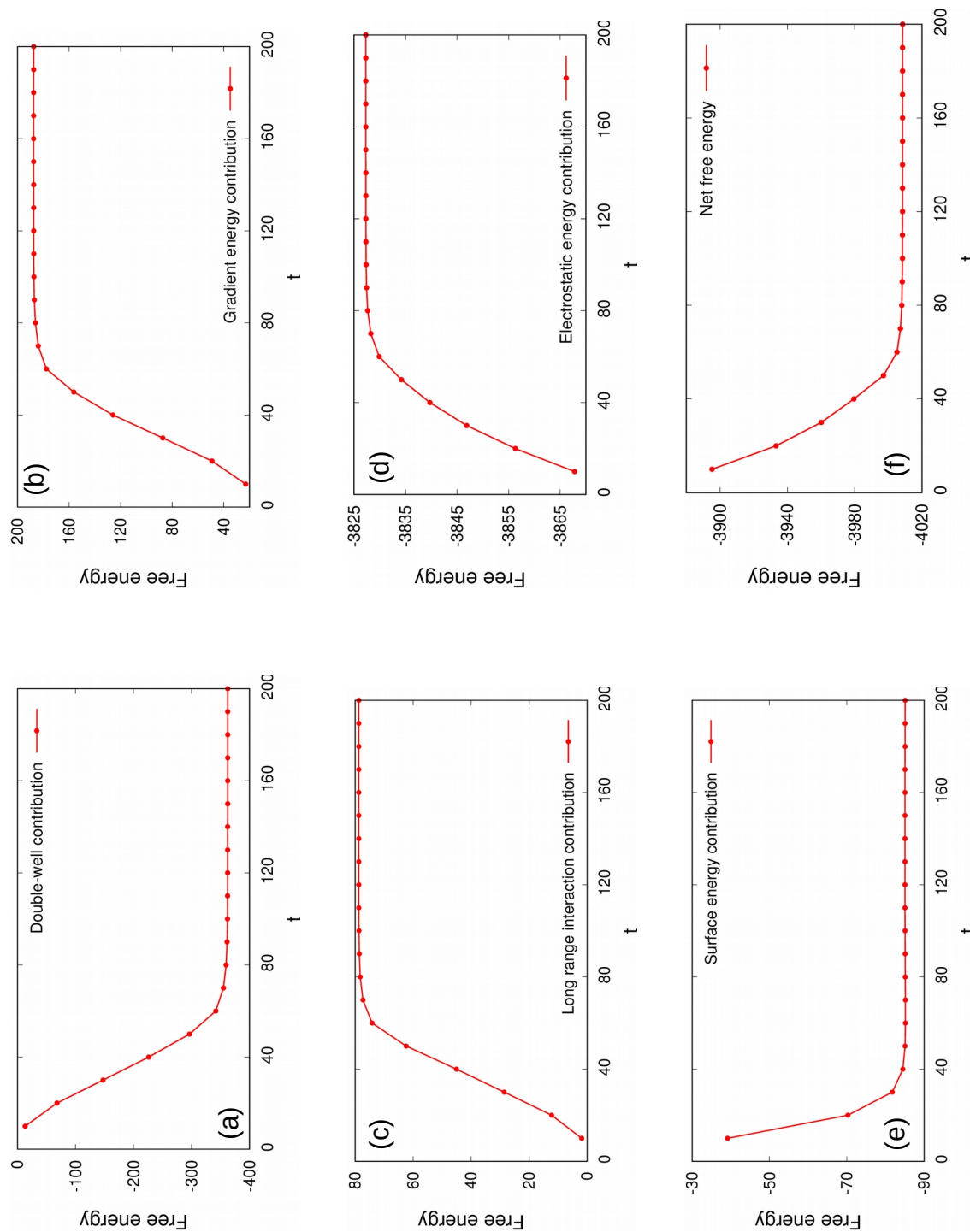


Figure 5.10: Temporal variation of the free energy contributions arising from the (a) double-well term, (b) gradient energy term, (c) long range interaction term, (d) electrostatic energy term and (e) surface energy term corresponding to the case  $h = 0.1$ ,  $E = 0.625$  and  $L_y = 64(6L_o)$ . (f) Net free energy obtained from the summation of all the contributions.

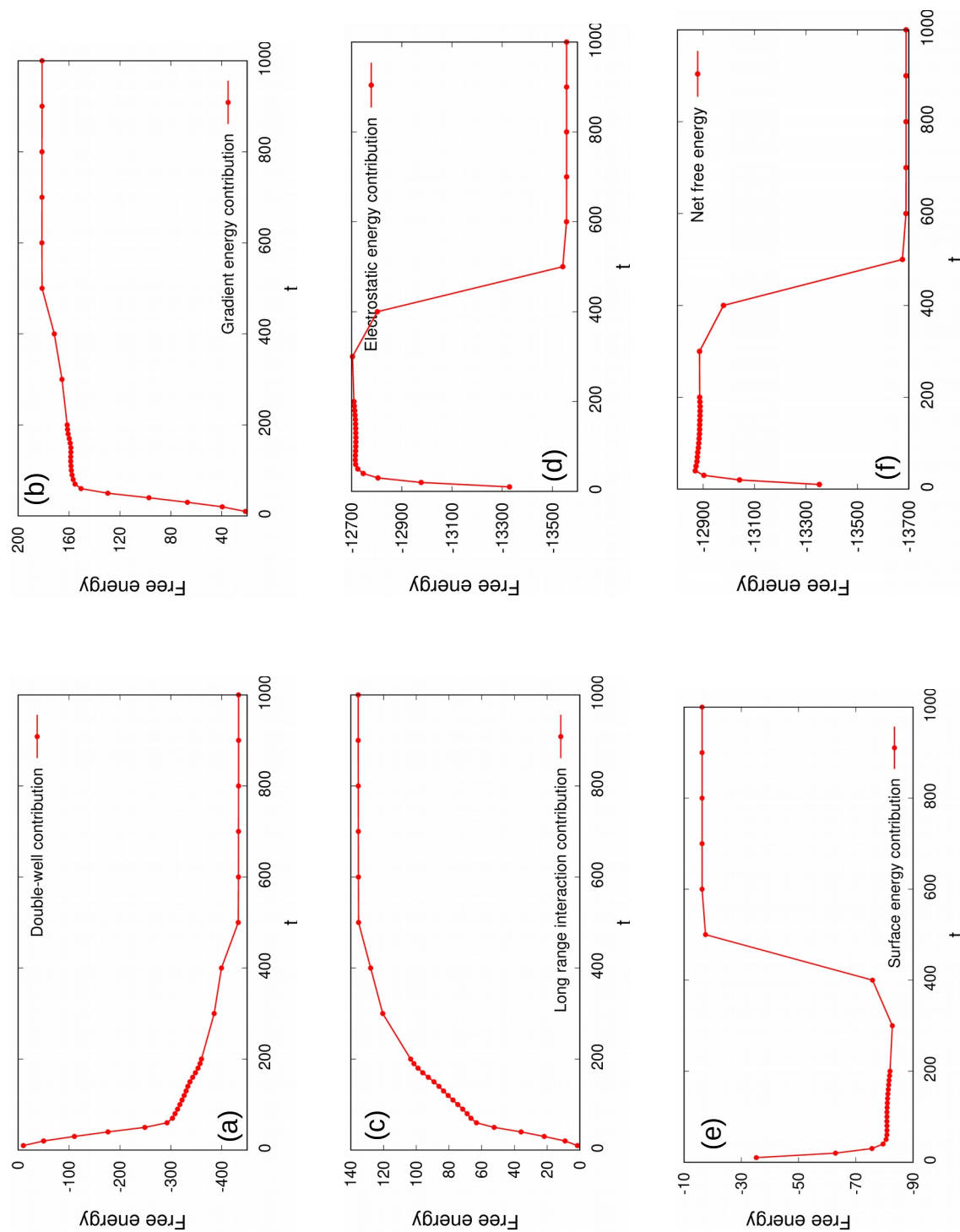


Figure 5.11: Temporal variation of the free energy contributions arising from the (a) double-well term, (b) gradient energy term, (c) long range interaction term, (d) electrostatic energy term and (e) surface energy term corresponding to the case  $h = 0.1$ ,  $E = 0.9375$  and  $L_y = 64(6L_o)$ . (f) Net free energy obtained from the summation of all the contributions.

be verified:  $E_c$  for  $h = 0.1$  and  $L_y = 64$  lies between 0.625 and 0.9375 (Fig. 5.9 (a)). Taking  $E_c = 0.9$  for  $L_y = 64$ ,  $E_c$  for  $L_y = 32$  can be calculated to be 1.27 which lies between the values of 1.25 and 1.562 in Fig. 5.9(b). Similar trend can be verified for  $h = 0.5$  in Fig. 5.9(a) and (b).

4. For higher substrate interaction strengths, i.e  $h = 1.0, 1.5$ , the range of stability of parallel configuration increases with decreasing film thickness (Fig. 5.9(a), (b), (d), (e)). For  $L_y < L_o$ , the parallel configuration is more stable.
5. Mixed morphologies are stable only for thicker films ( $L_y \geq 3L_o$ ) and for higher substrate interaction strength,  $h \geq 1$  (Fig. 5.9(a), (b)). Interestingly, the electric field required for the transition of parallel to mixed morphology, i.e. the first critical field is independent (or at most weakly dependent due to the discretized nature of the phase diagram) of substrate interaction strength (Fig. 5.9(a) and (b)). However, the second critical field i.e. the field required to convert mixed to perpendicular morphology is dependent strongly upon the substrate interaction strength (approximately linearly).
6. Next, consider the variation of the critical fields with film thickness for unstrained films ( $L_y = 64, 32$ ) for fixed substrate interaction strengths of  $h = 1.0, 1.5$  (Fig. 5.9 (a) and (b)). Clearly, both the critical fields depend upon the film thickness. The dependence of the first critical field, though, is stronger than the second critical field.
7. Interesting morphologies arise at  $L_y \sim 1.5L_o$  where the film thickness is incommensurable with the lamellar period. At low substrate affinities a usual parallel to perpendicular lamellae transition is observed but at higher affinities a wide range of hybrid structures results. The exact nature, though, is not clear in the present study.

A comment on the free energies of the different structures is also warranted. In analytical static calculations, a comparison of the free energies as a function of  $h$  and  $E$  of two states, say parallel and perpendicular is made to ascertain the stable configuration and the critical electric field required for the phase transition. The spontaneous phase transition from one configuration to the other in dynamic calculations, on the other hand, precludes the possibility to exactly pin point the critical value. Therefore, the phase boundaries (black dashed lines) in Fig.5.9 are just a guide to the eye. A comparison of the free energies of the two states, however, can certainly be made. The temporal variation of various contributions to the free energy in Eq.(3.59) corresponding to the case  $h = 0.1$ ,  $E = 0.625$  and  $L_y = 64(6L_o)$  (parallel configuration) is shown in Fig.5.10. Since we start

the simulations from a disordered state ( $\psi = 0$ ), the free energy arising from the double-well contribution (Fig.5.10(a)) decreases overtime as phase separation proceeds and the value of  $\psi$  reaches that of a segregated state (not necessarily  $\psi = \pm 1$ ). The increasing gradients in  $\psi$  increases the gradient energy contribution (Fig.5.10(b)). Similarly, the deviation of  $\psi$  from the average value of  $m = 0$ , increases the contribution from the long range term with time (Fig.5.10(c)). The free energy of the long range term was calculated from Eq.(3.12) by first solving the Poisson Eq.(3.8) subjected to the appropriate boundary condition. Due to the development of the parallel lamellae structure, the electrostatic energy increases (Fig.5.10(d)) because of the presence of unfavorable interfaces and the surface energy decreases (Fig.5.10(e)) simultaneously due to the wetting of the substrate by the preferred block. Although the electrostatic part is the main contributor to the total free energy, the net energy of the system decreases with time (Fig.5.10(f)) due to the decrease in the double-well and the surface energy terms.

The free energy for the case  $h = 0.1$ ,  $E = 0.9375$  and same film thickness which leads to perpendicular lamellae structure is shown in Fig.5.11. The double-well (Fig.5.11(a)), gradient (Fig.5.11(b)) and long range (Fig.5.11(c)) terms behave similarly and the magnitudes of the free energy from these terms are roughly the same order of magnitude as the previous case. The formation of parallel lamellae at initial stages (as also evident in Fig.5.2) leads to an increase of the electrostatic energy (Fig.5.11(d)) and decrease in the surface energy (Fig.5.11(e)). However, due to the higher applied electric field, the disruption and formation of perpendicular lamellae at later stages, reverses the trend. Due to the dominant contribution of the electrostatic energy (which is roughly four times higher than the previous case), the net free energy follows the same trend i.e. it does not decrease monotonically (Fig.5.11(f)). It is to be noted that this does not violate the second law of thermodynamics, since the system is connected to an external power source which does work on the system.

The net free energy decreases with increase in the applied electric field (for a given  $h$ ) as shown in Fig.5.12 because of the decrease in the electrostatic energy. The curve in Fig.5.12 represents the the minimum of the free energy curves of the parallel ( $F_{\parallel}(E)$ ), perpendicular ( $F_{\perp}(E)$ ) and mixed state ( $F_m(E)$ ) i.e.  $\min.\{F_{\parallel}(E), F_{\perp}(E), F_m(E)\}$ .

#### 5.2.4 Role of dielectric contrast

The effect of increasing the dielectric contrast i.e.  $\epsilon_A - \epsilon_B$  on the final configuration, will now be discussed. Increasing the contrast between the two blocks implies that the material is more responsive to an applied electric field and, as a consequence, if  $(\epsilon_A - \epsilon_B)$  is large, the resulting phase diagram is governed by the relative mismatch. In the studies

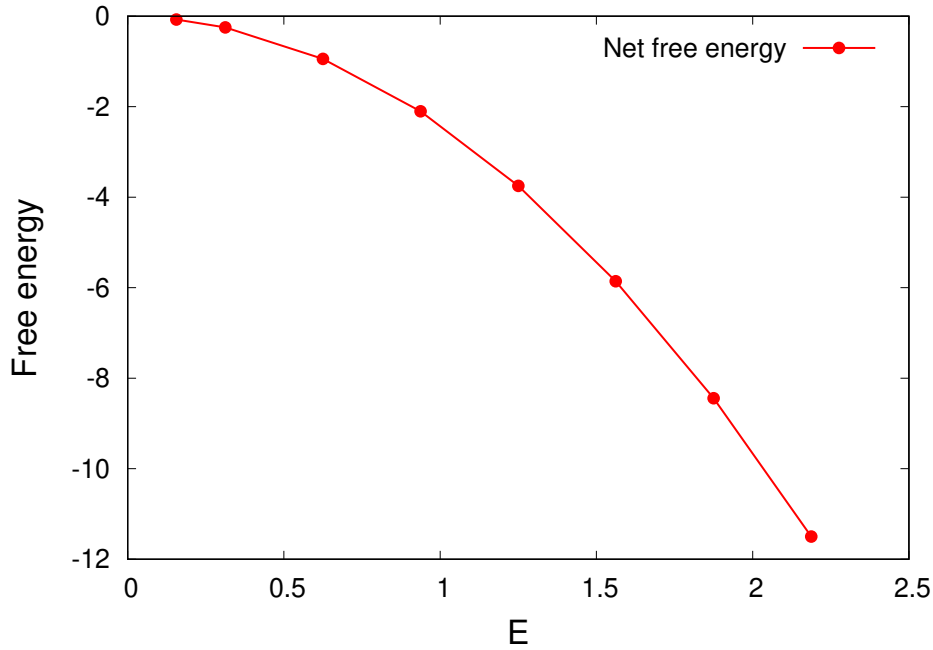


Figure 5.12: Variation of net free energy with applied electric field for  $h = 1.0$

so far, the values  $\Delta\epsilon = 1$  ( $\epsilon_A = 3$  and  $\epsilon_B = 2$ ) have been considered, which are close to the values reported by Amundson et al. [54] ( $\epsilon_A = 3.8$  and  $\epsilon_B = 2.5$ ) for PS-PMMA copolymer. If the permittivity difference  $\Delta\epsilon = 3.5$  is increased by selecting  $\epsilon_A = 6.0$  and  $\epsilon_B = 2.5$  as reported in Ref. [57, 56, 158], for the same copolymer system, an increase in electrostatic free energy contribution is expected for the same magnitude of applied field.

The discussion is restricted to unstrained films ( $L_y = 64, 32$ ). The resulting phase diagram is presented in Fig. 5.13 and the corresponding values of the critical electric fields are drastically lowered. According to the analytical calculations [56, 55], this decrease is proportional to  $\frac{\sqrt{\epsilon_A + \epsilon_B}}{\epsilon_A - \epsilon_B}$ . Considering the critical electric field to be  $E_c = 0.9$  for  $\Delta\epsilon = 1$  and  $L_y = 64$  and  $h = 0.1$  (Fig. 5.9(a)), the critical field on increasing the dielectric contrast to  $\Delta\epsilon = 3.5$  according to above equality (on holding  $L_y$  and  $h$  constant) yields a critical value of around  $E_c = 0.3$  which complies well with Fig. 5.13(a). A similar behavior is retrieved for  $L_y = 32$  as well.

The nature of the phase diagram changes dramatically and the region of mixed morphology in the phase diagram is diminished. With enhanced dielectric contrast, the dependence of the critical fields on the substrate interaction strength for a given film thickness becomes rather weak. This is contrary to the behavior at low dielectric contrast where the second critical field (mixed to perpendicular) displayed a strong dependency on substrate interaction strength. However, the dependency of the critical fields on film thickness for a given substrate interaction strengths is similar to that at low dielectric

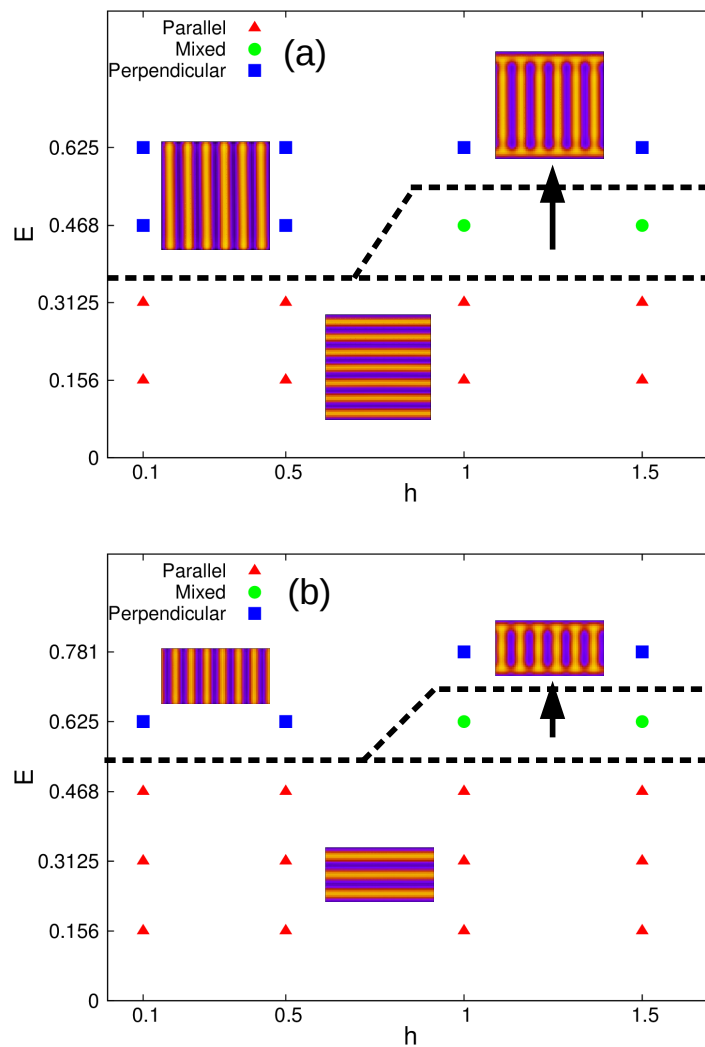


Figure 5.13: Phase diagram showing the stable arrangement at different magnitudes of electric field  $E$  and substrate interaction strength  $h$  for film thickness (a)  $L_y = 64(6L_o)$ , (b)  $L_y = 32(3L_o)$  for permittivity values of  $\epsilon_A = 6.0$  and  $\epsilon_B = 2.5$ .

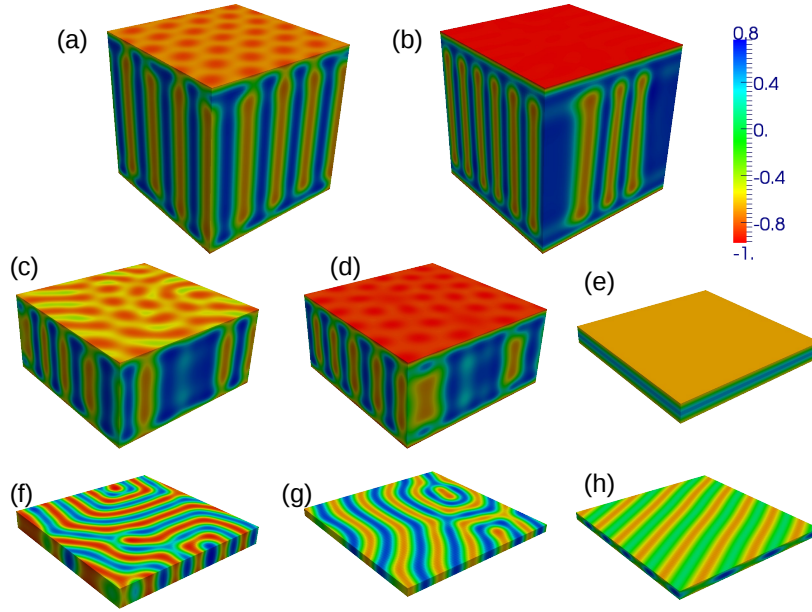


Figure 5.14: Microstructural patterns at (a)  $L_y = 64(6L_o), h = 0.5, E = 1.25$ , (b)  $L_y = 64(6L_o), h = 1.0, E = 1.25$ , (c)  $L_y = 32(3L_o), h = 0.5, E = 1.562$ , (d)  $L_y = 32(3L_o), h = 1.0, E = 1.562$ , (e)  $L_y = 8(0.8L_o), h = 0.1, E = 1.25$ , (f)  $L_y = 8(0.8L_o), h = 0.1, E = 1.562$ , (g)  $L_y = 4(0.4L_o), h = 0.1, E = 0.156$ , (h)  $L_y = 4(0.4L_o), h = 1.0, E = 2.1875$ . A comparison with the 2D morphologies in the phase diagram presented in Fig.5.9 suggests that the microstructure fall into the same adopted morphology classification in 3D as well.

contrast i.e. both fields depend on the film thickness with the dependency of the second critical field being higher than the first.

### 5.3 Discussions and Conclusions

The chapter is concluded with a critical assessment of the results from the present study to the experiments, analytical and SCFT calculations. The most relevant experimental study is due to Xu et al. [53, 7]. They studied thin films of varying thickness ( $4L_o, 10L_o, 20L_o, 100L_o$ ) [7]. For film thicknesses less than  $10L_o$ , substrate interaction was found to be dominant resulting in parallel arrangement, even on application of electric field of  $40V/\mu m$ . The substrate induced ordering length in their study was about  $5L_o$  and the segmental interaction or the segregation was  $\chi N = 26$ . The segregation in the present work is relatively weaker than their experiments ( $\chi N = 18$ ) and ordering length is around  $8L_o$  (with lowest substrate interaction strength). The critical field for lowest substrate interaction from our study is of the order of  $76V/\mu m$  and  $128V/\mu m$  for  $L_y = 6L_o$  and  $3L_o$  respectively for a dielectric contrast of  $\Delta\epsilon = 1$ . The second value is

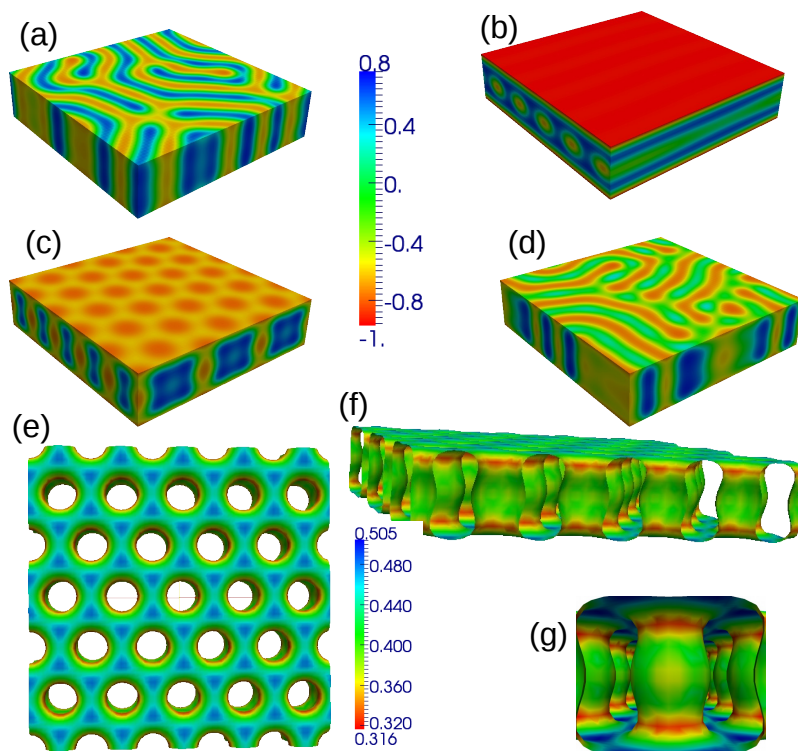


Figure 5.15: Microstructural patterns for  $L_y = 16(1.5L_o)$  at substrate affinity and electric field strength of (a)  $h = 0.1$ ,  $E = 0.9375$ , (b)  $h = 1.0$ ,  $E = 0.156$ , (c)  $h = 0.5$ ,  $E = 1.25$ , (d)  $h = 0.5$ ,  $E = 2.1875$ , (e) top view of the contour of the order parameter gradient of (c), (f) sideview of (e) and (g) a zoomed view of (f). The coexistence of parallel wetting layers and an inner parallel layer of cylinders can be seen in (b). The presence of electric field induces the formation of perpendicular cylinder in (c). However at higher field strengths, the system reverts to a perpendicular lamellae (d).

actually quiet high and may well exceed the dielectric breakdown of the material and in such cases only parallel ordering would be exhibited. It is remarked that in recent experiments, electric field of the order of  $120V/\mu m$  have been applied [71]. However, if the critical field for enhanced dielectric contrast of  $\Delta\epsilon = 3.5$  (the same as in experiment) is examined, the values are around  $40V/\mu m$  and  $52V/\mu m$  for  $L_y = 6L_o$  and  $3L_o$  respectively, which are well within experimental range. Given a higher segregation in experiments, the critical fields are expected to be higher than that in the present study. Infact using SCFT Matsen [158] calculated the critical field to be around  $57V/\mu m$  for the same experimental conditions of Xu et al. ( $\Delta\epsilon = 3.5$  and  $\chi N = 26$ ) for  $L_y = 10L_o$ , though substrate interaction was not explicitly considered. Moreover, at  $\chi N = 18$ , the critical field from their work would turn about to be roughly  $58V/\mu m$  for dielectric contrast of  $\Delta\epsilon = 3.5$  and  $L_y = 6L_o$ (Fig 5(a) in Ref. [158]).

A comparison of the present findings to that of Lin et al. [60] who studied sphere to cylinder transition is discussed next. Using SCFT calculations, a complete phase diagram was calculated. Their segregation also corresponds to  $\chi N = 18$ . The present work is thus complementary to their study. For weak substrate interaction, the critical field (maximum value) calculated by them is around  $32V/\mu m$  and  $45V/\mu m$  for  $L_y = 6L_o$  and  $3L_o$  respectively (Fig. 7 in ref. [60]). Considering that sphere to cylinder transition generally takes place at field strength lower than parallel to perpendicular lamellar transition, our values of  $40V/\mu m$  and  $52V/\mu m$  are quite in agreement with SCFT calculations. A similar comparison can also be made at higher substrate strengths.

The calculated phase diagrams are similar in spirit to that by Lyakhova et al. [57]. In both studies, the phase diagram is obtained from dynamic microstructure evolution rather than static calculations [56, 60]. The authors investigated parallel to perpendicular transition of lamellar morphology using dynamic SCFT coupled to perturbed solution of Maxwell equation for thin films of  $L_y = 4L_o$  and segregation of  $\chi N = 16$ . Mixed morphologies were however not observed in that study. In the present study, the system was allowed to evolve from a disordered state under combined electric and substrate field, whilst in the study of Lyakhova et al., electric field was applied to well developed microstructures. Possible difference can arise because of the initial level of ordering. Our results are qualitatively similar to the results of Lin et al. [60] who observed the presence of mixed phases in film thickness as low as  $3L_o$  in cylinder forming systems at a similar segregation.

A comparison of the calculated phase diagram to the analytical calculation of Tsori et al. [56] is made next. The authors computed the phase diagrams both in weak and strong segregation regime. The results presented correspond to an intermediate regime. Though our results are closer to WSL, the phase diagram presented in Fig. 5.9 is similar

to the analytical calculation of Tsori et. al in SSL (Fig. 8 and 9 in ref. [56]). It is remarked that the two phase diagrams correspond to two different segregation regimes and are based on different assumptions. The phase diagram calculated by Tsori et al. corresponds to SSL and is based on the assumption of finite surface ordering length and high dielectric contrast ( $\Delta\epsilon = 3.5$  as compared to our  $\Delta\epsilon = 1$ ). In WSL, they assumed the ordering length to be greater than the film thickness and mixed morphology was not considered. In the present study, mixed morphology is observed inspite of the ordering length being lower than the film thickness. The consideration of finite surface ordering length in context of WSL (and in the occurrence of mixed morphology in particular) might have been an over assumption. Moreover, only a single intermediate phase i.e. a mixed lamellae morphology was considered. The results of the present study, however, indicates the presence of other intermediate or hybrid structures, thus altering the phase diagram significantly from analytical theories.

The influence of wall interaction characteristics on the equilibrium morphologies is briefly discussed. The present work is restricted to symmetric substrate interaction. However, in principle two additional cases are possible. The substrate can be (i) antisymmetric i.e. both walls attract different monomers with same strength or (ii) asymmetric i.e. both walls have preference towards same or different monomers, but possess different interaction strength. The consideration of antisymmetric case may not lead to any new geometries other than the ones reported here. Only the region of their respective occurrence in the phase diagram might change, given that film thickness corresponding to integral number of lamellae spacing would then be the frustrated state and half-integral, the natural state. On the contrary, asymmetric interaction can potentially engender an additional type of mixed morphology, where the system adopts a parallel configuration on one side (where interaction strength is comparatively higher) and perpendicular configuration on the other (where interaction strength is weaker). However, it remains to be seen if the competing electric field can stabilize other morphologies, for instance, cylindrical that has been reported in the present study.

To summarize, the morphology evolution of a symmetric diblock copolymer under competing substrate interaction and electric field using a coupled Ohta-Kawasaki functional and Maxwell equation is studied. By solving the full Maxwell equation, the weak dielectric inhomogeneity is not assumed, making the model equally applicable irrespective of segregation. A good agreement with the analytical and SCFT calculations, amply demonstrates the predictive capability of the proposed model. A distinct advantage of coarse graining is the accessibility to large scale simulation, especially in three dimension. Moreover, in 3D the nature of mixed/hybrid morphologies are well defined and such a simple classification (parallel, perpendicular and mixed lamellae) may not be suffice. Our 2D results does point out that in the incommensurate films in the regime  $L_y < 2L_o$ , this

interplay of substrate, confinement and electric field leads to rich hybrid structures and even the occurrence of a parallel lamellae to perpendicular cylinder transition. Infact in recent experiment on gyroid forming copolymers by Crossland et al. [71] a large number of coexisting morphologies were observed at low dielectric contrast. Some preliminary 3D results which corroborates the findings of our present 2D study is presented in Fig. 5.14 and 5.15.

# Chapter 6

## Electric-field-induced lamellar to hexagonally perforated lamellar transition in diblock copolymer thin films : Kinetic pathways

### 6.1 Introduction

Hexagonally Perforated Lamellar (HPL) morphology is known to be a long-lived metastable state between lamellar and cylindrical phases in diblock copolymers [217, 30]. The structure of HPL encompasses the planar characteristics of lamellar phase (usually the minority component), hexagonal or cubic arrangement of the cylindrical phase (majority component) penetrating the parallel layers with three-fold connections similar to the gyroid phase [218, 219]. Owing to the technological importance of HPL as a key ingredient in the synthesis of nanoporous thin films, conceiving techniques capable of stabilizing the otherwise metastable HPL are of scientific interest [220, 221].

In this present chapter, a detailed 3-D numerical study is presented to explore this novel electric-field-induced lamellar to HPL transition with specific focus on the kinetic pathways of the transition. Previously, HPL phases heretofore known to be unstable in the bulk (thick films) are shown to be preserved in thin films in cylinder-forming BCPs due to surface reconstruction [43, 44]. The literature is replete with investigation that report the occurrence of HPL in thin films of triblock copolymers at *asymmetric* compositions [222] as well as in diblock-homopolymer blends [223]. However, to the best of our knowledge, any study focusing on electric-field-induced OOT *to* HPL morphology has never been reported.

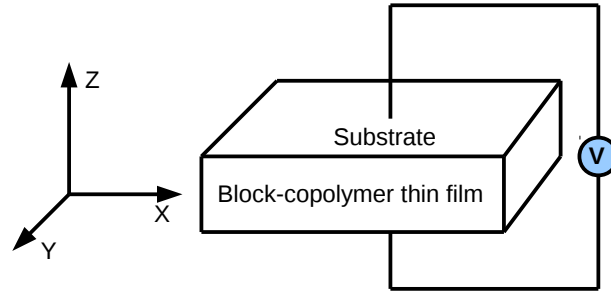


Figure 6.1: A schematic of the simulation geometry used in the present study. BCP thin film is confined between two rigid substrates in the  $z$  direction. The substrates have a preferential affinity towards the B monomer. Electric field is generated by imposing a constant voltage across the film thickness.

The simulation geometry chosen for the present study (Fig. 6.1) consists of two rigid surfaces at  $z = 0$  and  $z = L_z$  confining a BCP film across which a constant voltage is applied. Dirichlet boundary conditions are applied for voltage at  $z = 0$  and  $z = L_z$  with  $\phi|_{z=0} = +\frac{V}{2}$  and  $\phi|_{z=L_z} = -\frac{V}{2}$  while Neumann boundary conditions are applied in the lateral directions. Thus, the resulting electric field is aligned along the  $z$ -direction.

## 6.2 Results

### 6.2.1 Effect of substrate interaction, confinement and electric field : Phase diagram

To begin with, the the phase diagram arising out of the three way confluence of substrate affinity, confinement and electric field is described. The phase diagram for weak substrate affinity is presented in Fig. 6.2. In the absence of an electric field, the system mainly (except for  $L_z = 15(1.5L_o)$ ) adopts a parallel configuration with respect to the substrate. If  $L_z < 15(1.5L_o)$  a monolayer arrangement (BAB) evolves, while films with  $L_z > 15$  establish a bilayered arrangement (BABAB). However, films with  $L_z = 1.5L_o$ , a thickness that corresponds to maximum frustrated state, adopts a perpendicular configuration. The application of electric field induces a parallel to perpendicular transition above a threshold value. The characteristic patterns in the phase diagram are symmetric about  $L_z = 1.5L_o$ , with the critical field decreasing until  $L_z = 1.4L_o$  followed by a gradual increase thereafter.

The phase diagram, however, exhibits exotic behavior (Fig. 6.3) with an increase in the substrate affinity to  $h = 0.5$ . In the absence of electric field, larger substrate strength, while maintaining other parameters unchanged, leads to parallel ordering for each film

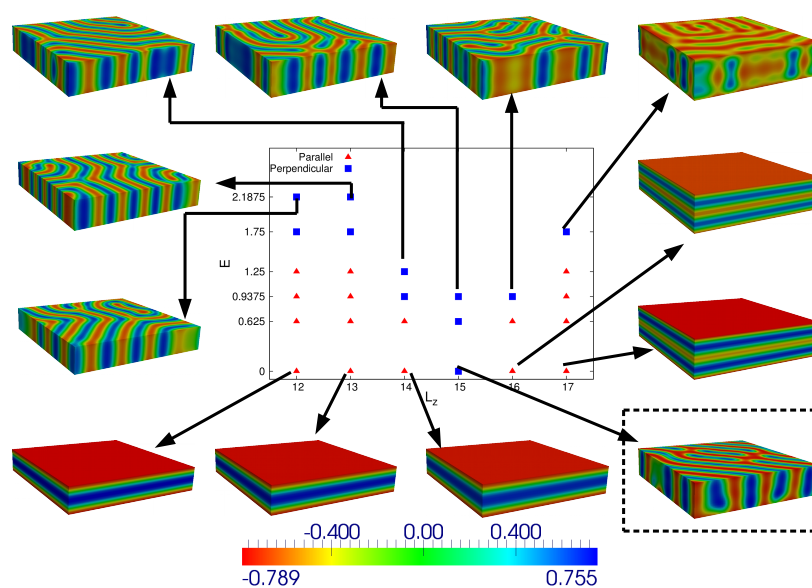


Figure 6.2: Phase diagram of a lamellae forming BCP at low substrate affinity,  $h = 0.1$ . In the absence of electric field ( $E = 0$ ), the film tends to adopt a parallel configuration with respect to the substrate. However, an exception can be seen at  $L_z = 15(1.5L_o)$  (enclosed in the dashed box, which corresponds to a highly frustrated state), where confinement alone leads to a morphological transition to a perpendicular state. For other film thicknesses, a critical magnitude of electric field is required to induce a change in the configuration. The morphologies in the phase diagram are symmetric about  $L_z = 15(1.5L_o)$ .

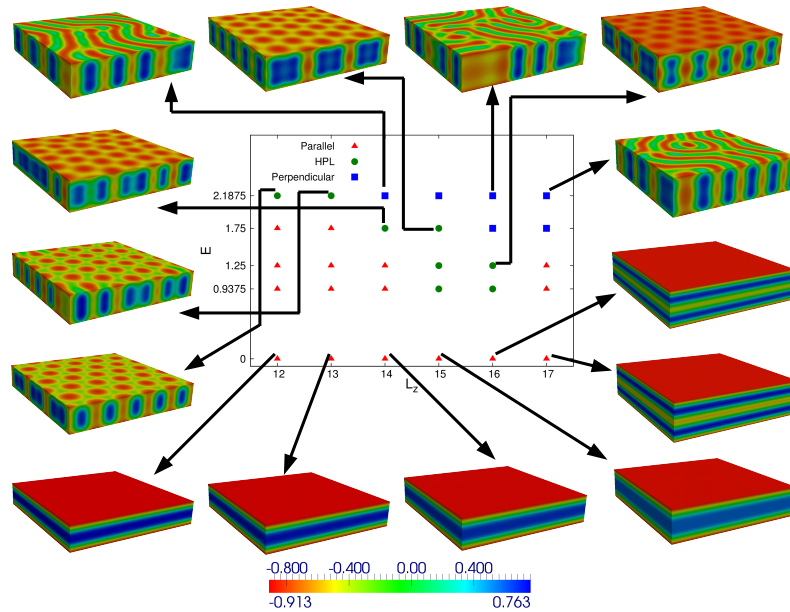


Figure 6.3: Phase diagram of a lamellae forming system at large substrate interaction strength  $h = 0.5$ . A parallel ordering is observed to evolve at all film thickness in the absence of electric field. However, it is noteworthy that two critical fields exist in the present case. Above the first critical field, a parallel to HPL transition occurs; the preferred component forms the cylindrical domains. A slight enrichment layer of the preferred component exists at the surfaces, but, the wetting layer, in general, is not found to be uniform. Electric field strength corresponding to the second critical value leads to the appearance of perpendicular lamellae.

thickness. The application of electric field, however, leads to a couple of fascinating morphological transitions corresponding to two distinct values of critical fields. Above the first critical field strength, transition from a parallel lamellae to HPL occurs. Analogously, a field strength corresponding to the second critical value effectuate formation of perpendicular lamellae. At this point, it is clarified that the lamellar to HPL transition is neither an outcome of a shift in critical temperature nor of the phase boundaries from symmetric to asymmetric range. The shift in the critical temperature results from the second order expansion term of the dielectric permittivity which is currently not being considered. Further, as a precautionary measure, the volume fractions of the two blocks is tracked which are equal at all simulation timesteps.

Thus, in all fairness, the transition is facilitated by the synergistic activity of substrate affinity, confinement and electric field. In the phase diagram, the HPL morphology can be seen to stabilize at a larger substrate affinity in the region between the two critical values of the applied electric field described above. It is well worth noting that it is the preferred component (attracted by substrate) that evolves into cylindrical domains. For the cases studied here, the substrate always has a preference towards the block B resulting

in the formation of perpendicular cylindrical arrays. Interestingly, the occurrence of cylindrical phase is prolific at  $L_z = 1.5L_o$  corresponding to the maximally frustrated state of the parallel lamellae system. Thus, the role of confinement in inducing the novel morphological transition needs to be emphasized. The HPL morphology was not observed beyond a film thickness of  $L_z = 1.6L_o$ . Since one cannot rule out the possibility of HPL morphology in other bilayer films ( $L_z > 1.6L_o$ ), a finer search is warranted in the parameter space of interest ( $1.25 < E < 1.75$ ). However, the range of the occurrence of HPL is certainly diminished. Moreover, as film thickness increases beyond bilayer arrangement, it is statistically improbable that the disintegrated layers would proceed to coalesce end-to-end such that a final HPL symmetry is attained.

## 6.2.2 Lamellar to HPL transition : Kinetic Pathways

### 6.2.2.1 Transition in monolayer films (BAB)

To gain meaningful insights into the mechanistic pathway leading to the morphological transition, the temporal evolution of the blocks upon initializing from a disordered state under attracting substrate and electric field is analyzed. Initial stages of microphase separation is predominantly governed by surface energetics leading to a parallel ordering across the film thickness ( $t = 100$ , Fig. 6.4(a)). At  $t = 350$  (Fig. 6.4 (b)), the applied electric field instigates a peristaltic mode of instability in the inner layer characterized by wave-like periodic constrictions. Subsequently, this instability leads to disintegration of the inner layer followed by coalescence in the direction of field. The 2-D cuts in the  $x - y$  plane (plane perpendicular to the applied electric field) are presented in Fig. 6.4(b). The ongoing coalescence process leads to the genesis of cylindrical domains of the preferred monomer(B) in the inner layers of A matrix (Fig. 6.4(b) middle and lower row). However, the substrate stays B-rich (of non-uniform composition) characterized by hexagonal patterning owing to the inner symmetry of its layers (Fig. 6.4(a)) .

The kinetic pathways of the morphological transition can be rigorously elucidated through the Minkowski functionals [224, 225, 226, 227]. This functional provides an efficient means to characterize complex microstructures through geometric and topological quantities, which for three dimensional images are the volume  $V$ , surface area  $S$ , mean curvature  $H$  and Euler characteristic  $\chi$ . The numerical technique and calculation procedure of the Minkowski functionals are adopted from the references [224, 227]. For the sake of completeness, a brief discussion is provided; however readers are referred to previously published literature where elaborate descriptions are presented.

A black and white image is generated from the order parameter by imposing a threshold value, which in the present case is the average magnitude of the order parameter

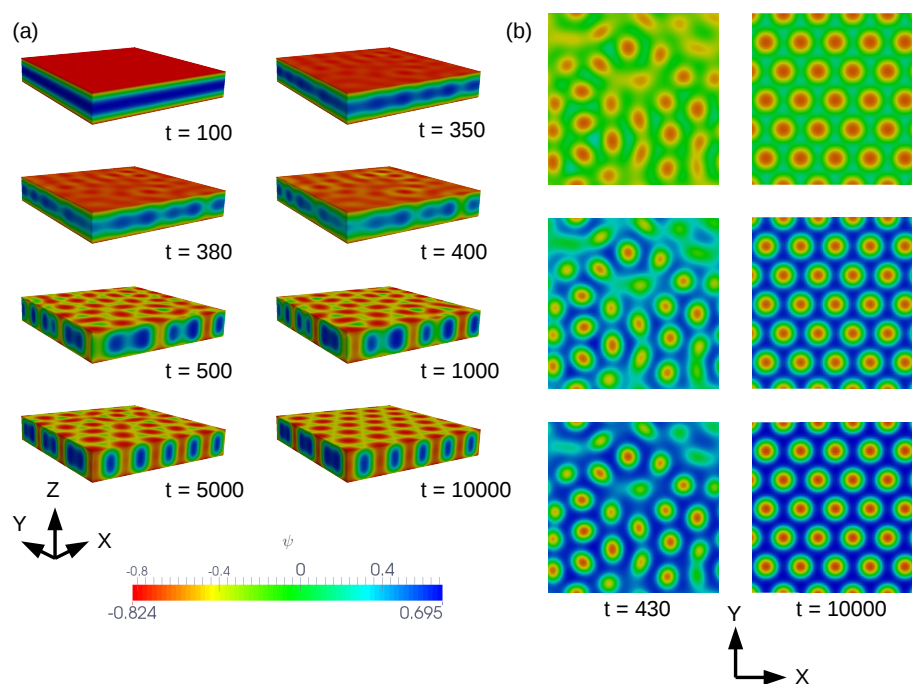


Figure 6.4: (a) Temporal evolution corresponding to  $t = 100$ ,  $t = 350$ ,  $t = 380$ ,  $t = 400$ ,  $t = 500$ ,  $t = 1000$ ,  $t = 5000$  and  $t = 10000$  for numerical parameters  $L_z = 1.2L_o$ ,  $h = 0.5$  and  $E = 2.1875$  depicting the kinetic pathway of lamellar to HPL transition in a monolayer film. (b) 2-D sectional views in  $x - y$  plane (plane perpendicular to the applied field) at  $z = 2$  (top),  $z = 4$  (middle) and  $z = 7$  (bottom) at  $t = 430$  (left column) and  $t = 10000$  (right column). Electric field induces a peristaltic instability mode in the inner layer which subsequently breaks and joins in the direction of the electric field, leading to the appearance of cylindrical domains.

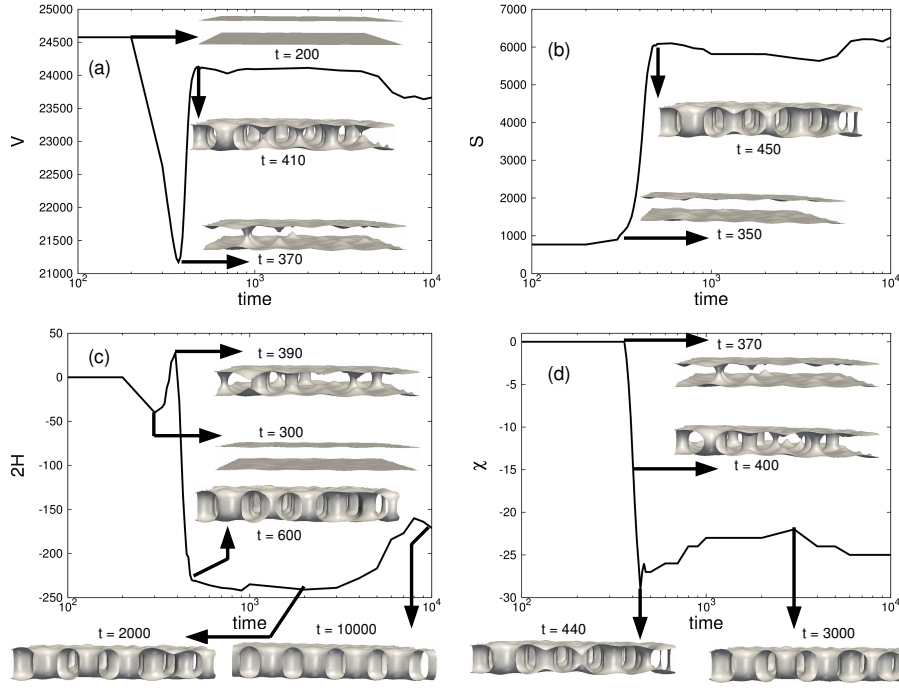


Figure 6.5: Minkowski functionals (a) volume ( $V$ ), (b) surface area ( $S$ ), (c) curvature ( $2H$ ) and (d) Euler number ( $\chi$ ) corresponding to the temporal evolution of Fig. 6.4.  $\psi = 0$  contours are also plotted alongside at representative timesteps to characterize the evolution process. Both the monomers have been rendered transparent for clarity. As evident by the contours, the temporal evolution can be categorized into two stages : Onset of peristaltic mode, followed by disintegration and coalescence, leading to the appearance of thin cylinders. This is followed by the coarsening and rearrangement of the cylinders.

( $\psi = 0$ ). The advantage of adopting such an approach in unraveling the kinetic pathways has been earlier highlighted in Ref.[227]. The number of open cubes ( $n_c$ ), number of open faces ( $n_f$ ), number of edges ( $n_e$ ) and number of vertices ( $n_v$ ) are computed by an algorithm formulated by Michielsen-De Raedt [224]. Finally, the four Minkowski functionals are calculated as,

$$\begin{aligned}
 V &= n_c \\
 S &= 6n_c + 2n_f \\
 2H &= 3n_c - 2n_f + n_e \\
 \chi &= -n_c + n_f - n_e + n_v.
 \end{aligned} \tag{6.1}$$

The temporal evolution of the four Minkowski functionals and the corresponding contour plots at representative timesteps are presented in Fig. 6.5. After an initial incubation period (until  $t = 200$ ), the electric field initiates a peristaltic mode of interface instability (similar to  $t = 350$ , Fig. 6.4). The inner layers begin to disintegrate which can

also be otherwise noted by a characteristic decrease in the volume  $V$ . The disintegration of the inner layer leads to exposed surfaces, thereby resulting in an increase of surface area  $S$  as shown in Fig.6.5(b). Meanwhile, the curvature  $2H$  first decreases from  $t = 200$  to  $t = 300$  due to initiation of the peristaltic interface instability. This is followed by a slight increase in  $2H$  to reach a maximum at  $t = 390$  due to the formation of perforations and thin cylindrical domains (Fig.6.5(c)). At this stage (at  $t = 370$ ), the Euler characteristic  $\chi$  first starts to decrease from zero to negative values depicting the formation of tunnels in the microstructure (cylinders joining the parallel layers in Fig.6.5(d)). The downward trend continues until  $t = 440$  as more and more perpendicular cylinders span across the parallel layers. The emergence of cylinders results in an increase of  $V$  ( $t = 370$  to  $t = 410$ ) indicating the reintegration of an A block. Meanwhile, the curvature  $2H$  decreases during the same time interval from ( $t = 390$  to  $t = 600$ ). In between  $t = 390$  and  $t = 600$ , the incipient cylindrical domains coarsen in the transverse direction as evident from the  $\psi = 0$  contours, resulting in a decrease of the curvature. After  $t = 1000$ , the Minkowski functionals stay predominantly unchanged for the most part, other than the occasional undulations due to the temporal rearrangement, indicating the completion of lamellar to HPL transition. The final Euler characteristic, as observed in Fig.6.5(d), is negative corresponding to a structure with many tunnels indicative of an HPL morphology.

### 6.2.2.2 Transition in bilayer films (BABAB)

The kinetic transition pathways in bilayer films is studied next. An exemplary morphological evolution is shown in Fig. 6.6. In this case, the kinetic pathway is similar to the case of monolayer films, i.e. surface induced ordering leads to incipient parallel lamellae, followed by their disruption and coalescence. However, the incubation time for the onset of the instability is observed to be different. Owing to a larger film thickness, the influence of substrate in modulating pattern formation is not as prominent leading to an early onset of the peristaltic instability in the inner layer ( $t = 200$  in Fig. 6.6 compared to  $t = 350$  in Fig. 6.4). The 2-D slices in the  $x - y$  plane are presented in Fig. 6.6(b). The disintegration of the parallel layers leads to a bicontinuous structure as seen in the 2-D sectional views at intermediate timestep,  $t = 300$  (Fig. 6.6(b) left column). The bicontinuous structure temporally evolves into circular spots of B monomer in the A matrix. It is worth noting that the radius of the spots (cylinder in 3-D) is larger at the center and decreases upon translating towards the substrate implying a shape modulation.

To comprehend the kinetic pathways, the evolution of the  $\psi = 0$  contours is tracked and analysis is performed with the help of Minkowski functionals in Fig.6.7. The temporal evolution of the Minkowski functionals are found to be different in the bilayer films, particularly the temporal variation of  $S$ ,  $2H$  and  $\chi$ . Similar to the case of monolayer

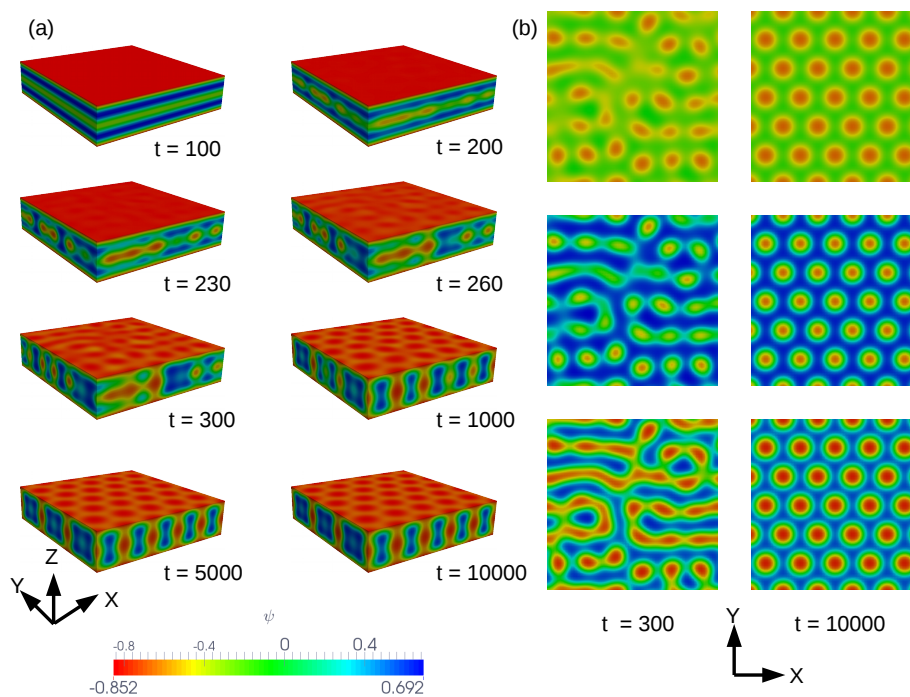


Figure 6.6: Temporal evolution corresponding to  $t = 100$ ,  $t = 200$ ,  $t = 230$ ,  $t = 260$ ,  $t = 300$ ,  $t = 1000$ ,  $t = 5000$  and  $t = 10000$  for numerical parameters  $L_z = 1.6L_o$ ,  $h = 0.5$  and  $E = 1.25$  depicting the kinetic pathway of lamellar to HPL transition in a bilayer film. (b) 2-D sectional view in  $x - y$  plane (plane perpendicular to the applied field) at  $z = 2$  (top),  $z = 5$  (middle) and  $z = 9$  (bottom) at  $t = 300$  (left column) and  $t = 10000$  (right column). The onset of instability, similar to the case of monolayer films is peristaltic where the inner layer disintegrates first and later joins the outer layers.

films, the volume  $V$  decreases while in this case surface area  $S$  increases initially owing to the disintegration of inner layer and subsequent joining leading to the formation of small neck-like regions as evident from the contour at  $t = 220$ . The formation of these connections between the inner layers lead to an increase of the curvature  $2H$  and to a decrease of the Euler number  $\chi$ . As soon as the tiny necks span across the width of inner layer,  $V$  and  $\chi$  attain minima (first local minima of  $\chi$ ) at  $t = 220$ . This is followed by a brief period of neck coalescence as highlighted by the contours at  $t = 240$  during which  $2H$  achieves a maximum, while  $\chi$  ascends towards a sharp peak. With time, the necks get aligned in the direction of electric field touching the outer layers as they continue to coarsen in the transverse direction leading to the formation of cylinders with thin interconnecting arms. At this timestep,  $S$  reaches its maximum value, while  $\chi$  plummets down to the global minimum. Obviously, the connecting arms are energetically unfavorable as the resulting interfaces are perpendicular to the direction of the applied electric field. As expected, these electrostatically penalizing junctions collapse in the next timesteps leading to a decrease in  $S$  and  $2H$  and an increase in  $\chi$ . This is followed by an in-plane rearrangement of cylinders towards hexagonal ordering as evident by more or less unaltered values of the Minkowski functionals.

A few comments regarding the differences of the kinetic pathways in monolayer and bilayer films are in order. Firstly, a comparison of the  $\chi$  curves for monolayer and bilayer films reveals that the latter has two successive sharp troughs in contrast to a unique minimum in monolayer films. This indicates that the lamellar to HPL transition in a bilayer film essentially proceeds as a two stage process. In bilayer films, the reorientation process initiates from the center of the film and proceeds outwards. The electric field initially disintegrates the inner layer which subsequently connects, indicated by the first trough in the  $\chi$  plot. As the connections get aligned in the direction of electric field, fresh joints are formed with the outer layer (alternatively viewed as perforations in the outer layer) resulting in interconnecting cylinders as also characterized by a second dip in the Euler number ( $\chi$ ). Secondly, the decreasing  $S$  stage is another distinguishing feature in the kinetic pathways of bilayer and monolayer films. On the contrary, the surface area saturates after reaching a pinnacle in monolayer films as a result of the evolution of well defined cylinders. However, the cylinders in bilayer films initially have interconnecting arms which later disintegrate causing a decreasing  $S$  upon the attainment of peak value. It is re-emphasized, that the kinetic pathway characterized by evolution of interconnecting cylinders is solely a feature specific to bilayer films.

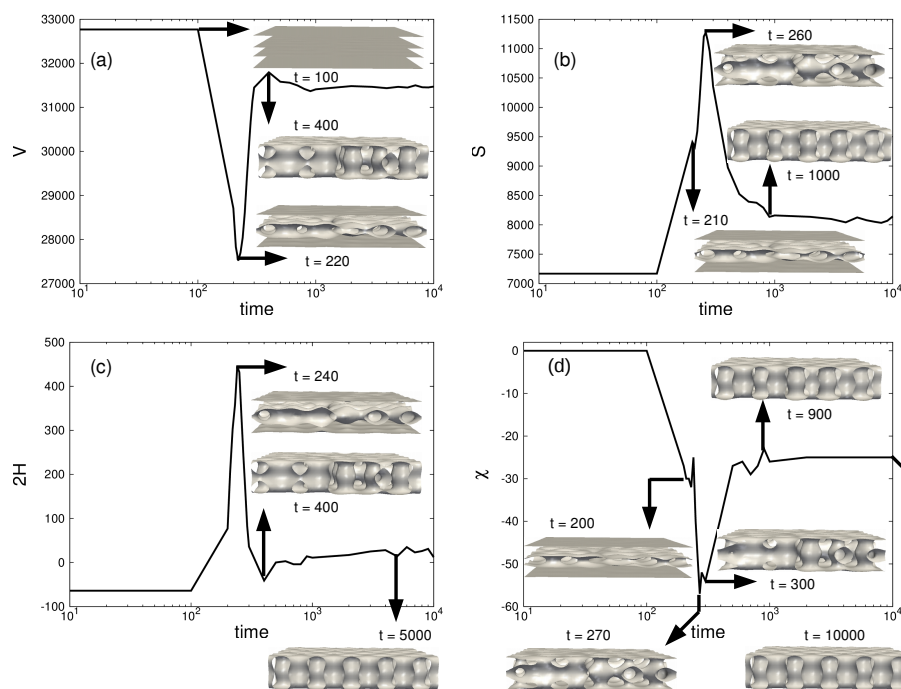


Figure 6.7: Minkowski functionals (a) volume ( $V$ ), (b) surface area ( $S$ ), (c) curvature ( $2H$ ) and (d) Euler number ( $\chi$ ) corresponding to the temporal evolution of Fig. 6.6.  $\psi = 0$  contours are also presented along the graph at representative timesteps to characterize the evolution process. Both the monomers have been rendered transparent for clarity. Unlike the case of monolayer films, the cylinders that form at an intermediate stage in the present case possess interconnecting arms. However, these electrostatically unfavorable junctions disintegrate and rearrange at later stages into a well-defined cylindrical arrays.

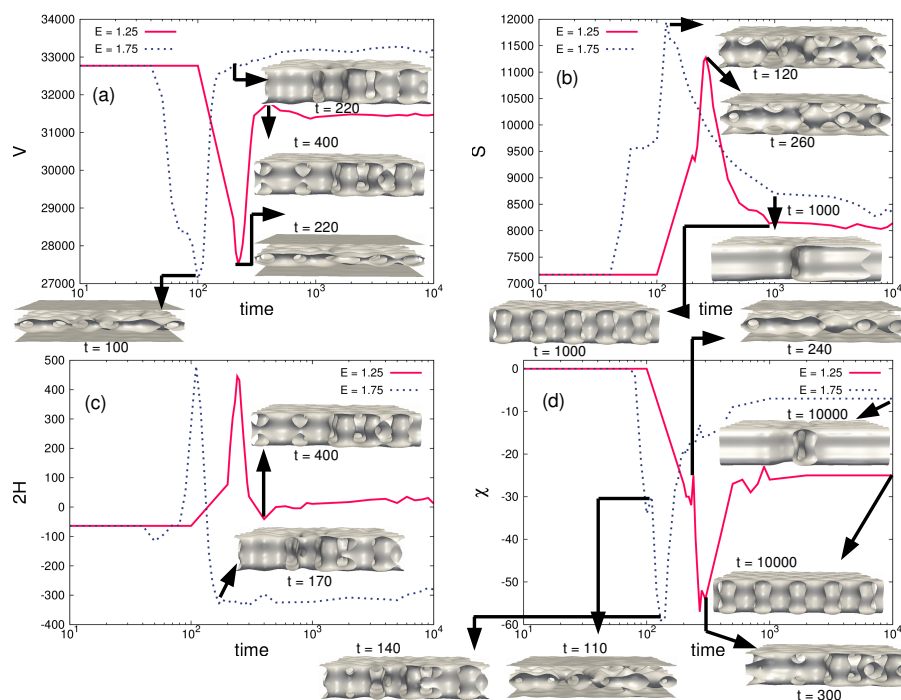


Figure 6.8: Comparison of the kinetic pathways between parallel lamellar to HPL transition ( $E = 1.25$ ) and parallel to perpendicular lamellar transition ( $E = 1.75$ ) using Minkowski functionals. The onset of the transition is faster at larger electric field strength. The initial stages of the transition are indiscernible (other than a difference in the timescale) in both cases where by cylinders with interconnecting arms evolve at an intermediate state. However, it is at this juncture that the kinetic pathways diverge from one another. At larger electric field strengths, the cylinders coalesce to form perpendicular lamellae while, at lower field strengths the interconnecting arms collapse forming cylindrical domains.

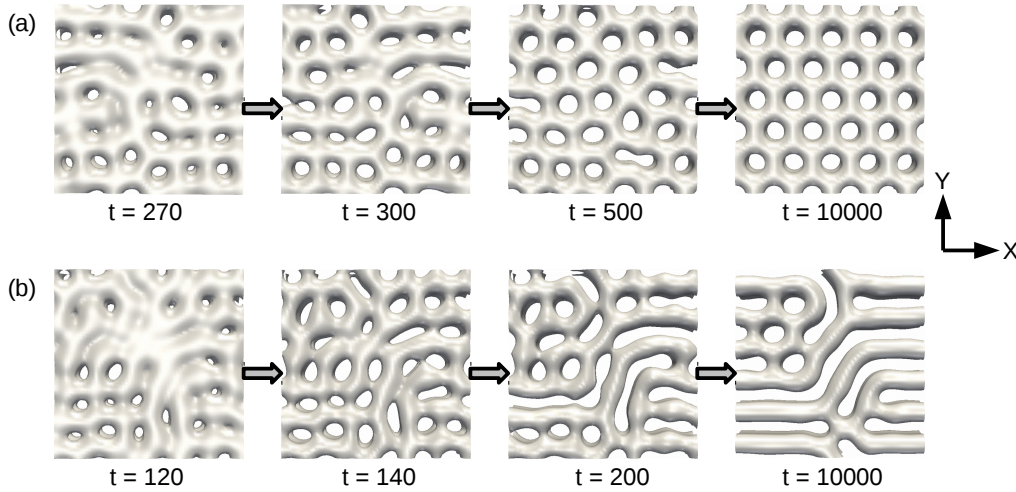


Figure 6.9: Overhead view corresponding to (a)  $L_z = 1.6L_o$ ,  $h = 0.5$  and  $E = 1.25$  and (b)  $L_z = 1.6L_o$ ,  $h = 0.5$  and  $E = 1.75$  depicting the development of perforations (cylinders in the center) at representative timesteps. At lower electric field, the perforations rearrange into hexagonal ordering. Larger field strengths, initially ensues a perforated intermediate structure. These perforations, however, coalesce forming perpendicular lamellae.

### 6.2.2.3 Perforated lamellae as an intermediate stage in parallel lamellar to perpendicular lamellar transition

The next question that naturally arises is how does the kinetic pathway for parallel to perpendicular lamellar transition differ from that of parallel lamellar to HPL transition in thin films? Do cylinders at all form at any stage of parallel to perpendicular lamellae transition? The answer is indeed affirmative as evident from the comparison of kinetic pathways discussed below.

As the kinetic pathways of bilayer films are more complex, the evolution of Minkowski functionals at two electric field strengths in Fig. 6.8 are compared. The plots correspond to  $E = 1.25$  where the parallel lamellae to HPL transition occurs and  $E = 1.75$ , where perpendicular lamellae evolve. Upon comparing the two cases, the evolution timescale is observed to be different though the pathway itself seems to be similar. Naturally, at a higher field strength the incubation period, i.e. the time before the onset of the transition is much shorter. During the initial stages of transition, the height of the peaks and troughs of the Minkowski functionals are nearly the same. As implied from the previous discussion of the kinetic pathways, these minima and maxima correspond to the formation of cylindrical domains with interconnections. It is only at the later stages that both the pathways diverge from one another, i.e. during the ascent of  $V$  and  $\chi$  and descent of  $2H$  and  $S$ . The quantities  $V$ ,  $S$  and  $\chi$  saturate at a higher value of the field strength  $E = 1.75$ , while the curvature  $2H$  settles down at a lower value.

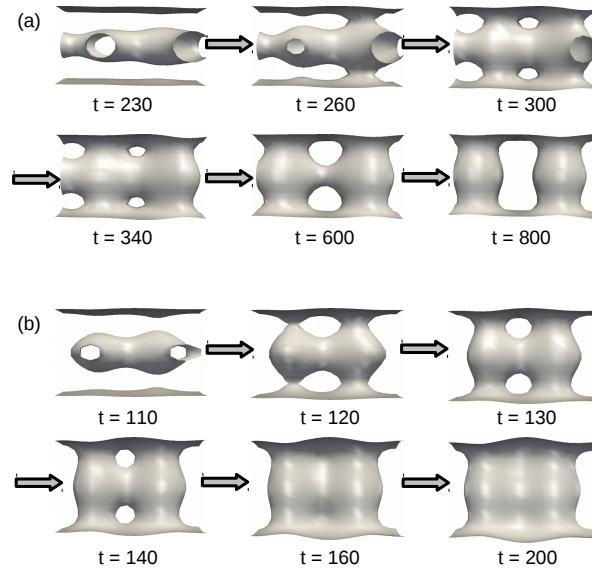


Figure 6.10: A small section of the entire simulation domain corresponding to (a)  $L_z = 1.6L_o$ ,  $h = 0.5$  and  $E = 1.25$  and (b)  $L_z = 1.6L_o$ ,  $h = 0.5$  and  $E = 1.75$  illustrate the cylinder splitting and merging events at representative timesteps

The disparate  $\chi$  values at different field strengths indicate topologically distinct BCP structures.  $\chi = -25$  corresponds to a HPL morphology i.e. surfaces with a number of passages, while the one with  $\chi = -7.5$  corresponds to a perpendicular morphology with a few defects. The overhead view is presented in Fig. 6.9 which depicts the kinetic mechanism by which perpendicular lamellae evolve from an intermediate perforated lamellae structure. At low electric field strengths, the initial perforations emerge, which are uneven in shape. These perforations temporally coalesce, coarsen and simultaneously undergo an inplane rearrangement into a hexagonal ordering. However, at larger electric field strengths, perforated lamellae evolve at an intermediate stage, which later coalesce to form perpendicular lamellae. A representative region of the simulation domain illustrating the merging and splitting phenomena is presented in Fig. 6.10. At low field strengths, the reorientation process results into an interconnected cylindrical domain. With time the interconnecting arms become thinner, and ultimately split to form isolated cylinders. However, at larger field strengths, the intermediate cylindrical domains that evolved ultimately merge leading to perpendicular lamellar morphology. Another point worth noting is the number of timesteps required to attain the respective final morphologies at different electric field strengths. Typically it is observed that a splitting event is comparatively slower than the merging process.

### 6.3 Discussion and Concluding Remarks

The presence of substrate affinity and confinement can markedly influence the electric-field-induced transition in monolayer and bilayer films. The simulations were initialized from a disordered state under the confluence of electric field and attracting substrate. Owing to the smaller film thickness, the surface-induced ordering is almost instantaneous (Fig. 6.4(a), 6.6(a)) leading to a parallel ordering. The dominating influence of electric field only sets in after a certain incubation period. Even if the simulation domain is initialized from a parallelly ordered lamellae (such as in Fig. 6.4(a), 6.6(a)) the final structure is found to be invariant. Thus, parallel lamellar to HPL transition can be considered as one of the variants of a broad spectrum of previously reported electric-field-induced-OOT as mentioned earlier. HPL phase, however, is not observed in the absence of substrate affinity. Furthermore, lamellar to HPL transition changes our perspective of the phase diagrams in symmetric BCPs. Previous numerical [56, 57] and analytical studies [55, 56] have reported parallel, perpendicular and mixed lamellae in symmetric block copolymers under the confluence of attracting substrates and electric field. Morphologies possessing a distinct symmetry (in a symmetric BCP) as the one reported in this article have never been previously reported.

Stability of monolayer [228] and multilayer films [158] subjected to a perpendicular electric field was investigated by Matsen using a self-consistent field theory. However, substrate affinity was not accounted for in strict sense. A cylindrical morphology was shown to form as an intermediate structure during parallel to perpendicular lamellar transition in monolayer films, when the instability was peristaltic [228]. The present simulations, on the other hand, emphasize the role of substrate affinity in stabilizing the HPL structure (and thus the cylindrical domains).

The relative stability of two morphologies in presence of electrostatic field and substrate affinity can be estimated thermodynamically by comparing the free energies as done in previous works [55, 56] for simple geometries such as parallel, perpendicular and mixed lamellar systems. The stability of a given morphology is dependent upon the magnitude of electric field  $E$ , the difference of the interfacial energy of the block and substrate  $\gamma_{AS} - \gamma_{BS}$  (which is equivalent to the model parameter  $h$ ) where,  $\gamma_{AS}$  and  $\gamma_{BS}$  represent the interfacial energies between a given block and the substrate and the dielectric constants of the two blocks. Of course, for strained films incommensuration effects such as lamellar contraction and expansion also needs to be taken into consideration. Moreover, for other intermediate morphologies such as mixed lamellae, interfacial energy at the junctions need to be accounted, additionally. Although, accounting for interfacial energy is straightforward for simple geometries [55, 56], extension of the same approach to complex geometries is non-trivial. However, heuristically, a dominant substrate interaction

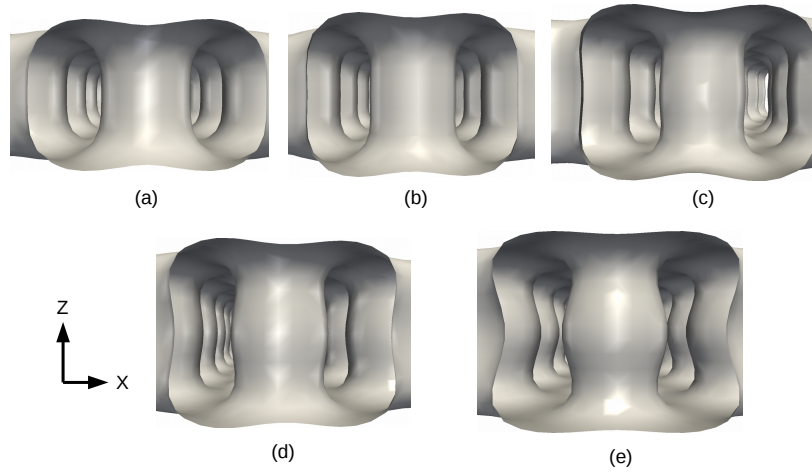


Figure 6.11: Shape modulation of the cylindrical domain for different film thicknesses,  $L_z$  : (a)  $1.2L_o$ , (b)  $1.3L_o$ , (c)  $1.4L_o$ , (d)  $1.5L_o$  and (e)  $1.6L_o$ . The magnitude of electric field corresponds to the highest strength for the respective film thickness as depicted in Fig. 6.3, where HPL morphology is stable.

facilitates a parallel ordering and a larger contribution from the electrostatic term will stabilize perpendicular arrangement. Moreover, it is also essential to examine the nature of competing external fields. Substrate interaction is typically a short-ranged field, while the electrostatic field is long-ranged. The influence of substrate affinity is localized close to confining substrates. On the contrary, electric field uniformly spans over the entire film thickness. Based on the above arguments, application of large electric fields can induce morphological transition to a lower energy state such as perpendicular lamellae, as shown in Figs. 6.2 and 6.3. Additionally, there exists a maximum permissible film thickness above which, transition to mixed lamellae configuration, is feasible, as reported in a number of previous studies [55, 56, 57, 53]. The film thicknesses considered in the present study are, however, lower than surface ordering length and the presence of substrate has a strong influence on the entire film. Transition to HPL morphology is a third possibility that has been explored. HPL structure, similar to the mixed lamellae, can be considered as an intermediate morphology comprising of parallel and perpendicular domains. Modulation to HPL morphology minimizes the electrostatic free energy via formation of perpendicular cylindrical channels, while the region in the immediate vicinity of the substrate is predominantly occupied by the preferred component so as to minimize interfacial energy. HPL morphology is shown to evolve in thin films and is presumably absent in thicker films because of short-ranged characteristic of the substrates.

An important implication of the reported lamellar to HPL transition is that it enhances the composition range where the occurrence of HPL morphology can be anticipated. Moreover, technologically, long standing perfectly ordered cylindrical arrays are

highly desirable in the fabrication of scaffolds, templates and memory storage devices [220, 221]. It is worth mentioning that cylindrical arrangement do not always manage to attain a perfect hexagonal ordering. Specifically, the HPL structures belonging to parallel lamellar to HPL transition region are defect-laden. To rule out the possibility of finite size effects, additional simulations with larger system size ( $L_x = L_y = 128\Delta x$ ) were performed without noting any appreciable changes (not shown here). The imperfect ordering can thus be attributed to the lower magnitude of the applied electric field incapable of supplying sufficient driving force for rearrangement. However, for most film thicknesses, a well-ordered structure resulted at electric field strengths closer to the HPL-perpendicular lamellar transition. Secondly, the predominant instability modes (due to the applied electric field) also determines whether the final structure is defect prone. Generally, there are two competing interface instability modes, namely peristaltic and undulatory characterized by out of and in phase undulations respectively of the inner lamellae. The kinetic pathway accompanying peristaltic mode leads to structures which are less prone to defects as opposed to the undulatory mode that gives rise to undesirable grain boundaries [228]. For the intermediate segregation regime considered in the present study, the peristaltic mode is dominant (as exemplified in Fig. 6.4 and 6.6) and as a result the structures are usually less prone to defects. However, in strong segregation regime, the undulatory mode predominates over peristaltic mode and the resulting structures are expected to be defect-laden (with a distinct possibility that the resulting structure may not even be HPL). Moreover, as an intermediate structure, HPL provides a more smoother transition pathway from parallel to perpendicular lamellae, thereby, leading to a final structure that is relatively free from defects.

In electric-field-induced OOTs, where the resultant morphology consists of cylinders (such as parallel to perpendicular cylinder [60], sphere to cylinder [57] or hexagonally perforated lamellar to cylinder [52]), shape modulations are generally observed. The shape modulations in the previous studies were attributed to varying substrate affinities as well as different values of the electric field strengths. Additionally, shape modulations depending upon film thickness were observed in the present study. Comparison of cylinder as a function of film thickness at same field strength is not possible. However, as mentioned before, since the most symmetric structures prevail at largest field strengths for a given film thickness, the respective structures (Fig. 6.11) are chosen for comparison. The shape modulation is a result of the HPL phases occurring at a symmetric composition. In monolayer films, the central layer is always A-rich because of the preferential affinity of B component for the substrate. As a result, for  $L_z = 1.2L_o$ , the cylinder is concave-shaped (thinner at the center). As the film thickness is progressively increased towards a bilayer configuration, the inner region becomes B-rich, with the cylinders displaying a significant distortion (bulge) at the center. The shape at  $L_z = 1.6L_o$  is concave closer to

the substrate to maximize the surface coverage, while maintaining a convex shape at the middle to conserve the overall volume fraction.

Another repercussion of electric-field-induced HPL transition is that it allows one the freedom to fabricate cylindrical channels of the desired block in a symmetric system. The substrate can be coated by a suitable compound (usually a random copolymer) such that it preferentially bonds with one of the blocks and thereby facilitate a parallel ordering. Upon application of electric field, the preferentially attracted block will evolve into cylindrical domains. A further comment on the magnitude of electric field strengths required for triggering such a morphological transition is in order. Multiplying the non-dimensional values of electric field in Fig. 6.3 by  $82V/\mu m$ , representative values of around  $76-180V/\mu m$  is obtained. The upper limit is actually quite high and may well exceed the dielectric breakdown limit of the polymeric system. However, field strengths of around  $120V/\mu m$  have been applied in recent experiments [71]. Moreover, a small dielectric mismatch between the two blocks ( $\epsilon_A = 3$ ,  $\epsilon_B = 2$  and  $\Delta\epsilon = 1$ ) has been chosen in the present work. A larger mismatch such as in the case of PS-PMMA system ( $\epsilon_{PMMA} = 6$ ,  $\epsilon_{PS} = 2.5$ ) lowers the field strengths (by a factor of  $\frac{\sqrt{\epsilon_A + \epsilon_B}}{\epsilon_A - \epsilon_B}$  [55, 56]). In such cases, a further reduction in the field strength can be achieved by placing the component with larger dielectric constant at the center [228].

To summarize, electric field, substrate affinity and confinement was shown to instigate a parallel lamellar to HPL transition in symmetric BCP thin films. HPL was found to be stable in film thickness range  $L_z = 1.2 - 1.6L_o$ . All, but  $L_z = 1.6L_o$  correspond to monolayer films. Incidentally,  $L_z = 1.6L_o$  is the only bilayer film where the HPL evolves as a stable phase.

## **Part IV**

**Results and Discussion :**

**Grain boundary grooving due to  
electromigration**

# Chapter 7

## Theory of thermal grooving : Comparison between phase-field simulations and Mullins' theory

### 7.1 Introduction

In this chapter, the phase-field model and its numerical implementation is benchmarked with the sharp-interface analytical theory of thermal grooving by Mullins [122] for isolated grooves i.e. for infinite grains. Grooving refers to the progressive deepening of the grain-boundary (GB) free surface intersection. When an initial flat surface is taken to an elevated temperature one of the many mass transport mechanisms such as surface diffusion [122], volume diffusion [123], evaporation-condensation [122] amongst others are activated. The present discussion is restricted to the mass transport mechanism solely by surface diffusion. At the elevated temperature, an initial groove develops at the surface-GB intersection (Fig.7.1) as a result of the system trying to attain the equilibrium dihedral angle, resulting in the reduction of GB length, while expelling material onto the surface. This results in formation of ridges as shown in Fig.7.1, instigating a curvature-gradient along the surface which further provides the impetus for mass flux by flattening the ridges. This momentarily upsets the dihedral angle resulting in further deepening of the groove by transporting material to the surface. Thus, the process of grooving goes on indefinitely.

Grooving is an ubiquitous phenomenon and has been extensively observed and studied in bicrystals of copper [229], tungsten [230], molybdenum [231], platinum/alumina interface [232], GB triple junctions of magnesia polycrystal [233], singular surfaces of Ni-rich NiAl [234], Ni-films on sapphire substrates [116] among several others. GB grooving

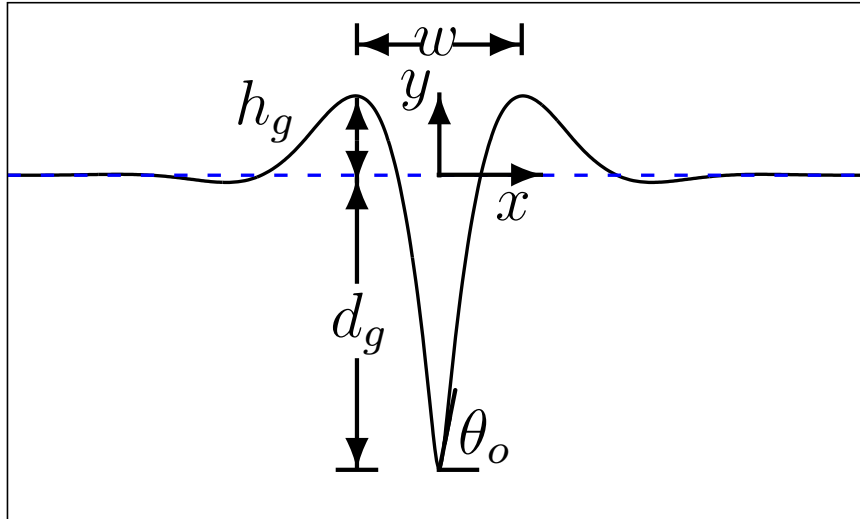


Figure 7.1: A schematic depicting the grain boundary groove along with the relevant groove characteristics.  $d_g$  represents the groove depth relative to the initial flat surface.  $h_g$  is the mass pile-up height above the flat surface. The groove width  $w$  is the distance between the abscissa of the maximum of the profile on either side of the grain boundary.  $\theta_o$  denotes the angle between the tangent and horizontal axis at the groove root.

leads to stagnation of grain growth in polycrystalline thin films where a large number of boundaries terminate on a surface [235, 236, 237]. GB grooving is responsible for microstructural degradation in form of thin film break up [238] and hole formation [239] in polycrystals. Grooving has also been reported in polycrystalline materials with internal voids such as solid-oxide fuel cells [240, 241, 242].

The mathematical treatment of GB grooving under surface diffusion was pioneered by Mullins which is revisited next. Only the basic steps of the derivation are listed and the complete derivation can be found in Ref. [122, 243]

## 7.2 Sharp-interface relations

Assume a surface profile  $y(x, t)$  in a Cartesian coordinate system evolving due to surface diffusion because of gradients in chemical potential. The chemical potential of an atom due to presence of curvature is given by [244],

$$\mu = \mu_o + \Omega\gamma_s\kappa_s, \quad (7.1)$$

where  $\mu_o$  represents the chemical potential of a flat surface,  $\Omega$  the atomic volume,  $\gamma_s$  the surface energy and  $\kappa_s$  denotes the curvature which is given by  $\kappa_s = -\frac{y''}{(1+y'^2)^{3/2}}$ . The

notation ' denotes the derivative w.r.t  $x$ . The surface flux induced due to curvature gradient reads as,

$$J_s = -\nu M \frac{\partial \mu}{\partial s}, \quad (7.2)$$

where  $\nu$  denotes the surface concentration of the atoms given by  $\nu = \frac{\delta_s}{\Omega}$  and  $M$  the atomic mobility which as per the Nernst-Einstein relation is given by  $M = \frac{D_s}{k_B T}$  and  $s$  denotes the arc length. Substituting Eq.(7.1) in Eq.(7.2) we get,

$$J_s = -\frac{\nu D_s \Omega \gamma_s}{k_B T} \frac{\partial \kappa}{\partial s} \quad (7.3)$$

where,  $\frac{\partial}{\partial s} = \frac{\partial}{\partial x} \frac{\partial x}{\partial s}$  and using  $\frac{\partial x}{\partial s} = \frac{1}{(1+y'^2)^{1/2}}$  yields,

$$J_s = \frac{\nu D_s \Omega \gamma_s}{k_B T} \frac{1}{(1+y'^2)^{1/2}} \frac{\partial}{\partial x} \left( \frac{y''}{(1+y'^2)^{3/2}} \right) \quad (7.4)$$

The mass conservation equation along the surface relates the surface flux divergence to the normal velocity as,

$$\frac{dJ_s}{ds} = -\frac{V_n}{\Omega} \quad (7.5)$$

Utilizing Eq.(7.4) we get,

$$V_n = -\frac{D_s \delta_s \Omega \gamma_s}{k_B T} \frac{1}{(1+y'^2)^{1/2}} \frac{\partial}{\partial x} \left( \frac{1}{(1+y'^2)^{1/2}} \frac{\partial}{\partial x} \left( \frac{y''}{(1+y'^2)^{3/2}} \right) \right) \quad (7.6)$$

A simple geometric projection of the normal velocity yields  $V_n = \frac{\partial y}{\partial t} \frac{1}{(1+y'^2)^{1/2}}$  (derivation is provided in appendix B) which on substitution in Eq.(7.6) leads to the kinetic equation of the surface profile as,

$$\frac{\partial y}{\partial t} = -B \frac{\partial}{\partial x} \left( \frac{1}{(1+y'^2)^{1/2}} \frac{\partial}{\partial x} \left( \frac{y''}{(1+y'^2)^{3/2}} \right) \right), \quad (7.7)$$

where  $B = \frac{D_s \delta_s \Omega \gamma_s}{k_B T}$  is the Mullins' constant. As evident, Eq.(7.7) is a highly non-linear partial differential equation (PDE) and as such difficult, if not impossible to obtain a closed form solution analytically. It is to be noted that the maximum slope of the profile corresponds to the root. To obtain a closed form solution, the above PDE can be linearized according to Mullins by employing SSA such that  $(y')^2 \ll 1$ . This linearization procedure reduces Eq.(7.7) to,

$$\frac{\partial y}{\partial t} = -B y'''''. \quad (7.8)$$

The above PDE is solved under the following initial and boundary conditions [122],

(i) the initial surface is flat i.e.,

$$y(x, 0) = 0.$$

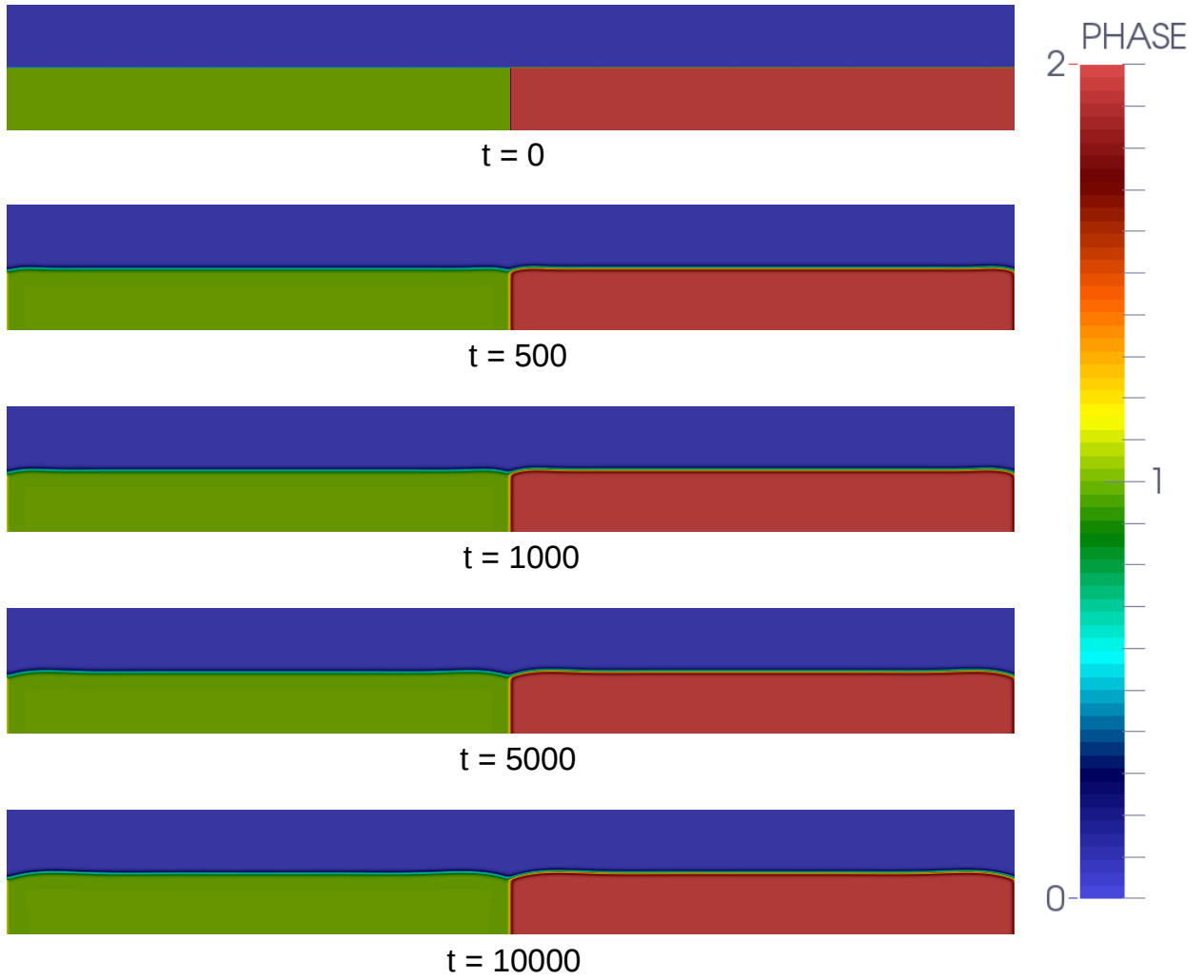


Figure 7.2: Temporal evolution a grain boundary groove obtained from phase-field simulation of an initial flat bicrystal.

(ii) constant slope at the root which under SSA translates into,

$$y_x(0, t) = m = \tan \theta_o .$$

(iii) continuity of the flux at the root that dictates no matter is transported along the GB, which under the small slope approximation (SSA) according to Eq.(7.4) reads as,

$$y_{xxx}(0, t) = 0 .$$

The Eq.(7.8) facilitates an analytical solution by using an integral transform such as Laplace or Fourier transform. Mullins solved the PDE employing a Laplace transform in time. However, Ref. [243] is followed and the PDE is solved utilizing Fourier cosine transform in space. The basic steps to attain the solution is as follows,

(i) Take cosine Fourier transform in space,

$$\frac{\partial y_c}{\partial t} = -BF_c[y_{xxxx}] \quad (7.9)$$

where,

$$\begin{aligned} y_c &= \int_0^\infty y(x, t) \cos(kx) dx \\ F_c[y_{xxxx}] &= \int_0^\infty y_{xxxx} \cos(kx) dx \end{aligned} \quad (7.10)$$

(ii) Integrate the r.h.s of Eq.(7.9) utilizing the Eq.(7.10), successively by parts and employing the boundary conditions leading to an ODE,

$$\frac{\partial y_c}{\partial t} = -Bk^2m - Bk^4y_c \quad (7.11)$$

(iii) Integrate via separation of variables and evaluate the integration constant from the initial condition to obtain,

$$y_c = -\frac{m}{k^2} \left[ 1 - \exp(-Bk^4t) \right] \quad (7.12)$$

(iv) Apply inverse transform to obtain the solution as,

$$y(x, t) = \frac{2}{\pi} \int_0^\infty y_c \cos(kx) dk. \quad (7.13)$$

The equation is readily inverted at  $x = 0$  as,

$$y(0, t) = -\frac{2m}{\pi} \int_0^\infty \left[ 1 - \exp(-Bk^4t) \right] \frac{dk}{k^2} \quad (7.14)$$

Integrating by parts and using the definition of gamma function  $\Gamma(z) = \int_0^\infty x^{z-1}e^{-x} dx$  the temporal deepening of the groove follows,

$$\begin{aligned} y(0, t) &= -\frac{m}{\sqrt{2}\Gamma(5/4)}(Bt)^{1/4} \\ &= -0.78m(Bt)^{1/4} = d_g \end{aligned} \quad (7.15)$$

The other important relations that can be derived at the root are,

$$\begin{aligned} y_x(0, t) &= m \\ y_{xx}(0, t) &= -\frac{m}{\sqrt{2}} \frac{(Bt)^{-1/4}}{\Gamma(3/4)} \\ y_{xxx}(0, t) &= 0 \end{aligned} \quad (7.16)$$

The second derivative at the root is evaluated in a similar manner by first taking the cosine Fourier transform followed by the inversion at the root.

- (v) Since the temporal evolution of the groove depth follows a  $t^{1/4}$  law according to Eq.(7.15), Mullins assumed a general solution of the form,

$$y(x, t) = m(Bt)^{1/4}Z(u) \quad (7.17)$$

where  $u = x/(Bt)^{1/4}$ . Substituting the partial derivatives of the solution in the PDE (7.8) the following ODE is obtained,

$$Z_{uuuu} - \frac{u}{4}Z_u + \frac{Z}{4} = 0 \quad (7.18)$$

Substituting a power series solution of the form  $Z(u) = \sum_{n=0}^{\infty} a_n u^n$ ,

$$\sum_{n=0}^{\infty} n(n-1)(n-2)(n-3)a_n u^{n-4} - \frac{1}{4} \sum_{n=0}^{\infty} n a_n u^n + \frac{1}{4} \sum_{n=0}^{\infty} a_n u^n = 0 \quad (7.19)$$

The coefficients can be determined by Frobenius method by equating the coefficients of same powers of  $u$  on both sides. However the first four coefficients are determined from Eqs.(7.15) and (7.16) as,

$$\begin{aligned} a_0 &= -\frac{1}{2^{1/2}\Gamma(5/4)} \\ a_1 &= 1 \\ a_2 &= -\frac{1}{2^{3/2}\Gamma(3/4)} \\ a_3 &= 0 \end{aligned} \quad (7.20)$$

The coefficients from the fourth term onwards can be evaluated from the recursive relation given by,

$$a_{n+4} = a_n \frac{n-1}{4(n+1)(n+2)(n+3)(n+4)} \quad (7.21)$$

## 7.3 Results

To benchmark the phase-field model with the analytical theory of Mullins, a bicrystalline set-up with an initial flat surface with a dihedral angle of  $\pi$  is chosen. The simulation set-up is shown in Fig.4.1(c). All the respective order parameters are assigned their respective equilibrium values and the system is allowed to evolve only under the action of surface diffusion. This is done by assigning  $M_s = 1$  and  $M_B = M_{GB} = 10^{-6}$ .

The temporal evolution of the groove obtained from phase-field simulation is shown in Fig.7.2. To distinguish between the vapor phase and the various grains of the solid

Table 7.1: Values of coefficients

$a_o$	$-7.803 \times 10^{-1}$
$a_1$	$10.000 \times 10^{-1}$
$a_2$	$-2.886 \times 10^{-1}$
$a_4$	$8.130 \times 10^{-3}$
$a_6$	$-2.004 \times 10^{-4}$
$a_8$	$3.625 \times 10^{-6}$
$a_{10}$	$-4.969 \times 10^{-8}$
$a_{12}$	$5.339 \times 10^{-10}$
$a_{14}$	$-4.655 \times 10^{-12}$

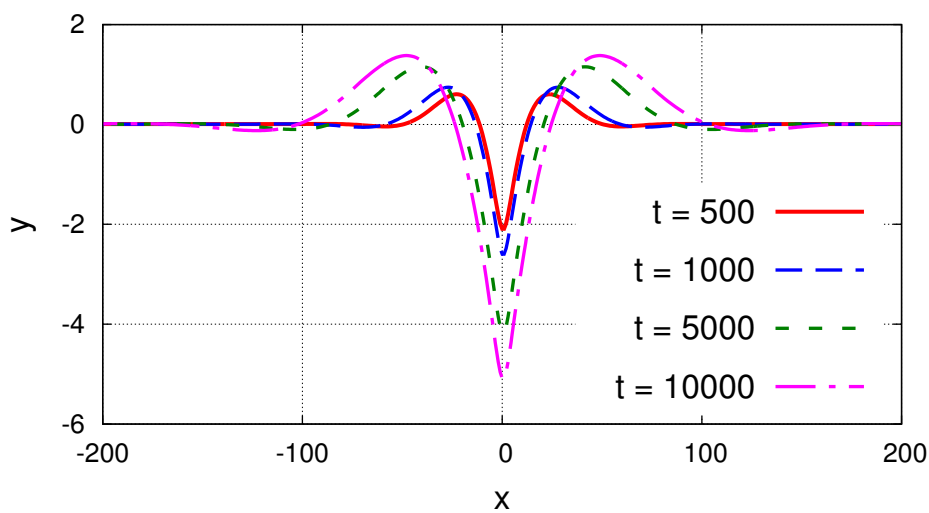


Figure 7.3: Temporal evolution of the surface obtained from the  $\rho = 0.5$  isoline. The phase-field simulations faithfully capture the maximum in the groove profile followed by a characteristic dip below the initial flat surface which is not predicted by Mullins' theory.

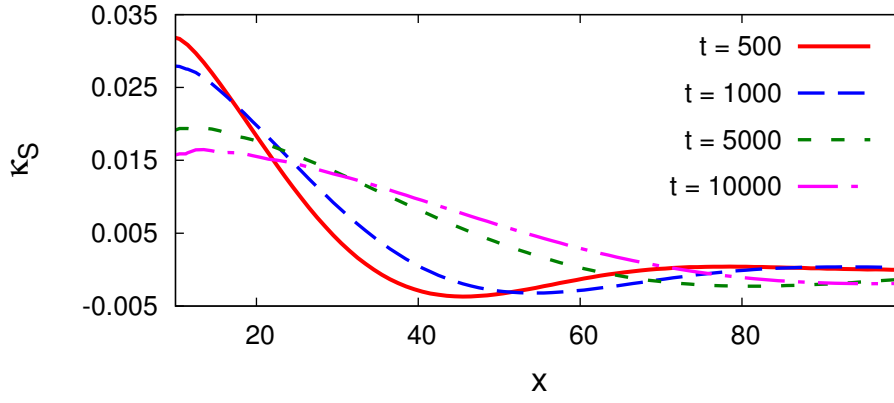


Figure 7.4: Variation of the curvature along the surface corresponding to the profiles in Fig.7.3 at different times.

phase the quantity  $\Phi = \sum_{i=1}^N i\eta_i$  is plotted. The temporal deepening of the groove along with the formation of ridges is evident in Fig.7.2. Since, the free surface in the present phase-field model is defined as the region where  $0 < \rho < 1$ , the  $\rho = 0.5$  isoline is shown in Fig.7.3 for the better assessment of the grooving process. The grooving initiates such that the dihedral angle as dictated by the surface energy  $\gamma_s$  and GB energy  $\gamma_{GB}$  is attained. This leads to mass transport from groove root towards the surface resulting in a pile-up (surface ridge). Subsequent groove deepening and widening take place under the action of curvature gradient-induced surface diffusion. The profiles exhibit a characteristic dip below the initial flat surface following the ridge.

Since, the process of thermal grooving is essentially a capillary-driven phenomenon, the variation of the mean curvature  $\kappa_s$  is plotted in Fig.7.4, to gain insights on the mass transport along the surface. Convex regions are denoted by positive sign and concave by negative. Therefore mass transport takes place from regions of high curvature to low in convex regions and vice-versa in concave regions. In other words, direction of mass transport follows from convex to concave regions. Thus at  $t = 500$ , atomic transport ensues towards the dipped region of the profile (the concave region) from either sides (convex regions). As a result of the mass transport, the concave region shifts towards the right overtime and the curvature at the vicinity of the root decreases as evident in Fig.7.4 at  $t > 1000$ . The decline of the curvature-gradients along the surfaces decreases the driving force for further grooving due to which the deepening continues but with an ever decreasing rate.

In deriving the analytical shape of the groove a boundary condition in terms of the equilibrium dihedral angle at the root was employed. Thus, it is necessary to validate whether the dihedral angle is correctly reproduced in the profiles obtained from phase-field simulations. Care must be taken to locate the groove root from the phase-field

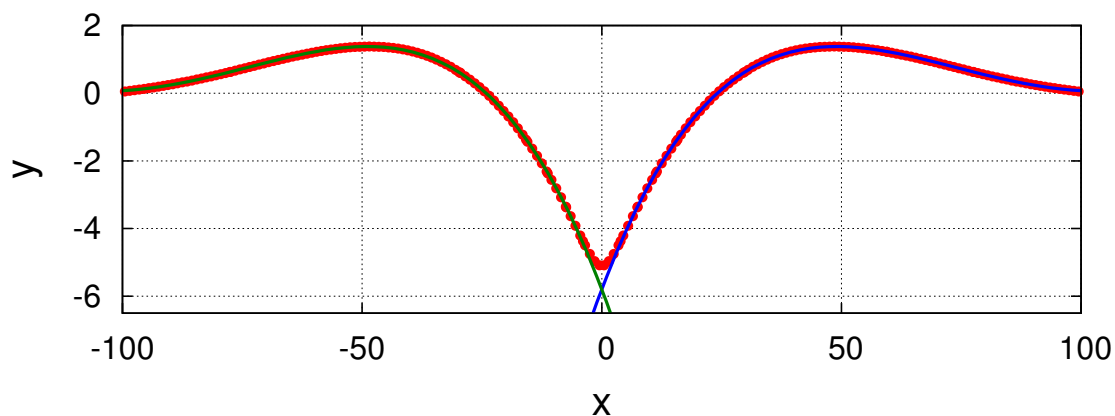


Figure 7.5: Measurement of the slope at the root from the groove profile. Profiles on either side of the GB are fitted with a fourth order polynomial.

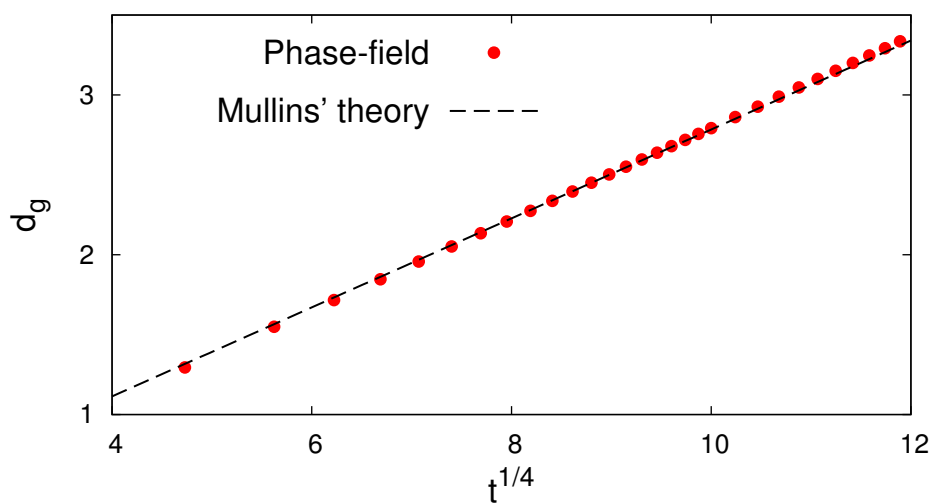


Figure 7.6: A comparison of the temporal evolution of the groove depth measured from the initial flat surface. The points correspond to data obtained from phase-field simulations where as the dashed line represents the analytical expression  $d_g = 0.78m(Bt)^{1/4}$  from Mullins' theory.

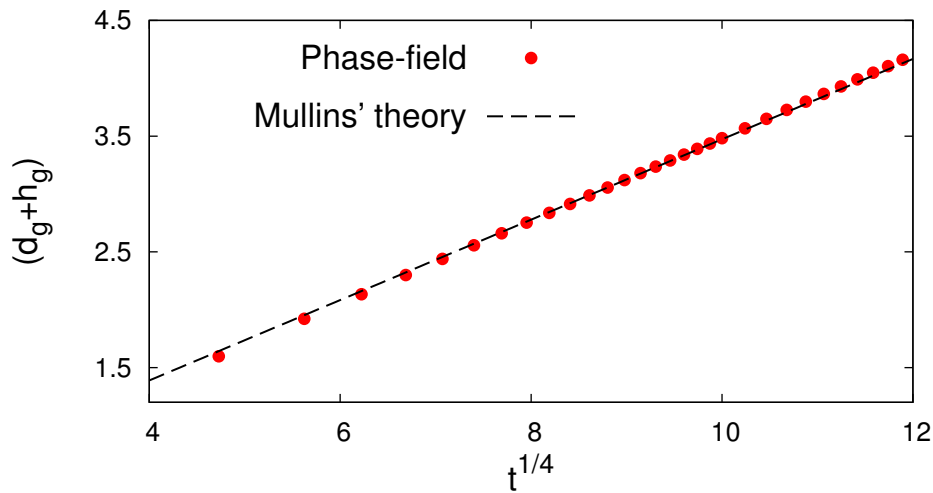


Figure 7.7: A comparison of the temporal evolution of the groove depth measured from the surface maximum. The points correspond to data obtained from phase-field simulations where as the dashed line represents the analytical expression  $(d_g + h_g) = 0.93m(Bt)^{1/4}$  from Mullins' theory.

simulations. In the sharp interface solution, invoking the symmetry of the problem about the groove root, only a single branch on the either side of the root is calculated. The other branch is obtained as the mirror image of the former and both branches intersect at a single point at the root. In the phase-field solution, however, due to the diffuse nature of the GB, both branches rather than intersecting sharply forms a blunt concave region. This is purely an artifact of the phase-field method. In order to locate the groove root precisely, we fit the  $\rho = 0.5$  level set on the either side of the GB by fourth order polynomial leaving out the points in the interfacial region. The root is defined as the intersection point of the fit. Consequently, while comparing to the sharp interface solution, the phase-field profile is adjusted such that the root obtained from the intersection is placed at  $y = 0$ . The fitted curve is shown in Fig. 7.5. The slope at the intersection point is calculated to be  $20.46^\circ$  which is close to the theoretical value of  $19.87^\circ$ .

A comparison of the groove depth  $d_g$  relative to the initial flat interface obtained from the phase-field method to that given by Eq.(7.15) is made next. The groove depth from the phase-field simulations are measured from the point of intersection of the fitted curve. The comparison of the groove depth between the sharp-interface and phase-field method is shown in Fig.7.6 where an excellent agreement between both the methods is observed.

Information regarding temporal evolution of other groove characteristics such as the maximum of the profile can also be found from Eq.(7.17). For instance, assuming

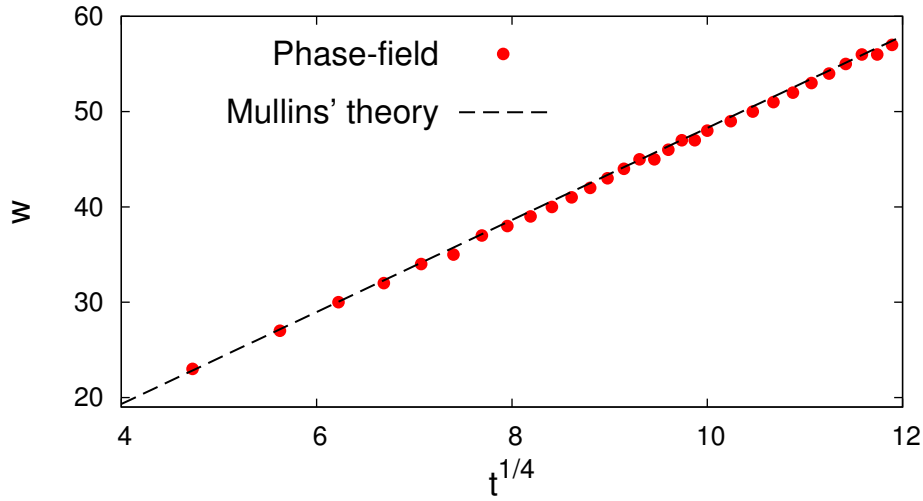


Figure 7.8: A comparison of the temporal evolution of the groove width. The points correspond to data obtained from phase-field simulations where as the dashed line represents the analytical expression  $w = 4.6(Bt)^{1/4}$  from Mullins' theory.

$(Bt)^{1/4} = 1$  the normalized groove profile can be written as,

$$\frac{y}{m} = Z(x) \quad (7.22)$$

The value of  $x$  at which the curve peaks can be evaluated by finding the roots of derivative of  $Z(x)$ . It can be shown that the curve attains a maximum at  $x = 2.3$ . Since, all the dimensions follow a  $t^{1/4}$  law, the temporal evolution of the groove width follows,

$$w = 4.6(Bt)^{1/4}. \quad (7.23)$$

It can also be shown that ordinate corresponding to  $x = 2.3$  i.e.  $Z(2.3) = 0.193$ . Since, the  $y$ -axis is normalized by a factor of  $m$ , the temporal evolution of the groove depth relative to the surface maximum ( $d_g + h_g$ ) follows,

$$d_g + h_g = 0.973m(Bt)^{1/4} \quad (7.24)$$

A comparison of the temporal law given by Eqs.(7.24) and (7.23) and that obtained from the simulations is given in Figs.7.7 and 7.8 respectively. The phase-field method is able to faithfully capture the behavior of the sharp-interface relations.

Since, all the groove dimensions namely the groove depth and width, follow a  $t^{1/4}$ , the profiles should exhibit time invariance. This can also be asserted by rearranging Eq.(7.17) as,

$$\frac{y}{t^{1/4}} = mB^{1/4}Z\left[\frac{1}{B} \frac{x}{t^{1/4}}\right] \quad (7.25)$$

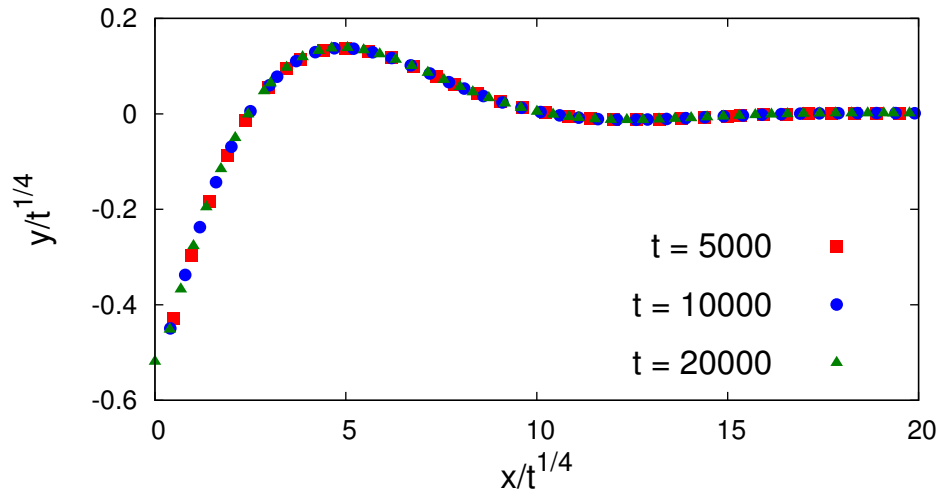


Figure 7.9: Self-similar behavior of the groove profile obtained from phase-field simulations. Since all the relevant length scales along  $x$  and  $y$  direction follow a  $t^{1/4}$  temporal behavior the axes have been scaled accordingly.

The dynamic scaling of the groove profiles evident from the collapse of the profiles at different times into a single curve is shown in Fig.7.9 where the axes have been scaled by the factor  $t^{1/4}$ .

The self-similar behavior of the profiles can also be interpreted in another way as follows. Rearranging Eq.(7.17) as

$$\frac{y}{m(Bt)^{1/4}} = Z\left[\frac{x}{(Bt)^{1/4}}\right] \quad (7.26)$$

Since the relevant dimensions in  $y$  and  $x$  directions are the groove depth and width respectively, the above Eq. can be written in terms of  $d_g$  and  $w$  from Eqs.(7.15) and (7.23) as,

$$\frac{y}{d_g/0.78} = Z\left[\frac{x}{w/4.6}\right] \quad (7.27)$$

The above normalization renders the profiles time invariant. The resulting normalized profiles are plotted in Fig.7.10 where the dynamical scaling of the curves is evident.

The advantage of normalizing the profiles by the latter procedure is that it facilitates a direct comparison with Mullins' solution as given in Fig.3 of Ref.[122]. A comparison of the normalized profile from Mullins and the phase-field method is shown in Fig.7.11. Both the solutions are in excellent agreement, with the phase-field profile predicting the minimum ( $x = 0$ ), the first zero of the profile ( $x = 1.14$ ), the maximum ( $x = 2.3$ ) and the point of inflection ( $x = 3.43$ ) with reasonable accuracy. This completes the benchmarking procedure of the phase-field model and its numerical implementation.

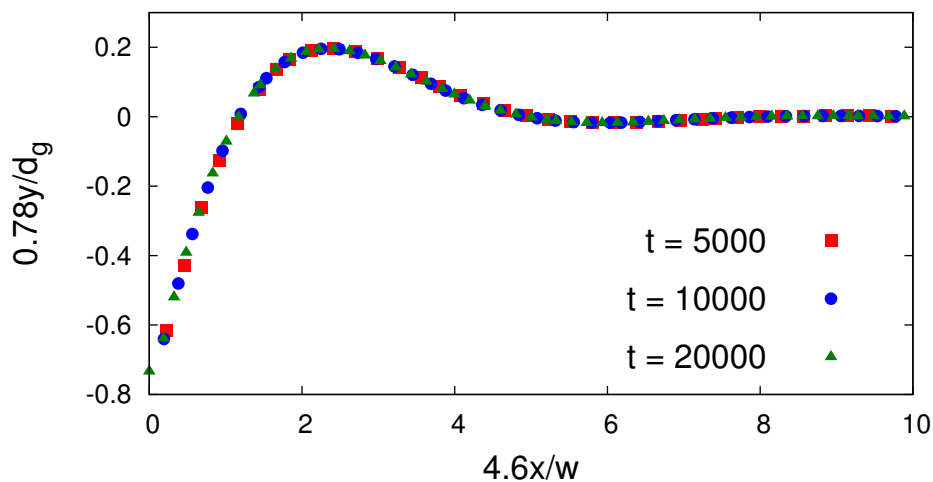


Figure 7.10: Self-similar behavior of the groove profile obtained from phase-field simulations. The  $x$  and  $y$  axes have been scaled by  $w/4.6$  and  $d_g/0.78$  respectively.

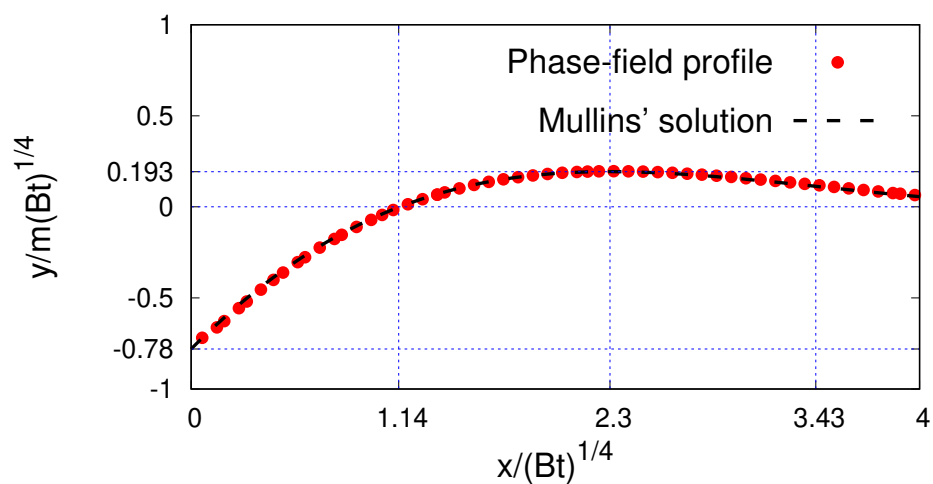


Figure 7.11: A comparison of the solution of the normalized profile obtained from phase-field simulation (points) and Mullins' theory (dashed line).

Table 7.2: Values of numerical parameters and the corresponding interfacial energies

$A$	$B$	$C$	$\kappa_\rho$	$\kappa_\eta$	$\gamma_s$	$\gamma_{GB}$	$\theta_o$
1	0.33	3	1	0.33	0.532	0.238	$13^\circ$
1	1	1	1	0.33	0.588	0.40	$20^\circ$
1	1	1	1	1	0.728	0.705	$30^\circ$
1	2	1	1	1	0.824	0.967	$36^\circ$

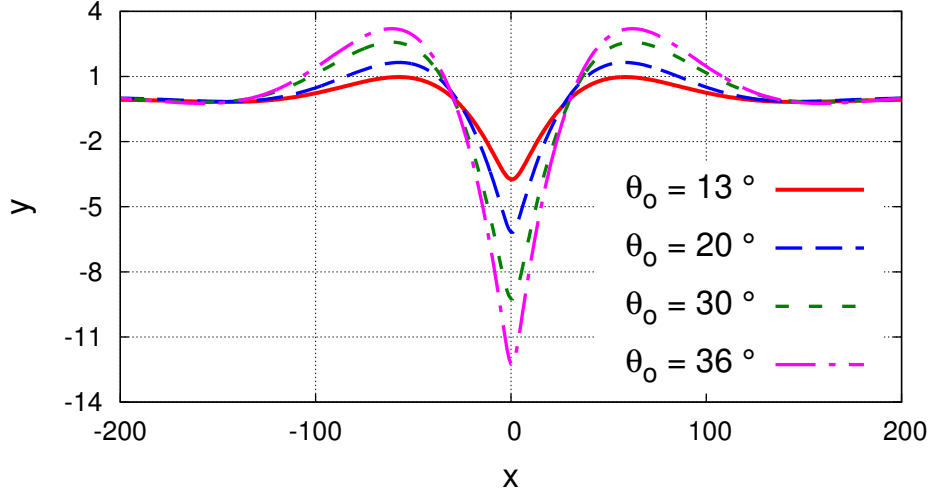


Figure 7.12: Effect of the slope at the root  $m(= \tan \theta_o)$  on the groove profile. Increasing  $m$  increases the groove depth. All the groove profiles correspond to  $t = 20000$ .

We next examine the effect of  $m(= \tan \theta_o)$  specifically the effect of SSA on grooving kinetics in Fig.7.12. The angle at the groove root is altered by manipulating the numerical parameters  $A, B, C, \kappa_\rho, \kappa_\eta$ , which in turn controls  $\gamma_s$  and  $\gamma_{GB}$ . The values of the numerical parameters and the corresponding angles at the root are provided in the Table 7.2. With increasing slope, the groove depth increases which is qualitatively in accordance with Eq.(7.15). The groove width shows a marginal increment with increasing  $m$  as evident from the shifting of the maximum of the profile of the positive branch towards right (and towards left of the negative branch). Although Eq.(7.23) predicts invariance of width on  $m$ , the increase can be attributed to the increasing value of  $\gamma_s$  which expedites the grooving process by increasing the kinetic coefficient  $B$ .

To quantify the effect of SSA quantitatively, the comparison of the groove depth obtained by analytical Eq.(7.15) and phase-field method is presented in Fig.7.13. Until about  $\theta_o = 20^\circ$  (i.e.  $m = 0.36$ ) the SSA and hence the linearized problem provides a reasonable estimate of the groove depth as seen from a good agreement between the two solutions. Deviations arise for the cases of  $\theta_o = 30^\circ(m = 0.577)$  and  $36^\circ(m = 0.726)$

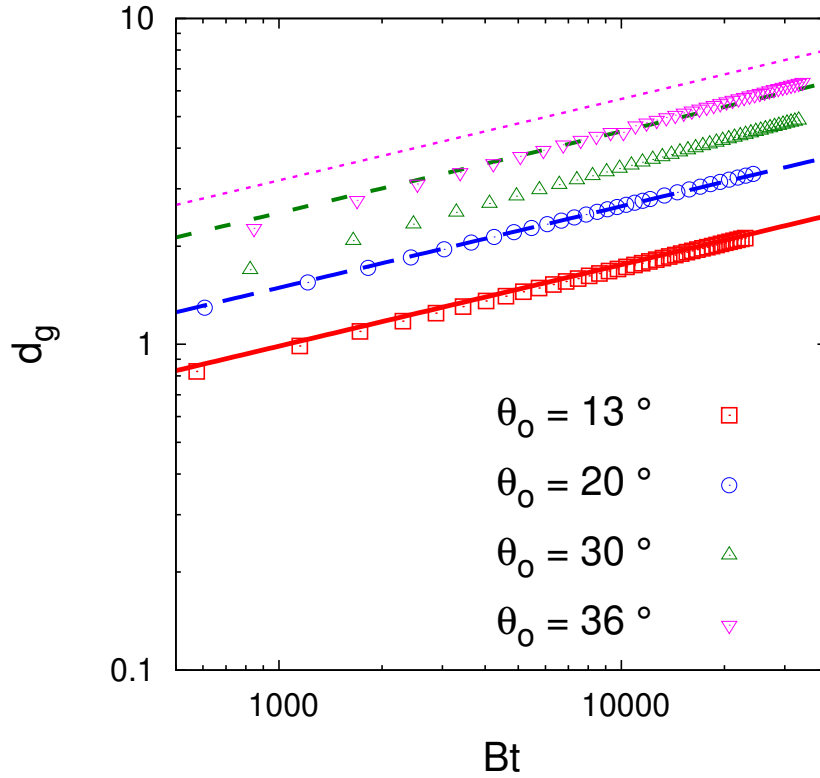


Figure 7.13: Effect of slope at the root on the groove depth. Higher values of  $\theta_o$  leads to deviation of the phase-field solution (points) from Mullins' analytical solution (lines).

where the groove depth obtained from the numerical solution is lower than analytical expression of Mullins by about 15%. The groove width, on the other hand is relatively independent of  $m$  in accordance with Mullins as shown in Fig.7.14. Interestingly both groove depth and width follow  $(Bt)^{1/4}$  temporal law even if the SSA is violated.

## 7.4 Discussion and Concluding remarks

The phase-field model is validated against Mullins' sharp-interface theory. A remarkable agreement between Mullins' theory and phase-field solution in terms of both the shape of the profile and the temporal evolution of the groove depth and width is observed. However certain key differences between the analytical theory and phase-field method warrant a further discussion. Firstly to make the solution analytically tractable, a SSA ( $m < 0.2$ ) was employed in the sharp-interface theory. The phase-field method, however, is not restricted by such an approximation and grooves of slope with an even higher value of  $m$  can be simulated with reasonable accuracy. The  $\gamma_s$  and  $\gamma_{GB}$  selected in the present study result in  $m = 0.3615$  which clearly violates the SSA. In spite of the violation, all the groove dimensions follow the small slope analytical solution of Mullins. The agreement

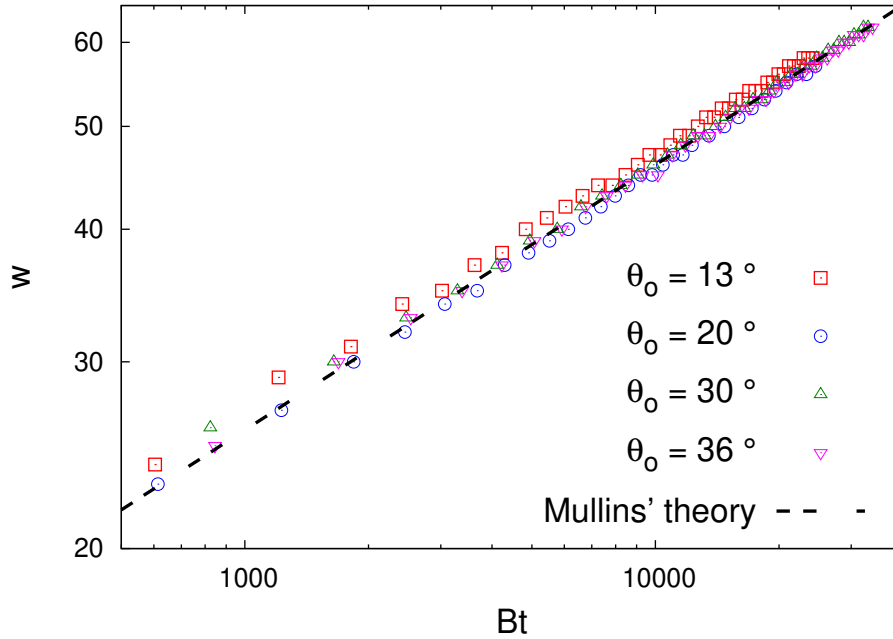


Figure 7.14: Effect of slope at the root on the groove width. The groove width is invariant to change in  $\theta_o$ . A good agreement with the analytical solution is also evident.

at higher  $m$  indicates that the analytical solution obtained from linearized eq. 7.8 serves as an excellent approximation of the complete non-linear Eq.(7.7).

In fact, the complete solution of the non-linear PDE for  $m$  ranging from 0 – 4 was obtained numerically by Robertson [245]. A deviation of about 10% from the Mullins' prediction of groove depth was reported for  $m > 0.7$ . However until  $m \leq 0.3$  which is close to the present case, the small slope solution was found to be a good approximation. A similar conclusion was also made by Zhang and Schneibel [246] in their finite difference numerical solution of GB grooving and by level set simulation of Khenner et al.[247].

A second interesting feature of the profile obtained from the phase-field method is the presence of a characteristic dip below the flat surface following the maximum. Such a dip is not predicted by Mullins' solution (because of the truncation of the series solution to 14 terms), but the possibility of which was advocated by Hillert in a private communication [122]. The numerical solution by Robertson [245], Zhang and Schneibel [246] and Khenner et al. [247], similar to the present phase-field method also exhibits a dip.

The dip is a characteristic signature of groove evolving under the action of surface diffusion. The evolution of grooves under volume diffusion was also simulated using the phase-field method by assigning  $M_B = 1$  and  $M_s = M_{GB} = 10^{-6}$  i.e. with a constant atomic mobility. As evident in Fig. 7.15, the volume diffusion-mediated groove does not sink below the flat surface following the maximum. Thus, the dominant mass transport

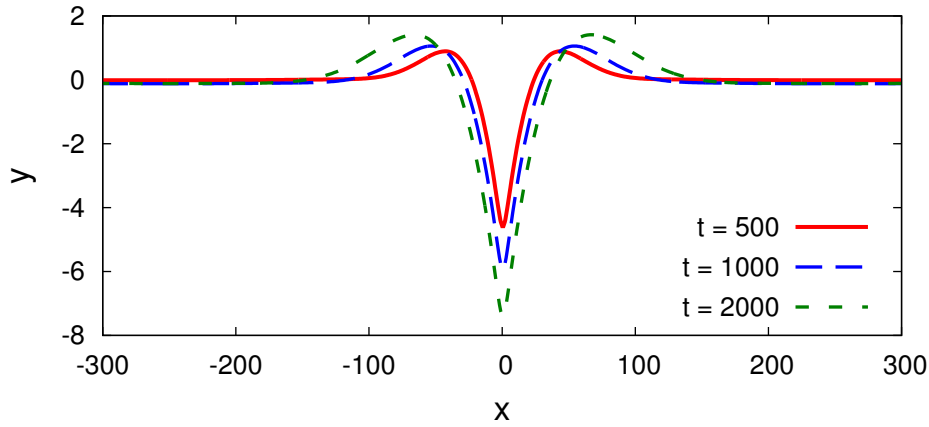


Figure 7.15: Temporal evolution of the grooves under the action of volume diffusion. Unlike the surface-diffusion-mediated grooves, the volume-diffusion-driven groove profiles do not exhibit a minimum following the ridge.

mechanism can be asserted from the shape of the profiles. In a related work Mullins derived the groove shapes under the influence of volume diffusion [123]. A critical comparison with Mullins' theory, however, is outside the scope of the present work.

Another modeling consideration that warrants a discussion is on the selection of the GB relaxation parameter,  $L_\eta$ . Due to the construction of the phase-field model, the evolution of the surface is governed by both Cahn-Hilliard and Allen-Cahn equation because of the gradients in both types of order parameters  $\rho$  and  $\eta_i$  across the surface. However, it is to be noted that the two equations give rise to two different geometric limits, namely, motion by surface laplacian of the curvature or surface diffusion (due to variable mobility Cahn-Hilliard Eq.) and motion by mean curvature or attachment-detachment kinetics (due to dynamics of Allen-Cahn Eq.) which are governed by the parameters  $M_s$  and  $L_\eta$ . In the present case, the appropriate law dictating the interface motion is surface diffusion. To fulfill this purpose, for a given  $M_s$ ,  $L_\eta$  needs to be chosen high enough such that the dynamics of Allen-Cahn Eq. is faster and the interface motion is diffusion-controlled rather than attachment-detachment. The effect of  $L_\eta$  on the shape of profiles for  $M_s = 1$  is shown in Fig.7.16. The shapes of the profiles are quite different for  $L_\eta = 0.001$  and  $0.01$  as compared to  $L_\eta = 0.1$  and  $1$ . Specifically, the profile corresponding to  $L_\eta = 0.001$  does not exhibit a prominent maximum. Although the profile for  $L_\eta = 0.01$  does exhibit the ridges on either side of the groove, the characteristic dip below the surface is absent in both profiles corresponding to  $L_\eta = 0.001$  and  $0.01$ . Other checks with  $M_s = 0.1$  and in terms of kinetics of grooving were also made (see Fig.7.17) and it was generally observed that for the present phase-field model  $M_s \geq 0.1L_\eta$  resulted in profiles independent of  $L_\eta$ . Although  $L_\eta$  could be selected to be a very high value, the restriction of small timestep width associated with higher values of  $L_\eta$  should also be

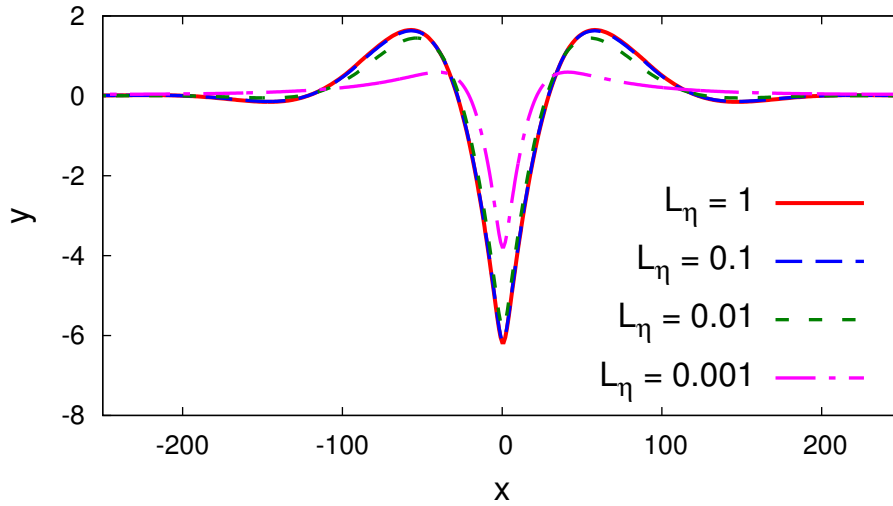


Figure 7.16: Temporal evolution of the grooves due to surface diffusion for different values of  $L_\eta$ . For smaller values of  $L_\eta$ , the profiles do not exhibit the dip below the original flat surface.

considered.

The present model is the diffuse-interface counterpart of the sharp-interface kinetic Eqs. of Cahn and Taylor [196], in that it combines motion by the two above mentioned geometric laws and thus can be efficiently employed to model phenomena that couples these laws such as concurrent grooving and grain growth in thin polycrystalline films [237, 248]. There,  $L_\eta$  can be chosen based on the considerations discussed above or by decoupling grooving and grain growth kinetics by making  $L_\eta$  to be position-dependent by enslaving it to the order-parameters  $\rho, \eta_i$  similar to the mobility function. Such a method has been employed in Ref.[207].

To summarize, the phase-field model is validated for surface diffusion-mediated GB grooving by a critical comparison with Mullins' solution. The model can be further applied to study other relevant metallurgical phenomenon which are governed by surface diffusion, for instance, sintering [249, 250], morphological stability of multilayer thin films [129, 251, 252], Rayleigh instability in solid state [253, 254, 255] amongst others.

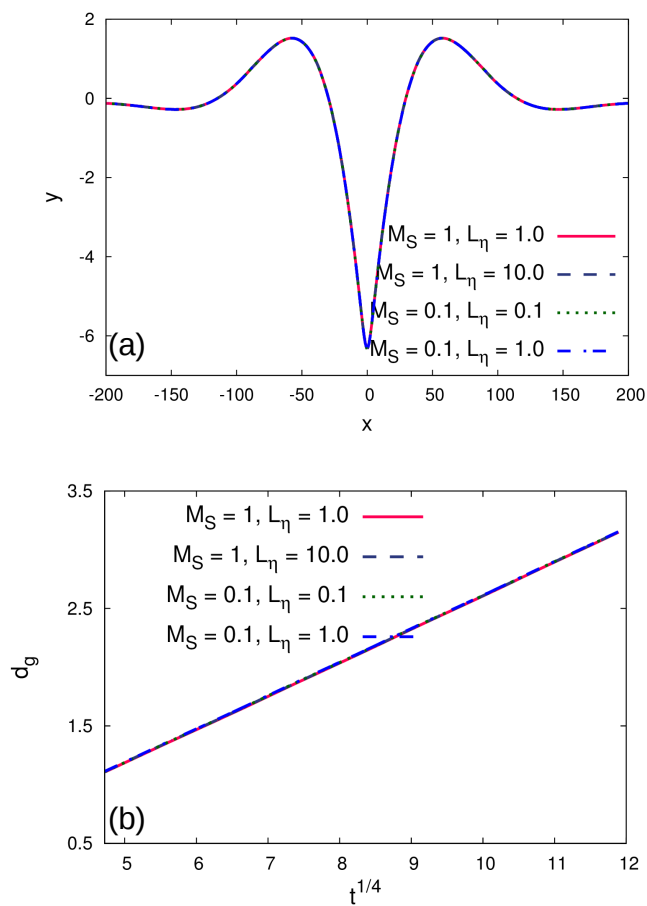


Figure 7.17: Temporal evolution of the (a) grooves due to surface diffusion and (b) groove depth for different combinations of  $M_S$  and  $L_\eta$ .

# Chapter 8

## Electromigration-induced surface drift and slit propagation in polycrystalline interconnects

### 8.1 Introduction

In the present chapter, the phase-field model of chapter 4 is employed to assess the role of surfaces and grain-boundaries as potential EM pathways.

While surface EM has garnered much attention [92, 136, 137], investigations on the influence of concurrent surface and GB diffusion on EM are rather limited [134]. As to how the surfaces and GBs participate in the damage proliferation is still a concern for the electronic industry. The numerical simulation results of damage initiation at GB grooves corresponding to the two rate limiting transport mechanisms is presented in Sec. 8.2. The results reveal that the concurrent surface and GB transport can drastically alter the damage modes and subsequent damage propagation depending upon the rate limiting transport mechanism. Synergy between our numerical findings and previous analytical and experimental observations are also discussed. Furthermore, implications of grain size distribution and coarsening on the damage initiation in polycrystalline interconnects are highlighted. Sec. 8.3 concludes the chapter.

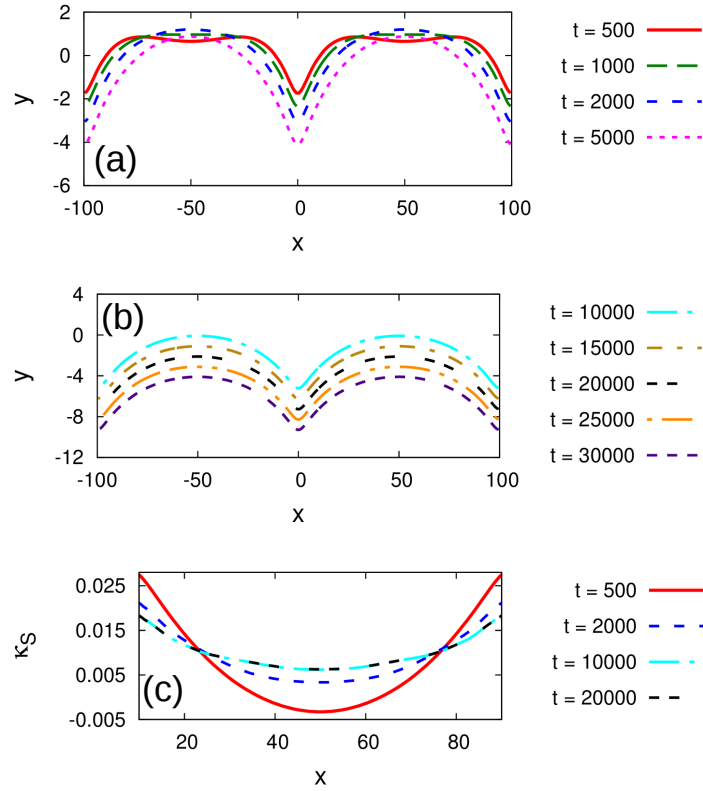


Figure 8.1: Temporal evolution of the groove profiles in GBDLR corresponding to (a) early and (b) late stages. Tails of neighboring grains merge to form circular arcs. Subsequently, the surface drifts in the direction of electron wind. (c) Curvature along the groove profile. The surface drifts preserving the shape as apparent from a constancy of curvature for  $t > 10000$ .

## 8.2 Results

### 8.2.1 GB diffusion-limited regime (GBDLR)

To begin with, the evolution of grooves when surface diffusion is faster or comparable to the GB diffusion is considered such that  $M_S/M_{GB} = 2$  where  $M_S$  and  $M_{GB}$  are the atomic mobilities in the surface and GB respectively.

#### 8.2.1.1 Morphological evolution

The evolution of the GB grooves at the triple junctions under the concurrent influence of capillarity and EM is shown in Fig. 8.1(a). A curvature-driven surface diffusion ensues from surface ridges (larger curvature), towards the grain center (smaller curvature). Temporal evolution of curvature, of the grain surface,  $\kappa_s$ , is plotted in Fig. 8.1(c). Eventually, the tails of the neighboring grooves overlap, elevating the depression at the grain

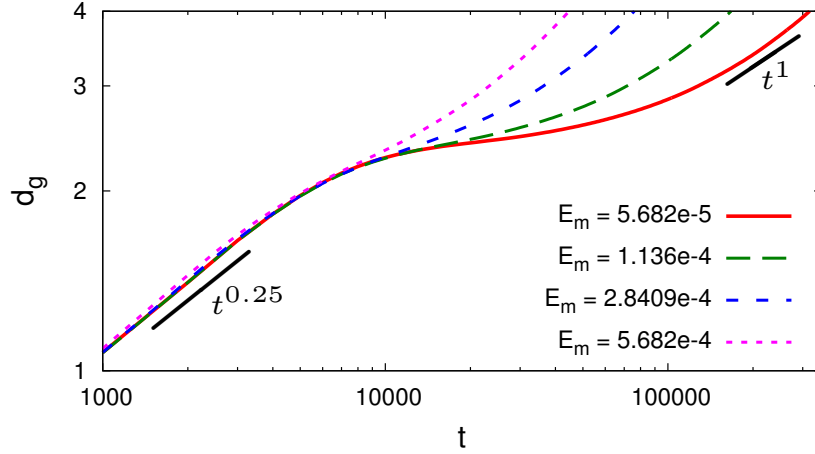


Figure 8.2: (a) Displacement-time curve at different field strengths for grain size of  $2L = 200\Delta x$  in GBDLR. Higher electric field facilitates the steady-state regime.

center. This elevation is characterized by a flattening of the curvature profile near the grain center due to the formation of a near semi-circular surface. As soon as the circular arc evolves, the grains start drifting in the direction of electron wind (Fig. 8.1(b)) which is reminiscent of the Blech-type drift velocity experiments [75, 87, 89]. Overlapping surface curvature profiles observed at larger time-steps suggest that the grains preserve their shape as they drift.

### 8.2.1.2 Grooving-Drift characteristics

The kinetics of groove displacement is measured from the temporally-evolving displacement of the groove root,  $d_g$ , relative to the initial flat surface. Two distinct regimes corresponding to initial grooving and subsequent drift are discernible in Fig. 8.2. During the grooving stage, no significant difference in the groove displacement is observed. A non-linear power fit of the form  $k_1 + k_2 t^n$  results in a temporal exponent of  $n = 1/4$ . The presence of EM does not alter the exponent which has also been predicted for thermal grooves [122], indicating that the initial stage is predominantly capillary driven. This capillary-mediated grooving is followed by short root deceleration which is prominent at low field strengths. A steady state is finally attained as evident from the linear temporal regime.

### 8.2.1.3 Effect of electric field

During drifting stage, the velocity can be expressed in terms of a simple mass balance equation as  $v = J_{GB}\Omega/L$  [5] where  $J_{GB}$  is the GB flux,  $\Omega$  is the atomic volume and  $L$  the

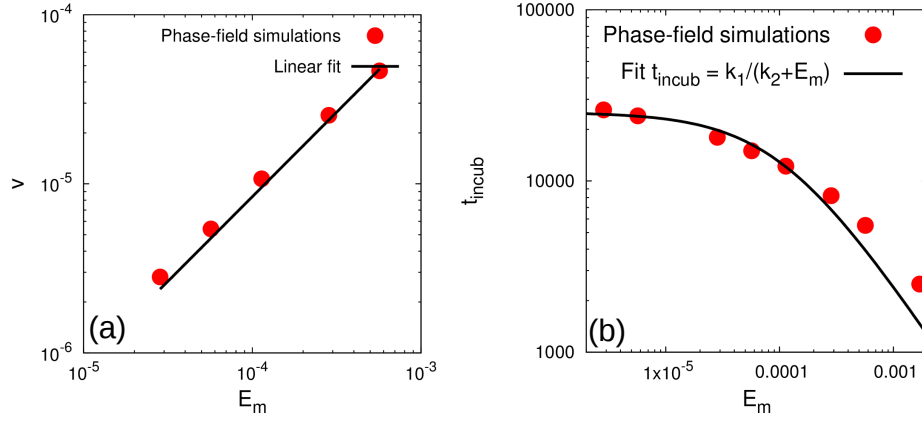


Figure 8.3: (a) Scaling of steady state drift velocity with electric field in GBDLR. A linear relationship is obeyed over a magnitude of electric field. (b) Variation of incubation period with electric field. At low field strengths, a capillary plateau is observed, while at high field strengths a linear regime is exhibited.

grain size. Since,  $J_{GB} = M_{GB}zeE_m$ , the velocity scales linearly with electric field. The steady state velocity extracted from the slope of the linear regime of  $d_g - t$  curve indeed obeys the linear scaling over a magnitude of electric field as shown in Fig.8.3(a).

The effect of current density  $j$  (or electric field because of their linear dependence due to Ohm's law) on damage kinetics is expressed according to modified Black's law [102],

$$t_f = \frac{1}{j^n} \exp\left(\frac{\Delta H}{k_B T}\right) \quad (8.1)$$

where,  $t_f$  is the time to failure and  $\Delta H$  is the activation energy of the process. The above expression can be used to extrapolate the EM test results which are performed at accelerated condition to the service condition. The value of the exponent  $n$  sheds light on the mechanism or rate limiting step of failure [256]. In the present case,  $t_f$  can be expressed as,

$$t_f = t_{incub} + t_{drift}, \quad (8.2)$$

where,  $t_{incub}$  is the incubation time before which drift initiates and  $t_{drift}$  is the time elapsed in drift. Since faster drift corresponds to shorter failure times i.e.  $v \propto 1/t_{drift}$ , the exponent of current density for the second term in the above expression turns out be  $n = 1$ . Furthermore, as the electric field tends to zero, the incubation time is expected to tend towards infinity. The variation of  $t_{incub}$  is plotted in Fig.8.3(b), where the data points are fit to function  $t_{incub} = k_1/(k_2 + E_m)$ . As,  $k_2 \gg E_m$ ,  $t_{incub} \sim k_1/k_2$  and the curve exhibits a plateau region corresponding to capillary dominated regime. On the other

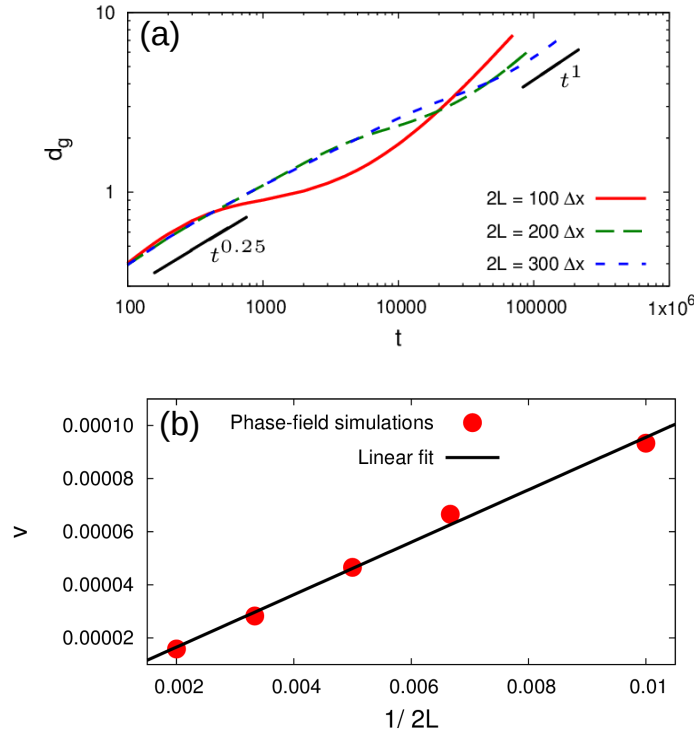


Figure 8.4: (a) Displacement-time curve depicting the grain size dependency on drift kinetics in GBDLR. Smaller grains, owing to rapid merging of neighboring tails, facilitate surface drift and attainment of steady state. (b) Velocity dependence on grain size. The steady-state velocity follows an inverse scaling with respect to the grain size. Electric field strength corresponds to  $E_m = 5.6818 \times 10^{-4}$ .

hand, at higher field strengths  $E_m \gg k_2$ ,  $t_{incub} \sim k_1/E_m$  and a linear tail corresponding to EM-dominated regime can be observed. Thus in EM dominated regime both stages should result in  $n = 1$  in Eq. 8.1.

#### 8.2.1.4 Effect of grain size

The dependency of grooving and drifting characteristics on the grain size is presented in Fig. 8.4(a). The root displacement during initial stage ( $t = 100 - 400$ ) is higher for smaller grain ( $2L = 100\Delta x$ ) owing to the prominence of curvature-driven flux due to overlap of neighboring groove tails. Since, the grooving stage is prolonged for larger grains, the displacement at intermittent stage ( $t = 500 - 11000$ ) is higher for larger grains, while, exhaustion of curvature-driven flux leads to a slowing down of smaller grain. However, since the smaller size grain facilitate the development of surface arc that initiates drifting, the steady state regime is attained faster, eventually surpassing the larger grains. The inverse scaling of the grain size during steady state drift according to the aforementioned

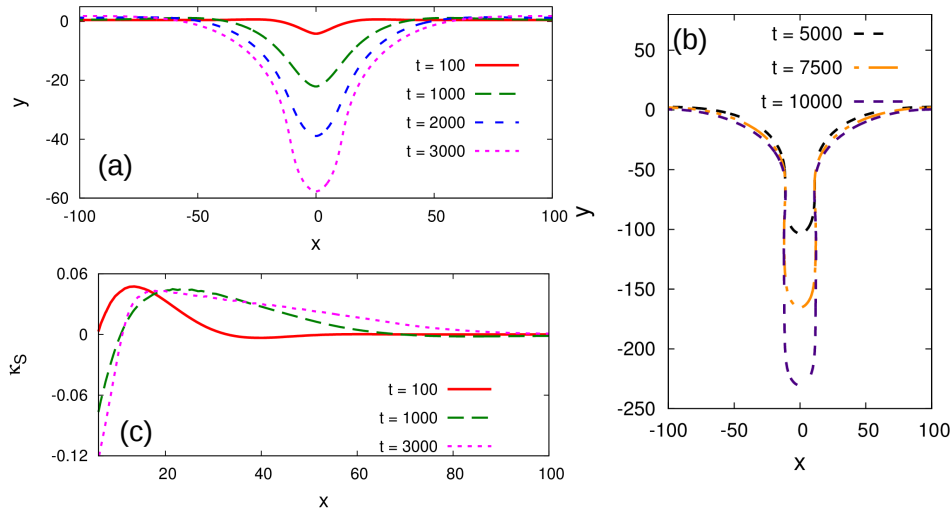


Figure 8.5: Temporal evolution of grooves in SDLR at (a) early, and (b) late stages. Faster GB transport leads to accelerated grooving, followed by the development of cavity at the root which eventually forms a channel-like slit that advances along the GB maintaining a constant width and shape. (c) Curvature profile along the groove. Slit formation changes the curvature of the root from convex to concave. The grain size and electric field strength corresponds to  $2L = 400\Delta x$  and  $E_m = 2.3674 \times 10^{-3}$  respectively.

mass balance relation is corroborated by the phase-field numerics in Fig. 8.4(b).

## 8.2.2 Surface diffusion limited regime (SDLR)

The case when transport through the GB is faster than that at the surface such that  $M_S/M_{GB} = 0.1$  is discussed next. The strength of electric field is selected to be one magnitude higher than than in GBDLR. In the following section, the cases pertaining to large grains and deviations arising due to finite grain sizes is dealt sequentially.

### 8.2.2.1 Morphological evolution

A predominance of GB diffusion accelerates the grooving rate in Fig. 8.5(a) as compared to Fig. 8.1(a). As a result of low surface diffusivity and large grain size, any overlap of the neighboring groove tails is found to be absent. The grooves temporally widen forming a cavity at the root. Ultimately, a narrow slit-like channel develops (Fig.8.5(b)) which then propagates along the GB preserving its width and shape. A fast GB diffusion flux is responsible for localizing the damage along GB as opposed to the Blech type regime where the entire surface drifts homogeneously. The trailing edge evolves through surface diffusion to form arcs as observed in Fig.8.5(b), and eventually starts drifting. In

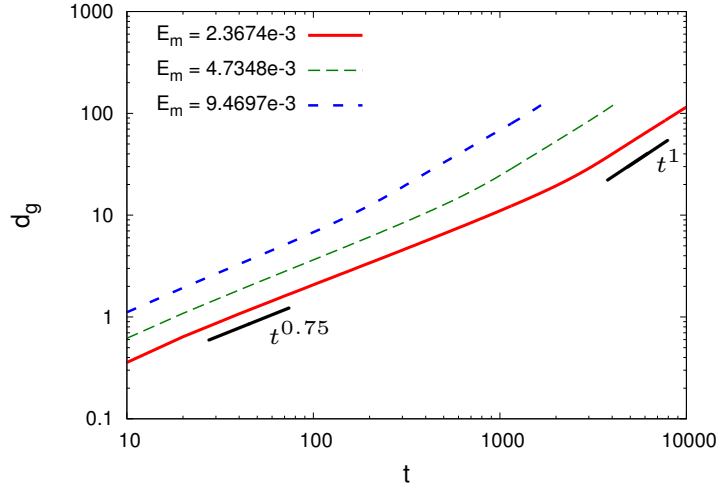


Figure 8.6: Displacement-time curve illustrating kinetics of slit propagation in SDLR. After an initial growth exponent  $3/4$ , the slit attains a dynamic steady-state.

other words, while the entire surface drifts conserving its shape when surface diffusion predominates, shape is conserved only near the tip region of the slit in SDLR. It is also worth noting that the convexity of the groove root is preserved when the surface drifts, as opposed to slit formation where the root curvature transitions from convex to concave (Fig. 8.5(c)) during evolution.

### 8.2.2.2 Slit propagation kinetics

The  $d_g - t$  curve corresponding to different electric field is plotted in Fig. 8.6. Similar to the Blech regime in Fig. 8.2, two distinct kinetic regions can be identified. In this case, the transient stage exhibits a faster kinetics evident from the temporal exponent of  $3/4$ . As the root detaches from the surface to form slit, it deepens with a steady-state velocity as evident from the linear exponent in the  $d_g - t$  curve. Larger field strengths hasten the transition to a steady-state.

### 8.2.2.3 Effect of electric field

The sharp interface GB grooving model proposed in [5, 257] predicts  $E^{3/2}$  dependency of slit kinetics. The velocities of the groove root computed via present phase-field simulations at different magnitudes of electric field strength, confirm the corresponding scaling law in Fig. 8.7. Drawing analogy from GBDLR, failure in the present case can be expressed as,

$$t_f = t_g + t_p \quad (8.3)$$

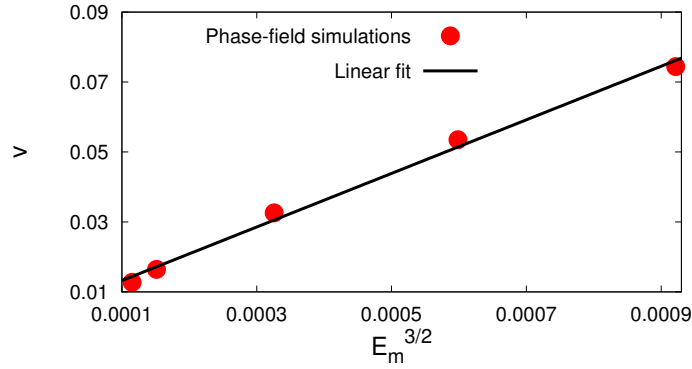


Figure 8.7: Velocity dependency on electric field in SDLR. Higher electric field leads to fast-propagating slits.

where,  $t_g$  and  $t_p$  correspond to the initial accelerated grooving and slit propagation stage respectively. The GB grooving model by Rosenberg and Ohring [78] suggests that the EM-induced grooving (not slit propagation) leads to hole formation in which the time to failure exhibits a  $E_m^{4/3}$  dependence. This relationship can also be inferred from Fig. 8.6 during the initial stages where  $d_g \propto t^{3/4}$  and the prefactor depends on the magnitude of  $E_m$ . If the groove root continues propagating following this temporal law,  $t_g \propto E_m^{4/3}$  proposed by Rosenberg and Ohring is expected. Thus, while the former ( $t_g$ ) will lead to  $n = 4/3$ , the latter ( $t_p$ ) gives rise to  $n = 3/2$ . Hence the exponent in Eq. (8.1) is anticipated to lie between  $4/3 - 3/2$  depending upon the rate limiting step.

#### 8.2.2.4 Effect of grain size

Traditionally, the sharp interface models analyze the slit dynamics independently once the slit is detached from the surface assuming an idealized geometry such that the slit surface is parabolic while the tip retains an equilibrium dihedral angle and is flat further away. It does not take into account the influence of initial grain size on slit kinetics. Our phase-field simulations, on the other hand, nicely captures the non-linearities associated with slit initiation from GB grooves and subsequent advancement without making any a priori assumptions on the slit shape. Hence, the proposition of grain size independence on slit kinetics are easily verified via the present simulations. The  $d_g - t$  curve corresponding to different grain sizes is presented in Fig. 8.8(a). Although, any difference in kinetics during the initial stages is indiscernible, deviation arises progressively in later stages in the order of increasing grain size. The overlapping of neighboring groove profiles in case of smaller grains leads to concomitant surface drift in addition to slit propagation. For the constant voltage set-up, this drifting leads to significant decrease in the GB flux leading to a slower kinetics at later stages. The steady state velocity corresponding to different

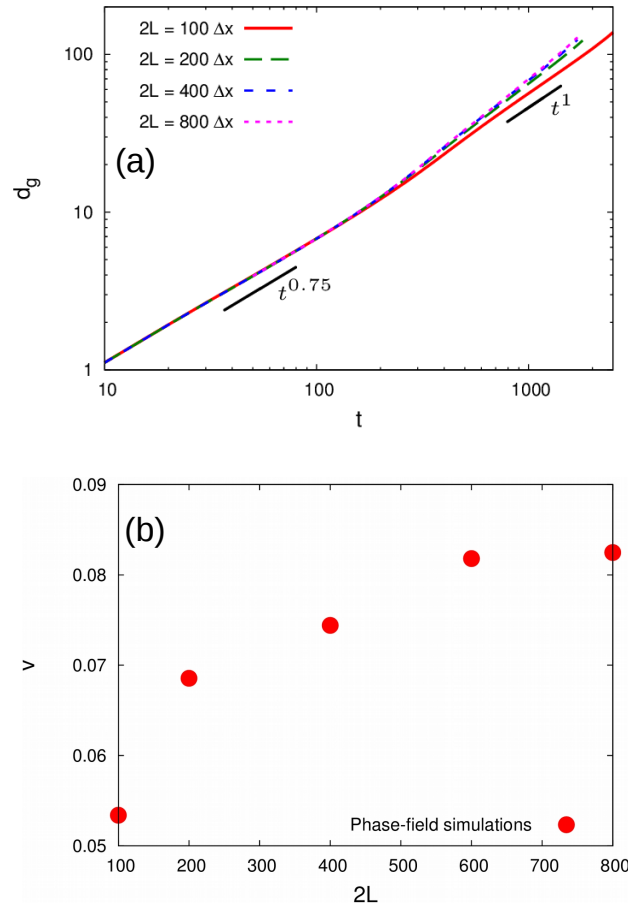


Figure 8.8: (a) Displacement-time curve in SDLR depicting the grain size dependency on slit kinetics. Deviation arises progressively at late stages in order of increasing grain size. (b) Velocity dependence on grain size. Slits originating from smaller grains lead to slower propagation. The dependency becomes weaker as the grain size is increased. The electric field strength corresponds to  $E_m = 9.4697 \times 10^{-3}$ .

grain sizes is plotted in Fig. 8.8(b). While the influence of the small grain sizes on slit kinetics is strong, the dependency becomes weaker as the grain size increases due to the absence or delay of simultaneous surface drift.

### 8.2.3 Role of surface and GB as EM pathway

To better assess the role of surface and GB as potential EM pathways, the surface and GB flux vectors superimposed on the groove profile is plotted. Fig. 8.9(a) corresponds to GBDLR (Fig.8.1(b) at  $t = 10000$ ). EM itself can act as a healing agent especially in the homogeneous displacement regime for the case discussed in Fig. 8.1. The convexity of root is sustained as the surface drifts and curvature gradient-driven surface flux points

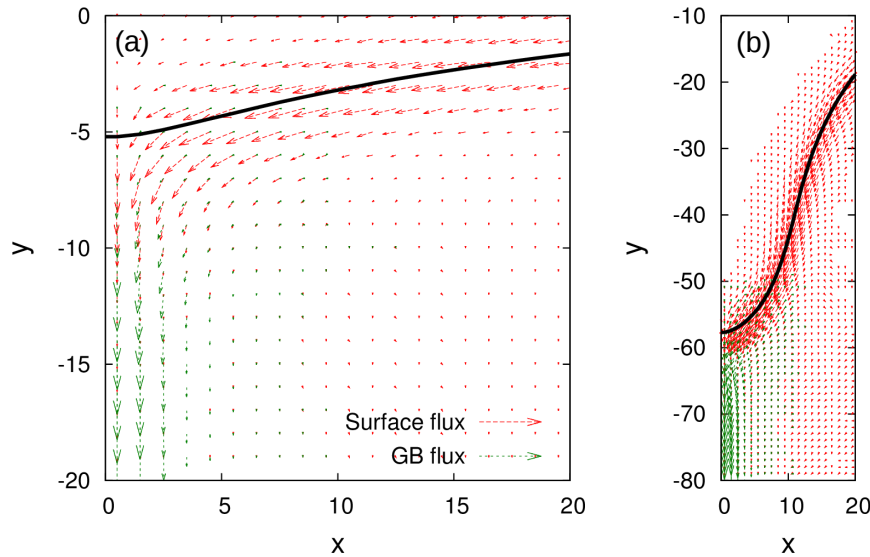


Figure 8.9: Surface (red arrows) and GB (green arrows) currents in (a) GBDLR and (b) SDLR. While EM-induced surface flux replenishes the groove root in GBDLR, curvature-gradients results in an additional mode of healing mechanism. The magnitude of flux vectors have been upscaled for clarity.

away from the root. The electric field lines are superimposed over the phase-fields that represent the grains and the underlayer in Fig. 8.10 (a) and (b). The field lines are initially straight i.e., there are no horizontal potential gradients. As the groove develops, the field lines twist, thereby, instigating a gradient in the electric potential along the freshly exposed surfaces. This in turn induces a healing flux along the electron wind, which is directed towards the groove root. While EM-induced GB flux,  $J_{GB}^E$ , leads to groove extension, surface currents replenish the groove.

The role and direction of various fluxes at different stages of damage is summarized

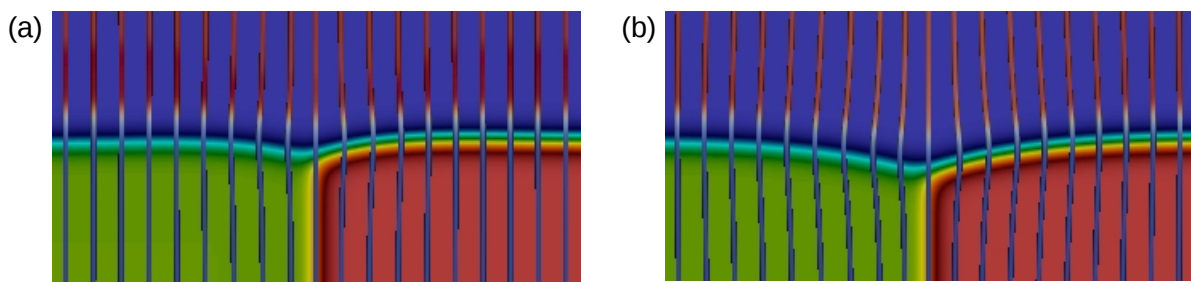


Figure 8.10: Electric field lines superposed over the phase field corresponding to (a) initial and (b) late stages. Grooving leads to distortion of the field lines which prompts a potential gradient and healing flux directed towards the root.

in Fig. 8.11. During initial stages of homogeneous displacement (Fig.8.11(a)), curvature gradient-induced surface flux  $J_S^{\nabla\kappa_S}$  and EM-induced GB flux  $J_{GB}^E$  lead to groove extension, while EM-induced surface flux  $J_S^E$  compensates it. The early stage contribution of the healing flux is marginal. However, as the groove deepens, freshly exposed surfaces temporally increase  $J_S^E$ . As the circular arcs of constant curvature emerge,  $J_S^{\nabla\kappa_S}$  exhausts while  $J_S^E$  saturates to a fixed value. Thus, the edge drift is governed by an interplay of  $J_S^E$  and  $J_{GB}^E$ , as shown in Fig. 8.11(b).

In SDLR, root concavity (Fig. 8.4(d)) promotes material transport towards the root. In addition to  $J_S^E$ , curvature-gradient induced surface flux  $J_S^{\nabla\kappa_S}$  also contributes towards the healing flux (Fig. 8.9(b) which corresponds to  $t = 3000$  of Fig.8.5(a)). Because of the dual healing mechanism of  $J_S^E + J_S^{\nabla\kappa_S}$ , surface currents near the root are intense, while relatively weaker further away because of sole effect of  $J_S^E$ . The mechanism of slit formation is summarized in Fig.8.11 (c) and (d). Origin of healing fluxes can therefore be curvature gradient- or EM-induced, or both, depending upon the predominance of capillarity over EM, or vice versa.

Thus, a homogeneous displacement is favored when  $J_S^E \gtrsim J_{GB}^E$  which is most likely to occur when  $M_S/M_{GB} \gtrsim 1$  and low to moderate field strengths since increasing electric field strengths would inadvertently increase  $J_S^E$ . On the other hand, groove-to-slit transition will result if  $J_{GB}^E \gg (J_S^E + J_S^{\nabla\kappa_S})$  which is preferable as  $M_{GB}/M_S \gg 1$  and high field strengths.

## 8.2.4 Polycrystalline line

Damage of bicrystalline configuration discussed hitherto although providing numerous fundamental insights, are of limited practical value. In reality, commercial interconnects are polycrystalline (more than 2 grains) with a mixed grain size distribution. As a result, curvature-driven grain coarsening can also potentially play a vital role in the initiation of damage. Naturally, in addition to the surface and GB diffusivities, the GB mobility ( $L_\eta$ ), that determines the coarsening rate, should also be considered in order to comprehend the damage mechanisms.

In this section, the phase-field model is extended to 3-D to numerically investigate the damage modes in polycrystalline interconnects. For simplicity, the present study is limited to 20 non-conserved order parameters corresponding to grains of different orientations and retain the columnar structure. Practically, such a configuration corresponds to an interconnect line blocked by a large single crystal. Starting from the polycrystalline grain distribution that is generated via a 2-D grain growth simulation (Fig. 8.12(a)), the focus is on the damage modes that are operative in SDLR. In the following 3-D simulations, the

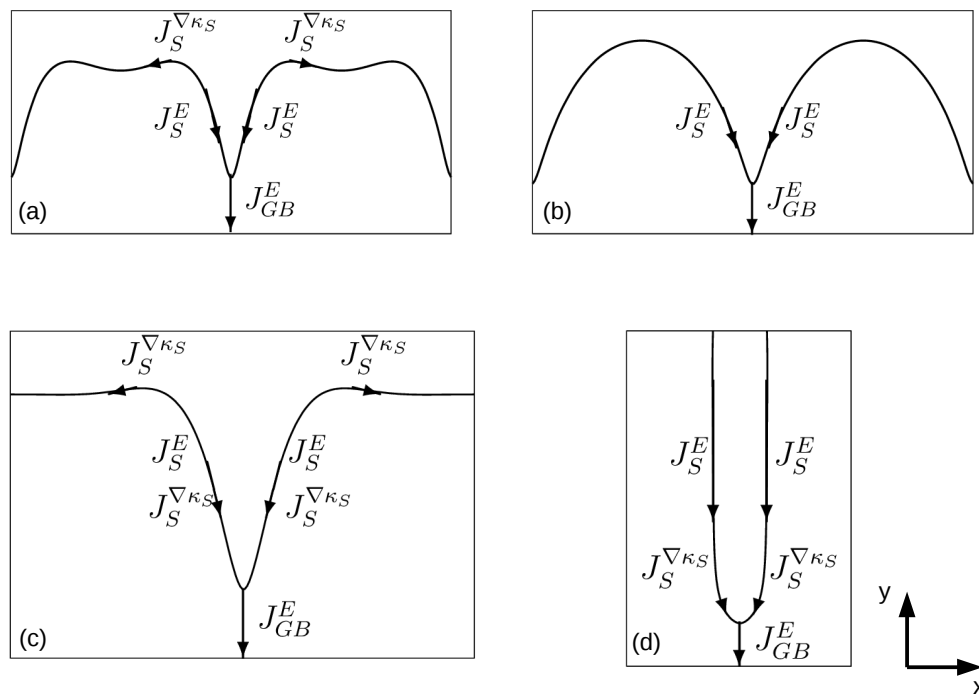


Figure 8.11: Schematic diagrams depicting the role of surface and GB in GB diffusion-limited regime at (a) early and (b) late stages. Curvature-induced surface flux  $J_S^{\nabla\kappa_S}$  and EM-induced GB flux  $J_{GB}^E$  lead to groove extension, while the EM-induced surface flux  $J_S^E$  heals the groove. The drifting is governed by an interplay of  $J_S^E$  and  $J_{GB}^E$ . Similar illustration in surface diffusion-limited regime at (c) early and (d) late stages. In addition to  $J_S^E$ ,  $J_S^{\nabla\kappa_S}$  also replenishes the groove.

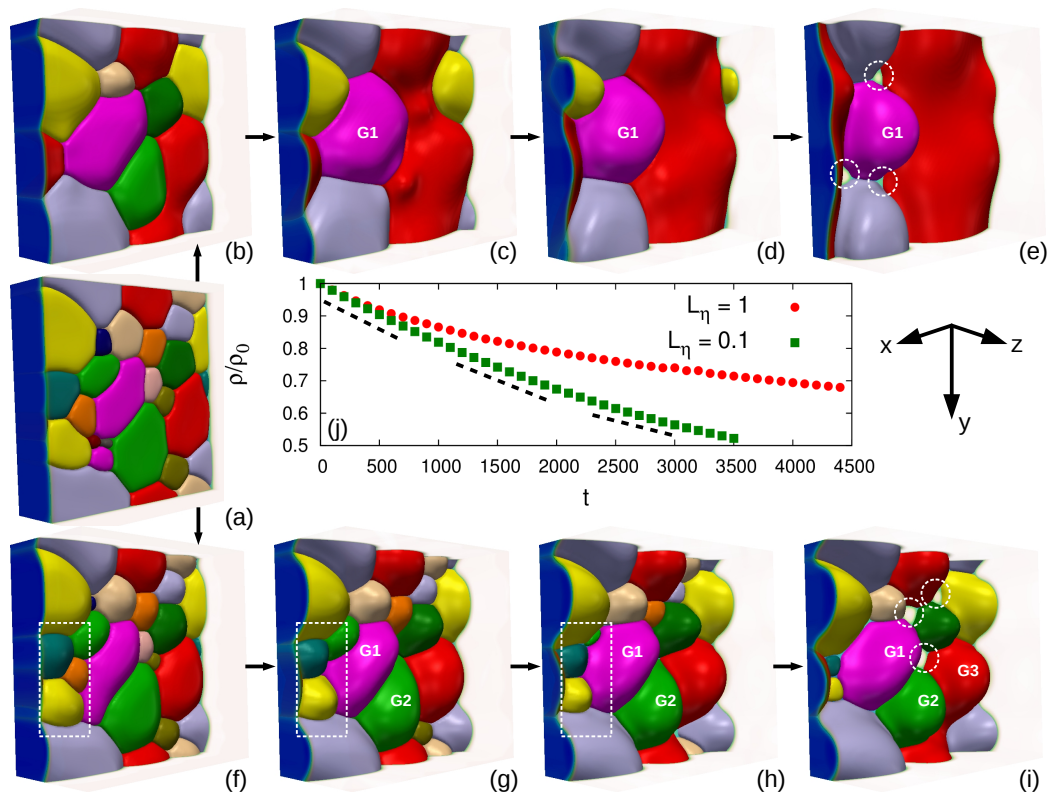


Figure 8.12: Damage in polycrystalline line initiating from a multi-grained structure (a)  $t = 0$  for high GB mobility ( $L_\eta = 1$ ) at (b)  $t = 500$ , (c)  $t = 1500$ , (d)  $t = 2500$ , (e)  $t = 4400$  and low GB mobility ( $L_\eta = 0.1$ ) corresponding to (f)  $t = 500$ , (g)  $t = 1500$ , (h)  $t = 2500$  and (i)  $t = 3500$  in SDLR. Smaller grains exhibit surface drifting (shown in white dotted box), while junctions around larger grains exhibit a propensity of slit formation. The triple and quadruple junctions are the preferential sites of failure (white dotted circles). (j) Temporal evolution of relative density of the interconnect depicting the drift of the polycrystalline line.

grain mobility ' $L_\eta$ ' is varied between 0.1 and 1.0 to decompose the influence of coarsening on damage proliferation. Every grain orientation is assigned a different color for clarity. Furthermore, the underlayer is rendered invisible for better visualization.

Upon comparing the number of grains in Figs. 8.12(b) with (f), it is observed that coarsening is enhanced at a larger value of  $L_\eta$ , wherein, smaller grains are consumed by larger ones. Concurrently, GB networks, that are a dominant pathway perish rapidly. GB grooves are clearly visible in both cases, though no noticeable differences in terms of failure initiation can be perceived.

To quantify EM-induced damage, the relative density of the interconnect is defined as  $\rho/\rho_o$  where  $\rho$  is the instantaneous density and  $\rho_o$  is the initial value. As the damage proceeds, this parameter quantifies the amount of drift along the line and the residual trailing edge. The temporal evolution of relative density is plotted in Fig. 8.12(j). Clearly, in the early stages ( $t = 500$ ), the extent of damage in both the lines are similar ( $\approx 10\%$ ). However, during later stage, smaller grains survive until longer times when  $L_\eta = 0.1$ , that results in thinning of areas with small grains. As an example, consider the smaller grains on the left edge of Figs. 8.12 (f), (g) and (h) enclosed in white dashed box, which drift faster than larger neighbors, designated as  $G1$  and  $G2$  in Figs. 8.12(g) and (h), respectively. On the other hand, larger grains ( $G1$ ) in both cases undergo marginal or almost no drift. This stagnancy is clearly evident in Fig.8.12(j) where at  $t = 2500$ , the smaller grain sample ( $L_\eta = 0.1$ ) displays a drift of 40% as compared to 25% in large grain test piece ( $L_\eta = 1$ ). This finding is in qualitative agreement with those for bi-crystalline configuration, where drift velocity was found be inversely related to grain size.

For  $L_\eta = 1$ , where grain coarsening is prevalent, propensity of slit initiation from the grooves, increase with time. However, at a lower  $L_\eta$  ( $=0.1$ ), the damage proceeds via a mixed mode wherein smaller grains exhibit thinning as slits develop along GB junctions of the larger grains, though the thinning is definitely reduced. This slit propensity is evident in slowing of the drift of the interconnect in Fig.8.12(j). While the drift between  $t = 1500$  to  $t = 2500$  is around 15%, it is little less than 10% between  $t = 2500$  and  $t = 3500$  for  $L_\eta = 0.1$  system. The curve plotted for  $L_\eta = 1$  is comparatively flatter due to morphogenesis of slits resulting in a large residual trailing edge.

Another consequence of a small GB mobility is that for the same line length, time to failure is smaller ( $t = 3500$  for  $L_\eta = 0.1$  in Fig.8.12(i) as compared to  $t = 4400$  for  $L_\eta = 1$  in Fig.8.12(e)). Clearly, interconnects with smaller average grain size would possess larger GB networks that accelerates surface drift. For deeper insights, it is worth investigating the primary sites of failure. To track the events that lead to failure, temporal evolution of the bottom plane of the line corresponding to  $L_\eta = 0.1$  are presented in Figs. 8.13(a)-(d). To demarcate the grains and GBs,  $\Phi = \sum \eta_i^2$  is plotted, such that  $\Phi = 0$  corresponds

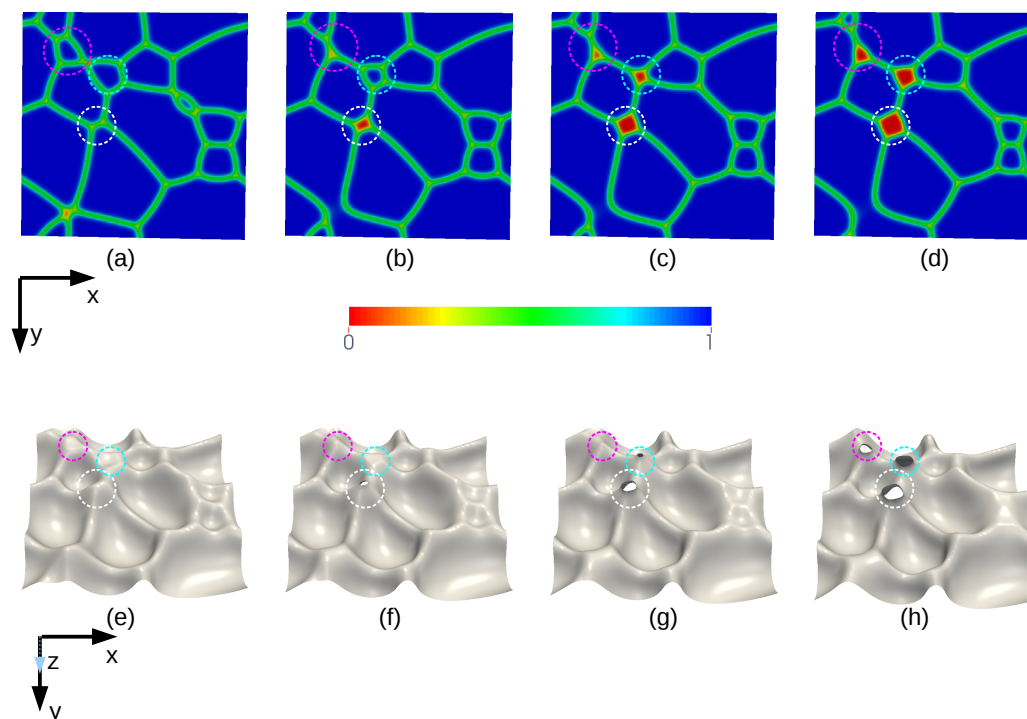


Figure 8.13: Temporal evolution of the bottom section of the polycrystalline line showing the predominant failure sites at (a)  $t = 2500$ , (b)  $t = 2900$ , (c)  $t = 3100$  and (d)  $t = 3500$  for  $L_\eta = 0.1$ . Here, grains illustrated in blue are separated by green GBs. The red color denotes the exposed underlayer domain due to hole formation by accelerated GB grooving initiating from the top surface. Temporal evolution of  $\rho = 0.5$  surface contour at (e)  $t = 2500$ , (f)  $t = 2900$ , (g)  $t = 3100$  and (h)  $t = 3500$ . Junctions around larger grains (shown in white dotted circle) are the ones that fail more readily. Dissolution of smaller grains leads to slit merging and subsequent failure (cyan and magenta dotted circle).

to the underlayer,  $\Phi = 1$  represents the grains of interconnect, and  $\Phi = 0.5$ , the GBs. Moreover, the  $\rho = 0.5$  surface contour is also shown in Figs. 8.13(e)-(h).

The first junctions of failure are the ones that are surrounded by larger grains designated as  $G1$ ,  $G2$ , and  $G3$  in Fig. 8.12(i) and enclosed inside white dotted circles in Figs. 8.13(a), (b), (e), and (f). GBs or junctions of larger grains, while acting as sites where slits initiate, also promote its proliferation, as discussed previously in Sec. 8.2. Moreover, the triple and quadruple junctions are comparatively more susceptible to damage, when compared with GBs. For instance, the damage occurs at a faster rate along the quadruple junction when  $L_\eta = 0.1$  (Figs. 8.12(i), 8.13(b), and 8.13(f)). Similarly in Fig. 8.12(e) ( $L_\eta = 1$ ), holes form at triple junctions around grain  $G1$ .

The second predominant failure sites are the grain junctions originating due to dissolution of smaller grains as shown in Fig.8.13 (magenta and cyan dotted circles), especially if the neighboring grains are large. Smaller grains, due to larger EM surface drift, entail large thinning, but when consumed by neighboring grains, cause slits to merge. This interesting event is nicely captured in Figs. 8.13(e)-(h) (in magenta and cyan dotted circles), where the protruded junctions from the neighborhood of smaller grain approach each other, as it continuously shrinks. Finally, the adjoining slit-tips coalesce before evolving in unison.

### 8.3 Discussions and Concluding Remarks

The present study is applicable to polycrystalline lines where GB-grooving proceeds via concurrent surface and GB atomic diffusion and EM. Our work comes closest to the experimental study of damage morphology of copper interconnects by Gladkikh et al. [76] and McCusker et al. [86]. Both surface condition and grain size distribution were reported to influence the damage modes. Absence of an overlayer (such as tantalum) which promotes oxidation and formation of oxide precipitates accelerate slit growth. Both these observations can be argued based on slow surface diffusion which concomitantly hinders the healing process which is corroborated by the present study. Global thinning of the sample was attributed to small grain size distribution. Surface diffusivity was assumed to be comparable to GB diffusivity (though the exact diffusivity values were not reported) to explain the observed damage modes by comparing the parameters to the GB grooving model in [5]. The aforementioned observation can also be rationalized on the basis of healing flux highlighted in the present work even in SDLR. A sufficient value of  $(J_S^E + J_S^{\nabla\kappa_S})$  outweighs  $J_{GB}^E$ , as a result of which root detachment phenomenon will not be observed. This non-detachment is expected to be observed at smaller grain size and lower electric field strength.

The present work builds upon the analytical theory of Klinger et al. [5, 95, 257] and highlights the importance of curvature gradient- and EM-induced surface healing flux that has not been accounted in previous investigations [5, 257]. Although the scaling laws derived in [5, 95, 257] are well reproduced by the phase-field method, incumbent healing fluxes delay the growth of damage by replenishing the groove root.

Our 2-D phase-field simulation results on homogeneous displacement are similar to ones obtained by Khenner et al. [140] using their level-set technique. However, numerical modeling of slit propagation is comparatively non-trivial. The main advantage of using a diffuse-interface approach, such as ours, is that the phenomenon of slit detachment from the surface becomes easily tractable, albeit with a finer grid resolution as compared to level-set. Moreover, the 2-D model was also extended to 3-D to investigate the failure of polycrystalline interconnects, where coarsening can modulate the damage mechanisms. For the first time, a mixed mode of damage is identified, wherein, smaller grains exhibit thinning while slits manifest around junctions of larger grains. Grain triple and quadruple junctions are identified as preferential sites of failure.

The model in the present form does not consider the Blech effect. As the sample drifts in the direction of electron wind, mass accumulation at the anode gives rise to back stresses that hinder the EM-induced displacement [87, 88]. The timescale on which back stress-gradients develop scales into hours, therefore, our predictions on early-stage damage propagation holds good. In addition, the presence of residual or thermal stress [258, 259] arising during fabrication or annealing cycle has also not been considered. In present framework, physics of both back-stress accumulation and thermal stress can be incorporated by solving a complete elastic boundary-value problem [137, 209] or through an atomistically-informed formalism of phase-field crystal (PFC) models [147]. Moreover, phenomena such as void nucleation at the cathode end and crystalline defects such as triple junctions and GBs, can also be studied using PFC. Here, it is important to mention that genesis of slits in SDLR, in the present work, is not a nucleation phenomenon, rather it is the manifestation of accelerated GB grooving. While, void nucleation results in an exponent of  $n = 2$  in Black's law (which is faithfully reproduced by PFC), the present work elucidates the damage in form of global thinning and intergranular slit initiating from GB grooves leading to  $n = 1$  and  $n = 3/2$  respectively in steady state. PFC studies, however, are currently limited to bulk-diffusion regimes.

Insights gained in the present work can be easily extrapolated to other technologically-relevant configurations, such as, near bamboo lines or slit initiation and growth along the side walls (for e.g. top surface) transverse to the line. While EM-induced GB transport will drain the root (as long as the GB is tilted) similar to the observation for the present configurations, the EM-induced surface healing flux is unidirectional. This unidirectional

---

healing will eventually result in formation of asymmetric grooves with a mass-depleted leeward side while the mass accumulates on the windward side [120, 142, 121]. However, the steady-state morphology and dynamics of slits are anticipated to be consistent with the ones presented in this chapter, as these characteristics arise solely on dimensional arguments.

# Chapter 9

## Effect of electromigration on grain-boundary grooving at finite grain size: Comparison of sharp interface and phase-field simulations

### 9.1 Introduction

A theoretical model proposed by Klinger and co-workers elucidated grain-boundary grooving as the mechanism of Blech electromigration in a periodic array of a polycrystalline interconnect [5, 126, 257]. The GB grooving model considers the concomitant effect of surface and GB diffusion on the interconnect reliability where the EM-induced GB flux causes extension of grooves while the capillarity driven surface diffusion maintains the shape of the surface. Depending on a non-dimensional parameter  $\alpha = \frac{J_{GB}\Omega L^2}{8B}$  where  $J_{GB}$  is the GB flux,  $L$  is the grain size,  $\Omega$  is the atomic volume and  $B = \frac{D_S\delta_S\Omega\gamma_S}{k_B T}$  is a kinetic constant, two distinct damage regimes are possible. Below a critical value of  $\alpha$  termed as “Mode A”, the surface drifts homogeneously preserving its shape. The “A-regime” is similar to the displacement of the test sample commonly observed in Blech drift velocity experiments [75, 87]. With EM-induced flux localized at the GBs, the grains at the drift front are displaced along the line. Subsequently the consecutive interior grains are removed, given a continuous GB network along the line exists [260]. This is typical in polycrystalline lines. Relaxing the small slope approximation (SSA), gives rise to the second regime, termed as “Mode B”, above a critical value of  $\alpha$ , in which the root detaches from the surface to form isolated slits propagating along GB. Physically, smaller grains, lower GB flux and lower surface diffusivity promotes the former regime and vice-versa.

The model is able to explain a number of drifting characteristics observed in seminal drift velocity experiments by Blech [75, 87, 89] such as drift velocity dependence on current density, grain size and also the measured activation energies [109].

Although the model has been successfully employed thereafter to rationalize the observed damage modes in polycrystalline interconnects [76, 86, 261], the proposed model overlooks a key aspect. Specifically, the surface evolution is governed solely due to curvature-gradient mediated surface diffusion, while the electric-field-driven diffusion along the groove walls is not accounted for. Furthermore the model is only applicable during steady state drift and does not enlighten the initial stages of grooving. Concurrent GB and surface EM are important, especially in copper interconnects as evident from the measured disparate activation energy values [106, 107, 86]. Moreover, the damage modes are observed to be dependent on surface conditions. For instance, surface contaminations, oxides, presence of passivation and underlayer which hinders the diffusion along the free surfaces lead to shorter lifetime and activation energy comparable to surface and metal-underlayer interface diffusion [107, 86, 106, 76].

In the present chapter, we revisit the problem of GB grooving under electromigration, specifically focusing on “Mode A” regime of homogeneous displacement, by utilizing both analytical and numerical methods. To make the analytical calculations (sharp interface) mathematically amenable, we follow the approach of Thouless [125] by invoking the SSA. The EM flux along the freshly exposed groove walls will also be neglected. Following Klinger et al. [5], SSA will be relaxed by solving the derived sharp interface relations numerically in steady state. Finally a phase-field or diffuse interface model which relaxes SSA as well as accounts for EM-driven flux along groove walls is employed [4] and compared with the sharp interface analytical and numerical solution. Since the SSA does not predict “Mode B” of slit propagation, it is kept outside the purview of the present chapter.

Our results suggest that surface EM acts as a healing agent which invariably leads to lower groove penetration in comparison to the sharp interface models. Moreover, the single parameter  $\alpha$  is shown to be inadequate to predict either the steady state shape or the kinetic regimes of damage. The present chapter is organized as follows. In the following section the sharp interface governing equation of the groove profile is derived, which is solved analytically in linear form and numerically in its complete non-linear form. Thereafter, the solution from sharp interface and phase-field model are critically compared in section 9.3 and the role of surface EM not accounted in sharp-interface model is highlighted. Section 9.4 concludes the chapter.

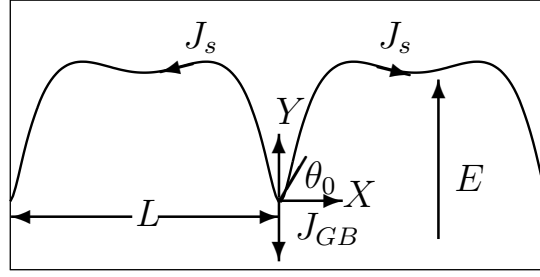


Figure 9.1: The schematic of the geometry used in the sharp-interface analytical model. The system consists of a two-dimensional periodic array of grains with grain size  $L$ . Starting from a flat surface, grain boundary grooves develop under the combined influence of capillary-mediated surface flux  $J_S$  and electromigration-induced grain boundary flux  $J_{GB}$  due to the applied electric field along the grain boundary.  $\theta_0$  is the angle made by the tangent at the groove root and the  $x$ -axis and is given by  $\sin^{-1}(\gamma_{GB}/2\gamma_S)$ .

## 9.2 Sharp Interface Relations

### 9.2.1 Analytical approach

We start with the linearized governing Eq.(7.8)

$$\frac{\partial y}{\partial t} = -By'''' . \quad (9.1)$$

The above PDE is solved under the following boundary conditions [125],

- (i) constant slope at the root which under SSA translates into,
 
$$y'(0, t) = m = \tan \theta_o .$$
- (ii) the periodicity of the problem also dictates,
 
$$y'(L/2, t) = 0 .$$
- (iii) the continuity of the flux at the groove root i.e.  $J_s = J_{GB}/2$  results in,
 
$$y'''(0, t) = \frac{J_{GB}\Omega}{2B}$$
 where the small slope version of Eq.(7.4) is utilized to calculate  $J_s$ .
- (iv) the flux at  $x = L/2$  is zero i.e.,
 
$$y'''(L/2, t) = 0 .$$

The third boundary condition couples the surface flux to the EM-induced GB flux at the groove root.  $J_{GB}$  is given by

$$J_{GB} = \frac{D_{GB}\delta_{GB}}{\Omega k_B T} z_{GB} e E \quad (9.2)$$

The complete solution of Eq.(9.1) can be written as a combination of [125, 129],

$$y(x, t) = v_{ss}t + y_{ss}(x) + y_{tr}(x, t), \quad (9.3)$$

where the first part represents the steady state translation or drift of the surface, the second term  $y_{ss}(x)$  denotes the time invariant profile and the last term  $y_{tr}(x, t)$  the transient part of the solution. The steady state part of the solution can be obtained by substituting  $v_{ss} = \frac{\partial y}{\partial t}$  and integrating Eq.(9.1) subjected to the aforementioned boundary conditions resulting in,

$$v_{ss} = \frac{J_{GB}\Omega}{L} \quad (9.4)$$

$$y_{ss}(x) = -\frac{J_{GB}\Omega}{24BL}x^4 + \frac{J_{GB}\Omega}{12B}x^3 - \left(\frac{J_{GB}\Omega L}{24B} + \frac{m}{L}\right)x^2 + mx \quad (9.5)$$

The transient part of the solution can be obtained by a standard technique of displacement from steady state [262] which renders the boundary conditions homogeneous, followed by separation of variables leading to,

$$y_{tr}(x, t) = \sum_{n=0}^{\infty} A_n \exp(-n^4 \frac{t}{\tau}) \cos(\frac{2n\pi}{L}x), \quad (9.6)$$

where  $\tau = \left(\frac{L}{2\pi}\right)^4/B$ ,  $A_0 = \frac{1}{L} \int_0^L -y_{ss}(x) \cos(\frac{2n\pi}{L}x)dx$  and  $A_n = \frac{2}{L} \int_0^L -y_{ss}(x) \cos(\frac{2n\pi}{L}x)dx$   $\forall n \neq 0$ . A further integration by parts term by term yields,

$$y_{tr}(x, t) = A_0 + \left\{ \sum_{n=1}^{\infty} \left( \frac{mL}{(n\pi)^2} + \frac{J_{GB}\Omega L^3}{8B(n\pi)^4} \right) \exp\left(-n^4 \frac{t}{\tau}\right) \cos\left(\frac{2n\pi}{L}x\right) \right\}$$

where  $A_0 = \frac{J_{GB}\Omega L^3}{720B} - \frac{mL}{6}$ . Substituting Eq.(9.4), (9.5) and (9.7) in Eq.(9.3) gives the complete solution as,

$$\begin{aligned} y(x, t) = & \frac{J_{GB}\Omega}{L}t + \frac{J_{GB}\Omega L^3}{720B} - \frac{mL}{6} - \frac{J_{GB}\Omega}{24BL}x^4 + \frac{J_{GB}\Omega}{12B}x^3 \\ & - \left(\frac{J_{GB}\Omega L}{24B} + \frac{m}{L}\right)x^2 + mx \\ & + \left\{ \sum_{n=1}^{\infty} \left( \frac{mL}{(n\pi)^2} + \frac{J_{GB}\Omega L^3}{8B(n\pi)^4} \right) \exp\left(-n^4 \frac{t}{\tau}\right) \cos\left(\frac{2n\pi}{L}x\right) \right\} \end{aligned} \quad (9.7)$$

It can be verified that for  $J_{GB} = 0$ , the above expression reverts to the solution by Hackney [262] for GB grooving of periodic array of grains with origin positioned at the groove root. Secondly, the terms involving  $A_1$  do not occur in the solution of Thouless [125] because of the different starting condition of profile of equal curvature rather than a flat one. Finally, the shape of the profile i.e. the steady state ( $y_{ss}(x)$ ) and the transient

( $y_{tr}(x, t)$ ) part is dependent on two non-dimensional parameters  $m$  and  $\alpha = \frac{J_{GB}\Omega L^2}{8B}$ . This can be seen by non-dimensionalizing the profile by  $\bar{x} = \frac{x}{L/2}$  and  $\bar{y} = \frac{y}{L/2}$ . Therefore, the steady state part of the solution given by Eq.(9.5) can be re-written as

$$\bar{y}_{ss}(\bar{x}) = -\frac{\alpha}{24}\bar{x}^4 + \frac{\alpha}{6}\bar{x}^3 - \left(\frac{\alpha}{6} + \frac{m}{2}\right)\bar{x}^2 + m\bar{x}. \quad (9.8)$$

Similarly, the transient part (Eq.9.7) can be written as,

$$\bar{Y}(\bar{x}, t) = \frac{\alpha}{45} - \frac{m}{3} + \left\{ \sum_{n=1}^{\infty} \left( \frac{2m}{(n\pi)^2} + \frac{2\alpha}{(n\pi)^4} \right) \exp\left(-n^4 \frac{t}{\tau}\right) \times \cos(n\pi\bar{x}) \right\}$$

In steady state, the groove depth relative to mean surface position is given by,

$$\bar{y}(0) = -\frac{m}{3} + \frac{\alpha}{45}. \quad (9.9)$$

While, the surface maximum from the mean position is given by,

$$\bar{y}(L/2) = \frac{m}{6} - \frac{7\alpha}{360}. \quad (9.10)$$

Thus for a negative  $\alpha$ , the groove is expected to become deeper and the surface maximum elevated compared to that in the absence of any GB flux.

## 9.2.2 Numerical Approach

We next solve the complete non-linear PDE (7.7) using a numerical technique. For this we follow the approach of Klinger et al. [5] by making the substitution  $z = \frac{y'}{\sqrt{1+y'^2}}$  and  $\frac{\partial y}{\partial t} = v_{ss}$  in Eq.(7.7) to obtain,

$$v_{ss} = -B \frac{\partial}{\partial x} \left( \sqrt{1-z^2} \frac{\partial}{\partial x} \left( \frac{\partial z}{\partial x} \right) \right) \quad (9.11)$$

$$v_{ss} = -B \frac{\partial}{\partial x} \left( \sqrt{1-z^2} \frac{\partial^2 z}{\partial x^2} \right) \quad (9.12)$$

$$v_{ss} = -\{J_s\}_x \Omega \quad (9.13)$$

Integrating the above Eq. and evaluating the integration constant from the condition of flux continuity  $J_s(0) = \frac{J_{GB}}{2}$  and using  $v_{ss} = \frac{J_{GB}\Omega}{L}$  from mass balance we get,

$$\frac{J_{GB}\Omega}{BL} x - \frac{J_{GB}\Omega}{2B} = -\sqrt{1-z^2} \frac{\partial^2 z}{\partial x^2} \quad (9.14)$$

Non-dimensionalizing the above Eq. by substituting  $\bar{x} = \frac{x}{L/2}$ ,  $z = \bar{z}$  and  $\alpha = \frac{J_{GB}\Omega L^2}{8B}$  we obtain,

$$\frac{\partial^2 \bar{z}}{\partial \bar{x}^2} = \frac{\alpha(1 - \bar{x})}{\sqrt{1 - \bar{z}^2}} \quad (9.15)$$

The above non-linear ordinary differential equation (ODE) needs to be evaluated for the boundary condition  $\bar{z}(0) = -\bar{z}(2) = \sin \theta_o$ . The ODE is solved using shooting method and the procedure involves the following steps,

- (i) The second order ODE (9.15) is converted to two first ODEs by making the substitution  $u_1 = \bar{z}$  and  $u_2 = \frac{\partial \bar{z}}{\partial \bar{x}}$ . The resulting ODEs write as,

$$\frac{\partial u_1}{\partial \bar{x}} = u_2 \quad (9.16)$$

$$\frac{\partial u_2}{\partial \bar{x}} = \frac{\alpha(1 - \bar{x})}{\sqrt{1 - u_1^2}}, \quad (9.17)$$

subjected to the boundary conditions  $u_1(0) = -u_1(2) = \sin \theta_0$

- (ii) The above boundary value problem (BVP) is transformed to an initial value problem by choosing  $u_2(0) = p$  where  $p$  is an initial guess. The system of ODEs (9.16) and (9.17) are then solved using fourth order Runge-Kutta method iteratively, to obtain the solution at  $u_1(2)$ . However the boundary condition dictates  $u_1(2, p) = -\sin \theta_0$ . Hence, the procedure is repeated with different values of  $p$  until the boundary condition at  $\bar{x} = 2$  is satisfied.
- (iii) To speed up the convergence procedure, after the first two iterations, the subsequent values of  $p$  are obtained by using the secant method by converting the BVP to a root finding problem for  $f(p) = u_1(2, p) + \sin \theta_0 = 0$  as,

$$p_{i+2} = p_{i+1} - (p_{i+1} - p_i) \frac{f(p_{i+1})}{f(p_{i+1}) - f(p_i)}. \quad (9.18)$$

The iteration is stopped when  $f(p) < 10^{-6}$ .

### 9.3 Results

The numerical parameters selected in the phase-field simulations are given in Table 9.1. In the present chapter both constant voltage (CV) and constant current (CC) EM testing are employed. It is important to note that in the CV set-up, as the surface drifts under the action of EM, the conductor length  $L_m$  decreases, as a result of which  $E_m$  (and concomitantly  $J_{GB}$ ) drops overtime. The reported  $E_m$  corresponds to the initial value.

Table 9.1: Non-dimensionalized numerical parameters used in the present study and corresponding interfacial properties

Parameter	Non-dimensional value
$\kappa_\rho$	1
$\kappa_\eta$	0.33
$A, B, C$	1
$M_B$	$10^{-6}$
$M_{GB}$	0.2, 0.5, 1.0, 2.0
$M_S$	1.0
$ze$	-5
$\phi$	$\pm 0.01, 0.05, 0.1$
$\sigma_m$	3
$\sigma_u$	0.3
$\Delta x, \Delta y$	0.5
$L_u, L_m$	$64 \Delta x$
$L$	$100 \Delta x$
$\Delta t$	0.001
$\gamma_S$	0.58
$\gamma_{GB}$	0.40
$\delta_S$	3.5
$\delta_{GB}$	2.4

On the other hand, in the CC set-up, ensures a constant  $E_m$  throughout the course of drift. Thus, the two BCs are motivated to test whether the assumption of constant GB flux  $J_{GB}$  is necessary to attain a steady state drift.

### 9.3.1 No grain boundary flux

#### 9.3.1.1 Steady state groove profiles

As a benchmark calculation, we first compare the solution obtained from the three methods in absence of any GB flux. The analytical equilibrium profile is a circular profile of equal curvature given by  $\bar{y}(\bar{x}) = -\frac{m}{2}\bar{x}^2 + m\bar{x}$  obtained by substituting  $\alpha = 0$  in Eq.(9.8). The numerical profile is obtained by solving Eq.(9.15) with  $\alpha = 0$ . The interface profile from the phase-field simulation is extracted as the  $\rho = 0.5$  level set. Care must be taken to locate the groove root from the phase-field simulations. In the sharp interface solu-

tion, invoking the symmetry of the problem about the groove root, only a single branch on the either side of the root is calculated. The other branch is obtained as the mirror image of the former and both branches intersect at a single point at the root. In the phase-field solution, however, due to the diffuse nature of the GB, both branches rather than intersecting sharply forms a blunt concave region. This is purely an artifact of the phase-field method. In order to locate the groove root precisely, we fit the  $\rho = 0.5$  level set on the either side of the GB by fourth order polynomial leaving out the points in the interfacial region. The root is defined as the intersection point of the fit. Consequently, while comparing to the sharp interface solution, the phase-field profile is adjusted such that the root obtained from the intersection is placed at  $y = 0$ .

The sharp-interface numerical and the phase-field solution show a good agreement as evident in Fig.9.2(a), while the analytical calculation predicts a slightly elevated profile. It is to be noted that  $\gamma_S$  and  $\gamma_{GB}$  selected in the present study corresponds to  $m(= \tan \theta_o) = 0.3615$  which clearly violates the SSA ( $m < 0.2$ ) employed in the analytical calculation. A consequence of such an approximation implies an overestimation of the curvature during groove evolution. However, even with such a simplified assumption the analytical solution is within 3% of both the non-linearized as well as the phase-field solution. This not only validates our phase-field formulation and its implementation but also indicates that the analytical solution obtained from the linearized PDE (9.1) serves as an excellent approximation of the complete non-linear problem in absence of any grain boundary flux.

### 9.3.1.2 Temporal evolution of the groove depth

We define the groove depth as the position of the groove root relative to the initial flat surface. For the analytical expression this translates to,

$$d_g = y(0, 0) - y(0, t) \quad (9.19)$$

which according to Eq.(9.7) with  $J_{GB} = 0$  can be written as,

$$d_g = \frac{mL}{6} - \frac{mL}{\pi^2} \sum_{n=1}^{\infty} \frac{1}{n^2} \exp\left(-n^4 \frac{t}{\tau}\right). \quad (9.20)$$

A comparison of the above expression to that from the phase-field simulation is presented in Fig.9.2(b). The position of the groove root from the simulations is determined as discussed above. The general agreement is quite good with the analytical expression overestimating the equilibrium groove depth by about 3.6%. The behavior of the early stages is particularly interesting, as it exhibits a slope of 1/4. This can be also be shown

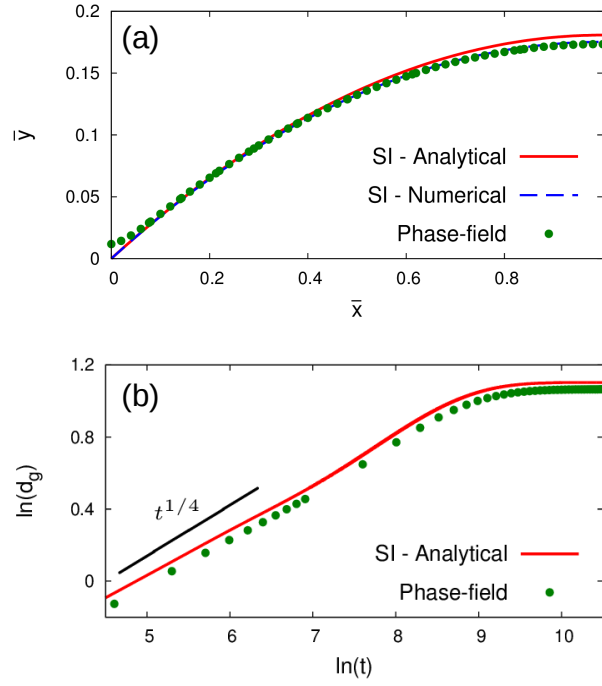


Figure 9.2: a) Comparison of the equilibrium groove profile obtained from the three methods for the case of no grain boundary flux. The agreement between the sharp-interface numerical and the phase-field method is good, while the analytical method based on the small slope approximation overestimates the curvature leading to a slightly elevated profile. (b) Comparison of the temporal evolution of the groove depth from the analytical and the phase-field method. Although the small slope approximation overestimates the groove depth, the initial  $t^{1/4}$  law predicted by the analytical method is preserved as evident from the curve obtained from the phase-field method.

more formally by using Mellins' transform as  $t \ll \tau$  [243],

$$\begin{aligned}
 d_g &= \frac{mL}{6} - \frac{mL}{\pi^2} \left\{ \frac{\pi^2}{6} - \frac{\pi}{2\sqrt{2}\Gamma(5/4)} \frac{2\pi}{L} (Bt)^{1/4} \right\} \\
 &= \frac{m(Bt)^{1/4}}{\sqrt{2}\Gamma(5/4)} \\
 &= 0.78m(Bt)^{1/4},
 \end{aligned} \tag{9.21}$$

which is same as the expression derived by Mullins for the case of isolated grooves. This extends the validity of Mullins' expression for groove depth for interacting grooves in finite grain systems at early times. Moreover, the simplification of SSA does not alter the  $t^{1/4}$  scaling, but only affects the constant prefactors appearing in the expression.

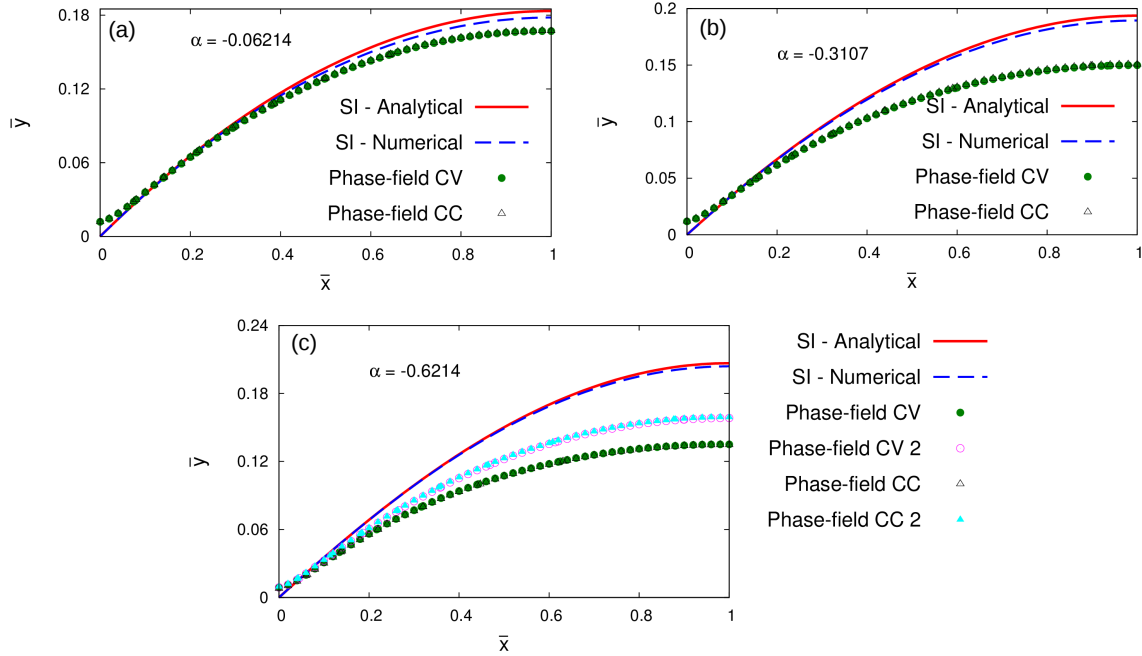


Figure 9.3: Steady state groove profiles obtained from the three methods for different values of non-dimensional parameter  $\alpha$ . The atomic mobilities  $M_{GB}$  and  $M_S$  are selected to be 0.5 and 1 respectively for all the SI-Analytical, SI-Numerical and Phase-field CV and CC cases. The grain boundary flux  $J_{GB}$  is varied by changing the applied potential  $\phi$  in constant voltage set-up or current density  $j$  in constant current set-up as (a)  $\phi = \pm 0.01$ ,  $j = 1.894 \times 10^{-5}$  such that  $J_{GB} = -2.41468 \times 10^{-4}$  and  $\alpha = -0.06214$ , (b)  $\phi = \pm 0.05$ ,  $j = 9.469 \times 10^{-5}$  such that  $J_{GB} = -1.2074 \times 10^{-3}$  and  $\alpha = -0.3107$  and (c)  $\phi = \pm 0.1$ ,  $j = 1.894 \times 10^{-4}$  such that  $J_{GB} = -2.41468 \times 10^{-3}$  and  $\alpha = -0.6214$ . The phase-field method consistently yields a flatter profile in comparison to the sharp-interface model. Additional set of phase field simulation in (c) corresponding to CV 2 and CC 2 for  $J_{GB} = -2.41468 \times 10^{-3}$  and  $\alpha = -0.6214$  with  $M_{GB} = 1$ ,  $M_S = 1$  and  $\phi = \pm 0.05$ ,  $j = 9.469 \times 10^{-5}$  leads to a second solution even though the sharp-interface model gives rise to a unique solution.

## 9.3.2 Grooving under electromigration

### 9.3.2.1 Steady state groove profiles

$J_{GB}$  can be varied by either changing the GB atomic mobility  $M_{GB}$  or alternatively by changing  $E_m$  across the conductor by adjusting the value of the prescribed potential at the domain edges according to Eq.(4.163). We first fix the value of  $M_S = 1$ ,  $M_{GB} = 0.5$  and vary the applied potential as  $\phi = \pm 0.01, 0.05, 0.1$  for the constant voltage case. Equivalently, the current density is varied as  $j = 1.894 \times 10^{-5}, 9.469 \times 10^{-5}, 1.894 \times 10^{-4}$  for the case of constant current such that,  $J_{GB} = -2.41468 \times 10^{-4}, -1.2074 \times 10^{-3}$  and  $-2.41468 \times 10^{-3}$  respectively. In terms of the non-dimensional parameter  $\alpha$ , the values correspond to  $-0.06214, -0.3107$  and  $-0.6214$  such that the values lie within the global steady state regime of surface evolution.

A critical comparison of the steady state profile from sharp interface analytical(Eq.9.6), numerical solutions and phase-field simulation is presented in Fig.9.3. With increasing values of  $\alpha$ , the numerical solution approaches the analytical solution. However, for the range of  $\alpha$  probed, the difference is not significant. A convincing agreement is also found for the steady state profiles obtained from the constant voltage and the constant current set up from the phase-field simulations. Moreover, a significant disagreement between the numerical and the phase-field solution can be observed for higher values of  $\alpha$  (Fig.9.3(b) and (c)) Another point to be noted is that height of the profiles i.e. the distance between the groove depth relative to the surface maximum increases with increasing magnitude of  $\alpha$ . On the contrary, the phase-field profiles consistently become flatter with increasing  $\alpha$ .

Another implication of the sharp interface analytical and numerical solution (Eqs.(9.5) and (9.15) respectively) is that the steady state profile depends on the parameter  $\alpha$ . In other words, the sharp-interface predicts a unique solution for a given  $\alpha$ . To ascertain the validity of the aforementioned claim, we perform an additional test indicated by CV 2 and CC 2 in Fig.9.3(c) at  $J_{GB} = -2.41468 \times 10^{-3}$  by increasing  $M_{GB} = 1$  and decreasing the applied potential  $\phi = \pm 0.05$  such that  $\alpha = -0.6214$ . The phase-field method results in a second solution for the same  $\alpha$  with the new profile elevated in comparison with the previous one. This essentially implies that shape of the grooves depend not only on the magnitude of  $J_{GB}$ , but also on the individual parameters determining the quantity.

### 9.3.2.2 Temporal evolution of groove depth

The analytical expression of the temporal variation of the groove depth in presence of electromigration can be written from Eq.(9.7) as,

$$d_g = -\frac{J_{GB}\Omega}{L}t - A_0 - \sum_{n=1}^{\infty} \frac{mL}{(n\pi)^2} \exp(-n^4t/\tau) - \sum_{n=1}^{\infty} \frac{J_{GB}\Omega L^3}{8B(n\pi)^4} \exp(-n^4t/\tau) \quad (9.22)$$

For  $t \ll \tau$  the above expression can be simplified using Mellins' transform as,

$$d_g = -\frac{J_{GB}\Omega}{L}t - \frac{m(Bt)^{1/4}}{\sqrt{2}\Gamma(5/4)} + \frac{J_{GB}\Omega}{2B} \frac{(Bt)^{3/4}}{\sqrt{2}\Gamma(7/4)} = -\frac{J_{GB}\Omega}{L}t - 0.78m(Bt)^{1/4} + 0.38\frac{J_{GB}\Omega}{B}(Bt)^{3/4} \quad (9.23)$$

Thus, in addition to the  $t^{1/4}$  dependence as in the case of  $J_{GB} = 0$ , two other time-dependent terms namely  $t^{3/4}$  and  $t$  arise in presence of external grain-boundary flux which become progressively important at larger  $t$ . We mention that the  $t^{1/4}$  dependence does not arise in the solution of Thouless [125] because of the different initial starting profile of equal curvature. Furthermore, the second ( $t^{1/4}$ ) and the third term ( $t^{3/4}$ ) of the solution is same as that derived by Genin et al. [124] for the case of isolated grooves under stress implying the validity of the solution in the case of finite grains when any overlap from the neighboring profiles is absent. Eventually for  $t \gg \tau$  the linear term in  $t$  responsible for uniform thinning dominates as,

$$d_g = -\frac{J_{GB}\Omega}{L}t + \frac{mL}{6} - \frac{J_{GB}\Omega L^3}{720B} \quad (9.24)$$

A comparison of the analytical expression and phase-field numerics for the three  $\alpha$  values are shown in Fig.9.4. For all the three cases, the early stage  $t^{1/4}$  behavior and the late stage linear drift in  $t$  are clearly observable from the phase-field computation. Secondly, with increasing  $J_{GB}(\alpha)$ , the overall agreement between the curves become poorer. The most striking feature of the disagreement is the increasing relative disparity until intermediate times. Specifically, if we observe the curves in Fig. 9.4 (b) and (c) at  $\ln 8 - \ln 10$  the disagreement appears to be significantly larger when compared to the early stages. At this point it is important to contrast this temporal disparity to the case of  $J_{GB} = 0$  in Fig.9.2(b) where the analytical and phase-field results differ by a constant factor throughout the evolution process. While the analytical solution enters a transient higher deepening rate regime followed by a slower kinetic regime, the phase-field curves exhibit an early dip and subsequently enter the steady state faster. The dip appears larger for  $\alpha = -0.6214$  obtained at lower  $M_{GB}$  and higher  $\phi/j$  (Phase-field CV/CC) than that at higher  $M_{GB}$  and lower  $\phi/j$  (Phase-field CV 2/CC 2) as observed in Fig.9.4(c).

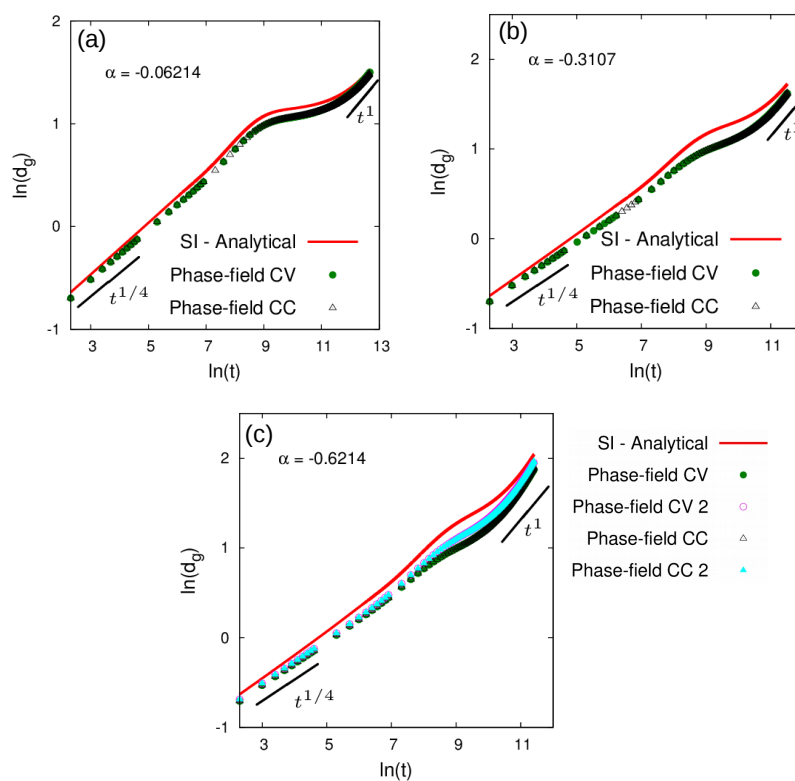


Figure 9.4: The temporal evolution of the groove displacement for the same parameter set used in Fig. 9.3. After an initial  $t^{1/4}$  temporal law, a linear regime implying a steady state drift is attained in both analytical and phase-field solution. The analytical solution, however, overestimates the displacement and more so at higher values of  $\alpha$ . In the intermediate times, the analytical solution transits to a higher deepening rate, which is suppressed in the phase-field solution eventually exhibiting an early dip.

### 9.3.2.3 Role of EM surface flux

Let us next try to resolve the source of these discrepancies by critically examining the assumptions involved in deriving the analytical and numerical solutions. The sharp interface analytical solution differs from the numerical counterpart only in the linearization of the governing equation i.e. the SSA. The phase-field computation, similar to the sharp-interface numerical solution does not rely on SSA and infact treats the complete non-linear problem. The minor disagreement between the analytical and numerical sharp interface solutions, while an increasing discrepancy with the phase-field solution in Fig.9.3 suggests the possibility of a different source of disparity other than the SSA.

The analytical and numerical solution of PDE (7.7) pertains to a generalized case of grooving under any kind of GB flux. In presence of EM, however, it overlooks an additional mode of transport in form of EM-induced surface flux ( $J_S^E$ ). Although the initial surface is perpendicular to the direction of electric field, the formation of GB grooves exposes a fraction of the free surface to the electron wind. The direction of this flux depends on the sign of  $ze$  which being negative is directed towards the groove root. Thus, while  $J_{GB}$  drains material out of the root,  $J_S^E$  provides a healing flux. In absence of  $J_{GB}$ , grooves develop at the surface-GB intersection as a result of the system trying to attain the equilibrium dihedral angle, resulting in the reduction of GB length, while expelling material onto the surface. This results in formation of ridges instigating curvature-gradients along the surface which further provide the impetus for mass flux  $J_S^{\nabla\kappa_s}$  by flattening the ridges. This momentarily upsets the dihedral angle resulting in further deepening of the groove by transporting material to the surface. This process is repeated until the circular profile of equal curvature develops. In presence of EM-induced GB flux,  $J_{GB}$  provides an additional driving force for GB reduction. As a result, both the groove depth and the surface maximum predicted by the sharp-interface calculation are higher in presence of  $J_{GB}$  than that solely evolving under  $J_S^{\nabla\kappa_s}$ . However, the presence of  $J_S^E$  (which is inherently accounted in phase-field simulations) would oppose both increment of groove depth and formation of ridges by transporting material back to the root. The magnitude of  $J_S^E$  depends on  $M_S$  and the projection of the electric field (which is dependent on applied potential for CV set-up and applied current density for CC set-up) on the surface. As we increase  $J_{GB}$  by increasing the applied potential,  $J_S^E$  infact increases concomitantly which induces a higher net flux along the freshly exposed groove walls. It is worth mentioning that  $J_S^E$  depends upon the shape of the evolving surface and increases as the groove deepens because of the exposed fresh surfaces until a steady shape is attained.

Thus  $J_{GB}$  obtained at a higher  $E_m$  (higher  $\phi$  or  $j$ ) and lower  $M_{GB}$ , inadvertently results in higher  $J_S^E$  than that at lower  $E_m$  (lower  $\phi$  or  $j$ ) and higher  $M_{GB}$ . That this is indeed true can be verified in Fig.9.5 where a representative instance of EM surface flux

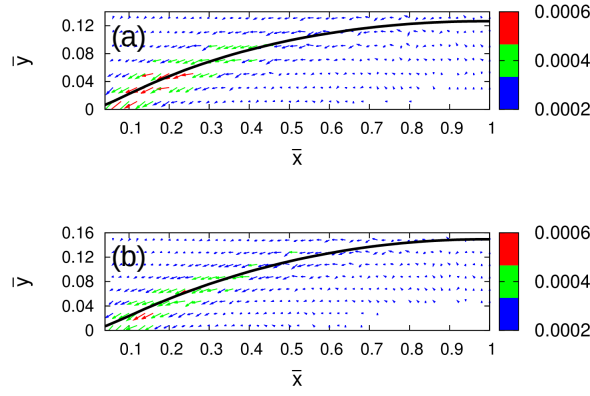


Figure 9.5: The net surface flux vectors for the two parameter sets corresponding to Fig.9.3(c) for the constant voltage set-up after the steady state shape of the groove profile has been attained. Higher applied electric field leads to higher healing surface flux in (a) as compared to (b) as evident from the number of high magnitude red arrows. As a result, the groove profile in Fig.9.3(c) is flatter as well as the groove displacement is lower in Fig.9.4(c) for the first set of parameter.

vectors for the two sets of parameters utilized in Fig.9.3(c) is presented. The intensity of EM surface flux currents near the root (signified by red arrows) for the former case is higher than the latter. This explains the flatness of the steady state profile and the greater dip in groove displacement for the first set of parameters in Fig.9.3(c) and Fig.9.4(c).

We next examine the effect of individual parameters comprising  $J_{GB}$  i.e.  $M_{GB}$  and  $E_m$ . The groove depth relative to the surface maximum,  $d = |y(0)| + |y(L/2)|$  (from Eq.(9.9) and (9.10)) from the analytical and phase-field method is plotted against  $E_m$  in Fig.9.6. We fix  $M_{GB}/M_S = 0.5$  and vary  $\phi = \pm 0.01, 0.05, 0.1$ . The sharp-interface analytical and numerical methods predict a linear increase of groove depth with increasing magnitude of  $E_m$ . Phase-field, on the other hand, exhibits an opposite trend albeit the decrease is non-linear. The groove depth decreases with increasing  $E_m$  because of enhanced  $J_S^E$ .

We next fix  $\phi = \pm 0.1$  and vary  $M_{GB} = 0.2, 0.5, 1.0, 2.0$ . The resulting curves are shown in Fig.9.7. A linear behavior can be observed with increasing  $M_{GB}$ , albeit the sharp-interface consistently overestimates the groove depth. Another point to note is that both the curves (sharp-interface and phase-field) do not exhibit same slope (or in other words are not parallel) and diverge at higher values, indicating that  $J_S^E$  does play a role even though the electric field across the conductor is equal in all the cases. Increasing  $E_m$  (keeping  $M_{GB}$  and  $M_S$  fixed) not only increases  $J_{GB}$ , but also has a direct effect on  $J_S^E$  as a result of which the groove depth decreases in the former case; the relatively slower rate of increase of the groove depth due to increment of  $M_{GB}$  (keeping  $E_m$  and  $M_S$  fixed) is more of a causality. Although  $M_{GB}$  does not directly affect  $J_S^E$ , it does lead

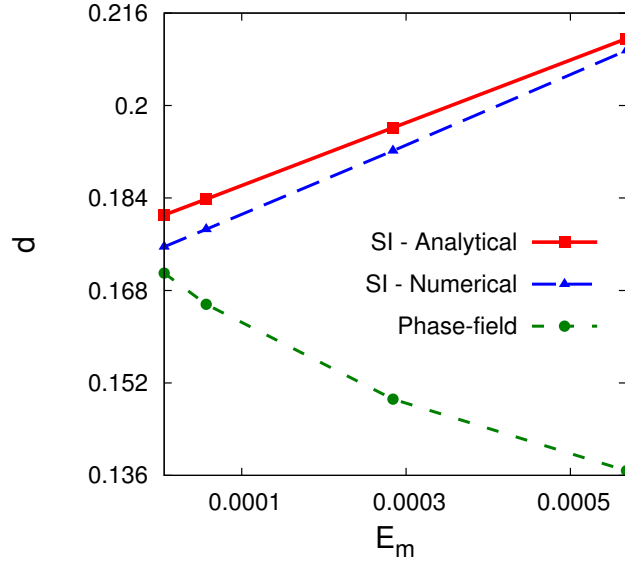


Figure 9.6: The variation of groove depth  $d$  measured from the surface maximum with the applied electric field  $E_m$ . While the sharp interface method (analytical as well as numerical) predicts an increase of  $d$  with increasing  $E_m$ , the phase-field method exhibits an opposite trend. The discrepancy can be rationalized on the basis of electromigration-induced surface flux not accounted in sharp-interface models which provides a healing effect leading to the premature arrest of groove penetration.

to larger groove extension and consequently a larger fraction of the exposed groove walls due to which  $J_S^E$  will be higher. However, in contrast to the former case the effect is not prominent enough to overcome the effect of increasing  $J_{GB}$ .

### 9.3.2.4 Drift velocity

We next examine the drift characteristics in light of drift velocity experiments. In drift velocity experiments, the drifting edge attains a steady state characterized by a linear displacement-time curve following an initial incubation period [89]. In the present case the initial grooving stage can be regarded as the incubation period. The origin of the incubation period can also be inferred from the two time dependent terms (first and last parentheses) in Eq.(9.7). While the former term relates to the surface drift which is dominant at larger  $t$ , the latter describes the groove extension and is pre-eminent at smaller  $t$ . Of course, the prefactors also dictate the transition between grooving and drift. A higher  $J_{GB}$  and a higher  $B$  will facilitate the advent of the drift stage, resulting in a shorter incubation stage. The above inference is quite consistent with the drift velocity experiments where the incubation period is found to be inversely dependent on temperature [89], which can be attributed to the Arrhenius type dependence of diffusivity

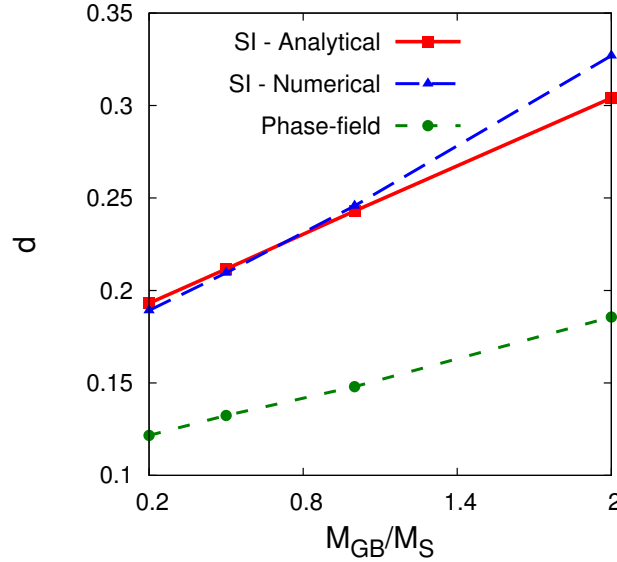


Figure 9.7: The variation of groove depth  $d$  measured from the surface maximum with grain boundary atomic mobility  $M_{GB}$  relative to surface atomic mobility  $M_S$ . Although both sharp interface (analytical as well as numerical) and phase-field model predict an increase of  $d$  with increasing  $M_{GB}$ , the sharp-interface method considerably overestimates the groove dimensions. The discrepancy increases with increasing  $M_{GB}$ .

on temperature as a result of which both  $M_{GB}$  (hence  $J_{GB}$ ) and  $M_S$  (hence  $B$ ) decrease.

The steady state velocity  $v_{ss}$  from simulations is extracted from the slope of the displacement-time curves (as in Fig.9.4) by fitting a straight line in the linear regime. It should be noted that presence of EM surface flux should not alter the kinetics of drift which is derivable through a mass balance equation given by Eq.(9.4). As a result, unlike the steady state profile, the steady state velocity should be invariant to the individual variation in  $M_{GB}$  and  $E_m$  as long as it results in equivalent  $J_{GB}$ . The universal scaling on  $J_{GB}\Omega/L$  is evident in Fig.9.8 where all the data points collapse on a single master curve. The results from the both CV and CC set-up converge towards the same steady state.

## 9.4 Discussion and Conclusion

In the present work we employ analytical and numerical approaches to investigate the effect of electromigration on GB-grooving. The sharp-interface theory based on Ref. [5] which is valid for arbitrary constant GB flux is shown to lead to significant errors when specifically applied to the case of EM. We conclude the chapter by summarizing the discrepancies originating out of the simplified assumptions involved in deriving the sharp-interface theory in light of the results obtained from the phase-field simulations.

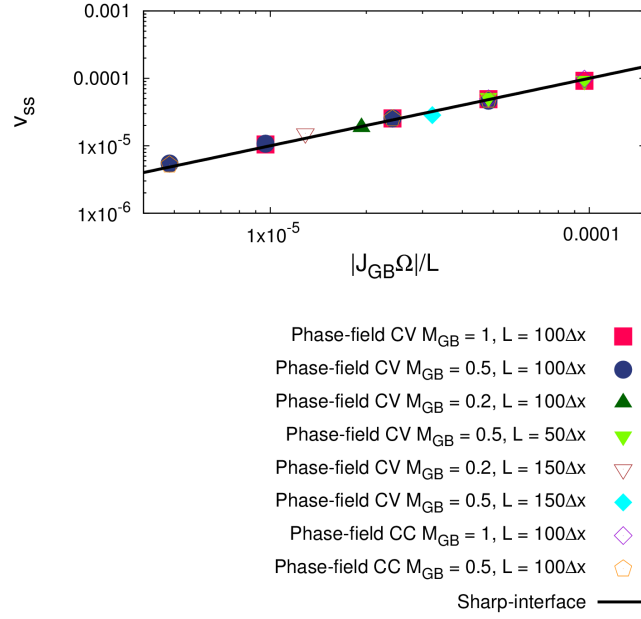


Figure 9.8: The universal scaling of steady state velocity on grain boundary flux  $J_{GB}$  and grain size  $L$ . The solid line represents the linear behavior of the sharp-interface model. The points correspond to the data obtained from the phase-field simulations for both constant voltage and constant current set-up.

1. *Morphological stability in terms of  $\alpha$*  : An important consequence of the present results is that the parameter  $\alpha = \frac{J_{GB}\Omega L^2}{8B}$  that has hitherto been used to predict groove shapes and damage mechanisms in polycrystalline interconnects [5, 76, 86] is infact inadequate to estimate either the correct steady state shape or the kinetic regime of damage. For instance, one can fix the ratio  $\frac{M_{GB}}{M_S}$  and increase  $\alpha$  by increasing the applied field  $E_m$  which should shift the kinetic regime from global steady state to the local steady state (slit along GB). However, as evident from the groove profiles in Fig.9.6, increasing  $\alpha$  by increasing  $E_m$  alone suppresses slit forming propensity because of enhanced  $J_S^E$ . Rather, the phase-field simulations emphasize the critical role of  $\frac{M_{GB}}{M_S}$  on the stability of the surface. Below a critical value of  $\frac{M_{GB}}{M_S}$  no slit solution is possible and increasing  $E_m$  leads to premature arrest of GB grooving. Thus, the presence of  $J_S^E$  introduces an additional degree of freedom to ascertain the morphological stability of the GB grooves.

Secondly, since  $J_S^E$  is governed by the shape of the profile, it is a time-dependent quantity which increases temporally as grooving proceeds. As a result, although the initial  $t^{1/4}$  and late stage  $t$  regime predicted by the analytical theory is preserved, the intermediate regime characterized by the interplay of the  $t^{1/4}$  and  $t^{3/4}$  dependence is suppressed as evident in Fig.9.4 The results derived from analytical expressions at

higher  $E_m$  and higher  $M_{GB}$  are more prone to errors as compared to the phase-field counterparts. Subsequently, the steady state is achieved faster. The steady state behavior, however, remains unaffected and scales linearly with  $J_{GB}$ .

2. *Small slope approximation* : Based on the assumption of SSA in analytical theory, a global steady state solution is always possible. However, as shown in Ref. [5], relaxing SSA results in a finite interval of  $\alpha$ , only within which a steady state is warranted. In this interval, the sharp interface analytical and numerical solution diverge as the limits of the steady state range is approached implying the breakdown of the SSA. Accounting for EM surface flux in the phase-field method further restricts the region of steady state solution (which is now characterized by two independent variables which are function of  $\frac{M_{GB}}{M_S}$  and  $E_m$ ). Moreover, in the new interval in addition to SSA, non-consideration of  $J_S^E$  leads to significant errors as evident from Fig.9.3.
3. *Scaling on grain size  $L$*  : A careful consideration of sharp-interface Eqs.(9.9) and (9.10) suggests that the scaled groove dimensions depend only upon the non-dimensional quantities  $m$  and  $\alpha$ . This essentially implies the invariance of the scaled groove dimensions on grain size  $L$ . The same also holds true for the sharp-interface numerical solution. However, as evident from the phase-field simulations,  $\alpha$  does not result in a unique solution. Furthermore, the presence of EM surface flux  $J_S^E$ , depends upon the fraction of exposed groove walls which in turn is dependent on the grain size. This results in the violation of the scale invariance of grain size according to the expression of  $\alpha$ .
4. *Constant GB flux* : Another simplification which makes the problem analytically tractable is the assumption of steady state GB diffusion and constant GB flux utilized to derive the flux boundary condition at the root [124]. A steady state GB diffusion is attained in both the cases following an initial transient stage in the simulations. While the assumption of constant GB flux in the phase-field simulations is true in constant current, drifting (as a result of which  $L_m$  decreases) will lead to decrease in the GB flux in the constant voltage set-up. As a result, a slightly higher steady state velocity was observed in the simulations with the constant current at higher  $J_{GB}$  values. For the cases, where grooving comes to a halt the groove depth is found to be higher for the constant current case. For the cases, where  $L_m$  changes significantly during the damage process, for instance in the case of slit propagation we expect the constant current and constant voltage to yield different results in terms of the steady state velocity.

The results presented in the chapter can significantly enhance our understanding of

damage morphologies in copper metal lines which are severely affected by the surface conditions [107, 76, 86]. If the surface diffusion along the freshly exposed groove walls are not blocked or hindered by passivation or impurities, EM-induced surface flux will promote damage my global thinning of grains and save the line from the more pervasive failure in form of intergranular slits.

Healing is an integral process of EM-induced damage. *In situ* experiments have previously demonstrated this aspect during void growth and migration in Aluminum interconnects [99, 263]. Premature termination of groove penetration in bamboo type lines was reported by Ogurtani and Akyildiz [120, 142] and Averbuch et al. [264] using computer simulations. Since most healing effects are generally time dependent, their consideration in analytical theories might not be all that straightforward. For instance, in the present case the  $J_S^E$  can be accounted by transforming the governing equation in terms of  $\theta$ , the surface tangent and  $x$  by replacing Eq.(7.3) by,  $J_S = \frac{D_s \delta_S}{\Omega k_B T} [-\Omega \gamma_S \frac{d\kappa}{ds} + zeE_m \sin \theta]$ , where  $\kappa = \frac{d\theta}{ds}$  and  $\frac{dx}{ds} = \cos \theta$ . Boundary condition in  $\theta$  is then needed to close the equation. However, this in turn requires the information of the shape of the profile itself. Such an approach is employed in the case of slit propagation by assuming a constant shape of the slit surface [95, 96, 94]. Although the governing equations turn out to be highly non-linear, the solution (which require numerical techniques) provides information only on the time-independent steady state shape.

The results presented in the chapter demonstrate that phase-field method is a promising tool to capture the entire temporal evolution of EM damage initiation, propagation and healing elegantly. Particularly fortifying is the ability of the phase-field method to capture the drift velocity characteristics over a magnitude of GB flux. Drift velocity experiments provide valuable information on the activation energy of the process, which in turn further identifies the dominant diffusional pathway.

# Chapter 10

## Grain boundary grooving in finite grains due to concurrent surface and grain boundary electromigration

### 10.1 Introduction

The theoretical GB grooving model by Klinger and Glickman [5, 126] considers the evolution of grooves under the combined influence of capillary-mediated surface diffusion and grain boundary electromigration (GBEM). The model, however, is limited on account of ignoring the EM-mediated surface flux running along the groove walls. It was shown in the previous chapter using a phase-field method (where EM-induced surface flux is inherently captured), that not considering such flux can lead to errors in ascertaining the temporal evolution of the groove root as well as the equilibrium groove profile. The aim of the present chapter is to extend the model of Ref. [5] to incorporate the effect of EM surface flux and study the steady state groove profiles. It will be shown that unlike the previous work, accounting the surface EM flux introduces an additional degree of freedom to describe the groove shapes. The present chapter is organized as follows. In the succeeding section (Sec. 10.2), the mathematical model of GB grooving under concurrent surface and GBEM is presented. Thereafter in Sec.10.4, the effect of model parameters on the groove profile is discussed. In addition, the steady state solution regimes in the model parameter space are explored. The model predictions are then critically compared with the solutions from the phase-field method and that from Ref. [5]. The chapter is concluded in Sec. 10.5 by a brief summary and discussion of the implications of the findings of the present work.

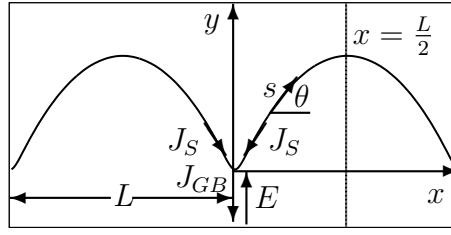


Figure 10.1: Schematic depicting the steady state groove profile and the choice of coordinate system (in a moving frame of reference) used in the present work. The origin is selected at the groove root. The applied electric field  $E$  in the interconnect is directed along GB. The steady-state groove shape is determined by the interplay of capillarity and EM-induced surface flux  $J_S$  and EM-induced GB flux  $J_{GB}$ . Invoking the symmetry of the groove profiles, the governing equations are derived for only half the grain size  $L/2$  where  $L$  is the grain size.  $\theta$  is the angle made by the surface arc  $s$  with the  $x$ -axis.

## 10.2 Sharp-interface model

Let  $x - y$  be the coordinate system in the moving frame of reference with the origin coinciding with the groove root as shown in Fig.10.1. The applied electric field  $E$  is directed parallel to the GB. The groove profile  $y(x, t)$  evolves due to the concurrent influence of chemical potential  $\mu$  and electric potential at the surface  $\phi_s$ . The surface flux of the atoms can be written as a linear combination of the driving force from the principle of linear irreversible thermodynamics as

$$J_s = -L_{11}\nabla_s\mu - L_{1e}\nabla_s\phi_s \quad (10.1)$$

$$= J_{chem} + J_{em} \quad (10.2)$$

The chemical part of the surface flux can be written in terms of the average drift velocity ( $\langle v \rangle$ ) of the surface concentration of atoms  $\nu$  as

$$J_{chem} = \nu \langle v \rangle = -\nu M_s \nabla_s \mu \quad (10.3)$$

On comparison with Eq.(10.1)  $L_{11} = \nu M_s$ . The chemical potential of an atom along the surface due to the presence of curvature is given by,

$$\mu = \mu_o + \Omega \gamma_s \kappa_s \quad (10.4)$$

where  $\mu_o$  is the chemical potential of a flat surface,  $\Omega$  the atomic volume,  $\gamma_s$  the surface energy and  $\kappa_s$  the curvature. Inserting Eq.(10.4) in (10.3),

$$J_{chem} = -\nu M_s \Omega \gamma_s \frac{d\kappa_s}{ds}. \quad (10.5)$$

The surface concentration of atoms  $\nu$  is given by  $\nu = \frac{\delta_s}{\Omega}$ .  $\delta_s$  is the thickness of the surface layer.  $M_s$  is the surface atomic mobility which is related to the surface diffusivity  $D_s$  according to the Nernst-Einstein relation as  $M = \frac{D_s}{k_B T}$ . Substituting the above relation in Eq.(10.5),

$$J_{chem} = -\frac{D_s \delta_s \gamma_s}{k_B T} \frac{d\kappa_s}{ds} \quad (10.6)$$

Similarly EM-induced surface flux can be written as

$$J_{em} = -\nu M_s F_{em} \quad (10.7)$$

where  $F_{em}$  represents the driving force for EM which can be approximated by an electrostatic force with an effective surface charge  $z_s e$  as

$$F_{em} = z_s e \frac{\partial \phi_s}{\partial s}. \quad (10.8)$$

Substituting in Eq.(10.7) and using the definition of  $\nu$  and  $M_s$  we have

$$J_{em} = -\frac{D_s \delta_s}{\Omega k_B T} z_s e \frac{\partial \phi_s}{\partial s} \quad (10.9)$$

Substituting Eqs.(10.6) and (10.9) in (10.1) the surface flux can be re-written as

$$J_s = -\frac{D_s \delta_s \gamma_s}{k_B T} \frac{d\kappa_s}{ds} + \frac{D_s \delta_s}{\Omega k_B T} z_s e E_t \quad (10.10)$$

where  $E_t = -\frac{\partial \phi_s}{\partial s}$  is the tangential component of the applied electric field along the surface and is given by  $\beta E \sin \theta$ . The coefficient  $\beta = 2\sigma_m / (\sigma_m + \sigma_u)$  depends upon the conductivity of the metal interconnect  $\sigma_m$  and the outer domain  $\sigma_u$ .  $\theta$  denotes the angle between the surface tangent and  $x$ -axis as shown in Fig.10.1. Rewriting Eq.(10.10) by utilizing the relation  $\kappa_s = -\frac{y'}{(1+y'^2)^{3/2}}$  where  $'$  denotes the derivative with respect to  $x$  co-ordinate and substituting  $F = \frac{y'}{\sqrt{(1+y'^2)}} = \sin \theta$ , such that  $\kappa_s = -\frac{dF}{dx}$ ,

$$J_s = \frac{D_s \delta_s \gamma_s}{k_B T} \sqrt{1-F^2} \frac{d^2 F}{dx^2} + \frac{D_s \delta_s}{\Omega k_B T} z_s e \beta E F. \quad (10.11)$$

Mass conservation along the surface relates divergence of surface flux to the normal velocity as,

$$\frac{dJ_s}{ds} = -\frac{V_n}{\Omega}. \quad (10.12)$$

Assuming the surface drifts in steady state with shape conserving profile,

$$V_n = V \cos \theta. \quad (10.13)$$

Substituting Eq.(10.13) in Eq.(10.12) and using the relation  $dx = \cos \theta ds$ ,

$$\frac{dJ_s}{dx} = -\frac{V}{\Omega}. \quad (10.14)$$

Integrating the above Eq. and finding the integration constant from the condition of continuity of flux at the root  $J_s(0) = J_{GB}/2$ ,

$$J_s + \frac{J_{GB}}{L}x - \frac{J_{GB}}{2} = 0 \quad (10.15)$$

where, the relation  $V = \frac{J_{GB}\Omega}{L}$  has been utilized from the mass balance at the groove root.  $L$  represents the grain size.  $J_{GB}$  is the EM-induced GB flux given by,

$$J_{GB} = \frac{D_{GB}\delta_{GB}}{\Omega k_B T} z_{GB} e E \quad (10.16)$$

where  $D_{GB}$  denotes the diffusivity at the GB,  $\delta_{GB}$  the GB thickness and  $z_{GB}e$  the effective charge of the diffusing species at the GB. Substituting Eqs.(10.11) and (10.16) in Eq.(10.15),

$$\frac{D_s \delta_s \gamma_s}{k_B T} \sqrt{1-F^2} \frac{d^2 F}{dx^2} + \frac{D_s \delta_s}{\Omega k_B T} z_s e E \beta F + \frac{D_{GB} \delta_{GB}}{2 \Omega k_B T} z_{GB} e E \left( \frac{x}{L/2} - 1 \right) = 0. \quad (10.17)$$

Dividing throughout by  $\frac{D_s \delta_s}{\Omega k_B T} z_s e E \beta$ ,

$$\frac{\gamma_s \Omega}{z_s e E \beta} \sqrt{1-F^2} \frac{d^2 F}{dx^2} + F + \frac{D_{GB} \delta_{GB} z_{GB}}{2 D_s \delta_s z_s \beta} \left( \frac{x}{L/2} - 1 \right) = 0. \quad (10.18)$$

Non-dimensionalizing the above Eq. by introducing  $\bar{x} = \frac{x}{L/2}$  the governing Eq. is obtained as,

$$\chi \sqrt{1-F^2} \frac{d^2 F}{d\bar{x}^2} + F + M(\bar{x} - 1) = 0 \quad (10.19)$$

where,

$$\chi = \frac{4\gamma_s \Omega}{z_s e E \beta L^2} \quad (10.20)$$

and

$$M = \frac{D_{GB} \delta_{GB} z_{GB}}{2 D_s \delta_s z_s \beta}. \quad (10.21)$$

Eq.(10.19) is solved subjected to the following boundary conditions,

$$F = \sin \theta_o = \Gamma \quad \text{at} \quad \bar{x} = 0 \quad (10.22)$$

where  $\Gamma = \frac{\gamma_{GB}}{2\gamma_s}$  and  $\gamma_{GB}$  is the grain-boundary energy. The symmetry of the problem also dictates,

$$F = 0 \quad \text{at} \quad \bar{x} = 1. \quad (10.23)$$

Two non-dimensional groups arise from the governing Eq.(10.19), namely  $\chi$  and  $M$ . The number  $\chi$  denotes the ratio of capillary force  $\frac{\gamma_s \Omega}{L^2}$  to the surface EM force  $z_s e E$ . Such a number has previously been defined to characterize shapes of voids in several theories of EM-mediated void migration [265, 92] and slit propagation [266, 96, 267]. In case of

circular voids, capillary force maintains the circular shape, while EM force induces shape changes due to mass transport. In the context of the present problem of GB-grooving, the capillary force leads to a surface profile of uniform curvature which is an arc of a circle as in the case of thermal grooves. The presence of EM, however, can significantly alter the steady-state surface profile which need not be circular. Such a case is expected to occur at  $|\chi| < 1$ . The second number  $M$  represents the ratio of rate of EM transport along the GB to that at the surface.

Most commercial interconnects are characterized by negative effective valence implying a dominant wind force. Hence  $z_s e$  and  $z_{GB} e$  are selected to be negative in the present work. This implies that the direction of  $J_s^E$  and  $J_{GB}$  is in the direction of electron wind. While  $J_{GB}$  drains the groove root,  $J_s^E$  transport material to the groove root. Thus  $\chi$  and  $M$  are negative and positive numbers respectively.  $\chi$  and  $M$  along with the groove angle  $\sin^{-1}(\Gamma)$  completely determines the steady state groove profile.

The second order non-linear ordinary differential Eq.(10.19) is solved using Runge-Kutta method coupled to a shooting method. The procedure involves converting the second order ODE to two first-order ODEs by making the substitutions,  $\bar{u}_1 = F$  and  $\bar{u}_2 = \frac{dF}{d\bar{x}}$ . The resulting coupled first order ODEs can then be written as,

$$\begin{aligned}\frac{d\bar{u}_1}{d\bar{x}} &= \bar{u}_2 \\ \frac{d\bar{u}_2}{d\bar{x}} &= \frac{-\bar{u}_1 + M(1 - \bar{x})}{\chi\sqrt{1 - \bar{u}_1^2}}\end{aligned}\quad (10.24)$$

which are solved under the modified boundary conditions  $\bar{u}_1 = \Gamma$  at  $\bar{x} = 0$  and  $\bar{u}_1 = 0$  at  $\bar{x} = 1$ .

### 10.3 Analytical solution of the linearized equation

An analytical solution of ODE (10.19) is permitted if  $\sqrt{1 - F^2} \approx 1$ . In other words, the linearization procedure implies assuming  $F^2 \ll 1$ . Since  $F = \sin \theta$ ,  $F = \frac{d\bar{y}}{d\bar{s}} \approx \frac{d\bar{y}}{d\bar{x}}$  ( $\sin \theta \approx \tan \theta$  for small  $\theta$ ). Thus, linearized version of Eq.(10.19) can be written as,

$$\chi \frac{d^3 \bar{y}}{d\bar{x}^3} + \frac{d\bar{y}}{d\bar{x}} = M(1 - \bar{x}) \quad (10.25)$$

subjected to the boundary conditions,

$$\begin{aligned}\bar{y} &= 0 & \text{at} & \bar{x} = 0 \\ \frac{d\bar{y}}{d\bar{x}} &= 0 & \text{at} & \bar{x} = 1 \\ \frac{d\bar{y}}{d\bar{x}} &= \Gamma & \text{at} & \bar{x} = 0\end{aligned}\quad (10.26)$$

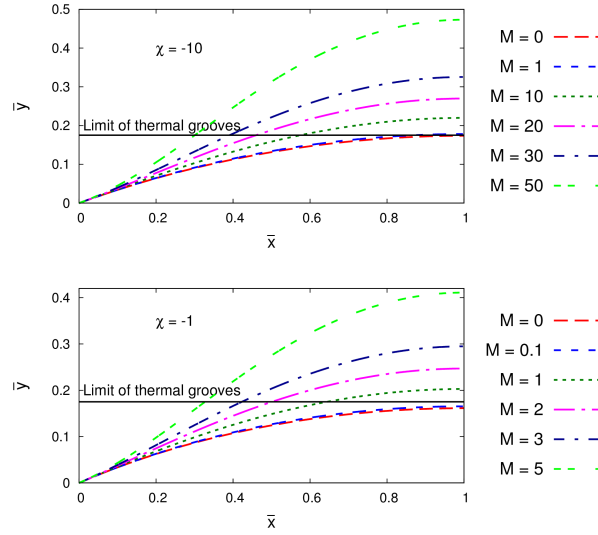


Figure 10.2: Effect of  $M$  on steady state groove profiles at (a) lower EM force  $\chi = -10$  and (b) higher EM force  $\chi = -1$ . The angle at the groove root corresponds to  $\Gamma = 0.34$ . In both cases, groove depth relative to the surface maximum increases with increasing value of  $M$ . At  $\chi = -10$  and  $M = 0$  (i.e.  $D_{GB} = 0$ ), the solution reverts to the case of thermal grooves. At  $\chi = -1$  and  $M = 0$ , a higher surface EM flux acts as a healing agent leading to lower equilibrium groove depth than the thermal groove.

It is to be noted that  $\frac{d\bar{y}}{d\bar{x}} = \frac{\Gamma}{\sqrt{1-\Gamma^2}}$  at  $\bar{x} = 0$ . However, the linearized version of the boundary condition is used in the rest of the derivation.

The solution of Eq.(10.25) which is a third order non-homogeneous linear ODE can be split into homogeneous and non-homogeneous part as [268],

$$\bar{y}(\bar{x}) = \bar{y}_h(\bar{x}) + \bar{y}_{nh}(\bar{x}) \quad (10.27)$$

The solution of the homogeneous part  $\bar{y}_h(\bar{x})$  satisfies the ODE,

$$\chi \frac{d^3 \bar{y}}{d\bar{x}^3} + \frac{d\bar{y}}{d\bar{x}} = 0 \quad (10.28)$$

has the form,

$$\bar{y}_h(\bar{x}) = C_1 + C_2 \exp\left(\frac{x}{\sqrt{\chi}}\right) + C_3 \exp\left(-\frac{x}{\sqrt{\chi}}\right) \quad (10.29)$$

assuming negative  $\chi$ . The solution of the non-homogeneous part  $\bar{y}_{nh}(\bar{x})$  can be found by assuming

$$\bar{y}_{nh}(\bar{x}) = k_1 \bar{x}^2 + k_2 \bar{x}. \quad (10.30)$$

Substituting the derivatives in Eq.(10.25) and comparing coefficient of each power of  $\bar{x}$ ,

$$\bar{y}_{nh}(\bar{x}) = -\frac{M}{2} \bar{x}^2 + M \bar{x}. \quad (10.31)$$

Hence, the complete solution can be written by combining Eqs.(10.29 and 10.31 as,

$$\bar{y}(\bar{x}) = C_1 + C_2 \exp\left(\frac{x}{\sqrt{\chi}}\right) + C_3 \exp\left(-\frac{x}{\sqrt{\chi}}\right) - \frac{M}{2}\bar{x}^2 + M\bar{x} \quad (10.32)$$

Employing the boundary conditions (10.26) the constants can be evaluated as,

$$\begin{aligned} C_1 &= -(C_2 + C_3) \\ C_2 &= \frac{\sqrt{\chi}(\Gamma - M) \exp\left(-\frac{1}{\sqrt{\chi}}\right)}{\exp\left(-\frac{1}{\sqrt{\chi}}\right) - \exp\left(\frac{1}{\sqrt{\chi}}\right)} \\ C_3 &= \frac{\sqrt{\chi}(\Gamma - M) \exp\left(\frac{1}{\sqrt{\chi}}\right)}{\exp\left(-\frac{1}{\sqrt{\chi}}\right) - \exp\left(\frac{1}{\sqrt{\chi}}\right)} \end{aligned} \quad (10.33)$$

## 10.4 Results

### 10.4.1 Effect of $M$ on the groove profile

The effect of  $M$  on the groove profile at two  $\chi$  values of  $-10$  and  $-1$  corresponding to lower and higher surface EM force respectively are presented in Fig.10.2. For a given  $\chi$ , the groove depth relative to the surface maximum increases with increasing value of  $M$ . This increase can be attributed to  $J_{GB}$  which drains the root by transporting material along the GB. Since higher  $M$  implies higher  $D_{GB}\delta_{GB}z_{GB}$ ,  $J_{GB}$  increases with increasing  $M$ . At higher  $\chi$  i.e. lower surface EM force or equivalently lower  $J_s^E$  and  $M = 0$  corresponding to no GB transport, the solution reverts to that of thermal groove as seen in Fig.10.2(a). Higher surface EM force ( $\chi = -1$ ), however, leads to enhanced  $J_s^E$  which acts as a healing mechanism by transporting material towards the groove root. As a result, the steady state groove depth is lower than that of thermal groove in Fig.10.2(b) for the case of  $M = 0$  and  $0.1$ .

### 10.4.2 Effect of $\chi$ on the groove profile

The effect of  $\chi$  on the steady state groove profiles is discussed next. At lower value of  $M(= 0.1)$  which corresponds to the case of faster mass transport along the surface than GB, the groove depth decreases with decreasing the magnitude of  $\chi$  as shown in

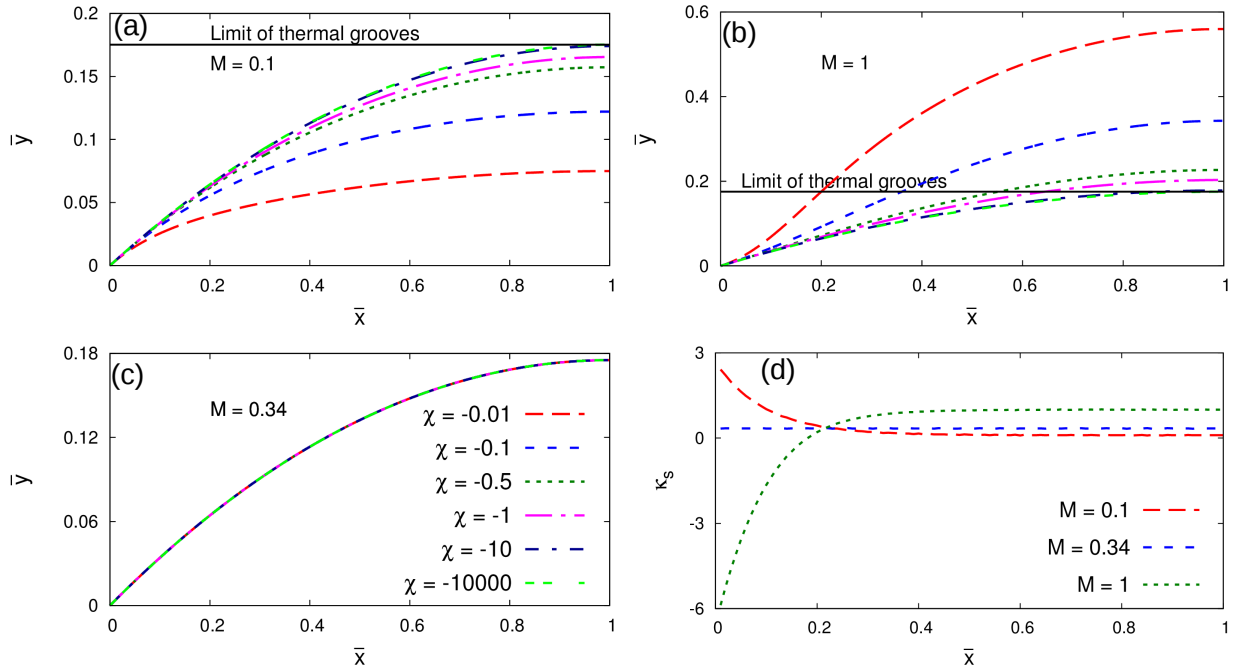


Figure 10.3: Effect of  $\chi$  on steady-state groove profiles obtained from the solution of the non-linear ODE : (a) At lower  $M(= 0.1)$ , the groove depth increases with increasing magnitude of  $\chi$  (the legend is same as (c)) until the limit of thermal groove owing to increasing EM-induced surface healing flux, (b) at higher  $M(= 1)$ , higher GB flux offsets the effect of surface flux and the groove depth decreases with increasing absolute values of  $\chi$ . (c) The groove profiles become independent of  $\chi$  at  $M = \Gamma = 0.34$ . At this value, the GB flux is equally compensated by the healing surface flux. (d) The curvatures along the profile for different values of  $M$  and  $\chi = -0.01$ . While, at  $M = 0.1$ , the profile exhibits convexity throughout, higher  $M = 1$  leads to concavity at the root.  $M = \Gamma$  results in profile of uniform curvature.

Fig.10.3(a). Decreasing  $\chi$  results in the increase of  $J_s^E$  which heals the groove. Moreover, higher surface EM force relative to the capillary force leads to flatter profiles for lower  $\chi$ . As surface EM force decreases, the groove depth tends towards the limit of thermal groove at higher magnitude of  $\chi$ .

The healing surface flux  $J_s^E$ , however, is unable to overcome a faster mass transport along GB for  $M = 1$  in Fig.10.3(b) as a result of which the dependency of profile on  $\chi$  is exactly reversed. The groove depth decreases with increasing absolute values of  $\chi$  until attaining the limit of thermal groove. The next question that naturally arises is at what value of  $M$  does this reversal occur? The behavior of the ODE (10.19) and the dependence of the solution on  $\chi$  and  $M$  can be approximately estimated from the linearized version of the equation which permits an analytical solution. It can be seen from Eqs.(10.32) and (10.33) that for  $M = \Gamma$ , the profiles become independent of  $\chi$ . For  $M < \Gamma$  the height of the profiles increases with  $\chi$ , while profiles become flatter for  $M > \Gamma$ . The non-linear ODE does indeed exhibit a similar behavior as shown in Fig.10.3(c) where the profiles for different values of  $\chi$  overlap for  $M = \Gamma = 0.34$ . It is worth mentioning that only at the condition of  $M = \Gamma$ , the profiles assumes a shape of uniform curvature similar to thermal grooves with a value of  $\kappa_s = M$  (Fig.10.3(d)).

The same inference regarding the value of  $M$  at which the dependency on  $\chi$  reverses can equivalently be drawn by considering the interplay between  $J_{GB}$  and  $J_s^E$ . The condition of uniform curvature renders  $J_s^{\nabla\kappa_s}$  to be zero. The profile is expected to be independent of  $\chi$  when  $J_s^E$  exactly counterbalances  $J_{GB}$ . It is to be noted that  $J_s^E$  varies at each point along the surface and is maximum at the vicinity of the root where the component of the electric field  $E \sin \theta$  is maximum. Thus equating  $J_{GB}$  and the value of  $J_s^E$  at the root gives,

$$\begin{aligned} \frac{D_{GB}\delta_{GB}}{\Omega k_B T} z_{GB} e E &= 2 \frac{D_s \delta_s}{\Omega k_B T} z_s e E \sin \theta_o \\ \Rightarrow M &= \sin \theta_o \end{aligned} \quad (10.34)$$

The factor 2 on the right-hand side of the above equation takes into account the surface flux flowing along both branches of the profile.

An additional pertinent remark regarding the shape of the profile is also in order. At low  $M(= 0.1)$  the surface profiles exhibit a convex shape throughout. Convexity at the root is also preserved for thermal grooves. However, at high values of  $M(= 1)$ , a faster mass transport across the GB promotes concavity at the root as evident in Fig.10.3(d). The transition of the curvature from convex to concave at the root has interesting implication on the contribution towards healing flux. In addition to  $J_s^E$ ,  $J_s^{\nabla\kappa_s}$  instigates atomic transport to the vicinity of the root.

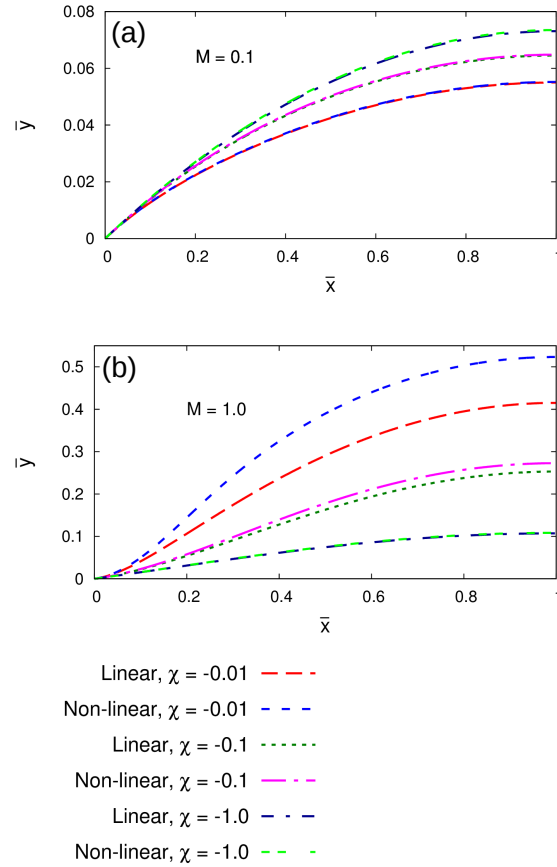


Figure 10.4: Comparison between the solutions obtained from the linearized and the non-linearized version of the governing equations at  $\Gamma = 0.15$ . (a) The linearized ODE provides a good approximation to the non-linearized equation at lower value of  $M (= 0.1)$ . (b) At higher  $M (= 1)$  the linearized and the non-linearized solutions diverge with decreasing absolute values of  $\chi$ .

### 10.4.3 Comparison of the solution of non-linear and linearized equation

Since the linearized ODE (10.25) makes the problem analytically tractable, it is imperative to assess the applicability and the range of validity of the solution in comparison to the non-linear counterpart Eq.(10.19). It is to be noted that the linearization procedure involves assuming  $F = \sin \theta \approx \tan \theta$  which is equivalent to the small slope approximation (SSA) introduced in the seminal work of Mullins [122]. Generally, the slope is maximum at the root and decreases further towards the grain center. The assumption is thus most likely to hold true for  $\Gamma \ll 1$ .

The case of  $\Gamma = 0.15$  is first considered, where, the above assumption is reasonably satisfied. At low  $M (= 0.1)$  corresponding to slower GB transport, a good agreement

between the profiles obtained from Eqs.(10.19) and (10.25) can be observed across all values of  $\chi$  in Fig.10.4(a). As GB transport increases to  $M = 1$  deviations emerge progressively as magnitude of  $\chi$  decreases in Fig.10.4(b). Higher  $M$  and low magnitude of  $\chi$  leads to faster groove extension, as a result of which curvature is underestimated due to utilization of the SSA in the linearized theory.

The case of  $\Gamma = 0.34$  is discussed next. Although the selected value of  $\Gamma$  violates the SSA to a certain degree, a reasonable agreement between the two solutions can be seen in Fig.10.5(a). Another interesting point to be noted is that unlike the case of  $\Gamma = 0.15$ , the linearized solution is more prone to errors at higher magnitude of  $\chi$ . A better consensus at lower absolute values of  $\chi$  can be attributed to higher  $J_s^E$  which in addition to  $J_s^{\nabla\kappa_s}$  opposes accumulation of curvature along the surface, thereby fulfilling the SSA to a greater extent. Given the simplified assumption in the linearized theory, the solution is well within 3% of the exact solution. At higher  $M(= 1)$  however, the two solutions again diverge with decreasing absolute of  $\chi$ .

The above comparison suggests that the linearized ODE 10.25 has a limited range of applicability. The linearized version provides a reasonable approximation only at lower  $M$  and at higher  $\chi$  values for higher  $M$ . Moreover, the linearized ODE 10.25 predicts solution for all possible combinations of  $\chi$ ,  $M$ , and  $\Gamma$  as evident from Eq.(10.32). The same, however, is not true for the non-linear ODE (10.19) as is discussed in the section 10.4.4.

#### 10.4.4 Steady state solution space

The non-linear ODE 10.19 does not possess a solution for all possible combinations of  $\chi$ ,  $M$  and  $\Gamma$ . A few typical two dimensional slices of the steady state solution regions from the three dimensional  $\chi - M - \Gamma$  space is studied.

The solution region in  $\chi - M$  space corresponding to  $\Gamma = 0.34$  is shown in Fig.10.6. The stability limit of  $M$  increases slowly at low  $\chi$  (i.e. greater surface EM force) until  $\chi = 0.1$  and rapidly thereafter. For simplicity, consider a given material system which fixes the parameters  $\gamma_s, z_s, z_{GB}, \Omega, \beta$  and fixed grain size  $L$ . For a given  $\chi$ , which fixes  $E$ , increasing  $M$  increases the ratio of  $D_{GB}/D_s$ . As a result, the upper limit of  $M$  for a given  $\chi$  is limited by the slow surface atomic transport which is incompetent to compensate for the rapid GB atomic transport to maintain a steady state shape. It can be seen in Fig.10.2 that increasing  $M$  promotes concavity at the root, which on further increase can lead to root detachment. Below a critical value of  $M$  (which appears close to 1) a steady state solution is always possible.

The steady state region enlarges at higher  $\chi$  and higher  $M$ . For instance at  $|\chi| = 10$ ,

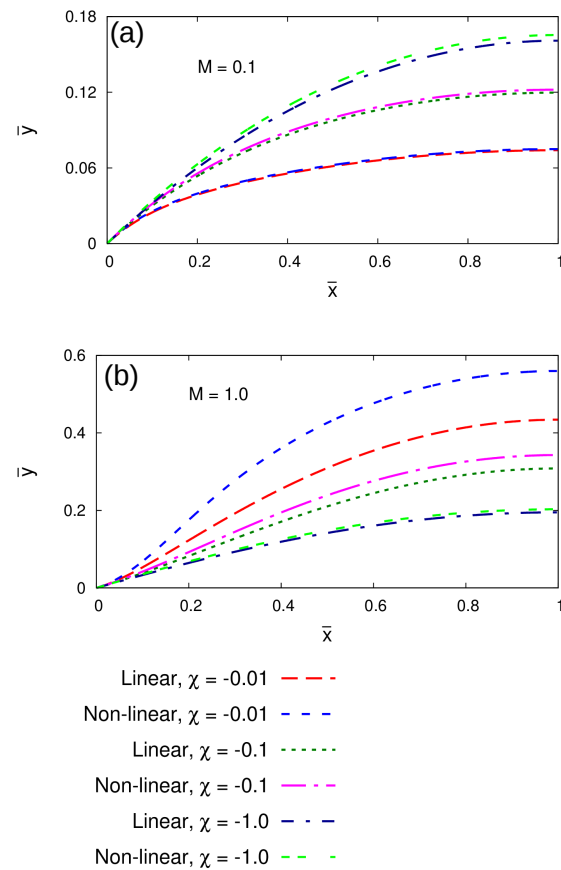


Figure 10.5: Comparison between the solutions obtained from the linearized and the non-linearized version of the governing equations at  $\Gamma = 0.34$ . (a) Even at higher value of  $\Gamma$  the linearized approximates the non-linearized solution within 1%. (b) At higher  $M (= 1)$  the linearized and the non-linearized solutions diverge with decreasing magnitude of  $\chi$ .

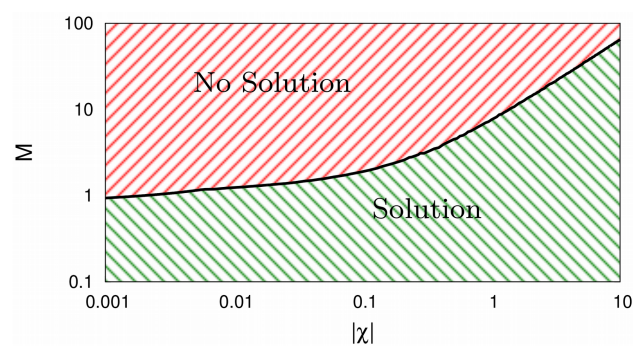


Figure 10.6: Regions of steady state solution in  $M - \chi$  space for  $\Gamma = 0.34$ .

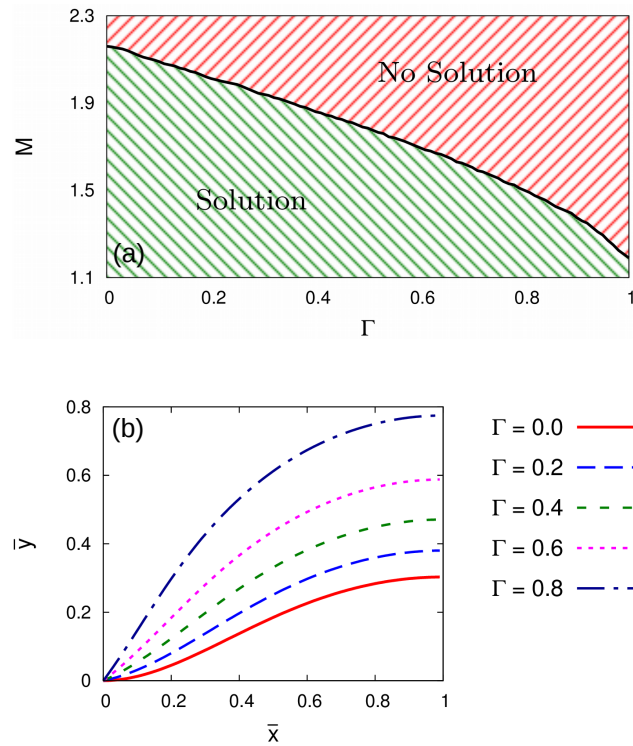


Figure 10.7: (a) Regions of steady-state solution in  $M - \Gamma$  space for  $\chi = -0.1$ . (b) Steady-state surface profiles for different values of  $\Gamma$  corresponding to the values of  $M$  at the limit of steady state (black solid line in (a)).

a steady state solution is possible for  $M$  as high as 68. Increasing  $\chi$ , implies decreasing  $E$  which decreases both EM surface and GB flux, but the latter to a larger extent. Hence a steady state is possible until higher values of  $M$  (which correspondingly increases  $J_{GB}$ ). This is also evident by comparing the profiles for  $M = 1$  at  $\chi = -10$  and  $\chi = -1$  in Fig.10.2 (a) and (b) respectively.

The solution region in  $\Gamma - M$  space for  $\chi = -0.1$  is presented in Fig.10.7. The solution space decreases approximately linearly with increase in  $\Gamma$  until a value of 0.9 after which it falls off rapidly. The reason behind the decline of the solution space can be rationalized as follows. For a fixed  $\chi$ , increasing  $\Gamma$  implies increase in the value of  $\sin \theta_o$  at the root, resulting in higher  $J_s^E$  due to favorable tangential component of electric field ( $E \sin \theta$ ) along the surface. One is tempted to assert that a higher  $J_{GB}$  is needed to maintain a steady-state. The groove profiles for  $\chi = -0.1$  at the upper limit of  $M$ , required for a steady-state solution are plotted in Fig.10.7(b). It is to be noted that at lower values of  $\Gamma$ , the root exhibits concavity, instigating healing due to EM as well as curvature-induced surface flux. At higher  $\Gamma$ , the convexity at the root is preserved and the healing flux is only EM-induced. The increase in the maximum permissible value of  $M$  with decreasing

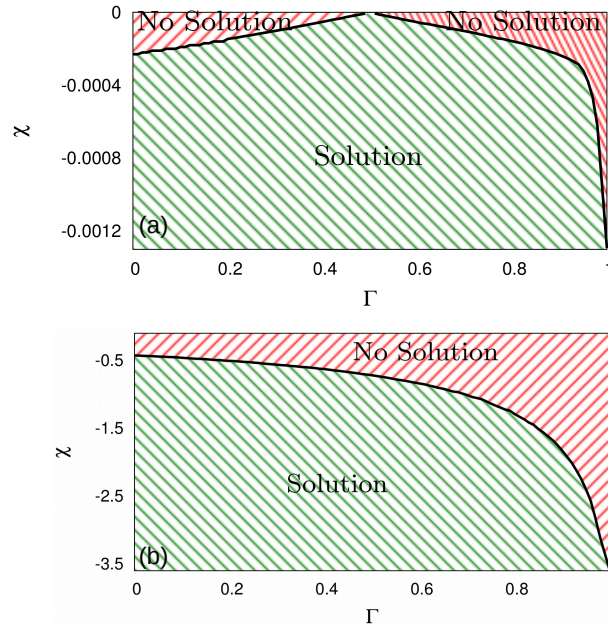


Figure 10.8: Regions of steady state solution in  $\chi - \Gamma$  space for (a)  $M = 0.5$  and (b)  $M = 5$ .

$\Gamma$  can be attributed to the dual healing surface flux as a result of which a higher  $J_{GB}$  and hence higher  $M$  is required to maintain a steady-state.

Two typical solution regions in  $\Gamma - \chi$  space corresponding to  $M = 0.5$  and  $M = 5$  are shown in Fig.10.8 (a) and (b) respectively. At  $M = 0.5$ , the steady state solution region first increases until  $\Gamma = 0.5$  roughly linearly and decreases thereafter. The initial decrease is again linear up to  $\Gamma = 0.9$ , followed by a steep decline. Solution exists for all possible values of  $\chi$  at  $\Gamma = 0.5 = M$ . It may be recalled that it is precisely at this point that the profiles are invariant of  $\chi$ . Below  $\Gamma = 0.5$  increasing  $\Gamma$ , increases the angular component of  $J_s^E$  which is counterbalanced only at higher  $E$  or lower magnitude of  $\chi$  (for a fixed  $M$ ) which correspondingly increases  $J_{GB}$  (and  $J_s^E$  as well but to a lesser degree). Beyond  $\Gamma = 0.5$ , a further increase in  $\Gamma$  presumably increases  $J_s^E$  to an extent where a solution is only possible at higher magnitude of  $\chi$  (or lower  $E$ ) values which concomitantly lowers the effect of  $J_s^E$ . A similar behavior is observed at  $M = 5$  in Fig.10.8(b) where the solution region moves towards higher absolute values of  $\chi$ . However, the solution region does not exhibit any discontinuity. Moreover, a higher value of  $M$  will promote concavity at the root. Hence solution is possible until lower magnitudes of  $\chi$  for lower  $\Gamma$  because of the dual healing mechanism.

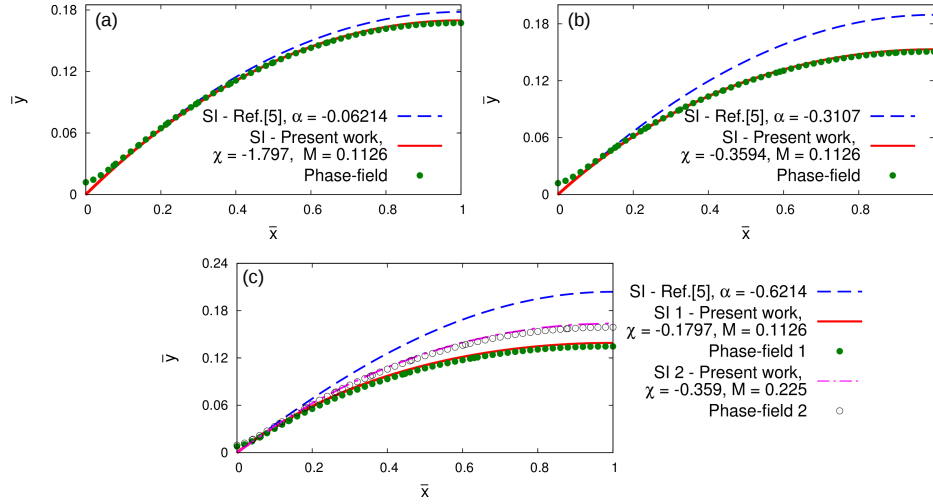


Figure 10.9: Comparison of the solution of the profiles obtained from the sharp interface model and the phase-field model for three different sets of parameters. The solution from the sharp interface theory of Ref. [5] is also presented for comparison. In contrast to the present model where the parameters  $\chi$  and  $M$  determine the groove shape, the profile in Ref. [5] is characterized by a single parameter  $\alpha$ . While doubling and halving  $M_{GB}/M_S$  and  $E$  results in a unique  $\alpha$  and consequently a single solution, in the present framework different values of  $\chi$  and  $M$  are obtained giving rise to two distinct profile as presented in (c).

### 10.4.5 Comparison with Phase-field model

The phase-field simulations were conducted with a drift velocity set up. A bicrystal of the metal interconnect sharing a planar interface with the underlayer domain is allowed to evolve under an applied electric field (through a constant current boundary condition) directed along the GB. The applied current and the ratio of atomic mobility at the GB and surface  $M_{GB}/M_s$  were varied to change the parameters  $\chi$  and  $M$ . The surface is allowed to evolve until a steady state is achieved. A number of different checks were made to ascertain if the steady state has been attained. For instance, steady state in terms of velocity is deduced by tracking the velocity of the groove root. Shape invariance of the groove profiles is determined from the condition of constancy of curvature, profile perimeter and groove depth relative to the surface maximum. Few benchmark phase-field calculations regarding attainment of steady state are provided in Appendix D.

The ratio of atomic mobilities  $M_{GB}/M_S$  to 0.5 is first fixed, which results in a value of  $M = 0.1126$  and vary the applied electric field to vary  $\chi$ . The groove profile from phase-field simulation is defined as the 0.5 contour line of the conserved order parameter which distinguishes the interconnect and the underlayer domain. The profile from the sharp-interface theory of Klinger et al. [5] is also computed for the sake of comparison. A

good agreement between the profiles predicted by the present sharp-interface and phase-field model is observed over a magnitude of  $\chi$  values as evident in Fig.10.9. Secondly contrary to the prediction of the present work, the model in Ref. [5] predicts an increase in the groove depth relative to the surface maximum with increasing value of  $\chi$ . The discrepancy can be attributed to the inconsideration of EM surface flux, as a result the deviation is significant at higher values of  $\chi$ . Moreover, the solution of Ref. [5] depends only on a single parameter  $\alpha = \frac{J_{GB}\Omega L^2}{8B}$ . This implies, for a given material system one can obtain a profile by fixing the ratio  $\frac{D_{GB}}{D_s}$  and  $E$ . Alternatively,  $\frac{D_{GB}}{D_s}$  and  $E$  can be doubled and halved respectively to obtain the same value of  $\alpha$  and hence a unique profile. However in the framework of the present theory, varying  $\frac{D_{GB}}{D_s}$  and  $E$  independently leads to distinct values of  $\chi$  and  $M$ , thereby resulting in two different curves as shown in Fig.10.9(c). The prediction of the sharp-interface model is further corroborated by the phase-field simulations which also results in two distinct curves. It is also worth noting that the local electric field projection along the surface used in the sharp interface model turns out to be an excellent estimate, although a slight deviation is observed at lower magnitude of  $\chi$  (higher field strength).

Additional simulations were performed to validate the other predictions of the sharp-interface model such as increase of the groove depth with increasing  $M$ , profile invariance on  $\chi$  at  $M = \Gamma$  and the effect of  $\frac{\sigma_u}{\sigma_m}$ . In all cases a good agreement between the sharp-interface and phase-field simulations were observed as provided in the Appendix E .

## 10.5 Discussion and Conclusion

A sharp-interface mathematical model was formulated to study GB grooving under concurrent capillary and EM-mediated surface diffusion and EM-induced GB diffusion. The theory is applicable to polycrystalline interconnects where the damage proceeds through concurrent surface and GBEM. Grooves can initiate wherever GBs intersect a free surface either external or internal for example at voids. The present work can be considered as an extension of the work of Klinger et al. [5] concerning GB grooving in presence of GB flux. The theory presented there, was general in nature and valid for arbitrary GB flux irrespective of the exact nature of the external driving force (for instance applied stress or electromigration). A surface stability map in terms of non-dimensional groups  $\alpha(= \frac{J_{GB}\Omega L^2}{8B})$  and  $\Gamma$  was determined. Below a critical value of  $\alpha$ , a global steady state similar to the one considered in the present work ensues, where the entire surface drifts preserving its shape, while narrow channel-like slits manifest due to accelerated grooving above this critical value.

The theory [5] was subsequently applied to rationalize the damage modes during

accelerated EM testing [109, 76, 86, 85]. The EM surface flux along the groove walls was, however, not considered. The present work highlights that accounting for EM surface flux introduces an additional degree of freedom to ascertain the steady state region which is now characterized in terms of  $\chi$ ,  $M$ , and  $\Gamma$ . Moreover,  $J_s^E$  induces a healing surface flux as a result of which the equilibrium groove depths in certain cases can be lower than that of thermal grooves. Such a case does not arise in the previous work.

A comment on what is to be expected in the non-steady state regions where a solution is forbidden is made next. Higher GB flux either due to higher  $M$  or lower  $\chi$  depletes the root resulting in the detachment from the surface to form a slit, with the surface trailing behind. The genesis of a slit was also suggested in the theory of Klinger et al. [5] and has recently been corroborated by phase-field simulations [3]. Theoretically, slits can be analyzed independently by assuming a local steady state.

GB segregation has been advocated as a mechanism to reduce or eliminate GBEM in metals [269, 270]. The present work on the other hand emphasizes the role of surface diffusion along freshly created surfaces as a measure to counter GBEM. Such a case is expected at lower values of  $M$  which in turn could be due to the presence of GB impurities and/or lower  $\chi$ . However, at lower  $\chi$  corresponding to higher applied electric field, Joule's heating could play an important role leading to an additional mode of mass transport mechanism of thermomigration. Thermomigration acting in unison with EM leads to intriguing effects as discussed in [271] and more recently in [121].

**Part V**  
**Conclusions and Future Directions**

# Chapter 11

## Conclusions and future directions

### 11.1 Conclusions

Electric-field-induced directed self-assembly of diblock copolymers and grain boundary grooving in metal interconnects were studied. To this end, two phase-field models were formulated and employed. The feasibility of the phase-field method in capturing the essential physics of the problems and tackling the microstructure evolution efficiently and elegantly was amply demonstrated. Furthermore, the results significantly enhances our current understanding of field-directed pattern formation in block copolymers and EM failure mechanism in interconnects. The findings, highlights and the objectives fulfilled in the present dissertation can be summarized as follows :

#### 1. Directed assembly of block copolymers

In chapter 5, the effect of concurrent external agencies such as substrate affinity, electric field and confinement in modulating the morphologies of lamellae block copolymer was studied. The phase diagrams (or morphology) in electric-field-substrate strength space presented, can serve as a guideline to the experimentalists regarding the appropriate selection of process parameters.

A time-dependent-Ginzburg-Landau (TDGL) model which complements the Ohta-Kawasaki functional with electrostatic and surface energies was employed. Although the model is phenomenological in a sense that it lacks the details of the molecular chain interactions, it is now well established that all possible block-copolymer morphologies observed experimentally can be reproduced by the Ohta-Kawasaki functional [166]. In fact, the phase diagrams obtained using the method have been critically compared to the existing analytical theories and more rigorous simulation techniques such as Self-Consistent field theory (SCFT) and Dynamic Density

functional theory (DDFT) with good agreement.

The numerical simulation methods such as the one presented here (or SCFT or DDFT for that matter) do provide a detailed exposition on the range of possible morphologies as compared to the analytical treatments. In analytical methods, the possibility of a given structure for the prescribed parameters is deduced by comparing the free energies of the expected, albeit, only simple morphologies. For instance, in the case of symmetric diblock copolymers, this corresponds to the parallel, mixed and perpendicular structures. The results presented in chapter 4, does however indicate the possibility of other intermediate morphologies such as holes and perforated lamellae, specially in thin films where incommensurability effects are important.

Although the superiority of the TDGL-based models over SCFT and DDFT certainly cannot be claimed, the computational efficiency in accessing large length and time scales lends support to the applicability of these methods. TDGL models can be used as a precursor for the more-informed SCFT and DDFT studies where a large parametric space needs to be investigated. TDGL models can also accentuate a faster bridging between simulations and experiments.

In chapter 6, a novel parallel-to-hexagonally-perforated-lamellar transition was elucidated in monolayer and bilayer thin films. The perforated lamellar morphology is one of the most attractive and technologically relevant structure, however it is usually only metastable in the bulk. Although there have been previous attempts to stabilize the HPL structure in supported films [272] or by application of shear [273], this is the first report of such a phase transition in presence of electric field. Since electric fields are relatively easier to apply than shear, specially in thin films, the present method provides a viable alternative to modulate such a structure. Technologically, selective removal of the component forming the cylindrical phase generates a porous structure which could find applications as scaffolds and templates [220, 221].

## 2. Grain boundary grooving under electromigration

In chapter 7, the phase-field model for GB grooving was validated by a critical comparison with the seminal work of Mullins. It was shown that the results obtained employing the small slope approximation in the work of Mullins is applicable beyond this restriction but within reasonable limits. A characteristic dip following the maximum which is not present in Mullins' solution of surface diffusion-mediated profile but envisaged by Hillert [122] is observed in the phase-field solution.

Chapter 8 deals with the study of the underlying mechanisms responsible for EM-mediated GB grooving in nano-scale interconnects. Using the phase-field method

that accounts for curvature-driven diffusion in conjunction with surface and grain boundary electromigration, two modes of damage namely surface drift and slit propagation are analyzed. Various scaling laws for experimentally relevant observables such as grain size, electric field strength and drift velocity are evaluated under accelerated electromigration testing conditions. The scaling laws can be extrapolated to the actual service condition which could provide guidelines for efficient design and reliability of electronic device. Moreover, to the best of our knowledge, this is the first time a numerical model has been extended to study spatio-temporal damage initiation, propagation, self-healing, grain coarsening in three-dimensional interconnects.

In chapter 9, the limitation of the existing sharp-interface theories in tackling the problem of EM-induced grooving was highlighted by a critical comparison with the findings from the phase-field approach. Specifically, it was shown that a single parameter  $\alpha(= \frac{J_{GB}\Omega L^2}{8B})$  that has been used until now to rationalize microstructural damage during concurrent capillary-induced surface diffusion and grain boundary electromigration in unpassivated films is inadequate to characterize either the groove shape or damage mode. Healing flux in terms of electromigration-induced surface electromigration along freshly exposed groove walls lead to premature arrest of grooving and delay damage dissemination. A significant highlight is the possibility to conduct virtual drift velocity experiments using the phase-field method. A good agreement with the sharp-interface theory over a magnitude of GB flux corroborates the claim.

In chapter 10, a new sharp interface model was formulated to address the phenomenon of grain boundary grooving due to surface and grain boundary electromigration. It was shown that unlike the existing sharp interface theory, two parameters  $\chi(= \frac{4\gamma_s\Omega}{z_s e E \beta L^2})$  and  $M(= \frac{D_{GB}\delta_{GB}z_{GB}}{2D_s\delta_s z_s \beta})$  are necessary to uniquely determine the groove shapes. The discrepancy highlighted in chapter 8 is resolved as evident from the good agreement between the solutions of the new model and the phase-field method.

## 11.2 Future directions

Although the works presented in the thesis is complete in its own right, several interesting extensions are possible. The straightforward continuation of the present work is discussed first.

### 1. Directed assembly of block copolymers

The work in the thesis explores only the effect of uniform field. As a result of

the dielectric contrast mechanism at play, only perpendicular lamellar structure is favorable in thick films (in absence of any substrate affinity). In non-uniform field, however, dielectrophoretic mechanism which implies that the material with higher permittivity is preferred in regions of high electric field and vice-versa will also dictate the stability of the resulting morphology, due to which a parallel lamellae can also be stabilized in presence of the electric field [274]. Non-uniform electric field can be generated by assigning a spatially varying electric field across the domain edges [275] or by topographically patterned electrode [276]. The length of the electrodes can additionally dictate the final morphology.

While the work in the thesis is mostly focused on symmetric diblock copolymer, the model is certainly not restricted to lamellar morphology and other order-order transitions can definitely be studied. Intriguing among them is the recent experimentally observed hexagonally perforated lamellar to lamellar transition [67], the kinetic pathway of which is not fully understood yet. Gyroid to lamellae transition at high temperatures (low segregation) has recently been reported via a molecular dynamics simulation [277], which so far has not been observed experimentally. It remains to be seen whether such a transition can be observed through the present approach.

Modeling efforts should be directed towards the incorporation of mobile ions in the TDGL framework, either confined to one of the blocks and/or substrate. Former leads to reduction in the applied field required to cause a parallel to perpendicular transition while the latter enhances the critical field [278, 279, 280]. Cues can be taken from SCFT where such an attempt have already been made [280]. Furthermore, the extension to study the effect of electric field and dielectric contrast in triblock terpolymer would also be interesting. In this regard, a TDGL model for non-frustrated triblock terpolymer has recently been formulated by Millett [281].

## 2. Grain boundary grooving under electromigration

In the scope of the present thesis all properties kinetic as well as interfacial were assumed to be isotropic. Most interconnect materials are face-centered-cubic metals which are characterized by strong surface adatom mobility. Anisotropy in surface mobility has been reported to lead to oscillatory dynamics in single crystal islands [211, 212, 213]. Presence of surface mobility anisotropy is expected to lead to richness in grooving dynamics as well.

In the study pertaining to polycrystalline interconnects a columnar grain structure was assumed for simplicity. In a regular grain structure, however slit can propagate along the line through the grain boundaries, forming an island microstructure [109]. The study of slit merging and splitting in addition to grain coarsening in such cases

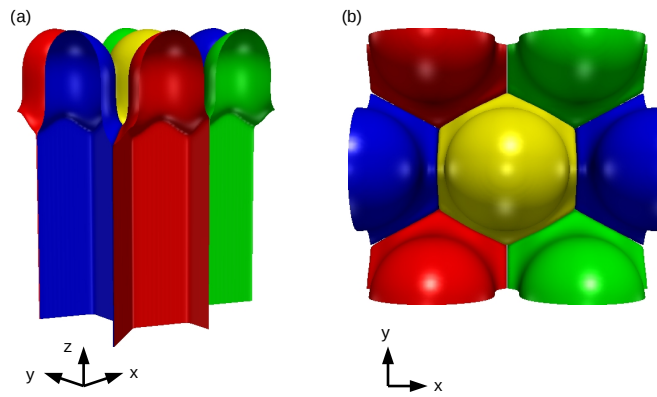


*Figure 11.1: Three dimensional phase-field simulation depicting intergranular slit propagation at triple junction and grain boundary, (a) side view and (b) top view. Each grain orientation is assigned a different color. Slit originating at triple junctions appears wider and propagates faster than the ones at grain boundaries. The trailing edge continues to evolve via surface diffusion.*

is worth investigating.

Although we have considered a simple bicrystalline set up, extension of present work to study triple junctions is straightforward. An exemplary simulation of slit formation at triple junction is presented in Fig.11.1. A mere visual inspection suggests that the slit emanating at the GB triple junction (TJ) propagates faster than the one at GB. Moreover, the slit at the TJ appears to be wider. This raises the following important concerns regarding the slit manifesting at TJ. How does the slit characteristics at TJ differ from those at GB? Does the width and velocity scaling laws hold for slit at TJ? What is the role of healing flux at TJ? What happens if for a certain magnitude of electric field the slit solution exists at TJ but not at GB? Such a scenario was already envisaged by Klinger et al. [5] in which they postulated that the trailing edge evolving via surface diffusion will form a bridge resulting in a slit closure. This will result in a transition of a slit to a void advancing along GB.

The ability to capture the self-healing of grooves during electromigration has been the highlight of the phase-field method. The presence of grain triple junctions are known to be the positions of accelerated grooving leading to pit formation [282]. How does the grain triple junction dynamics are affected by the healing fluxes remains to be explored.

The work in the thesis primarily focuses on monocomponent system, while alloy systems are also gaining popularity as interconnect materials. Phase-field model can be readily extended to multicomponent system [283]. On such an extension the model can be applied to study the effect of grooving in bi-component systems.

Specifically slow diffusing species are known to segregate at the surface [284] which can alter the healing kinetics along the surface. GB segregation can also be modeled within the phase-field framework [285, 286, 287, 288] which is known to inhibit GB electromigration [289, 290, 269]. In addition, insights into the phenomenon of precipitate drifting, coarsening, interaction with grain boundaries due to electromigration can be investigated [291].

The incorporation of stresses in terms of vacancy accumulation, back-stress along the line and residual stress in the interconnect line originating from the fabrication is an absolute must to complete the understanding of the electromigration-induced grooving in interconnects. Stress-driven diffusion mechanisms and can be rigorously addressed by solving self-consistently the elastostatic boundary-value problem for the interconnect line together with the electrostatic and diffusion problems [137, 209].

Although a good agreement between the sharp interface and phase-field solutions have been observed, the presented model by no means can be termed as quantitative. In phase-field, the term quantitative is reserved for models which exhibit results independent of interface thickness [292, 293, 294, 295, 296]. To this end, decoupling of the equilibrium interfacial profile from concentration field is necessary. To achieve this property, dropping of the gradient energy coefficient in  $\rho$  seems indispensable. This results in a coupling of a second order conserved equation, in contrast to the fourth order, utilized in the present model and the usual second order non-conserved equation. It is to be noted that although such models have been utilized in the past to model surface diffusion [297, 121], no formal asymptotic analysis so far exists, to show that these set of equations does indeed correctly converge to even sharp-interface limit. It is also worth noting that the sharp-interface Mullins' equation is a fourth order partial differential equation which bears a strong resemblance to the fourth order Cahn-Hilliard equation. Attempt towards quantitative modeling of the electromigration phenomenon is highly desirable to facilitate a direct comparison with experiments.

### 11.3 Other avenues ....

In the course of the dissertation, only two representative phenomenon where applied electric field modulates microstructure evolution in soft matter and affects atomic transport in metal interconnects were chosen to demonstrate the ability of phase-field method in tackling moving boundary problems with electric field coupling. However, the potential of the phase-field method can be employed to unravel the underlying physics of several other

phenomenon. A few important among them are discussed in closing the dissertation.

Electrostatic field-induced instability can be utilized to guide and replicate patterns in thin liquid films [12, 13]. Spatially homogeneous and heterogeneous fields generated by using topographically patterned electrode causing the displacement of liquid from the regions of low field to high field, leading to the formation of ordered arrays of hexagons or annular rings of liquid columns [298]. Cahn-Hilliard-Navier-Stokes equation supplemented with the electrostatic model can be employed to study the non-linear pattern formation which involves interface instability and shape bifurcations, gracefully. In addition, the competition between the destabilizing force between contact surface and soft elastic films (polymeric films) in terms of van der Waals and electric field and restoring elastic force leads to rich morphological transitions [299, 300].

Electrostatic-field-induced surface instability can also be utilized to guide growth of nano/micro scale islands in conductors [301, 302]. Similar instability arising due to electromechanical interaction known as Stranski-Krastanow instability are also prominent in conducting metallic thin films [303, 304]. The stability of the surface with respect to perturbations depends on the surface energy, the elastic energy due to lattice mismatch between the film and the substrate and the electrostatic energy. The mass transport governing mechanism is surface diffusion. Phase-field method can provide efficient guidelines to exploit mesoscale patterning in such cases. Elasto-electric coupling appeals as a promising area going forward.

**Part VI**  
**Appendices**

# Appendix A

## Different sharp interface limits of the phase-field model of chapter 4

The coupled system of Cahn-Hilliard, Allen-Cahn and Laplace equation exhibits different sharp interface limits depending upon the scaling of Allen-Cahn mobility ( $L_\eta$ ) relative to the Cahn-Hilliard mobility  $M$ . In other words, the relative fastness or slowness of the Allen-Cahn equation with respect to the Cahn-Hilliard equation determines the overall dynamics of the interfaces. Here, we summarize three such possible motion of interfaces which can be derived along similar lines following section 4.5.

### A.1 Case I : $M \rightarrow M/\epsilon$ and $L_\eta \rightarrow L_\eta/\epsilon$

The evolution equations for the interphase boundary under this scaling can be written as

$$\epsilon^2 \frac{\partial \rho}{\partial t} = \nabla \cdot M(\rho) \nabla \left[ \frac{\partial f(\rho, \eta)}{\partial \rho} - 2\epsilon^2 \nabla^2 \rho + \epsilon \Lambda \phi \right] \quad (\text{A.1})$$

$$\epsilon^2 \frac{\partial \eta}{\partial t} = -L_\eta \left[ \frac{\partial f(\rho, \eta)}{\partial \eta} - 2q\epsilon^2 \nabla^2 \eta \right] \quad (\text{A.2})$$

$$\nabla \cdot [\sigma(\rho) \nabla \phi] = 0 \quad (\text{A.3})$$

The motion of the interphase boundary (surface) is then given by

$$V_n = \overline{M}_S \left[ \gamma_S \frac{\partial^2 \kappa}{\partial s^2} + \frac{\partial^2}{\partial s^2} \left( \frac{V_n}{L_\eta} \int_{-\infty}^{+\infty} \left( \frac{\partial \hat{\eta}^0}{\partial z} \right)^2 dz \right) + \Lambda \frac{\partial^2 \hat{\phi}^0}{\partial s^2} \right] \quad (\text{A.4})$$

which is motion by combined surface laplacian of mean curvature, surface laplacian of surface attachment kinetics and surface laplacian of electric potential. For the antiphase

boundaries, since  $\rho \approx 1$  and  $\nabla\rho \approx 0$ , the motion is dictated by the dynamics of the  $\eta_1$  and  $\eta_2$  equations,

$$\epsilon^2 \frac{\partial \eta_i}{\partial t} = -L_\eta \left[ \frac{\partial f(\rho, \eta)}{\partial \eta_i} - 2q\epsilon^2 \nabla^2 \eta_i \right] \quad (\text{A.5})$$

where  $i = 1, 2$ . Following the derivation in section 4.5 for an antiphase boundary it can be shown that,

$$V_n = 2q\kappa_{GB}L_\eta \quad (\text{A.6})$$

where,  $\kappa_{GB}$  is the curvature of the grain boundary and the antiphase boundary moves via the motion by mean curvature. However, because of the construction of the  $f(\rho, \eta_i)$  as given by Eq.4.22,  $\rho$  dips from the equilibrium value across the grain boundary. For a significant dip, Cahn-Hilliard Eq.A.1 also needs to be considered and the sharp interface limit is modified as,

$$V_n = 2q\kappa_{GB}L_\eta - \frac{2\kappa_{GB}L_\eta \int_{-\infty}^{+\infty} (\frac{\partial \rho^0}{\partial z})^2 dz}{\int_{-\infty}^{+\infty} (\frac{\partial \eta_1^0}{\partial z})^2 + (\frac{\partial \eta_2^0}{\partial z})^2 dz} \quad (\text{A.7})$$

where, the second term is analogous to the solute drag effect and retards the grain boundary motion. In the present work, the numerical parameters were so chosen as to negate the contribution arising out of the second term.

## A.2 Case II : $M \rightarrow M/\epsilon$ and $L_\eta \rightarrow L_\eta/\epsilon^3$

The evolution equations under this scaling can be written as

$$\epsilon^2 \frac{\partial \rho}{\partial t} = \nabla \cdot M(\rho) \nabla \left[ \frac{\partial f(\rho, \eta)}{\partial \rho} - 2\epsilon^2 \nabla^2 \rho + \epsilon \Lambda \phi \right] \quad (\text{A.8})$$

$$\epsilon^4 \frac{\partial \eta}{\partial t} = -L_\eta \left[ \frac{\partial f(\rho, \eta)}{\partial \eta} - 2q\epsilon^2 \nabla^2 \eta \right] \quad (\text{A.9})$$

$$\nabla \cdot [\sigma(\rho) \nabla \phi] = 0 \quad (\text{A.10})$$

The motion of the interphase boundary is given by

$$V_n = \overline{M}_S \left[ \gamma_S \frac{\partial^2 \kappa}{\partial s^2} + \Lambda \frac{\partial^2 \phi^0}{\partial s^2} \right] \quad (\text{A.11})$$

which is motion by combined surface laplacian of mean curvature and surface laplacian of electric potential as derived in section 4.5. For the antiphase boundary, it can be shown,

$$\gamma_{GB} \kappa_{GB} = 0 \quad (\text{A.12})$$

implying that the grain boundary is in its equilibrium configuration or in other words it is flat.

### A.3 Case III : Degenerate $L_\eta$ with different scalings

Similar to the atomic mobilities, the relaxation parameter  $L_\eta$  can also be chosen to be different for the interphase and the antiphase boundaries by enslaving them to the field variables such as

$$L_\eta(\rho, \eta_i) = L_B + 16L_S\rho^2(1 - \rho)^2 + 4L_{GB}\sqrt{\eta_i^2\eta_j^2}. \quad (\text{A.13})$$

For the interphase boundary, we then use the scaling  $M \rightarrow M/\epsilon$  and  $L_S \rightarrow L_S/\epsilon^3$  such that the motion is governed by surface laplacian of the curvature and electric potential. For the antiphase boundary we adopt the scaling  $L_{GB} \rightarrow L_{GB}/\epsilon$  to recover the traditional motion by mean curvature.

# Appendix B

## Relating normal velocity $V_n$ and $\frac{\partial y}{\partial t}$

Two geometric constructions relating  $V_n$  and  $\frac{\partial y}{\partial t}$  are possible. However, only one of them is consistent with the mass conservation Eq.(7.5) as discussed next.

### B.1 Possibility 1

The first possibility is to draw the normal velocity  $V_n$  from a point on the curve  $y(x, t)$ , and then drop a perpendicular on  $\frac{\partial y}{\partial t}$  as shown in Fig.B.1. The point of intersection is then  $y(x, t + \Delta t)$ . In such a case,  $V_n$  is the hypotenuse and  $\frac{\partial y}{\partial t}$  is the base so that,

$$V_n \cos \theta = \frac{\partial y}{\partial t} \quad (\text{B.1})$$

$$\implies V_n \frac{dx}{ds} = \frac{\partial y}{\partial t} \quad (\text{B.2})$$

$$\implies V_n \frac{1}{\sqrt{1 + \left(\frac{dy}{dx}\right)^2}} = \frac{\partial y}{\partial t} \quad (\text{B.3})$$

$$\implies V_n = \sqrt{1 + \left(\frac{dy}{dx}\right)^2} \frac{\partial y}{\partial t} \quad (\text{B.4})$$

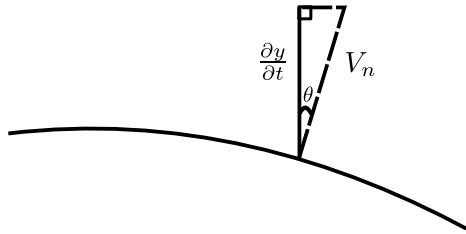


Figure B.1: Geometric construction depicting the first possibility in which the projection of normal velocity  $V_n$  along  $y$ -direction is taken to be  $\frac{\partial y}{\partial t}$ .

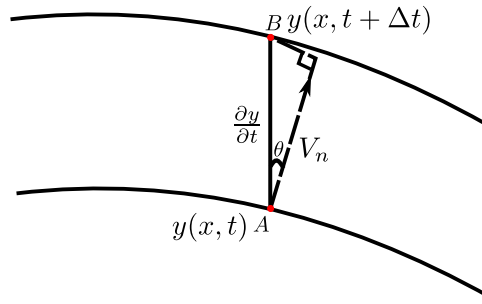


Figure B.2: Geometric construction depicting the second possibility in which the points  $A$  and  $B$  on the curve  $y(x, t)$  and  $y(x, t + \Delta t)$  respectively are joined. The perpendicular is then dropped on the normal velocity  $V_n$ .

Using this procedure one can generate the locus of all the points corresponding to  $y(x, t + \Delta t)$ .

## B.2 Possibility 2

The alternative way is to join  $y(x, t)$  ( $A$ ) to  $y(x, t + \Delta t)$  ( $B$ ) which gives  $\frac{\partial y}{\partial t}$  and then drop a perpendicular on the vector  $V_n$  as shown in Fig.B.2. In this case,  $\frac{\partial y}{\partial t}$  is the hypotenuse and  $V_n$  is the base so that

$$V_n = \frac{\partial y}{\partial t} \cos \theta \quad (\text{B.5})$$

$$\Rightarrow V_n = \frac{\partial y}{\partial t} \frac{1}{\sqrt{1 + \left(\frac{dy}{dx}\right)^2}} \quad (\text{B.6})$$

But it is to be noted that  $y(x, t + \Delta t)$  was assumed beforehand.

## B.3 What does the mass conservation equation mean ?

Consider an infinitesimally small control volume along the surface as in Fig.B.3. Assuming  $J_s > J_{s+\Delta s}$ , so that more atoms enter the control volume than leaving it, all the elements in the control volume will grow equally in the next timestep by an amount  $V_n \Delta t$  in the normal direction.

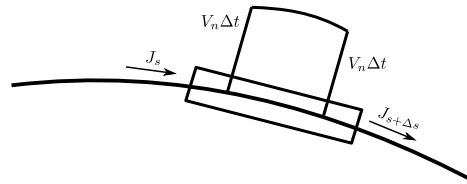


Figure B.3: Interpretation of the mass conservation Eq.(7.5). Accumulation or loss of atoms in a control volume leads to movement of the segment along the normal direction.

## B.4 Which possibility is consistent with the mass conservation equation ?

Let us try to understand which approach is correct and consistent with the geometric law  $\frac{dJ}{ds} = -\frac{V_n}{\Omega}$  proposed by Mullins.

### B.4.1 Possibility 1

Assume a curve  $y(x, t)$  with two points  $y(x_1, t)(A)$  and  $y(x_2, t)(B)$  inside the control volume as in Fig.B.4. Since the accumulation of atoms lead to normal displacement of the control volume, we displace the curve by an amount  $V_n \Delta t$  (one can assume  $\Delta t = 1$  so that the curve in the control volume is displaced by  $V_n$ ). The locus of the points as a result of this normal displacement gives the curve  $y(x, t + \Delta t)$  which is unique. Thus, the points  $A$  and  $B$  after displacement should also lie on this curve and is given by  $y(x_1, t + \Delta t)(A')$  and  $y(x_2, t + \Delta t)(B')$ . However, if we proceed via construction 1 as in Fig.B.1 we end getting a locus of different set of points  $A''B''$  as shown by green line in Fig.B.4 which does not coincide with the curve  $A'B'$ . Since the green curve does not coincide with  $y(x, t + \Delta t)$  the points on it would also not be equidistant in the normal direction from  $y(x, t)$ .

### B.4.2 Possibility 2

The second construction, however would remain consistent as shown in Fig.B.5. It is to be noted that in this case  $\frac{\partial y}{\partial t}$  is perpendicular to  $V_n$  for infinitesimally small arc lengths.

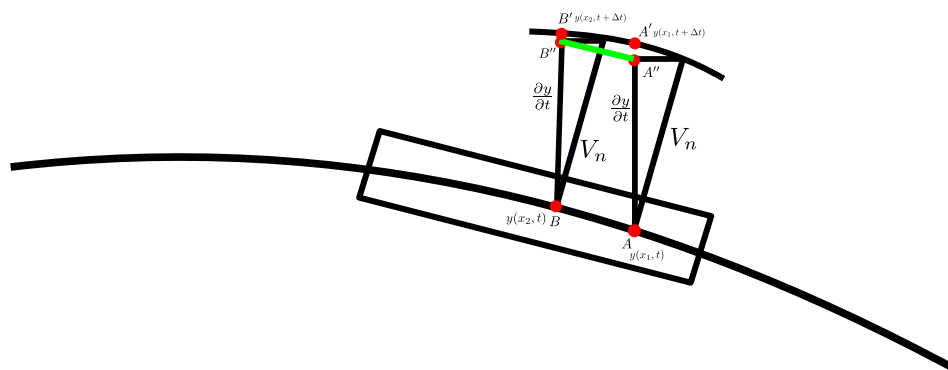


Figure B.4: Geometric construction depicting that the first possibility is inconsistent with the mass conservation equation.

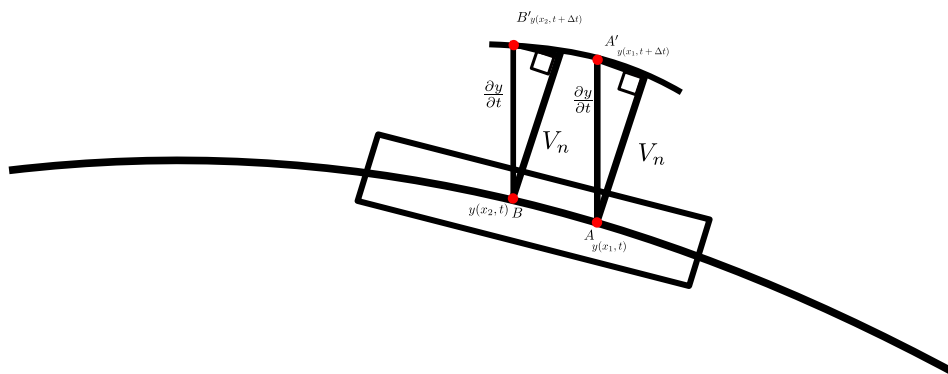


Figure B.5: Geometric construction depicting that the second possibility is consistent with the mass conservation equation.

# Appendix C

## Calculation of curvature along the profile

The curvature from the  $\rho = 0.5$  level set is defined by the divergence of the normal vector as,

$$\kappa_s = \nabla \cdot \hat{\mathbf{n}} \quad (\text{C.1})$$

where,  $\hat{\mathbf{n}} = \frac{\nabla \rho}{|\nabla \rho|}$ . The above expression can be simplified in two dimensions as,

$$\kappa_s = \frac{\rho_{xx}\rho_y^2 - 2\rho_x\rho_y\rho_{xy} + \rho_{yy}\rho_x^2}{(\rho_x^2 + \rho_y^2)^{3/2}} \quad (\text{C.2})$$

The curvature is calculated along the  $\rho = 0.5$  contour. Since these points not necessarily lie on regular lattice points, the location of such points are first calculated from neighboring two lattice points through a linear interpolation. Following [305], the derivatives are also linearly interpolated from these nearest neighboring lattice points. The derivatives are discretized using second-order accurate central difference scheme as,

$$\begin{aligned} \rho_x &= \frac{\rho_{i+1,j} - \rho_{i-1,j}}{2\Delta x} \\ \rho_{xx} &= \frac{\rho_{i+1,j} - 2\rho_{i,j} + \rho_{i-1,j}}{\Delta x^2} \\ \rho_{xy} &= \frac{\rho_{i+1,j+1} - \rho_{i-1,j+1} - \rho_{i+1,j-1} + \rho_{i-1,j-1}}{4\Delta x\Delta y} \end{aligned} \quad (\text{C.3})$$

where  $i, j$  are the indices along  $x$  and  $y$  axes respectively. Thus, the first and the second derivatives in Eq.C.2 comprises of information from 4 neighboring grid points, while, the mixed derivatives from 8 neighboring grid points.

# Appendix D

## Determination of steady state

### D.1 Groove depth

The simplest way to ascertain the shape invariance of the profile is by measuring the groove depth. The groove depth is defined as the distance between the minimum and the maximum of the groove profile obtained from  $\rho = 0.5$  contour. Since the  $\rho = 0.5$  values do not necessarily lie on the regular grid cells, these locations are calculated by a linear interpolation between the neighboring cells both in  $x$  and  $y$  directions independently. However, first, the effect of grid discretization on the groove profiles needs to be checked. It has been previously pointed out [292, 306] that corresponding to a given driving force the interface movement is plagued by time-periodic oscillations and even artificial pinning. Hence the lattice discretization needs to be chosen such that the oscillations of the interface on the scale of  $\Delta x$  measured in units of  $\sqrt{\kappa_\rho/A}$  remains effectively small. The effect of lattice spacing on the groove profile is shown in Fig. D.1 (a). For a coarser mesh, the effect of lattice pinning is visible. Accordingly, in the regime of the driving force (current density) used in the present study, a grid spacing of  $\Delta x = 0.5$  was seen to give results free from grid effects.

The temporal evolution of the groove depth corresponding to the profiles in Fig.10.9 of chapter 10 is shown in Fig. D.1(b). All the profiles attain a constant value after an initial rise.

### D.2 Profile perimeter

Another measure of the shape invariance is through the evaluation of the profile perimeter. The perimeter is calculated through summation of the distances between the neighboring

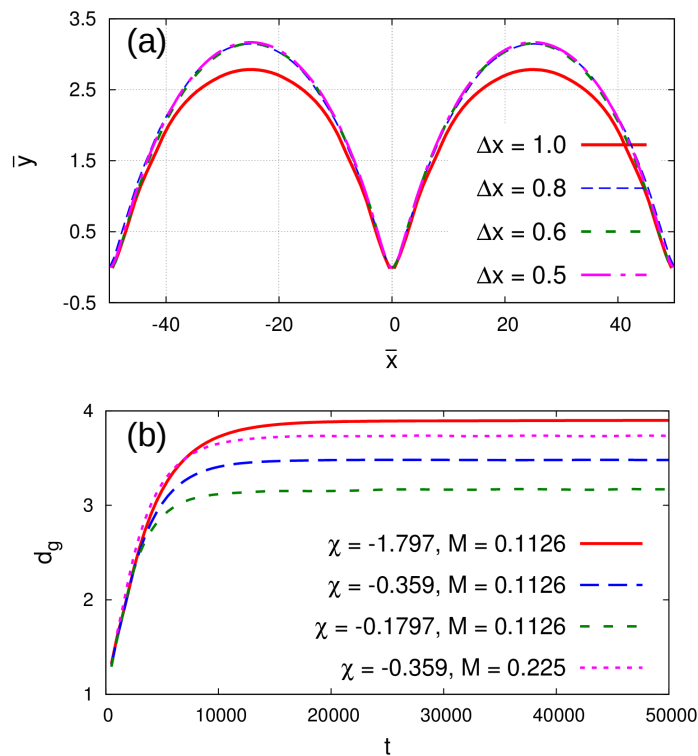


Figure D.1: (a) Effect of grid discretization  $\Delta x$  on the profile shapes corresponding to parameters  $\chi = -0.1797$ ,  $M = 0.1126$ .  $\Delta x$  is measured in units of  $\sqrt{\kappa_\rho/A}$ . At higher  $\Delta x$  effect of coarser mesh in terms of pinning is visible. Accordingly, a finer discretization of  $\Delta x = 0.5$  is used in all the simulations. (b) Temporal evolution of the groove depth corresponding to the profiles in Fig.9 in the main article.

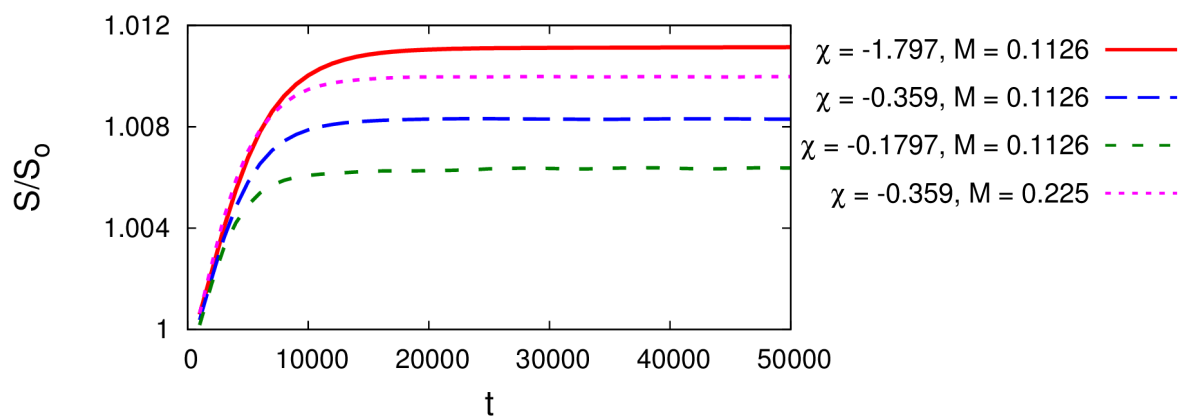


Figure D.2: Temporal evolution of the profile perimeter corresponding to the profiles in Fig.10.9 of chapter 10.

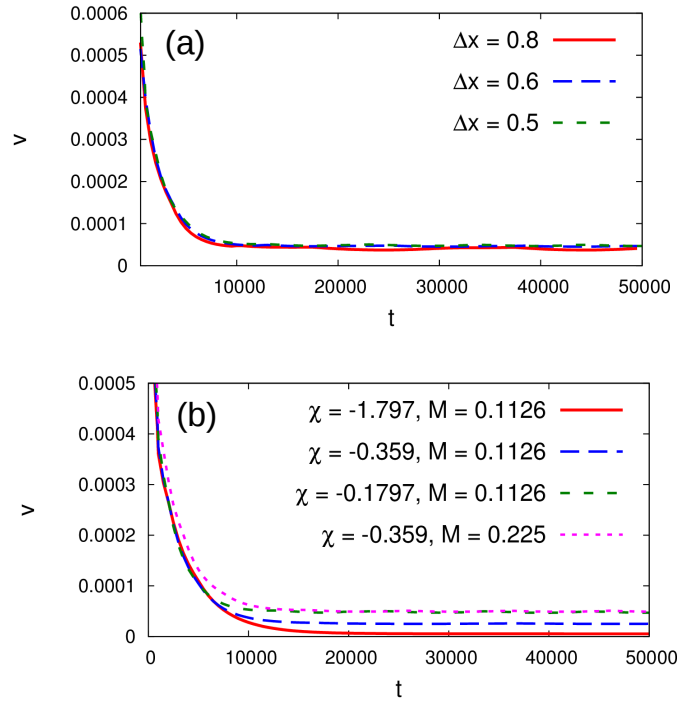


Figure D.3: (a) Effect of lattice discretization on the steady state velocity. (b) Temporal evolution of the root velocity corresponding to the profiles in Fig.10.9 of chapter 10.

points  $(x_1, y_1)$  and  $(x_2, y_2)$  on the  $\rho = 0.5$  profile by the distance formula  $\sqrt{(x_2 - x_1)^2 + (y_2 - y_1)^2}$ . The temporal evolution of the normalized profile perimeter corresponding to the profiles in Fig.10.9 is shown in Fig. D.2.

### D.3 Steady state velocity

The steady-state in terms of kinetics can be ascertained by following the velocity of the groove root. The velocity is calculated numerically from the position of the groove root between the successive time as,

$$v = \frac{x(t + \Delta t) - x(t)}{\Delta t} \quad (\text{D.1})$$

The steady state velocity is shown in Fig.D.3 along with effect of lattice discretization  $\Delta x$ . It is noteworthy that the profiles corresponding to the parameters Fig.10.9(c) of chapter 10 converge to the same steady state velocity owing to the same GB flux  $J_{GB}$  in both the cases.

# Appendix E

## Additional benchmark comparisons of the sharp-interface model of chapter 10 and phase-field solutions

### E.1 Effect of $M$ on groove profiles

The sharp-interface theory predicts an increase of the groove depth with increasing  $M$  for a given  $\chi$  as discussed in Fig.10.2 of chapter 10. A similar trend is predicted by the phase-field simulations as well as shown in Fig.E.1.

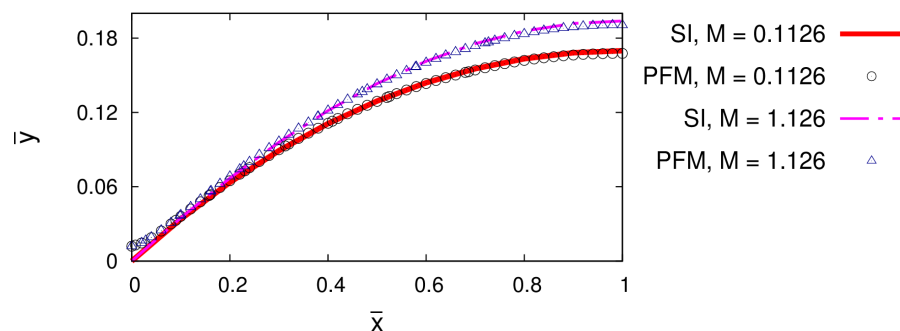


Figure E.1: Comparison of the groove profiles obtained from sharp interface (SI) and phase-field method (PFM) for different value of  $M$  for  $\chi = -1.797$ . With increasing  $M$  the groove depth relative to surface maximum increases.

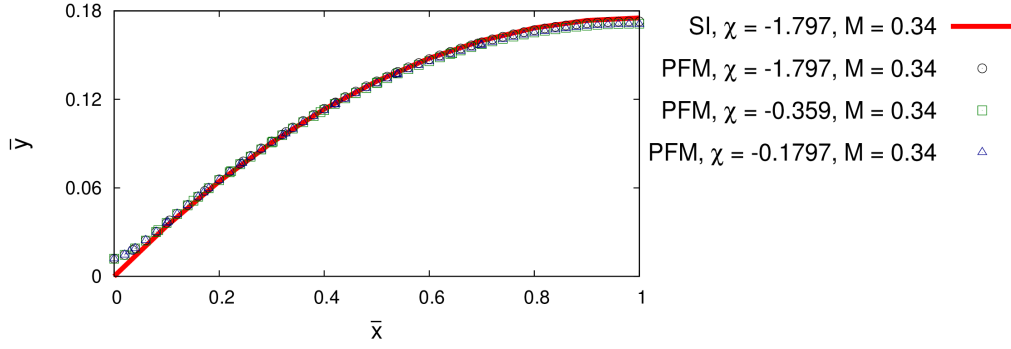


Figure E.2: Comparison of the groove profiles obtained from sharp interface (SI) and phase-field method (PFM) for different value of  $\chi$  at  $M = \Gamma = 0.34$ . For clarity only one of the SI curve is shown. The profiles are invariant on the value of  $\chi$ .

## E.2 Invariance of groove profile on $\chi$ for $M = \Gamma$

To check the validity of profile invariance on  $\chi$  we select a value  $M = \Gamma$ .  $D_s$  is held constant for all the simulations by ascribing constant values to  $M_s$  (and also to  $\kappa_\rho$  and  $\kappa_\eta$ ). The value of  $D_{GB}$  needed to attain  $M = \Gamma$  can be calculated from

$$\frac{D_{GB}\delta_{GB}z_{GB}}{2\beta D_s\delta_s z_s} = M = 0.34. \quad (\text{E.1})$$

Since  $\Omega = k_B T = 1$  in non-dimensionalized units we have from Eqs.(4.156) and (4.157)  $D_s\delta_s = \overline{M}_s$ . For  $M_s = 1$ ,  $D_s\delta_s = 2.088$ . Furthermore, for the selected value of  $\sigma_m/\sigma_u = 10$ ,  $\beta = 1.818$ . Therefore, from the above equation  $D_{GB}\delta_{GB} = 2.581 = \overline{M}_{GB}$ . Since  $M_{GB} = 1$  results in  $\overline{M}_{GB} = 1.7108$ , to obtain the desired value of 2.581 we need to choose  $M_{GB} = 1.5$  in the phase-field simulations. The resulting  $\chi$ -invariant profiles where  $\chi$  is varied over an order of magnitude is shown in Fig.E.2.

## E.3 Effect of conductivity ratio on groove profiles

The effect of conductivity ratio between the metal interconnect and the underlayer  $\sigma_m/\sigma_u$  is shown in Fig.E.3. The case of  $\sigma_m/\sigma_u = 1$  corresponds to case where electric field at every point in the domain is same and is equal to the applied electric field. As the ratio is decreased, the electric field at the surface increases as a result of which the profiles become flatter.

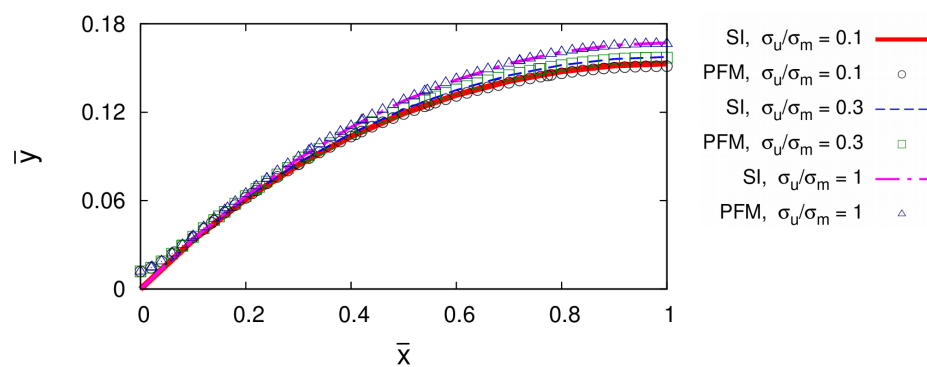


Figure E.3: Comparison of the groove profiles obtained from sharp interface (SI) and phase-field method (PFM) for applied electric field of  $E = 2.84 \times 10^{-4}$  and different ratios of  $\frac{\sigma_u}{\sigma_m}$  such that  $\chi = -0.359, -0.4246$  and  $-0.653$  and  $M = 0.1126, 0.1331$  and  $0.2047$ , corresponding to  $\frac{\sigma_u}{\sigma_m} = 0.1, 0.3$  and  $1$  respectively. Higher ratios leads to deeper grooves.

# Appendix F

## Phase-field model with only grain boundary electromigration (GBEM)

The EM-induced surface flux in the phase-field model can be cut off by rearranging the evolution Eq.4.26 for the conserved order parameter as

$$\frac{\partial \rho}{\partial t} = \nabla \cdot M(\rho) \nabla \mu + \nabla \cdot M(\eta_i) z e \nabla \phi \quad (\text{F.1})$$

$$= \nabla \cdot 16M_S \rho^2 (1 - \rho)^2 \left[ \frac{\partial f(\rho, \eta_i)}{\partial \rho} - 2\kappa \nabla^2 \rho \right] + \nabla \cdot 4M_{GB} \sqrt{\eta_i^2 \eta_j^2} z e \nabla \phi \quad (\text{F.2})$$

Due to the pre-factor  $M(\eta_i)$ , EM is limited to the GB, while the surface evolves only under the action of capillarity. Thus the sharp-interface relations given in Chapter 9 and that of Klinger et al.[5] are recovered.

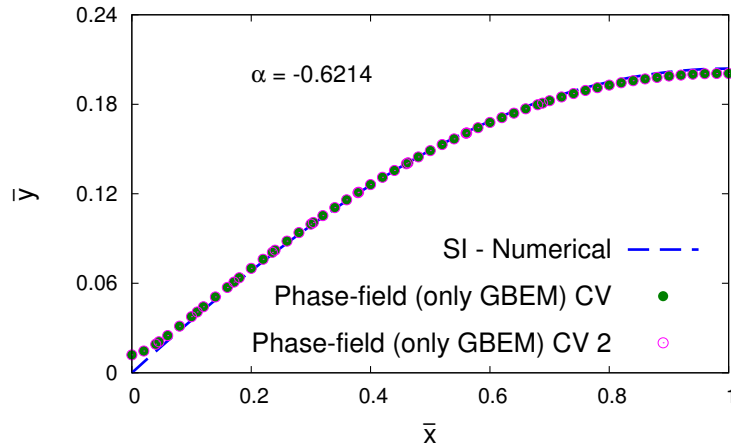


Figure F.1: Restricting EM to GB leads to a good agreement between the sharp-interface and phase-field solutions. The parameter corresponds to Fig.9.3(c).

The results performed with the modified above equation while unaltering the Allen-Cahn and Laplace equation show a good agreement with the sharp-interface solution of Klinger et al.[5]. The steady state groove profile is shown in Fig.F.1. Since now the profile shape is only dependent on the non-dimensional group  $\alpha$ , the phase-field solution corresponding to the two parameter set of Fig.9.3(c) leads to a unique solution. Furthermore the groove displacement also shows a good agreement with the sharp-interface analytical solution as evident in Fig.F.2.

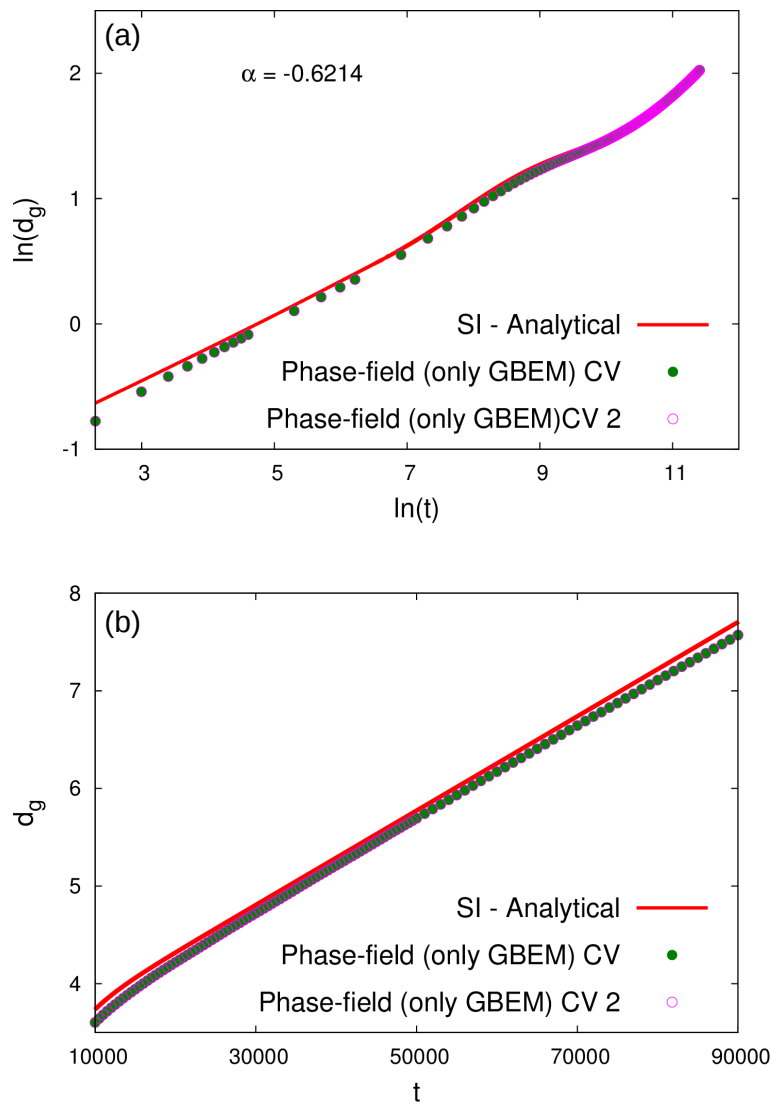


Figure F.2: (a) Comparison of the groove displacement from the sharp-interface analytical solution Eq.(9.22) and phase-field simulations. The slight deviation is due to the small slope approximation employed in the sharp-interface solution. (b) Same as (a) highlighting the late stages of groove displacement.

# List of Symbols

## Directed assembly of block copolymers

Symbol	Description	Page No.
$d_o$	Equilibrium lamellar spacing	20
$f$	Relative length of A monomer chain	35
$f(\psi)$	Bulk free energy density	36
$g$	Parameter related to the deviation of interaction parameter at the surface	44
$h_o/h_L$	Substrate affinity strength at two ends of the film	48
$m$	Difference in the average volume fraction of A and B polymers	36
$n_c$	Number of open cubes	116
$n_e$	Number of edges	116
$n_f$	Number of open faces	116
$n_v$	Number of vertices	116
$t$	Time	38
$v_o$	Volume occupied by one polymer chain	48
$z$	Co-ordination number	46
$A$	Interfacial area	17
$A(t)$	Time-dependent amplitude of perturbation	39
$B$	Long range interaction parameter	36
$C$	Number of contacts between wall and mixture molecules	46
$C_m$	Effective capacitance of mixed lamellae	20
$C_{\parallel}$	Effective capacitance of parallel lamellae	17
$C_{\perp}$	Effective capacitance of perpendicular lamellae	18
$D$	Domain size	41
$\mathbf{E}/E$	Electric field	22/49
$\mathbf{E}_0$	Applied electric field	22

Symbol	Description	Page No.
$\mathbf{E}_1$	Deviation of the electric field from the applied value	22
$E_c$	Critical electric field	19
$E_{\parallel m}$	Critical electric field for parallel to mixed lamellae transition	20
$E_{m\perp}$	Critical electric field for mixed to perpendicular lamellae transition	20
$F$	Free energy functional	36
$F_{bulk}$	Bulk free energy density	48
$F_{electrostatic}$	Electrostatic free energy density	48
$F_{es}$	Electrostatic energy	17
$F_m$	Free energy of mixed lamellae	20
$F_{\parallel}$	Free energy of parallel lamellae	18
$F_{\perp}$	Free energy in perpendicular lamellae	18
$F_s$	Interfacial energy	17
$F_{surface}$	Surface free energy	48
$\Delta F$	Excess free energy	42
$H$	Mean curvature	114
$L/L_y/L_z$	Film thickness	17/49/111
$L_o$	Equilibrium lamellar spacing	13
$N$	Degree of polymerization	11
$N_o$	Total number of lattice sites	44
$N_A$	Number of A type monomers	35
$N_B$	Number of B type monomers	35
$S$	Surface area	114
$S(k_x, k_y)$	Structure factor	84
$V$	Voltage/Volume	18/22
$V_c$	Critical voltage	18
$V_m$	Average molecular volume	42
$\beta(t)$	Degree of alignment	84
$\gamma_{AB}$	Interfacial energy between A and B block	17
$\gamma_{AS}$	Interfacial energy between A block and substrate	11
$\gamma_{BS}$	Interfacial energy between B block and substrate	11
$\delta$	Non-dimensional parameter related to the interfacial energies of two blocks and substrate	22
$\epsilon_m$	Effective dielectric constant of mixed lamellae	20
$\epsilon_o$	Permittivity of free space	48

Symbol	Description	Page No.
$\epsilon_A$	Dielectric constant of A block	17
$\epsilon_B$	Dielectric constant of B block	17
$\epsilon_{AA}$	Bond energy between A-A atoms	35
$\epsilon'_{AA}$	Bond energy between A-A atoms adjacent to the wall	47
$\epsilon_{AB}$	Bond energy between A-B atoms	35
$\epsilon'_{AB}$	Bond energy between A-B atoms adjacent to the wall	47
$\epsilon_{AW}$	Bond energy between A atoms and wall	45
$\epsilon_{BB}$	Bond energy between B-B atoms	35
$\epsilon'_{BB}$	Bond energy between B-B atoms adjacent to the wall	47
$\epsilon_{BW}$	Bond energy between B atoms and wall	45
$\epsilon_{\parallel}$	Effective dielectric constant of parallel lamellae	20
$\epsilon_{\perp}$	Effective dielectric constant of perpendicular lamellae	20
$\bar{\epsilon}$	Average permittivity	22
$\tilde{\epsilon}$	Length scale parameter	37
$\Delta\epsilon$	Difference between the permittivity of A and B blocks	22
$\kappa$	Gradient energy coefficient	36
$\mu$	Chemical potential	38
$\mu_1$	Surface chemical potential	44
$\rho(y, t)$	Average density profile	81
$\phi$	Electric potential	22
$\chi$	Flory-Huggins parameter/ Euler characteristic	11/114
$\chi_{AW}$	Interaction parameter between A atoms and wall	46
$\chi_{BW}$	Interaction parameter between B atoms and wall	46
$\chi_W$	Interaction parameter at the vicinity of the wall	47
$\psi$	Scaled composition	36
$\psi_S$	Scaled composition at the surface	41

## Grain boundary grooving due to electromigration

Symbol	Description	Page No.
$d$	Average grain size/Groove depth relative to the surface maximum	28/180
$d_g$	Groove depth/displacement from the initial position	130/150
$e$	Electronic charge	24
$f$	Bulk free energy per atom	55

Symbol	Description	Page No.
$h_g$	Surface maximum from the initial position	130
$j$	Current density	27
$k_B$	Boltzmann constant	27
$m$	Slope at the groove root	132
$n_e$	Number of conducting electrons	27
$\Delta p$	Momentum transfer to the ions due to electron wind	27
$q$	Ratio of gradient energy coefficient of conserved and non-conserved order parameter	64
$q_A$	Valence of species A	52
$s$	Surface arc length	131
$t$	Time	53
$t_f$	Mean time to failure	27
$v$	Non-dimensional velocity	150
$v_d$	Drift velocity	28
$v_{ss}$	Steady state velocity	182
$w$	Width of the interconnect line/ Groove width	28/130
$z$	Effective charge of the diffusing species	24
$z_e$	Effective charge due to electrostatic contribution	24
$z_w$	Effective charge due to electron-wind contribution	24
$z_S$	Effective charge of the species at the surface	31
$z_{GB}$	Effective charge of the species at the grain boundary	31
$A, B, C$	Barrier height of the free energy	57
$A_o$	Initial amplitude of perturbation	78
$A_t$	Amplitude of perturbation at a given time	78
$B$	Mullins Constant	31
$C_A$	Concentration of species A	53
$C_V$	Concentration of vacancy	54
$D_B$	Bulk diffusivity	77
$D_S$	Surface diffusivity	31
$D_{GB}$	Grain boundary diffusivity	31
$E$	Electric field	24
$E_m$	Electric field in the interconnect domain	79
$E_t$	Tangential component of the electric field	188
$E_M$	Activation energy of the electromigration process	28
$F$	Free energy functional	55
$F_{eff}/F_{em}$	Effective driving force for electromigration	24/188

Symbol	Description	Page No.
$G$	Free energy	53
$G_v^f$	Free energy of formation of vacancy	53
$\Delta H$	Activation energy of the electromigration process	27
$J_{chem}$	Chemical flux	187
$J_e$	Flux of electrons	53
$J_{em}$	Electromigration flux	187
$J_A$	Flux of species A	52
$J_S$	Surface flux	131
$J_S^E$	Electromigration-induced surface flux	158
$J_S^{\nabla\kappa_S}$	Capillary-induced surface flux	158
$J_{GB}$	Grain boundary flux	31
$J_{GB}^E$	Electromigration-induced grain boundary flux	158
$J_V$	Flux of vacancy	52
$L$	Grain size	31
$L_{ee}$	Kinetic coefficient for the flow of electrons	53
$L_m$	Length of the interconnect domain	56
$L_u$	Length of the underlayer domain	56
$L_{AA}$	Kinetic coefficient for the diffusion of species A	52
$L_{Ae}$	Kinetic coefficient relating to the interaction between species A and electron	52
$L_\eta$	Grain boundary relaxation parameter	58
$M$	Ratio of electromigration-induced grain boundary to surface transport	181
$M_B$	Bulk atomic mobility	58
$M_S$	Surface atomic mobility	58
$M_{GB}$	Grain boundary atomic mobility	58
$M(\rho, \eta)$	Position dependent atomic mobility	58
$N$	Number of grains in the solid/interconnect domain	55
$N_a$	Number of thermally activated ions	27
$N_A$	Number of A atoms	53
$N_V$	Number of atoms per volume	55
$N_{Va}$	Number of vacancies	53
$R$	Rate of mass transport	27
$R_m$	Resistance of interconnect	56
$R_u$	Resistance of underlayer	56
$T$	Temperature	27

Symbol	Description	Page No.
$V$	Volume/Voltage	53/62
$V_n$	Normal velocity	77
$\alpha$	Non-dimensional parameter characterizing electromigration-induced grain boundary transport to capillary-mediated surface transport	31
$\beta$	Constant related to interconnect and underlayer conductivity	188
$\gamma_S$	Surface energy	31
$\gamma_{GB}$	Grain boundary energy	72
$\Gamma$	Half of the ratio of grain boundary to surface energy	189
$\delta_S$	Surface width	31
$\delta_{GB}$	Grain boundary width	31
$\epsilon$	Parameter related to interface width	64
$\eta$	Grain order parameter (non-conserved)	55
$\theta$	Angle between surface tangent and horizontal axis	187
$\theta_o$	Angle between surface tangent and horizontal axis at the groove root	130
$\kappa_\rho$	Gradient energy coefficient of the conserved order parameter	55
$\kappa_\eta$	Gradient energy coefficient of the non-conserved order parameter	55
$\kappa_S$	Mean curvature	130
$\Lambda$	Ratio of electrostatic energy to chemical energy	64
$\lambda$	Wavelength	78
$\mu$	Chemical potential	58
$\mu_o$	Chemical potential of a flat surface	130
$\mu_A$	Chemical potential of species A	52
$\mu_V$	Chemical potential of vacancies	52
$\mu_\rho$	Variational derivative of free energy functional with respect to conserved order parameter	64
$\mu_\eta$	Variational derivative of free energy functional with respect to non-conserved order parameter	64
$\nu$	Surface concentration of atoms	131
$\rho$	Scaled density variable (conserved order parameter)	55
$\rho_r$	Resistivity	28
$\sigma$	Conductivity	53

<b>Symbol</b>	<b>Description</b>	<b>Page No.</b>
$\sigma_m$	Conductivity of the interconnect domain	59
$\sigma_u$	Conductivity of the underlayer domain	59
$\phi$	Electric potential	52
$\phi_s$	Electric potential along the surface	187
$\chi$	Ratio of capillary to surface electromigration force	189
$\Omega$	Atomic volume/Domain	31/64
$\Omega_V$	Atomic volume of vacancy	54

## Numerical discretization

<b>Symbol</b>	<b>Description</b>	<b>Page No.</b>
$N_x, N_y$	Number of grid points in $x$ and $y$ directions	62
$L_x, L_y$	Length of the simulation domain in $x$ and $y$ directions	49
$i, j$	Discrete grid position in $x$ and $y$ directions	50
$\Delta x, \Delta y$	Spatial discretization width in $x$ and $y$ directions	50
$t$	Time	51
$\Delta t$	Temporal discretization width	51
$\omega$	Relaxation parameter for successive-over-relaxation algorithm	59
$n$	Iteration step	61

# Bibliography

- [1] A. Mukherjee, R. Mukherjee, K. Ankit, A. Bhattacharya, and B. Nestler. Influence of substrate interaction and confinement on electric-field-induced transition in symmetric block-copolymer thin films. *Phys. Rev. E*, 93(3):032504, 2016.
- [2] A. Mukherjee, K. Ankit, A. Reiter, M. Selzer, and B. Nestler. Electric-field-induced lamellar to hexagonally perforated lamellar transition in diblock copolymer thin films: kinetic pathways. *Phys. Chem. Chem. Phys.*, 18(36):25609–25620, 2016.
- [3] A. Mukherjee, K. Ankit, M. Selzer, and B. Nestler. Electromigration-induced surface drift and slit propagation in polycrystalline interconnects: Insights from phase-field simulations. *Phys. Rev. Appl.*, 9(4):044004, 2018.
- [4] A. Mukherjee, K. Ankit, R. Mukherjee, and B. Nestler. Phase-field modeling of grain-boundary grooving under electromigration. *J. Electron. Mater.*, 45(12):6233–6246, 2016.
- [5] L. Klinger, E. Glickman, V. Fradkov, W. Mullins, and C. Bauer. Extensions of thermal grooving for arbitrary grain-boundary flux. *J. Appl. Phys.*, 78(6):3833–3838, 1995.
- [6] K. Amundson, E. Helfand, X. Quan, and S. D. Smith. Alignment of lamellar block copolymer microstructure in an electric field. 1. alignment kinetics. *Macromolecules*, 26(11):2698–2703, 1993.
- [7] T. Xu, Y. Zhu, S. P. Gido, and T. P. Russell. Electric field alignment of symmetric diblock copolymer thin films. *Macromolecules*, 37(7):2625–2629, 2004.
- [8] G. Venugopal, S. Krause, and G. Wnek. Modification of polymer blend morphology using electric fields. *J. Polym. Sci. Pol. Lett.*, 27(12):497–501, 1989.
- [9] G. Venugopal and S. Krause. Development of phase morphologies of poly (methyl methacrylate)-polystyrene-toluene mixtures in electric fields. *Macromolecules*, 25(18):4626–4634, 1992.

- [10] G. I. Taylor. Disintegration of water drops in an electric field. *Proc. R. Soc. Lond. A*, 280(1382):383–397, 1964.
- [11] G. Taylor and A. McEwan. The stability of a horizontal fluid interface in a vertical electric field. *J. Fluid Mech.*, 22(1):1–15, 1965.
- [12] E. Schäffer, T. Thurn-Albrecht, T. P. Russell, and U. Steiner. Electrically induced structure formation and pattern transfer. *Nature*, 403(6772):874, 2000.
- [13] M. D. Morariu, N. E. Voicu, E. Schäffer, Z. Lin, T. P. Russell, and U. Steiner. Hierarchical structure formation and pattern replication induced by an electric field. *Nat. Mater.*, 2(1):48, 2003.
- [14] H. Conrad. Influence of an electric or magnetic field on the liquid–solid transformation in materials and on the microstructure of the solid. *Mat. Sci. Eng. A - Struct.*, 287(2):205–212, 2000.
- [15] F. Li, L. L. Regel, and W. R. Wilcox. The influence of electric current pulses on the microstructure of the mnbi/bi eutectic. *J. Cryst. Growth*, 223(1-2):251–264, 2001.
- [16] J. Li, P. Ni, L. Wang, and Y. Tan. Influence of direct electric current on solidification process of al–si alloy. *Mat. Sci. Semicon. Proc.*, 61:79–84, 2017.
- [17] Y. Zhang, X. Miao, Z. Shen, Q. Han, C. Song, and Q. Zhai. Macro segregation formation mechanism of the primary silicon phase in directionally solidified al–si hypereutectic alloys under the impact of electric currents. *Acta Mater.*, 97:357–366, 2015.
- [18] K. Vashchenko, D. Chernega, S. Vorobev, N. Lysenko, and Y. E. Yakovchuk. Effect of electric current on the solidification of cast iron. *Met. Sci. Heat Treat.*, 16(3):261–265, 1974.
- [19] D. Yang and H. Conrad. Enhanced sintering rate of zirconia (3y-tzp) by application of a small ac electric field. *Scripta Mater.*, 63(3):328–331, 2010.
- [20] H. Conrad and D. Yang. Dependence of the sintering rate and related grain size of yttria-stabilized polycrystalline zirconia (3y-tzp) on the strength of an applied dc electric field. *Mat. Sci. Eng. A - Struct.*, 528(29-30):8523–8529, 2011.
- [21] S. K. Jha and R. Raj. The effect of electric field on sintering and electrical conductivity of titania. *J. Am. Ceram. Soc.*, 97(2):527–534, 2014.
- [22] I. Blech. Electromigration and crevice formation in thin metallic films. *Thin Solid Films*, 13(1):117–129, 1972.

- [23] P. S. Ho and T. Kwok. Electromigration in metals. *Rep. Prog. Phys.*, 52(3):301, 1989.
- [24] M. Z. Mayers, J. W. Kaminski, and T. F. Miller III. Suppression of dendrite formation via pulse charging in rechargeable lithium metal batteries. *J. Phys. Chem. C*, 116(50):26214–26221, 2012.
- [25] M. S. Park, S. B. Ma, D. J. Lee, D. Im, S.-G. Doo, and O. Yamamoto. A highly reversible lithium metal anode. *Sci. Rep-UK*, 4:3815, 2014.
- [26] F. S. Bates. Polymer-polymer phase behavior. *Science*, 251(4996):898–905, 1991.
- [27] F. S. Bates and G. H. Fredrickson. Block copolymer thermodynamics: theory and experiment. *Annu. Rev. Phys. Chem.*, 41(1):525–557, 1990.
- [28] L. Leibler. Theory of microphase separation in block copolymers. *Macromolecules*, 13(6):1602–1617, 1980.
- [29] T. Ohta and K. Kawasaki. Equilibrium morphology of block copolymer melts. *Macromolecules*, 19(10):2621–2632, 1986.
- [30] A. K. Khandpur, S. Foerster, F. S. Bates, I. W. Hamley, A. J. Ryan, W. Bras, K. Almdal, and K. Mortensen. Polyisoprene-polystyrene diblock copolymer phase diagram near the order-disorder transition. *Macromolecules*, 28(26):8796–8806, 1995.
- [31] N. Koneripalli, R. Levicky, F. S. Bates, J. Ankner, H. Kaiser, and S. K. Satija. Confinement-induced morphological changes in diblock copolymer films. *Langmuir*, 12(26):6681–6690, 1996.
- [32] A. Chremos, K. Margaritis, and A. Z. Panagiotopoulos. Ultra thin films of diblock copolymers under shear. *Soft Matter*, 6(15):3588–3595, 2010.
- [33] K. Schmidt, A. Böker, H. Zettl, F. Schubert, H. Hänsel, F. Fischer, T. M. Weiss, V. Abetz, A. Zvelindovsky, G. Sevink, and G. Krausch. Influence of initial order on the microscopic mechanism of electric field induced alignment of block copolymer microdomains. *Langmuir*, 21(25):11974–11980, 2005.
- [34] P. W. Majewski, M. Gopinadhan, and C. O. Osuji. Magnetic field alignment of block copolymers and polymer nanocomposites: scalable microstructure control in functional soft materials. *J. Polym. Sci. Pol. Phys.*, 50(1):2–8, 2012.
- [35] G. H. Fredrickson. Surface ordering phenomena in block copolymer melts. *Macromolecules*, 20(10):2535–2542, 1987.

- [36] K. R. Shull. Mean-field theory of block copolymers: bulk melts, surfaces, and thin films. *Macromolecules*, 25(8):2122–2133, 1992.
- [37] G. Brown and A. Chakrabarti. Surface-induced ordering in block copolymer melts. *J. Chem. Phys.*, 101(4):3310–3317, 1994.
- [38] M. S. Turner. Equilibrium properties of a diblock copolymer lamellar phase confined between flat plates. *Phys. Rev. Lett.*, 69(12):1788, 1992.
- [39] D. Walton, G. Kellogg, A. Mayes, P. Lambooy, and T. Russell. A free energy model for confined diblock copolymers. *Macromolecules*, 27(21):6225–6228, 1994.
- [40] M. Kikuchi and K. Binder. Microphase separation in thin films of the symmetric diblock-copolymer melt. *J. Chem. Phys.*, 101(4):3367–3377, 1994.
- [41] G. Brown and A. Chakrabarti. Ordering of block copolymer melts in confined geometry. *J. Chem. Phys.*, 102(3):1440–1448, 1995.
- [42] Q. Wang, Q. Yan, P. F. Nealey, and J. J. de Pablo. Monte carlo simulations of diblock copolymer thin films confined between two homogeneous surfaces. *J. Chem. Phys.*, 112(1):450–464, 2000.
- [43] H. Huinink, J. Brokken-Zijp, M. Van Dijk, and G. Sevink. Asymmetric block copolymers confined in a thin film. *J. Chem. Phys.*, 112(5):2452–2462, 2000.
- [44] K. Lyakhova, G. Sevink, A. Zvelindovsky, A. Horvat, and R. Magerle. Role of dissimilar interfaces in thin films of cylinder-forming block copolymers. *J. Chem. Phys.*, 120(2):1127–1137, 2004.
- [45] V. Olszowka, M. Hund, V. Kuntermann, S. Scherdel, L. Tsarkova, and A. Boker. Electric field alignment of a block copolymer nanopattern: direct observation of the microscopic mechanism. *ACS nano*, 3(5):1091–1096, 2009.
- [46] P. Lambooy, T. Russell, G. Kellogg, A. Mayes, P. Gallagher, and S. Satija. Observed frustration in confined block copolymers. *Phys. Rev. Lett.*, 72(18):2899, 1994.
- [47] W. Li, M. Liu, F. Qiu, and A.-C. Shi. Phase diagram of diblock copolymers confined in thin films. *J. Phys. Chem. B*, 117(17):5280–5288, 2013.
- [48] M. J. Fasolka, P. Banerjee, A. M. Mayes, G. Pickett, and A. C. Balazs. Morphology of ultrathin supported diblock copolymer films: Theory and experiment. *Macromolecules*, 33(15):5702–5712, 2000.
- [49] N. Koneripalli, F. S. Bates, and G. H. Fredrickson. Fractal hole growth in strained block copolymer films. *Phys. Rev. Lett.*, 81(9):1861, 1998.

- [50] S.-H. Lee, H. Kang, J. Cho, Y. S. Kim, and K. Char. Dual morphology of islands and fractal holes in block copolymer thin films. *Macromolecules*, 34(24):8405–8408, 2001.
- [51] D. Q. Ly, T. Honda, T. Kawakatsu, and A. V. Zvelindovsky. Kinetic pathway of gyroid-to-cylinder transition in diblock copolymer melt under an electric field. *Macromolecules*, 40(8):2928–2935, 2007.
- [52] D. Q. Ly, T. Honda, T. Kawakatsu, and A. V. Zvelindovsky. Hexagonally perforated lamella-to-cylinder transition in a diblock copolymer thin film under an electric field. *Macromolecules*, 41(12):4501–4505, 2008.
- [53] T. Xu, C. J. Hawker, and T. P. Russell. Interfacial energy effects on the electric field alignment of symmetric diblock copolymers. *Macromolecules*, 36(16):6178–6182, 2003.
- [54] K. Amundson, E. Helfand, X. Quan, S. D. Hudson, and S. D. Smith. Alignment of lamellar block copolymer microstructure in an electric field. 2. mechanisms of alignment. *Macromolecules*, 27(22):6559–6570, 1994.
- [55] G. Pereira and D. Williams. Diblock copolymer melts in electric fields: the transition from parallel to perpendicular alignment using a capacitor analogy. *Macromolecules*, 32(24):8115–8120, 1999.
- [56] Y. Tsori and D. Andelman. Thin film diblock copolymers in electric field: transition from perpendicular to parallel lamellae. *Macromolecules*, 35(13):5161–5170, 2002.
- [57] K. Lyakhova, A. Zvelindovsky, and G. Sevink. Kinetic pathways of order-to-order phase transitions in block copolymer films under an electric field. *Macromolecules*, 39(8):3024–3037, 2006.
- [58] J. Wu, X. Wang, Y. Ji, L. He, and S. Li. Phase diagrams of diblock copolymers in electric fields: a self-consistent field theory study. *Phys. Chem. Chem. Phys.*, 18(15):10309–10319, 2016.
- [59] M. Matsen. Electric field alignment in thin films of cylinder-forming diblock copolymer. *Macromolecules*, 39(16):5512–5520, 2006.
- [60] C.-Y. Lin and M. Schick. Self-consistent field study of the alignment by an electric field of a cylindrical phase of block copolymer. *J. Chem. Phys.*, 125(3):034902, 2006.

- [61] M. Matsen. Converting the nanodomains of a diblock-copolymer thin film from spheres to cylinders with an external electric field. *J. Chem. Phys.*, 124(7):074906, 2006.
- [62] J.-Y. Wang, W. Chen, and T. P. Russell. Influence of interfacial energy on electric-field-induced sphere-to-cylinder transition in block copolymer thin films. *Macromolecules*, 41(19):7227–7231, 2008.
- [63] D. Ly, M. Pinna, T. Honda, T. Kawakatsu, and A. Zvelindovsky. Kinetic pathways of sphere-to-cylinder transition in diblock copolymer melt under electric field. *J. Chem. Phys.*, 138(7):074904, 2013.
- [64] M. Pinna and A. V. Zvelindovsky. Kinetic pathways of gyroid-to-cylinder transitions in diblock copolymers under external fields: cell dynamics simulation. *Soft Matter*, 4(2):316–327, 2008.
- [65] K. Schmidt, C. W. Pester, H. G. Schoberth, H. Zettl, K. A. Schindler, and A. Böker. Electric field induced gyroid-to-cylinder transitions in concentrated diblock copolymer solutions. *Macromolecules*, 43(9):4268–4274, 2010.
- [66] D. Q. Ly, T. Honda, T. Kawakatsu, and A. V. Zvelindovsky. Electric field-induced transitions in perforated lamella of aba triblock copolymer thin film. *Soft Matter*, 5(23):4814–4822, 2009.
- [67] C. W. Pester, K. Schmidt, M. Ruppel, H. G. Schoberth, and A. Böker. Electric-field-induced order–order transition from hexagonally perforated lamellae to lamellae. *Macromolecules*, 48(17):6206–6213, 2015.
- [68] Y. Tsori. Colloquium: Phase transitions in polymers and liquids in electric fields. *Rev. Mod. Phys.*, 81(4):1471, 2009.
- [69] C. W. Pester, C. Liedel, M. Ruppel, and A. Böker. Block copolymers in electric fields. *Prog. Polym. Sci.*, 64:182–214, 2017.
- [70] B. Ashok, M. Muthukumar, and T. Russell. Confined thin film diblock copolymer in the presence of an electric field. *J. Chem. Phys.*, 115(3):1559–1564, 2001.
- [71] E. J. Crossland, S. Ludwigs, M. A. Hillmyer, and U. Steiner. Control of gyroid forming block copolymer templates: effects of an electric field and surface topography. *Soft Matter*, 6(3):670–676, 2010.
- [72] H. Ceric and S. Selberherr. Electromigration in submicron interconnect features of integrated circuits. *Mater. Sci. Eng. R*, 71(5):53–86, 2011.

- [73] J. Lloyd. Electromigration failure. *J. Appl. Phys.*, 69(11):7601–7604, 1991.
- [74] J. Lloyd. Electromigration in integrated circuit conductors. *J. Phys. D Appl. Phys.*, 32(17):R109, 1999.
- [75] I. Blech and E. Kinsbron. Electromigration in thin gold films on molybdenum surfaces. *Thin Solid Films*, 25(2):327–334, 1975.
- [76] A. Gladkikh, M. Karpovskii, A. Palevskii, and Y. S. Kaganovskii. Effect of microstructure on electromigration kinetics in cu lines. *J. Phys. D Appl. Phys.*, 31(14):1626, 1998.
- [77] R. De Orto, H. Ceric, and S. Selberherr. Physically based models of electromigration: From black's equation to modern tcad models. *Microelectron. Reliab.*, 50(6):775–789, 2010.
- [78] R. Rosenberg and M. Ohring. Void formation and growth during electromigration in thin films. *J. Appl. Phys.*, 42(13):5671–5679, 1971.
- [79] Z. Islam, B. Wang, and A. Haque. Current density effects on the microstructure of zirconium thin films. *Scripta Mater.*, 144:18–21, 2018.
- [80] L. Berenbaum. Electromigration damage of grain-boundary triple points in al thin films. *J. Appl. Phys.*, 42(2):880–882, 1971.
- [81] H. Ma, F. La Mattina, I. Shorubalko, R. Spolenak, and M. Seita. Engineering the grain boundary network of thin films via ion-irradiation: Towards improved electromigration resistance. *Acta Mater.*, 123:272–284, 2017.
- [82] Z. Suo. Electromigration-induced dislocation climb and multiplication in conducting lines. *Acta Metall. Mater.*
- [83] S. Baker, Y.-C. Joo, M. Knauss, and E. Arzt. Electromigration damage in mechanically deformed al conductor lines: dislocations as fast diffusion paths. *Acta mater.*, 48(9):2199–2208, 2000.
- [84] C. Hau-Riege and C. Thompson. Electromigration in cu interconnects with very different grain structures. *Appl. Phys. Lett.*, 78(22):3451–3453, 2001.
- [85] L. Arnaud, T. Berger, and G. Reibold. Evidence of grain-boundary versus interface diffusion in electromigration experiments in copper damascene interconnects. *J. Appl. Phys.*, 93(1):192–204, 2003.
- [86] N. McCusker, H. Gamble, and B. Armstrong. Surface electromigration in copper interconnects. *Microelectron. Reliab.*, 40(1):69–76, 2000.

- [87] I. A. Blech. Electromigration in thin aluminum films on titanium nitride. *J. Appl. Phys.*, 47(4):1203–1208, 1976.
- [88] I. Blech and K. Tai. Measurement of stress gradients generated by electromigration. *Appl. Phys. Lett.*, 30(8):387–389, 1977.
- [89] E. Kinsbron, I. Blech, and Y. Komem. The threshold current density and incubation time to electromigration in gold films. *Thin Solid Films*, 46(2):139–150, 1977.
- [90] O. Kraft and E. Arzt. Electromigration mechanisms in conductor lines: void shape changes and slit-like failure. *Acta mater.*, 45(4):1599–1611, 1997.
- [91] E. Arzt, O. Kraft, W. D. Nix, and J. Sanchez Jr. Electromigration failure by shape change of voids in bamboo lines. *J. Appl. Phys.*, 76(3):1563–1571, 1994.
- [92] M. R. Gungor and D. Maroudas. Theoretical analysis of electromigration-induced failure of metallic thin films due to transgranular void propagation. *J. Appl. Phys.*, 85(4):2233–2246, 1999.
- [93] Y. Yao, L. M. Keer, and M. E. Fine. Electromigration effect on pancake type void propagation near the interface of bulk solder and intermetallic compound. *J. Appl. Phys.*, 105(6):063710, 2009.
- [94] Y. Yao, Y. Wang, L. M. Keer, and M. E. Fine. An analytical method to predict electromigration-induced finger-shaped void growth in snagcu solder interconnect. *Scripta Mater.*, 95:7–10, 2015.
- [95] L. Klinger, X. Chu, W. Mullins, and C. Bauer. Grain-boundary slit propagation in an electric field. *J. Appl. Phys.*, 80(12):6670–6676, 1996.
- [96] C.-Y. Liu, S. Lee, and T.-j. Chuang. Grain boundary crack growth in interconnects with an electric current. *Mat. Sci. Eng. B - Solid*, 86(2):101–108, 2001.
- [97] H.-W. Hsueh, F.-Y. Hung, and T.-S. Lui. A study on electromigration-inducing intergranular fracture of fine silver alloy wires. *Appl. Phys. Lett.*, 110(3):031902, 2017.
- [98] J. Nucci, A. Straub, E. Bischoff, E. Arzt, and C. Volkert. Growth of electromigration-induced hillocks in al interconnects. *J. Mater. Res.*, 17(10):2727–2735, 2002.
- [99] S. Riege, J. Prybyla, and A. Hunt. Influence of microstructure on electromigration dynamics in submicron al interconnects: Real-time imaging. *Appl. Phys. Lett.*, 69(16):2367–2369, 1996.

- [100] A. Gladkikh, Y. Lereah, E. Glickman, M. Karpovski, A. Palevski, and J. Schubert. Hillock formation during electromigration in cu and al thin films: Three-dimensional grain growth. *Appl. Phys. Lett.*, 66(10):1214–1215, 1995.
- [101] M.-S. Yoon, M.-K. Ko, O.-H. Kim, Y.-B. Park, W. D. Nix, and Y.-C. Joo. In-situ observation of electromigration in eutectic snpb solder lines: atomic migration and hillock formation. *J. Electron. Mater.*, 36(5):562–567, 2007.
- [102] J. R. Black. Electromigration failure modes in aluminum metallization for semiconductor devices. *P. IEEE*, 57(9):1587–1594, 1969.
- [103] M. Korhonen, P. Bo/rgeesen, K. Tu, and C.-Y. Li. Stress evolution due to electromigration in confined metal lines. *J. Appl. Phys.*, 73(8):3790–3799, 1993.
- [104] Y. Wang and Y. Yao. A theoretical analysis to current exponent variation regularity and electromigration-induced failure. *J. Appl. Phys.*, 121(6):065701, 2017.
- [105] C.-K. Hu, R. Rosenberg, and K. Lee. Electromigration path in cu thin-film lines. *Appl. Phys. Lett.*, 74(20):2945–2947, 1999.
- [106] J. Lloyd and J. Clement. Electromigration in copper conductors. *Thin solid films*, 262(1-2):135–141, 1995.
- [107] A. Gladkikh, Y. Lereah, M. Karpovski, A. Palevski, and Y. S. Kaganovskii. Activation energy of electromigration in copper thin film conductor lines. In *MRS Proceedings*, volume 428, page 55. Cambridge Univ Press, 1996.
- [108] C. Hu, K. Lee, L. Gignac, and R. Carruthers. Electromigration in 0.25  $\mu\text{m}$  wide cu line on w. *Thin Solid Films*, 308:443–447, 1997.
- [109] E. Glickman and M. Nathan. On the unusual electromigration behavior of copper interconnects. *J. Appl. Phys.*, 80(7):3782–3791, 1996.
- [110] M. Shatzkes and J. Lloyd. A model for conductor failure considering diffusion concurrently with electromigration resulting in a current exponent of 2. *J. Appl. Phys.*, 59(11):3890–3893, 1986.
- [111] R. Kirchheim. Stress and electromigration in al-lines of integrated circuits. *Acta Metall. Mater.*, 40(2):309–323, 1992.
- [112] J. Clement and C. Thompson. Modeling electromigration-induced stress evolution in confined metal lines. *J. Appl. Phys.*, 78(2):900–904, 1995.
- [113] M. Ohring. Electromigration damage in thin films due to grain boundary grooving processes. *J. Appl. Phys.*, 42(7):2653–2661, 1971.

- [114] N. Gazit, L. Klinger, and E. Rabkin. Chemically-induced solid-state dewetting of thin au films. *Acta Mater.*, 129:300–311, 2017.
- [115] P. Jacquet, R. Podor, J. Ravaux, J. Lautru, J. Teisseire, I. Gozhyk, J. Jupille, and R. Lazzari. On the solid-state dewetting of polycrystalline thin films: Capillary versus grain growth approach. *Acta Mater.*, 143:281–290, 2018.
- [116] D. Amram, L. Klinger, N. Gazit, H. Gluska, and E. Rabkin. Grain boundary grooving in thin films revisited: the role of interface diffusion. *Acta Mater.*, 69:386–396, 2014.
- [117] V. Derkach, A. Novick-Cohen, and E. Rabkin. Grain boundaries effects on hole morphology and growth during solid state dewetting of thin films. *Scripta Mater.*, 134:115–118, 2017.
- [118] K. Maeda, A. Niitsu, H. Morito, K. Shiga, and K. Fujiwara. In situ observation of grain boundary groove at the crystal/melt interface in cu. *Scripta Mater.*, 146:169–172, 2018.
- [119] T. O. Ogurtani and O. Akyildiz. Cathode edge displacement by voiding coupled with grain boundary grooving in bamboo like metallic interconnects by surface drift-diffusion under the capillary and electromigration forces. *Int. J. Solids Struct.*, 45(3-4):921–942, 2008.
- [120] T. O. Ogurtani and O. Akyildiz. Grain boundary grooving and cathode voiding in bamboo-like metallic interconnects by surface drift diffusion under the capillary and electromigration forces. *J. Appl. Phys.*, 97(9):093520, 2005.
- [121] S. Chakraborty, P. Kumar, and A. Choudhury. Phase-field modeling of grain-boundary grooving and migration under electric current and thermal gradient. *Acta Mater.*, 153:377–390, 2018.
- [122] W. W. Mullins. Theory of thermal grooving. *J. Appl. Phys.*, 28(3):333–339, 1957.
- [123] W. Mullins. Grain boundary grooving by volume diffusion. *T. Am. I. Min. Met. Eng.*, 218(2):354–361, 1960.
- [124] F. Genin, W. Mullins, and P. Wynblatt. The effect of stress on grain boundary grooving. *Acta Metall. Mater.*, 41(12):3541–3547, 1993.
- [125] M. Thouless. Effect of surface diffusion on the creep of thin films and sintered arrays of particles. *Acta Metall. Mater.*, 41(4):1057–1064, 1993.

- [126] L. Klinger, E. Glickman, V. Fradkov, W. Mullins, and C. Bauer. Effect of surface and grain-boundary diffusion on interconnect reliability. *MRS Online Proceedings Library Archive*, 391, 1995.
- [127] H. Vogel and L. Ratke. Instability of grain boundary grooves due to equilibrium grain boundary diffusion. *Acta Metall. Mater.*, 39(4):641–649, 1991.
- [128] F. Genin. The initial stages of the formation of holes and hillocks in thin films under equal biaxial stress. *Acta Metall. Mater.*, 43(12):4289–4300, 1995.
- [129] J. Wang and P. M. Anderson. Pinch-off maps for the design of morphologically stable multilayer thin films with immiscible phases. *Acta mater.*, 53(19):5089–5099, 2005.
- [130] T. Berger, L. Arnaud, R. Gonella, G. Lormand, and Y. Morand. Electromigration characterization of damascene copper interconnects using normally and highly accelerated tests. *Microelectron. Reliab.*, 40(8-10):1311–1316, 2000.
- [131] O. Kononenko, V. Matveev, and D. Field. The energy of activation of electromigration in aluminum conductors tested by the drift-velocity method. *Russ. Microelectron.*, 29(5):316–323, 2000.
- [132] R. Kirchheim and U. Kaeber. Atomistic and computer modeling of metallization failure of integrated circuits by electromigration. *J. Appl. Phys.*, 70(1):172–181, 1991.
- [133] R. Gleixner and W. Nix. A physically based model of electromigration and stress-induced void formation in microelectronic interconnects. *J. Appl. Phys.*, 86(4):1932–1944, 1999.
- [134] A. F. Bower and S. Shankar. A finite element model of electromigration induced void nucleation, growth and evolution in interconnects. *Model. Simul. Mater. Sc.*, 15(8):923, 2007.
- [135] Y.-W. Chang, Y. Cheng, F. Xu, L. Helfen, T. Tian, M. Di Michiel, C. Chen, K.-N. Tu, and T. Baumbach. Study of electromigration-induced formation of discrete voids in flip-chip solder joints by in-situ 3d laminography observation and finite-element modeling. *Acta Mater.*, 117:100–110, 2016.
- [136] M. Mahadevan and R. M. Bradley. Simulations and theory of electromigration-induced slit formation in unpassivated single-crystal metal lines. *Phys. Rev. B*, 59(16):11037, 1999.

- [137] D. N. Bhate, A. Kumar, and A. F. Bower. Diffuse interface model for electromigration and stress voiding. *J. Appl. Phys.*, 87(4):1712–1721, 2000.
- [138] J. W. Barrett, H. Garcke, and R. Nürnberg. A phase field model for the electromigration of intergranular voids. *Interface Free Bound.*, 9(2):171–210, 2007.
- [139] P. Zhou and J. Wang. Modeling of the coalescence of micro-voids under the influence of elastic stresses and electromigration. In *Electronic Packaging Technology (ICEPT), 2014 15th International Conference on*, pages 1047–1051. IEEE, 2014.
- [140] M. Khenner, A. Averbuch, M. Israeli, M. Nathan, and E. Glickman. Level set modeling of transient electromigration grooving. *Comp. Mater. Sci.*, 20(2):235–250, 2001.
- [141] T. O. Ogurtani. Variational formulation of irreversible thermodynamics of surfaces and interfaces with grain-boundary triple-junction singularities under the capillary and electromigration forces in anisotropic two-dimensional space. *Phys. Rev. B*, 73(23):235408, 2006.
- [142] O. Akyildiz and T. Omer Ogurtani. Grain boundary grooving induced by the anisotropic surface drift diffusion driven by the capillary and electromigration forces: Simulations. *J. Appl. Phys.*, 110(4):043521, 2011.
- [143] R. Zhang, I. Rungger, S. Sanvito, and S. Hou. Current-induced energy barrier suppression for electromigration from first principles. *Phys. Rev. B*, 84:085445, Aug 2011.
- [144] K. H. Bevan, W. Zhu, G. M. Stocks, H. Guo, and Z. Zhang. Local fields in conductor surface electromigration: A first-principles study in the low-bias ballistic limit. *Phys. Rev. B*, 85:235421, Jun 2012.
- [145] M. Rusanen, P. Kuhn, and J. Krug. Kinetic monte carlo simulations of oscillatory shape evolution for electromigration-driven islands. *Phys. Rev. B*, 74(24):245423, 2006.
- [146] A. Latz, S. Sindermann, L. Brendel, G. Dumpich, F.-J. M. zu Heringdorf, and D. Wolf. Simulation of electromigration effects on voids in monocrystalline ag films. *Phys. Rev. B*, 85(3):035449, 2012.
- [147] N. Wang, K. H. Bevan, and N. Provatas. Phase-field-crystal model for electromigration in metal interconnects. *Phys. Rev. Lett.*, 117(15):155901, 2016.

- [148] M. Park, S. Gibbons, and R. Arróyave. Phase-field simulations of intermetallic compound evolution in cu/sn solder joints under electromigration. *Acta Mater.*, 61(19):7142–7154, 2013.
- [149] P. Zhou and W. C. Johnson. A diffuse interface model of intermediate-phase growth under the influence of electromigration. *J. Electron. Mater.*, 40(9):1867, 2011.
- [150] E. Helfand. Theory of inhomogeneous polymers: Fundamentals of the gaussian random-walk model. *J. Chem. Phys.*, 62(3):999–1005, 1975.
- [151] M. W. Matsen and M. Schick. Stable and unstable phases of a diblock copolymer melt. *Phys. Rev. Lett.*, 72(16):2660, 1994.
- [152] J. Fraaije. Dynamic density functional theory for microphase separation kinetics of block copolymer melts. *J. Chem. Phys.*, 99(11):9202–9212, 1993.
- [153] J. Fraaije, B. Van Vlimmeren, N. Maurits, M. Postma, O. Evers, C. Hoffmann, P. Altevogt, and G. Goldbeck-Wood. The dynamic mean-field density functional method and its application to the mesoscopic dynamics of quenched block copolymer melts. *J. Chem. Phys.*, 106(10):4260–4269, 1997.
- [154] I. W. Hamley. Cell dynamics simulations of block copolymers. *Macromol. Theor. Simul.*, 9(7):363–380, 2000.
- [155] M. Pinna and A. Zvelindovsky. Large scale simulation of block copolymers with cell dynamics. *Eur. Phys. J. B*, 85(6):210, 2012.
- [156] Y. Tsori, D. Andelman, C.-Y. Lin, and M. Schick. Block copolymers in electric fields: A comparison of single-mode and self-consistent-field approximations. *Macromolecules*, 39(1):289–293, 2006.
- [157] C.-Y. Lin, M. Schick, and D. Andelman. Structural changes of diblock copolymer melts due to an external electric field: a self-consistent-field theory study. *Macromolecules*, 38(13):5766–5773, 2005.
- [158] M. W. Matsen. Undulation instability in block-copolymer lamellae subjected to a perpendicular electric field. *Soft Matter*, 2(12):1048–1056, 2006.
- [159] M. Bahiana and Y. Oono. Cell dynamical system approach to block copolymers. *Phys. Rev. A*, 41(12):6763, 1990.
- [160] A. Chakrabarti, R. Toral, and J. D. Gunton. Microphase separation in block copolymers. *Phys. Rev. Lett.*, 63(24):2661, 1989.

- [161] A. Chakrabarti, R. Toral, and J. D. Gunton. Scaling behavior of a model of block copolymers in three dimensions. *Phys. Rev. A*, 44(10):6503, 1991.
- [162] X.-F. Wu and Y. A. Dzenis. Phase-field modeling of the formation of lamellar nanostructures in diblock copolymer thin films under inplanar electric fields. *Phys. Rev. E*, 77(3):031807, 2008.
- [163] R. Choksi and X. Ren. On the derivation of a density functional theory for microphase separation of diblock copolymers. *J. Stat. Phys.*, 113(1-2):151–176, 2003.
- [164] F. Liu and N. Goldenfeld. Dynamics of phase separation in block copolymer melts. *Phys. Rev. A*, 39(9):4805, 1989.
- [165] J. W. Cahn and J. E. Hilliard. Free energy of a nonuniform system. i. interfacial free energy. *J. Chem. Phys.*, 28(2):258–267, 1958.
- [166] R. Choksi, M. A. Peletier, and J. Williams. On the phase diagram for microphase separation of diblock copolymers: an approach via a nonlocal cahn–hilliard functional. *SIAM J. Appl. Math.*, 69(6):1712–1738, 2009.
- [167] D. Jeong, J. Shin, Y. Li, Y. Choi, J.-H. Jung, S. Lee, and J. Kim. Numerical analysis of energy-minimizing wavelengths of equilibrium states for diblock copolymers. *Curr. Appl. Phys.*, 14(9):1263–1272, 2014.
- [168] Y. Oono and M. Bahiana.  $\lambda$ -power law for copolymer lamellar thickness implies a  $\lambda$ -power law for spinodal decomposition. *Phys. Rev. Lett.*, 61(9):1109, 1988.
- [169] S. Ghosh, A. Mukherjee, T. Abinandanan, and S. Bose. Particles with selective wetting affect spinodal decomposition microstructures. *Phys. Chem. Chem. Phys.*, 19(23):15424–15432, 2017.
- [170] Y. Oono and M. Bahiana. Block copolymer lamellar thickness; an exactly solvable model. *J. Phys.-Condens. Mater*, 1(31):5297, 1989.
- [171] I. Podariu and A. Chakrabarti. Morphology of asymmetric diblock copolymer thin films. *J. Chem. Phys.*, 118(24):11249–11257, 2003.
- [172] R. Choksi, M. Maras, and J. Williams. 2d phase diagram for minimizers of a cahn–hilliard functional with long-range interactions. *SIAM J. Appl. Dyn. Syst.*, 10(4):1344–1362, 2011.
- [173] Y. Oono and S. Puri. Computationally efficient modeling of ordering of quenched phases. *Phys. Rev. Lett.*, 58(8):836, 1987.

- [174] Y. Oono and S. Puri. Study of phase-separation dynamics by use of cell dynamical systems. i. modeling. *Phys. Rev. A*, 38(1):434, 1988.
- [175] P. Teixeira and B. Mulder. scoment on “study of phase-separation dynamics by use of cell dynamical systems. i. nmodeling”. *Phys. Rev. E*, 55(3):3789, 1997.
- [176] S. Qi and Z.-G. Wang. Kinetics of phase transitions in weakly segregated block copolymers: Pseudostable and transient states. *Phys. Rev. E*, 55(2):1682, 1997.
- [177] J. W. Cahn. Critical point wetting. *J. Chem. Phys.*, 66(8):3667–3672, 1977.
- [178] I. Schmidt and K. Binder. Model calculations for wetting transitions in polymer mixtures. *J. Phys. (Paris)*, 46(10):1631–1644, 1985.
- [179] R. A. Jerry and E. B. Nauman. Phase transitions in thin films of a binary mixture. *Phys. Lett. A*, 167(2):198–204, 1992.
- [180] Y. Tsori and D. Andelman. Diblock copolymer thin films: Parallel and perpendicular lamellar phases in the weak segregation limit. *Eur. Phys. J. E*, 5(1):605–614, 2001.
- [181] L. D. Landau, J. Bell, M. Kearsley, L. Pitaevskii, E. Lifshitz, and J. Sykes. *Electrodynamics of continuous media*, volume 8. elsevier, 1984.
- [182] P. C. Hohenberg and B. I. Halperin. Theory of dynamic critical phenomena. *Rev. Mod. Phys.*, 49(3):435, 1977.
- [183] S. Puri and K. Binder. Surface-directed spinodal decomposition: phenomenology and numerical results. *Phys. Rev. A*, 46(8):R4487, 1992.
- [184] R. W. Balluffi, S. Allen, and W. C. Carter. *Kinetics of materials*. John Wiley & Sons, 2005.
- [185] R. Landauer. Spatial variation of currents and fields due to localized scatterers in metallic conduction (and comment). *J. Math. Phys.*, 37(10):5259–5268, 1996.
- [186] R. Mukherjee, T. Chakrabarti, E. A. Anumol, T. A. Abinandanan, and N. Ravishankar. Thermal stability of spherical nanoporous aggregates and formation of hollow structures by sintering a phase-field study. *ACS nano*, 5(4):2700–2706, 2011.
- [187] Y. U. Wang. Computer modeling and simulation of solid-state sintering: A phase field approach. *Acta mater.*, 54(4):953–961, 2006.
- [188] R. Mukherjee. *Phase field modelling of polycrystalline materials with surfaces*. PhD Thesis, Indian Institute of Science, 2011.

- [189] N. Moelans, B. Blanpain, and P. Wollants. Quantitative analysis of grain boundary properties in a generalized phase field model for grain growth in anisotropic systems. *Phys. Rev. B*, 78(2):024113, 2008.
- [190] D. Fan and L.-Q. Chen. Computer simulation of grain growth using a continuum field model. *Acta Mater.*, 45(2):611–622, 1997.
- [191] S. M. Allen and J. W. Cahn. A microscopic theory for antiphase boundary motion and its application to antiphase domain coarsening. *Acta Metall. Mater.*, 27(6):1085–1095, 1979.
- [192] J. Zhu, L.-Q. Chen, J. Shen, and V. Tikare. Coarsening kinetics from a variable-mobility cahn-hilliard equation: Application of a semi-implicit fourier spectral method. *Phys. Rev. E*, 60(4):3564, 1999.
- [193] J. K. Wolterink, G. Barkema, and S. Puri. Spinodal decomposition via surface diffusion in polymer mixtures. *Phys. Rev. E*, 74(1):011804, 2006.
- [194] W. Jiang, W. Bao, C. V. Thompson, and D. J. Srolovitz. Phase field approach for simulating solid-state dewetting problems. *Acta mater.*, 60(15):5578–5592, 2012.
- [195] H. D. Ceniceros and C. J. García-Cervera. A new approach for the numerical solution of diffusion equations with variable and degenerate mobility. *J. Comput. Phys.*, 246:1–10, 2013.
- [196] J. W. Cahn and J. E. Taylor. Overview no. 113 surface motion by surface diffusion. *Acta Metall. Mater.*, 42(4):1045–1063, 1994.
- [197] A. A. Lee, A. Münch, and E. Süli. Degenerate mobilities in phase field models are insufficient to capture surface diffusion. *Appl. Phys. Lett.*, 107(8):081603, 2015.
- [198] A. A. Lee, A. Munch, and E. Suli. Sharp-interface limits of the cahn–hilliard equation with degenerate mobility. *SIAM J. Appl. Math.*, 76(2):433–456, 2016.
- [199] K. Ahmed, T. Allen, and A. El-Azab. Phase field modeling for grain growth in porous solids. *J. Mater. Sci.*, 51(3):1261–1277, 2016.
- [200] C. Gugenberger, R. Spatschek, and K. Kassner. Comparison of phase-field models for surface diffusion. *Phys. Rev. E*, 78(1):016703, 2008.
- [201] J. Deng. A phase field model of sintering with direction-dependent diffusion. *Mater. Trans.*, 53(2):385–389, 2012.

- [202] K. Ahmed, C. Yablinsky, A. Schulte, T. Allen, and A. El-Azab. Phase field modeling of the effect of porosity on grain growth kinetics in polycrystalline ceramics. *Model. Simul. Mater. Sc.*, 21(6):065005, 2013.
- [203] A. Novick-Cohen. Triple-junction motion for an allen–cahn/cahn–hilliard system. *Physica D*, 137(1-2):1–24, 2000.
- [204] M. Mahadevan and R. M. Bradley. Phase field model of surface electromigration in single crystal metal thin films. *Physica D*, 126(3-4):201–213, 1999.
- [205] S. G. Kim, W. T. Kim, and T. Suzuki. Interfacial compositions of solid and liquid in a phase-field model with finite interface thickness for isothermal solidification in binary alloys. *Phys. Rev. E*, 58(3):3316, 1998.
- [206] W. W. Mullins. Flattening of a nearly plane solid surface due to capillarity. *J. Appl. Phys.*, 30(1):77–83, 1959.
- [207] C. Joshi, T. Abinandanan, R. Mukherjee, and A. Choudhury. Destabilisation of nanoporous membranes through gb grooving and grain growth. *Comp. Mater. Sci.*, 139:75–83, 2017.
- [208] P. Zhou and W. C. Johnson. Discussion on the mechanism of electromigration from the perspective of electromagnetism. *J. Electron. Mater.*, 39(12):2583–2587, 2010.
- [209] N. Wang and N. Provatas. Role of stress-driven interfacial instability in the failure of confined electric interconnects. *Phys. Rev. Appl.*, 7:024032, Feb 2017.
- [210] S.-B. Liang, C.-B. Ke, M.-B. Zhou, and X.-P. Zhang. Phase field simulation of morphological evolution and migration of the microvoid in small scale solder interconnects driven by temperature gradient. In *Electronic Packaging Technology (ICEPT), 2016 17th International Conference on*, pages 953–957. IEEE, 2016.
- [211] P. Kuhn, J. Krug, F. Hausser, and A. Voigt. Complex shape evolution of electromigration-driven single-layer islands. *Phys. Rev. Lett.*, 94(16):166105, 2005.
- [212] A. Kumar, D. Dasgupta, and D. Maroudas. Complex pattern formation from current-driven dynamics of single-layer homoepitaxial islands on crystalline conducting substrates. *Phys. Rev. Appl.*, 8(1):014035, 2017.
- [213] D. Dasgupta, A. Kumar, and D. Maroudas. Analysis of current-driven oscillatory dynamics of single-layer homoepitaxial islands on crystalline conducting substrates. *Surf. Sci.*, 669:25–33, 2018.

- [214] L.-T. Yan and X.-M. Xie. Wetting-layer formation mechanisms of surface-directed phase separation under different quench depths with off-critical compositions in polymer binary mixture. *J. Chem. Phys.*, 126(6):064908, 2007.
- [215] H. Hori, O. Urakawa, O. Yano, and Q. Tran-Cong-Miyata. Phase separation of binary polymer mixtures under an electric field. *Macromolecules*, 40(2):389–394, 2007.
- [216] G. Zhang and G. Qiao. Polymerization-induced spinodal decomposition of ethylene glycol/phenolic resin solutions under electric fields. *J. Chem. Phys.*, 139(13):134903, 2013.
- [217] S. Foerster, A. K. Khandpur, J. Zhao, F. S. Bates, I. W. Hamley, A. J. Ryan, and W. Bras. Complex phase behavior of polyisoprene-polystyrene diblock copolymers near the order-disorder transition. *Macromolecules*, 27(23):6922–6935, 1994.
- [218] I. W. Hamley, K. A. Koppi, J. H. Rosedale, F. S. Bates, K. Almdal, and K. Mortensen. Hexagonal mesophases between lamellae and cylinders in a diblock copolymer melt. *Macromolecules*, 26(22):5959–5970, 1993.
- [219] M. W. Matsen and F. Bates. Origins of complex self-assembly in block copolymers. *Macromolecules*, 29(23):7641–7644, 1996.
- [220] A. S. Zalusky, R. Olayo-Valles, J. H. Wolf, and M. A. Hillmyer. Ordered nanoporous polymers from polystyrene-poly lactide block copolymers. *J. Am. Chem. Soc.*, 124(43):12761–12773, 2002.
- [221] S. Ludwigs, A. Böker, A. Voronov, N. Rehse, R. Magerle, and G. Krausch. Self-assembly of functional nanostructures from abc triblock copolymers. *Nat. Mater.*, 2(11):744–747, 2003.
- [222] A. Knoll, A. Horvat, K. Lyakhova, G. Krausch, G. Sevink, A. Zvelindovsky, and R. Magerle. Phase behavior in thin films of cylinder-forming block copolymers. *Phys. Rev. Lett.*, 89(3):035501, 2002.
- [223] M. Disko, K. Liang, S. Behal, R. Roe, and K. Jeon. Catenoid-lamellar phase in blends of styrene-butadiene diblock copolymer and homopolymer. *Macromolecules*, 26(11):2983–2986, 1993.
- [224] K. Michielsen and H. De Raedt. Morphological image analysis. *Comput. Phys. Commun.*, 132(1):94–103, 2000.
- [225] K. Michielsen and H. De Raedt. Integral-geometry morphological image analysis. *Phys. Rep.*, 347(6):461–538, 2001.

- [226] A. Aksimentiev, M. Fialkowski, and R. Holyst. Morphology of surfaces in mesoscopic polymers, surfactants, electrons, or reaction-diffusion systems: Methods, simulations, and measurements. *Adv. Chem. Phys.*, 121:141–240, 2002.
- [227] G. Sevink and A. Zvelindovsky. Kinetic pathways of sheared block copolymer systems derived from minkowski functionals. *J. Chem. Phys.*, 121(8):3864–3873, 2004.
- [228] M. Matsen. Stability of a block-copolymer lamella in a strong electric field. *Phys. Rev. Lett.*, 95(25):258302, 2005.
- [229] W. Mullins and P. Shewmon. The kinetics of grain boundary grooving in copper. *Acta Metall. Mater.*, 7(3):163–170, 1959.
- [230] P. Sachenko, J. Schneibel, J. Swadener, and W. Zhang. Experimental and simulated grain boundary groove profiles in tungsten. *Phil. Mag. Lett.*, 80(9):627–631, 2000.
- [231] E. Rabkin, A. Gabelev, L. Klinger, V. Semenov, and S. Bozhko. Grain boundary grooving in molybdenum bicrystals. *J. Mater. Sci.*, 41(16):5151–5160, 2006.
- [232] M. McLean and E. Hondros. A study of grain-boundary grooving at the platinum/alumina interface. *J. Mater. Sci.*, 6(1):19–24, 1971.
- [233] D. M. Saylor and G. S. Rohrer. Measuring the influence of grain-boundary misorientation on thermal groove geometry in ceramic polycrystals. *J. Am. Ceram. Soc.*, 82(6):1529–1536, 1999.
- [234] E. Rabkin, L. Klinger, and V. Semenov. Grain boundary grooving at the singular surfaces. *Acta Mater.*, 48(7):1533–1540, 2000.
- [235] W. Mullins. The effect of thermal grooving on grain boundary motion. *Acta Metall. Mater.*, 6(6):414–427, 1958.
- [236] J. Palmer, C. Thompson, and H. I. Smith. Grain growth and grain size distributions in thin germanium films. *J. Appl. Phys.*, 62(6):2492–2497, 1987.
- [237] H. Frost, C. Thompson, and D. Walton. Simulation of thin film grain structures. grain growth stagnation. *Acta Metall. Mater.*, 38(8):1455–1462, 1990.
- [238] K. Miller, F. Lange, and D. Marshall. The instability of polycrystalline thin films: Experiment and theory. *J. Mater. Res.*, 5(1):151–160, 1990.
- [239] D. Srolovitz and S. Safran. Capillary instabilities in thin films. ii. kinetics. *J. Appl. Phys.*, 60(1):255–260, 1986.

- [240] M. Keane, M. K. Mahapatra, A. Verma, and P. Singh. Lsm-ysz interactions and anode delamination in solid oxide electrolysis cells. *Int. J. Hydrogen Energ.*, 37(22):16776–16785, 2012.
- [241] T. Ryll, H. Galinski, L. Schlagenhauf, P. Elser, J. L. Rupp, A. Bieberle-Hutter, and L. J. Gauckler. Microscopic and nanoscopic three-phase-boundaries of platinum thin-film electrodes on ysz electrolyte. *Adv. Funct. Mater.*, 21(3):565–572, 2011.
- [242] Y.-S. Chou and J. W. Stevenson. Novel silver/mica multilayer compressive seals for solid-oxide fuel cells: The effect of thermal cycling and material degradation on leak behavior. *J. Mater. Res.*, 18(9):2243–2250, 2003.
- [243] P. Martin. Thermal grooving by surface diffusion: Mullins revisited and extended to multiple grooves. *Q. Appl. Math.*, 67(1):125–136, 2009.
- [244] C. Herring. The physics of powder metallurgy ed we kingston. *New York: McGraw-Hill*, page 143, 1951.
- [245] W. Robertson. Grain-boundary grooving by surface diffusion for finite surface slopes. *J. Appl. Phys.*, 42(1):463–467, 1971.
- [246] W. Zhang and J. H. Schneibel. Numerical simulation of grain-boundary grooving by surface diffusion. *Comp. Mater. Sci.*, 3(3):347–358, 1995.
- [247] M. Khenner, A. Averbuch, M. Israeli, and M. Nathan. Numerical simulation of grain-boundary grooving by level set method. *J. Comput. Phys.*, 170(2):764–784, 2001.
- [248] H. Frost, C. Thompson, and D. Walton. Simulation of thin film grain structures. abnormal grain growth. *Acta Metall. Mater.*, 40(4):779–793, 1992.
- [249] R. M. German. Sintering theory and practice. *Solar-Terrestrial Physics (Solnechno-zemnaya fizika)*, page 568, 1996.
- [250] I.-W. Chen and X.-H. Wang. Sintering dense nanocrystalline ceramics without final-stage grain growth. *Nature*, 404(6774):168, 2000.
- [251] A. Lewis, D. Josell, and T. P. Weihs. Stability in thin film multilayers and microlaminates: the role of free energy, structure, and orientation at interfaces and grain boundaries. *Scripta Mater.*, 48(8):1079–1085, 2003.
- [252] H. Wan, Y. Shen, J. Wang, Z. Shen, and X. Jin. A predictive model for microstructure evolution in metallic multilayers with immiscible constituents. *Acta Mater.*, 60(19):6869–6881, 2012.

- [253] S. Karim, M. Toimil-Molaes, A. Balogh, W. Ensinger, T. Cornelius, E. Khan, and R. Neumann. Morphological evolution of au nanowires controlled by rayleigh instability. *Nanotechnology*, 17(24):5954, 2006.
- [254] A. J. Bernoff, A. L. Bertozzi, and T. P. Witelski. Axisymmetric surface diffusion: dynamics and stability of self-similar pinchoff. *J. Stat. Phys.*, 93(3-4):725–776, 1998.
- [255] M. K. Santala and A. M. Glaeser. Rayleigh instabilities in crystalline solids: Evolution of finite-aspect-ratio pore channels in sapphire. *Acta Mater.*, 56(9):1967–1980, 2008.
- [256] J. Lloyd. Blacks law revisited nucleation and growth in electromigration failure. *Microelectron. Reliab.*, 47(9):1468–1472, 2007.
- [257] E. Glickman and L. Klinger. Grain boundary grooving as the mechanism of the blech electromigration in interconnects. In *MRS Proceedings*, volume 391, page 243. Cambridge Univ Press, 1995.
- [258] S.-H. Rhee, Y. Du, and P. S. Ho. Thermal stress characteristics of cu/oxide and cu/low-k submicron interconnect structures. *J. Appl. Phys.*, 93(7):3926–3933, 2003.
- [259] I. Noyan, C. E. Murray, J. S. Chey, and C. C. Goldsmith. Finite size effects in stress analysis of interconnect structures. *Appl. Phys. Lett.*, 85(5):724–726, 2004.
- [260] J. Proost, J. DHaen, M. Jin, and B. Verlinden. On the atomistic details of electromigration-induced drift. *Scripta mater.*, 50(2):267–271, 2004.
- [261] O. Kononenko, V. Matveev, and D. Field. Em activation energy in aluminum conductors tested by the drift velocity method. *Scripta Mater.*, 42(6):621–626, 2000.
- [262] S. Hackney and G. Ojard. Grain boundary grooving at finite grain size. *Scripta Metall. Mater.*, 22(11):1731–1735, 1988.
- [263] A. Hunt, S. Riege, and J. Prybyla. Healing processes in submicron al interconnects after electromigration failure. *Appl. Phys. Lett.*, 70(19):2541–2543, 1997.
- [264] A. Averbuch, M. Israeli, M. Nathan, and I. Ravve. Surface evolution in bare bamboo-type metal lines under diffusion and electric field effects. *J. Comput. Phys.*, 188(2):640–677, 2003.
- [265] W. Yang, W. Wang, and Z. Suo. Cavity and dislocation instability due to electric current. *J. Mech. Phys. Solids*, 42(6):897–911, 1994.

- [266] Z. Suo, W. Wang, and M. Yang. Electromigration instability: Transgranular slits in interconnects. *Appl. Phys. Lett.*, 64(15):1944–1946, 1994.
- [267] J. Santoki, A. Mukherjee, D. Schneider, M. Selzer, and B. Nestler. Phase-field study of electromigration-induced shape evolution of a transgranular finger-like slit. *J. Electron. Mater.*, 48(1):182–193, 2019.
- [268] E. Kreyszig. *Advanced engineering mathematics*. John Wiley & Sons, 2010.
- [269] E. Glickman and M. Molotskii. On the effect of grain boundary segregation on electromigration driving force in thin metal films. *Mater. Lett.*, 26(1-2):65–68, 1996.
- [270] E. E. Glickman. Grain boundary electromigration in thin films: interface reaction and segregation effects. In *Defect Diffus. Forum*, volume 156, pages 147–160. Trans Tech Publ, 1998.
- [271] N. Somaiah, D. Sharma, and P. Kumar. Electric current induced forward and anomalous backward mass transport. *J. Phys. D Appl. Phys.*, 49(20):20LT01, 2016.
- [272] I. Park, S. Park, H.-W. Park, T. Chang, H. Yang, and C. Y. Ryu. Unexpected hexagonally perforated layer morphology of ps-b-pmma block copolymer in supported thin film. *Macromolecules*, 39(1):315–318, 2006.
- [273] L. Zhu, P. Huang, S. Z. Cheng, Q. Ge, R. P. Quirk, E. L. Thomas, B. Lotz, J.-C. Wittmann, B. S. Hsiao, F. Yeh, et al. Dislocation-controlled perforated layer phase in a peo-b-ps diblock copolymer. *Phys. Rev. Lett.*, 86(26):6030, 2001.
- [274] Y. Tsori. Lamellar phases in nonuniform electric fields: Breaking the in-plane rotation symmetry and the role of dielectric constant mismatch. *Macromolecules*, 40(5):1698–1702, 2007.
- [275] D. Kan and X. He. Tuning phase structures of a symmetrical diblock copolymer with a patterned electric field. *Soft matter*, 12(19):4449–4456, 2016.
- [276] U. Welling and M. Müller. Ordering block copolymers with structured electrodes. *Soft matter*, 13(2):486–495, 2017.
- [277] Q. Zhang, R. Xu, D. Kan, and X. He. Molecular dynamics simulation of electric-field-induced self-assembly of diblock copolymers. *J. Chem. Phys.*, 144(23):234901, 2016.
- [278] Y. Tsori, F. Tournilhac, D. Andelman, and L. Leibler. Structural changes in block copolymers: coupling of electric field and mobile ions. *Phys. Rev. Lett.*, 90(14):145504, 2003.

- [279] G. G. Putzel, D. Andelman, Y. Tsori, and M. Schick. Ionic effects on the electric field needed to orient dielectric lamellae. *J. Chem. Phys.*, 132(16):164903, 2010.
- [280] A. Dehghan, M. Schick, and A.-C. Shi. Effect of mobile ions on the electric field needed to orient charged diblock copolymer thin films. *J. Chem. Phys.*, 143(13):134902, 2015.
- [281] P. C. Millett. Time-dependent ginzburg-landau model for nonfrustrated linear a b c triblock terpolymers. *Phys. Rev. E*, 92(2):022602, 2015.
- [282] F. Genin, W. Mullins, and P. Wynblatt. Capillary instabilities in thin films: a model of thermal pitting at grain boundary vertices. *Acta Metall. Mater.*, 40(12):3239–3248, 1992.
- [283] B. Nestler, H. Garcke, and B. Stinner. Multicomponent alloy solidification: phase-field modeling and simulations. *Phys. Rev. E*, 71(4):041609, 2005.
- [284] L. Klinger. Surface evolution in two-component system. *Acta mater.*, 50(13):3385–3395, 2002.
- [285] P.-R. Cha, S. G. Kim, D.-H. Yeon, and J.-K. Yoon. A phase field model for the solute drag on moving grain boundaries. *Acta mater.*, 50(15):3817–3829, 2002.
- [286] K. Grönhagen and J. gren. Grain-boundary segregation and dynamic solute drag theorya phase-field approach. *Acta mater.*, 55(3):955–960, 2007.
- [287] S. G. Kim and Y. B. Park. Grain boundary segregation, solute drag and abnormal grain growth. *Acta Mater.*, 56(15):3739–3753, 2008.
- [288] J. Li, J. Wang, and G. Yang. Phase field modeling of grain boundary migration with solute drag. *Acta Mater.*, 57(7):2108–2120, 2009.
- [289] T. Surholt and C. Herzig. Grain boundary self-diffusion in cu polycrystals of different purity. *Acta mater.*, 45(9):3817–3823, 1997.
- [290] M. Shabalin and D. Fuks. Density functional theory study of the influence of segregation of s or fe impurities on electromigration in nano-grained copper interconnects. *J. Appl. Phys.*, 117(19):195303, 2015.
- [291] Q. Ma and Z. Suo. Precipitate drifting and coarsening caused by electromigration. *J. Appl. Phys.*, 74(9):5457–5462, 1993.
- [292] A. Karma and W.-J. Rappel. Quantitative phase-field modeling of dendritic growth in two and three dimensions. *Phys. Rev. E*, 57(4):4323, 1998.

- [293] B. Echebarria, R. Folch, A. Karma, and M. Plapp. Quantitative phase-field model of alloy solidification. *Phys. Rev. E*, 70(6):061604, 2004.
- [294] R. Folch and M. Plapp. Quantitative phase-field modeling of two-phase growth. *Phys. Rev. E*, 72(1):011602, 2005.
- [295] N. Ofori-Opoku and N. Provatas. A quantitative multi-phase field model of polycrystalline alloy solidification. *Acta Mater.*, 58(6):2155–2164, 2010.
- [296] A. Choudhury and B. Nestler. Grand-potential formulation for multicomponent phase transformations combined with thin-interface asymptotics of the double-obstacle potential. *Phys. Rev. E*, 85(2):021602, 2012.
- [297] L. Amirouche and M. Plapp. Phase-field modeling of the discontinuous precipitation reaction. *Acta mater.*, 57(1):237–247, 2009.
- [298] R. Verma, A. Sharma, K. Kargupta, and J. Bhaumik. Electric field induced instability and pattern formation in thin liquid films. *Langmuir*, 21(8):3710–3721, 2005.
- [299] N. Arun, A. Sharma, V. B. Shenoy, and K. Narayan. Electric-field-controlled surface instabilities in soft elastic films. *Adv. Mater.*, 18(5):660–663, 2006.
- [300] J. Sarkar, A. Sharma, and V. B. Shenoy. Electric-field induced instabilities and morphological phase transitions in soft elastic films. *Phys. Rev. E*, 77(3):031604, 2008.
- [301] D. Du and D. Srolovitz. Electrostatic field-induced surface instability. *Appl. Phys. Lett.*, 85(21):4917–4919, 2004.
- [302] V. Gill, P. Guduru, and B. Sheldon. Electric field induced surface diffusion and micro/nano-scale island growth. *Int. J. Solids Struct.*, 45(3-4):943–958, 2008.
- [303] F. Yang and W. Song. Morphological instability of elastic thin films—effect of electromechanical interaction. *Appl. Phys. Lett.*, 87(11):111912, 2005.
- [304] C.-h. Chiu, C. Poh, and Z. Huang. Morphological stability of the stranski-krastanow systems under an electric field. *Appl. Phys. Lett.*, 88(24):241906, 2006.
- [305] W. T. Gózdź and R. Hołyst. Triply periodic surfaces and multiply continuous structures from the landau model of microemulsions. *Phys. Rev. E*, 54(5):5012, 1996.
- [306] J. W. Cahn. Theory of crystal growth and interface motion in crystalline materials. *Acta Metall. Mater.*, 8(8):554–562, 1960.